



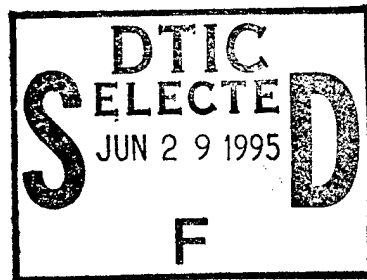
**US Army Corps  
of Engineers**

Waterways Experiment  
Station

Technical Report CERC-95-4  
May 1995

# Directional Wind Wave Characteristics at Harvest Platform

*by Charles E. Long*



DTIC QUALITY INSPECTED 8

Approved For Public Release; Distribution Is Unlimited

19950628 025

DTIC QUALITY INSPECTED 8

Prepared for Headquarters, U.S. Army Corps of Engineers

The contents of this report are not to be used for advertising, publication, or promotional purposes. Citation of trade names does not constitute an official endorsement or approval of the use of such commercial products.



PRINTED ON RECYCLED PAPER

# Directional Wind Wave Characteristics at Harvest Platform

by Charles E. Long

U.S. Army Corps of Engineers  
Waterways Experiment Station  
3909 Halls Ferry Road  
Vicksburg, MS 39180-6199

Accession For	
NTIS CRA&I	<input checked="" type="checkbox"/>
DTIC TAB	<input type="checkbox"/>
Unannounced	<input type="checkbox"/>
Justification .....	
By .....	
Distribution /	
Availability Codes	
Dist	Avail and/or Special
A-1	

Final report

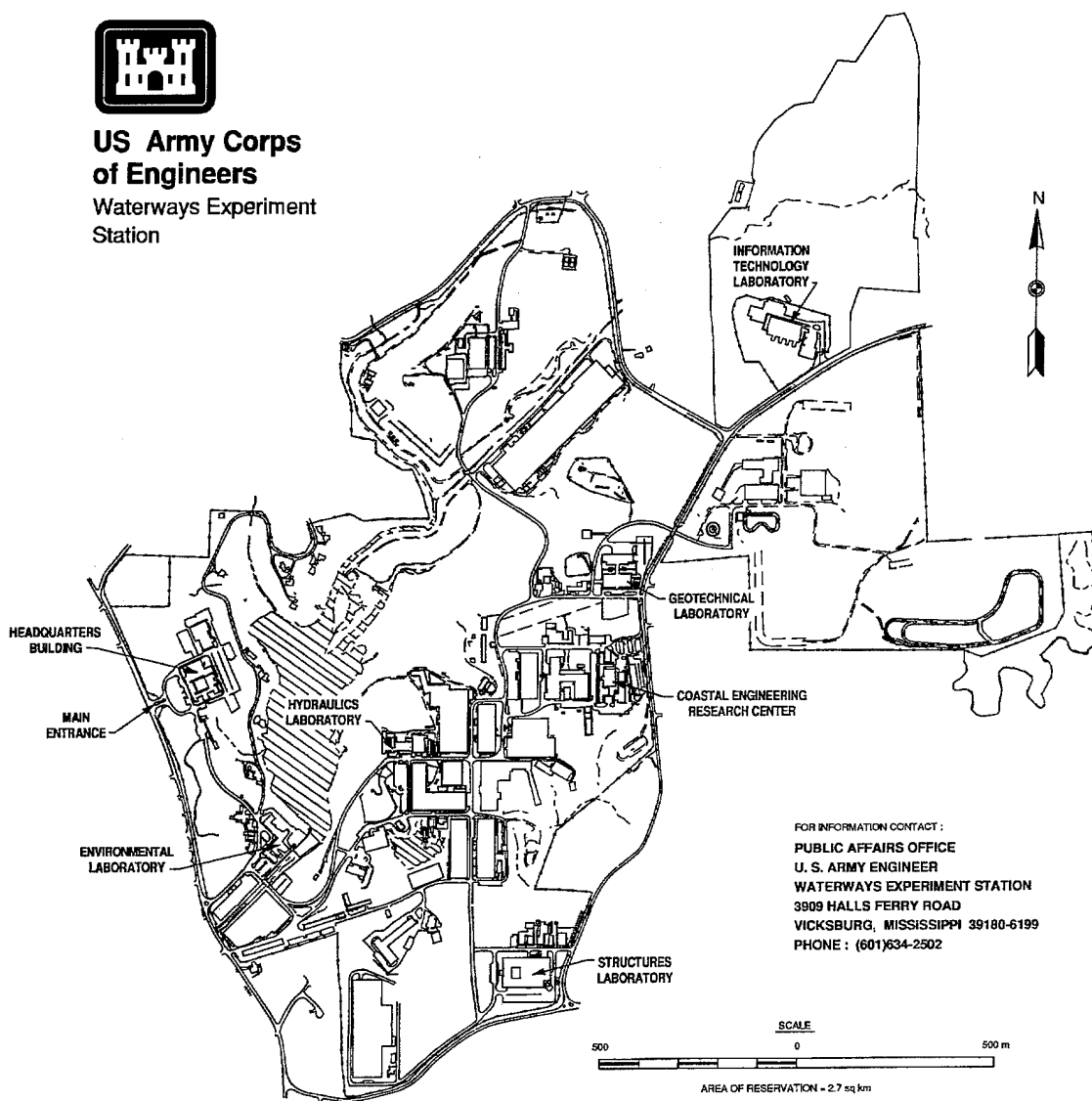
Approved for public release; distribution is unlimited

Prepared for U.S. Army Corps of Engineers  
Washington, DC 20314-1000

Under Work Unit 32484



**US Army Corps  
of Engineers**  
Waterways Experiment  
Station



**Waterways Experiment Station Cataloging-in-Publication Data**

Long, Charles E.

Directional wind wave characteristics at Harvest Platform / by Charles E. Long ; prepared for U.S. Army Corps of Engineers.

182 p. : ill. ; 28 cm. — (Technical report ; CERC-95-4)

Includes bibliographic references.

1. Ocean waves — Measurement — Instruments. 2. Wind waves — Measurement. 3. Water waves — Measurement. 4. Frequency spectra. I. United States. Army. Corps of Engineers. II. U.S. Army Engineer Waterways Experiment Station. III. Coastal Engineering Research Center (U.S.) IV. Title. V. Series: Technical report (U.S. Army Engineer Waterways Experiment Station) ; CERC-95-4.

TA7 W34 no.CERC-95-4

# Contents

---

Preface .....	v
1—Introduction .....	1
2—Directional Gauge .....	4
Gauge Layout .....	4
Pressure Gauges and Data Collection Scheme .....	5
3—Primary Data Analysis .....	7
Error Checking .....	7
Frequency-Direction Spectra .....	12
4—Characterizing Parameters .....	16
Bulk Parameters .....	16
Frequency-Dependent Parameters .....	21
Summary of Parameters .....	24
5—Bulk Parametric Behavior .....	25
Time Series of Bulk Parameters .....	25
Bulk Parameter Probability Densities .....	32
Parameter Correlations with Wave Height .....	40
Summary of Bulk Parameters .....	47
6—Frequency-Dependent Parameters .....	48
Spectral Density and Peak Direction .....	48
Circular Moment Parameters .....	52
Quartile Spread and Asymmetry .....	56
Modal Analysis .....	60
Summary of Frequency-Dependent Parameters .....	62
7—Examples of Spectra .....	63

8—Characteristic Directional Distribution Functions . . . . .	67
Classification Algorithms . . . . .	67
Resulting Distributions . . . . .	69
9—Accuracy of Directional Distribution Estimates . . . . .	72
Test Method . . . . .	72
Test Distributions . . . . .	75
Test Results . . . . .	76
10—Accuracy of Directional Parameters . . . . .	80
Peak Direction . . . . .	80
Circular Moment Parameters . . . . .	83
Quartile Parameters . . . . .	89
Summary of Parameter Accuracy . . . . .	91
11—Summary . . . . .	94
Gauge and Basic Data Set . . . . .	94
Bulk Parameters . . . . .	95
Frequency-Dependent Parameters . . . . .	96
Representative Results . . . . .	97
Gauge Accuracy . . . . .	98
Closing Comment . . . . .	98
References . . . . .	100
Appendix A: Time Series Graphs of Bulk Parameters . . . . .	A1
Appendix B: Graphs of Example Spectra . . . . .	B1
Appendix C: Graphs of Characteristic Directional Distributions . . . . .	C1
Appendix D: Graphs of Test Results . . . . .	D1
Appendix E: Notation . . . . .	E1

SF 298

# Preface

---

This report describes measurement and results of analysis of wind wave directional distributions at Texaco Oil Company's Harvest Platform, located near the 200-m (656-ft) isobath about 20 km (10.8 n.m.) west of Point Conception, California. The work was motivated by a need to quantify and develop a climatology of the variability in natural wind wave energy distributions at a deepwater site on the exposed California coast. A six-element, high-resolution directional wave gauge was used for this purpose. This effort was authorized by Headquarters, U.S. Army Corps of Engineers (HQUSACE), under Civil Works Coastal Flooding and Storm Protection Program Research Work Unit 32484, "Directionality of Waves in Shallow Water." Funds were provided through the Coastal Engineering Research Center (CERC), U.S. Army Engineer Waterways Experiment Station (WES), under the program management of Ms. Carolyn M. Holmes, CERC. Messrs. John H. Lockhart, Jr., Charles Chesnutt, Barry W. Holliday, and John F. C. Sanda were HQUSACE Technical Monitors.

This report was prepared by Dr. Charles E. Long at WES's Field Research Facility (FRF) in Duck, NC, under the direct supervision of Mr. William A. Birkemeier, Chief, FRF, and Mr. Thomas W. Richardson, Chief, Engineering Development Division (EDD), CERC. General supervision was provided by Dr. James R. Houston and Mr. Charles C. Calhoun, Jr., Director and Assistant Director, CERC, respectively.

Mr. David D. McGehee, Prototype Measurement and Analysis Branch, EDD, CERC, was instrumental in coordinating the efforts of CERC and the State of California in gauge installation. Drs. Robert T. Guza and Thomas H. C. Herbers of the Center for Coastal Studies, Scripps Institution of Oceanography (SIO), and Dr. Joan M. Oltman-Shay of Quest Integrated, Inc., Kent, Washington, assisted in gauge array design. Data transfer between SIO and the FRF was coordinated through SIO's Coastal Data Information Program, under the direction of Dr. Richard J. Seymour, with particularly helpful assistance from Ms. Julianna Thomas. The contributions of all of these individuals are gratefully acknowledged.

At the time of publication of this report, Director of WES was Dr. Robert W. Whalin. Commander was COL Bruce K. Howard, EN.

# 1 Introduction

---

Long-term observations of well-resolved, deep-ocean, wind wave frequency-direction energy spectra are essential for advancing knowledge in ocean surface dynamics. This knowledge is required for such things as providing ground truth to help interpret satellite imagery of the ocean surface, testing evolution and propagation models of open-ocean wind waves, and establishing seaward boundary conditions for models of wave propagation and transformation from deep water to coastal regions. The latter problem is of considerable interest in coastal engineering because wind waves generated offshore are among the dominant forcing mechanisms for coastal dynamic processes.

This problem is particularly pronounced in the region of the Southern California Bight (Figure 1), where waves generated in the deep ocean must propagate past a number of offshore islands to reach the coast. Refractive, diffractive, and dissipative effects of the bathymetry around the islands have strong local effects on the amount of wave energy reaching the shore, and these effects are quite sensitive to the directions of incident wave propagation (O'Reilly and Guza 1991, 1993). To gain insight into the nature of directionally distributed wind wave energy from the open ocean in the vicinity of the Southern California Bight, a high-resolution directional wave gauge has been installed on a deepwater oil production platform near the north end of the bight. Called the Harvest Platform, the structure is owned by Texaco Oil Company, which allowed the platform to be used for scientific purposes through an agreement with the State of California.

As indicated in Figure 1, Harvest Platform is located about 20 km (10.8 n.m.) west of Point Conception, California, in water with a mean depth of 202 m (663 ft). Waves originating in the greater Pacific Ocean can reach the platform via relatively unobstructed paths from the north, west, and south, and thus represent conditions on the seaward side of the offshore island chain. Though the water depth is considerable, it is expected that some bathymetrically induced transformation occurs for low-frequency wind waves in the vicinity of the platform. With a nominal frequency range of 0.04 to 0.3 Hz, wind waves obeying linear wave theory have wavelengths in the range 18 to 870 m (59 to 2,854 ft) in water of about 200-m (656-ft) depth. Waves with lengths of about twice the water depth and longer will be influenced by the ocean bottom. Thus, waves with lengths of 400 to 870 m (1,312 to 2,854 ft), or frequencies in the range 0.04 to 0.06 Hz, are expected to be affected. The



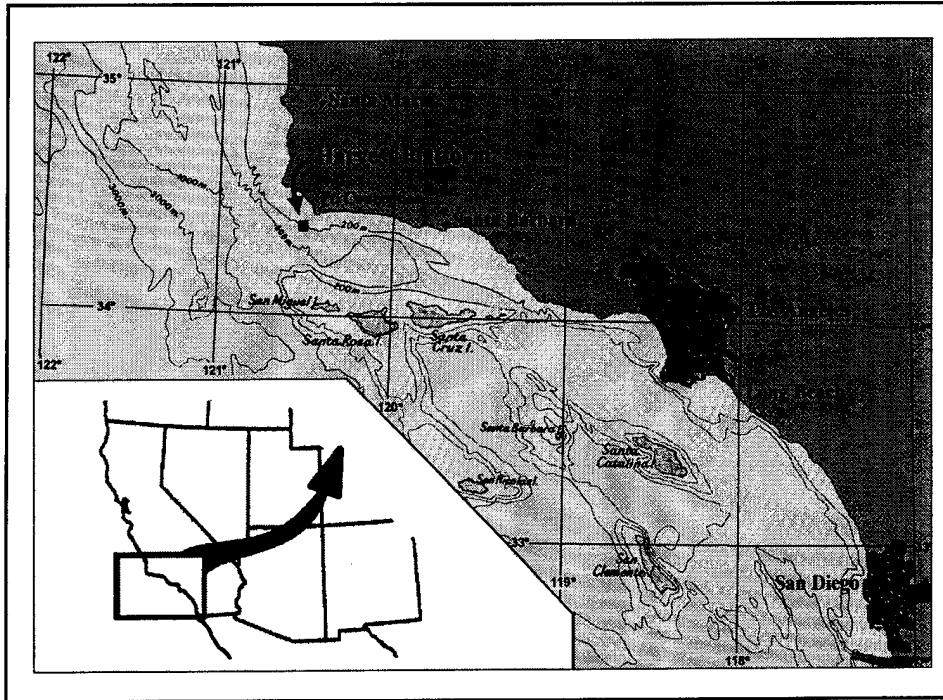


Figure 1. Southern California Bight and location of Harvest Platform

primary effect is a modest turning of the deepwater wave propagation direction towards a bathymetry-normal azimuth. This process can be modeled with reasonable simplicity so that true deepwater conditions can be estimated from observations at Harvest Platform.

Because the platform structure is stationary, reasonably rigid, and of considerable horizontal dimensions, it is nearly ideal for deploying a spatial array of subsurface pressure sensors to establish the geometry of a directional wave gauge. When coupled with a high-resolution mathematical analysis technique, the system allows routine collection of well-resolved wind wave frequency-direction spectra that can be accumulated in a database for use in climatological studies as well as the objectives mentioned above.

The primary purpose of this report is to describe some of the characteristics of directionally distributed wave energy observed at Harvest Platform in the course of 1 year. The directional gauge was installed and operating as of mid-November 1992. It is convenient to report observations beginning on 1 January 1993 and to include all observations during calendar year 1993. This report additionally includes several parts related to the design and expected performance of the directional gauge. Chapter 2 describes the gauge geometry, including some of its design considerations and constraints, and the data collection scheme. Chapter 3 shows the basic directional estimation algorithm along with routine error-checking procedures. Chapter 4 defines some parameters used to characterize the observations. Chapters 5 and 6 discuss how these parameters behave for bulk spectra and at individual frequencies, respectively. Time series graphs of bulk parameters are presented in Appendix A. Representative frequency-direction spectra are discussed in Chapter 7, and

illustrated in Appendix B. Chapter 8 discusses, and Appendix C illustrates, some characteristic directional distribution functions derived from classifying, grouping, and averaging observations from the whole data set. Chapters 9 and 10 contain analyses of directional resolution and parametric resolution, respectively, based on the characteristic distributions described in Chapter 8. Graphs of test results discussed in Chapter 9 are presented in Appendix D. Main results of this study are summarized in Chapter 11.

## 2 Directional Gauge

---

### Gauge Layout

The fundamental detector in a directional gauge of the type used here is a set or *array* of subsurface pressure gauges. A number of design considerations and constraints had to be satisfied in constructing the Harvest Platform array. These conditions resulted in some compromises in both wave frequency and direction resolving ability of the final design. For the spacings (called *lags*) between pairs of gauges to be tuned to the wind waves of interest, one would like long lags for long waves and shorter lags for short waves within the wind wave frequency band. It is desired to have the gauges near the ocean surface so that signals from high-frequency waves are not overly attenuated by depth, and, at the same time, have the gauges deep enough so that they do not become exposed to air in the troughs of extremely large waves.

Conditions for reasonable wave detection had to be balanced against the geometrical and logistical constraints of an operating oil platform. In plan view, Harvest Platform has a rectangular outline of nominal dimensions 23 m (75 ft) by 65 m (213 ft). These dimensions represent the largest possible horizontal gauge spacings in two orthogonal directions. Additional limitations were imposed on these dimensions by the availability of structural members on which to mount the gauges. A safe gauge depth was determined to be in excess of 9 m (29.5 ft), based on observations from prior gauging of an extreme wave height of about 18 m (59 ft).<sup>1</sup> A depth that satisfied this constraint and that also had platform structure for gauge mounting was about 16 m (52.5 ft).

In initial array design, it was determined that nine gauges would provide the best wave response by establishing lag spacings that increased in reasonably uniform increments within the spatial constraints of the platform. Additionally, it was desired to establish redundant lags to ensure that wave data were not being compromised by passing around and through the open structure of Harvest Platform itself. Funding limitations reduced to six the number

---

<sup>1</sup> Personal communication, 1991, Dr. R. J. Seymour, Coastal Data Information Program (CDIP), Scripps Institution of Oceanography (SIO).

of gauges that could be purchased, installed, and maintained on a regular basis.

The array design that evolved from these constraints, and the one installed on Harvest Platform, is shown in plan view in Figure 2. This figure also shows the gauge numbering scheme, the orientation of the array relative to geophysical coordinates, and the direction convention used in this report. The outside dimensions of the array are 22.7 m (74.5 ft) by 59.4 m (194.9 ft), which utilizes almost the whole of the platform dimensions. Because the gauges are mounted on a fixed structure, their positions are known to within a few centimeters. Note that the regular spacing of the gauges provides a number of redundant lags for testing platform interference. Specifically, cross spectra of wave signals between gauge pairs 1-4, 2-3, and 5-6 should be identical, as should cross spectra between gauge pairs 1-2 and 4-3, as well as 1-5 and 4-6. An example of such cross spectra computed from measured wave signals is shown in Chapter 3.

All six gauges were mounted at 15.72 m (51.57 ft) below mean sea level, which satisfies the safe depth constraint. Surface correction of wave signals from this depth using the linear wave pressure response function (*Shore Protection Manual* 1984) is quite conservative in that the signal-to-noise ratio for these gauges is quite high (typically order 100) at the highest resolvable wave frequency. This highest frequency is established not by frequency response limitations, but by the shortest lag spacing of the array. To avoid aliasing in directional estimation, the shortest wavelength that can be resolved is twice the shortest lag spacing, or 45.4 m (149.0 ft) for this array. This wavelength corresponds to a wave frequency of about 0.18 Hz. To be conservatively clear of aliasing effects, signal analysis used in this report was truncated at 0.16 Hz for directional estimation.

Though the final installed array was less than theoretically ideal, its response and direction-resolving ability are quite reasonable. Quantification of directional resolution for this array is presented in Chapters 9 and 10 of this report.

## Pressure Gauges and Data Collection Scheme

Individual sensors were Model TJE absolute pressure sensors manufactured by Sensotec Transducer Company with operating ranges of 0 to 100 psia (0 to 689.5 kPa), and a manufacturer's stated accuracy of  $\pm 0.1$  percent of full scale. The set of six gauges on Harvest Platform were sampled simultaneously at 1 Hz, digitized, then fed to a concentrator where the set of samples was buffered. Buffered signals were periodically transmitted to shore through a telephone connection, and ultimately stored on the main computer of the CDIP, Ocean Engineering Research Group, Marine Research Division, SIO, La Jolla, CA.

Sample sets known as *collections* consist of time series of data from each of the six gauges. Each time series is 8,192 sec (2 hr 16 min 32 sec) in-

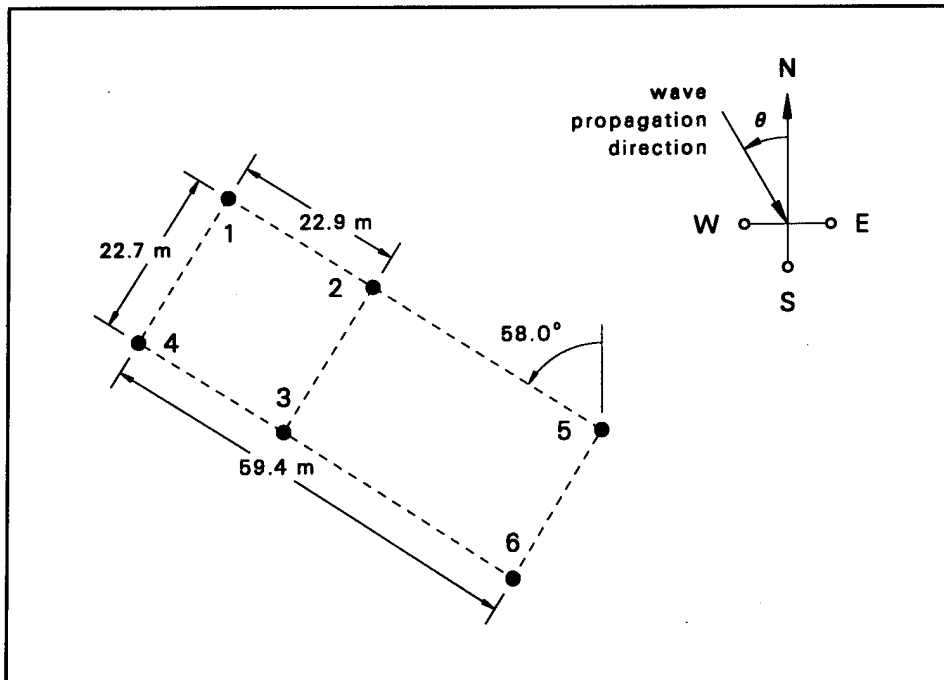


Figure 2. Dimensions and orientation of the Harvest Platform array

length. Collections were made eight times daily, at approximately 3-hr intervals. From 1 January to 2 July 1993, nominal collection start times were 0100, 0400, 0700, 1000, 1300, 1600, 1900, and 2200 Greenwich Mean Time (GMT). From 3 July to 31 December 1993, nominal collection start times were 0200, 0500, 0800, 1100, 1400, 1700, 2000, and 2300 GMT. Actual collection start times varied by several minutes on either side of a given nominal start time because the amount of time required to establish a phone link varied from collection to collection.

Data processing for results presented in this report was not performed at the CDIP site, and so is independent of the processing done and published by that group (CDIP *Monthly Reports*). Data collections were transferred to the Field Research Facility (FRF) of the U.S. Army Engineer Waterways Experiment Station's Coastal Engineering Research Center for processing by high-resolution techniques that are different from those used by CDIP. Initially, data transfer was achieved by way of magnetic tape, but later was accomplished over an electronic network.

All possible collections are not represented in the data set used for this report. A number of collections were lost because of the inability to establish or maintain electrically clean phone links to the concentrator on Harvest Platform. An additional number of collections were not processed because data did not satisfy error-checking constraints established at the FRF analysis site. These error-checking methods are discussed in Chapter 3 of this report. Of the maximum possible 2,920 collections during calendar year 1993, a total of 2,339 collections were acquired and processed.

### 3 Primary Data Analysis

---

For logistically successful collections, initial data processing was done by checking data quality through a series of gauge intercomparisons, and, for data of sufficient quality, computing frequency-direction spectra as primary results. All of these steps rely on Fourier analysis of pressure gauge time series data, and subsequent computation of cross-spectral densities. A discussion of error-checking procedures then leads logically to the subsequent steps involved in frequency-direction spectral computation.

#### Error Checking

The first step in data processing is computation of discrete estimates of frequency autospectra of pressure signals, and surface-corrected cross-spectral densities of signals from all pairs of gauges. Cross spectra are denoted  $C_{ij}(f_n) - iQ_{ij}(f_n)$ , where  $C_{ij}(f_n)$  is the coincident spectrum,  $Q_{ij}(f_n)$  is the quadrature spectrum,  $i$  and  $j$  are indices ranging in value from 1 to 6 that refer to the gauge numbers shown in Figure 2, and  $f_n$  is the  $n^{\text{th}}$  of a set of  $N$  discrete frequencies.<sup>1</sup> Frequency autospectra are denoted  $S(f_n)$ , and, if surface corrected, are identically equal to  $C_{ii}(f_n)$ . All spectra are computed using Welch's method (Welch 1967) with standard Fourier analysis techniques (Bendat and Piersol 1971).

In a collection, the 8,192-sec time series from each gauge is analyzed in 15 half-lapped segments of 1,024 sec duration. Each segment is demeaned, tapered with a variance-preserving window, and converted to the frequency domain with a discrete Fourier transform. At this point, the analysis is split into two parts: estimates of pressure autospectra from each gauge at depth, and estimates of surface-corrected cross spectra of sea surface displacement. For cross-spectral estimates, each transformed segment of pressure data is corrected to a sea surface displacement transform using the linear wave pressure response function (Dean and Dalrymple 1984). Raw cross-spectral estimates are formed from temporally corresponding transform segments among all pairs of gauges. Raw autospectral estimates are formed from each of the 15 transform segments for each individual gauge.

---

<sup>1</sup> For convenience, symbols and abbreviations are listed in the notation (Appendix E).

For both autospectra and cross spectra, smooth estimates are formed by averaging raw estimates over all 15 segments, and further smoothing is achieved by averaging results over 10 adjacent frequency bands. Final resolution frequency bandwidth is  $df = 0.00977$  Hz, and, because of the spatial Nyquist limits discussed in Chapter 2, the wind wave pass band of frequencies ranges from 0.044 to 0.162 Hz, which corresponds to ( $N =$ ) 13 discrete frequency bands. Degrees of freedom for spectral estimates range from 160 to about 200, depending on the extent to which the second halves of time series segments are correlated with the first halves (Welch 1967).

### Autospectral intercomparisons

One part of error checking is graphic intercomparisons among the six pressure gauges of signal means and autospectra, an example of which is shown in the lower left graph of Figure 3. Frequency autospectral estimates of data from all six pressure gauges are plotted on the same set of axes from the first resolvable frequency band out to the temporal Nyquist frequency (0.5 Hz, half the 1-Hz sampling frequency). As can be seen, the most energetic parts of the spectra are in the analysis pass band of frequencies. At the highest frequencies shown in this graph are the spectra of what is dominantly system and data transmission noise, called the *noise floor*. If a pressure gauge is malfunctioning, its autospectrum will deviate from the main group of curves, and become immediately obvious. A deviate noise floor from one of the gauges indicates spiky or jumpy data, another cause for concern.

The small inset graph in the lower left graph of Figure 3 is an analysis of signal means. The closely packed, nearly constant group of symbols represents the deviations of the segment means from the median of the set of segment means for each of the 15 segments. If a gauge develops significant drift problems, it will become immediately obvious as a symbol that deviates from the main group of symbols. As shown, Figure 3 is somewhat difficult to read, but it has been reduced in this report for publication purposes, and is much easier to read in its original size. The triangle symbols in the small inset graph show the deviation of the indicated water surface from mean sea level (gauge height off the bottom plus median of gauge mean depths for each segment minus the total long-term mean ocean depth of 202 m), and is therefore an indication of tide stage at Harvest Platform for each of the 15 segments in a collection.

### Coherence and phase comparisons

The next step in general analysis, and one useful for error checking, is the computation of a dimensionless cross spectrum  $M_{ij}(f_n)$ , which can be expressed as a complex, Hermitian matrix in terms of dimensional cross spectra by

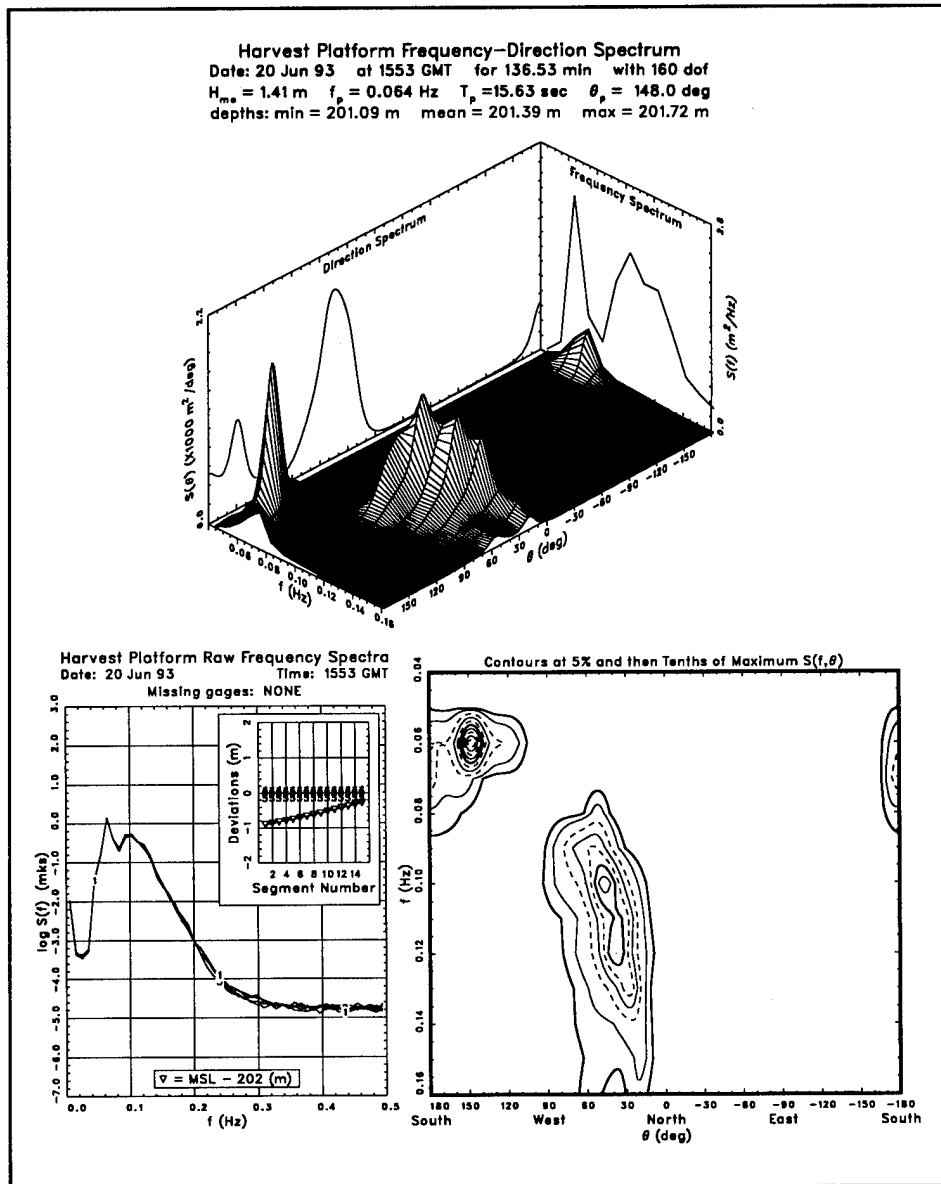


Figure 3. Autospectral intercomparison and frequency-direction spectral estimate

$$M_{ij}(f_n) = \frac{C_{ij}(f_n) - iQ_{ij}(f_n)}{\sqrt{C_{ii}(f_n)} \sqrt{C_{jj}(f_n)}} \quad (1)$$

Equation 1 is used in directional spectral estimation, but its use in error checking is in its relation to coherence and phase estimates. Coherence of signals from gauges  $i$  and  $j$  at discrete frequency  $f_n$  is defined in terms of the dimensionless cross spectrum as



$$\Gamma_{ij}^2(f_n) = |M_{ij}(f_n)|^2 \quad (2)$$

Signal phase difference of gauge  $i$  relative to gauge  $j$  at frequency  $f_n$  is

$$\phi_{ij}(f_n) = \tan^{-1} \left[ \frac{\text{Im}[M_{ij}(f_n)]}{\text{Re}[M_{ij}(f_n)]} \right] \quad (3)$$

where  $\text{Re}[\ ]$  and  $\text{Im}[\ ]$  are the real and imaginary parts, respectively, of the entity contained in square brackets.

As mentioned in Chapter 2, if multiple pairs of gauges are arranged so that each pair is separated by the same distance and has the same directional orientation from one gauge to the second gauge, then in a uniform wave field, cross spectra of the pairs of gauges should be identical. In the Harvest Platform array there are several such sets of pairs as can be seen in Figure 2. Specifically, in terms of coherences and phases defined by Equations 2 and 3, one would expect

$$\Gamma_{14}(f_n) = \Gamma_{23}(f_n) = \Gamma_{56}(f_n) \quad \phi_{14}(f_n) = \phi_{23}(f_n) = \phi_{56}(f_n) \quad (4)$$

as well as

$$\Gamma_{12}(f_n) = \Gamma_{43}(f_n) \quad \phi_{12}(f_n) = \phi_{43}(f_n) \quad (5)$$

and

$$\Gamma_{15}(f_n) = \Gamma_{46}(f_n) \quad \phi_{15}(f_n) = \phi_{46}(f_n) \quad (6)$$

Figure 4 is an example of coherence and phase error checking, showing graphs of the seven coherence and phase functions named in Equations 4, 5, and 6 (upper, middle, and lower sets of graphs in Figure 4, respectively). For any set of wave approach directions, some of the gauges are on the up-wave side of the platform, and others are on the down-wave side. If the platform legs, risers, and other structural members caused significant distortion of the wave field, there would be clear disagreement among the various curves illustrated in Figure 4. No such disagreement is obvious in Figure 4, which is exemplary of acceptable collections, so it is concluded that Harvest Platform does not interfere in a significant way with wind waves as observed by these gauges.

An occasional problem occurs in the data collection procedure that is also detectable with coherence and phase plots. Sometimes a data point is dropped during telephone transmission from the data buffer. When this happens, the time series of data for the affected gauge is effectively shifted by one time step relative to data from the other gauges. If not caught, a lost data point

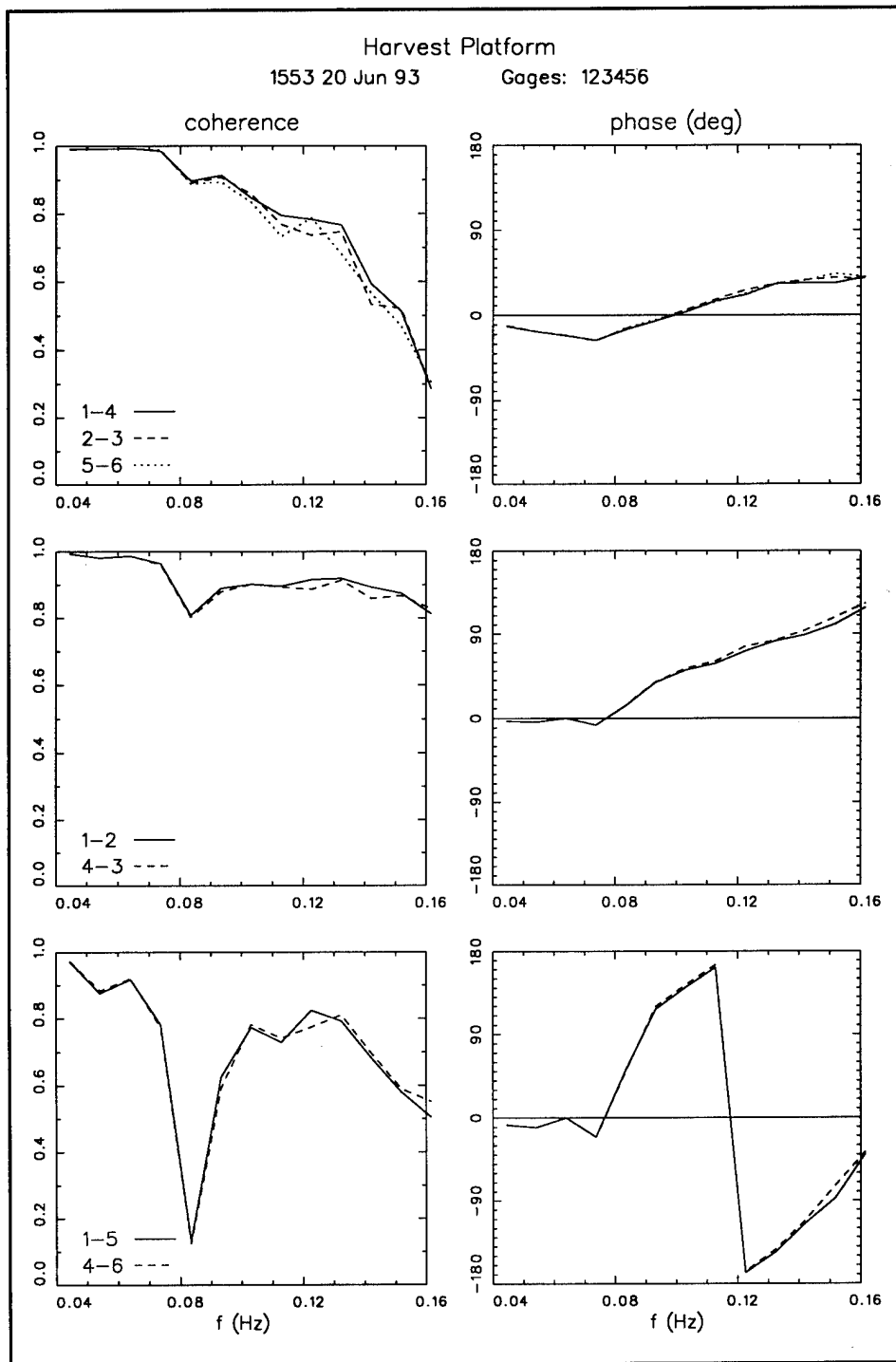


Figure 4. Sample coherence and phase function comparisons

can have devastating effects on directional spectral estimation. However, such a data loss is readily apparent in a graphic display like Figure 4. At a 1-Hz sample rate, a single lost data point early in a collection induces a phase shift of about 15 deg for 0.04-Hz waves and about 60 deg for 0.16-Hz waves. If the phase function curves like those in Figure 4 deviate from each other by

such phase shifts, it is quite apparent. If a data point is lost later in a collection, the evident phase shifts are relatively less because only part of a time series is then out of phase with other gauge records. If a data point is lost late in a collection, it is difficult to detect in graphs like those of Figure 4, but the effect of the lost point is greatly reduced because most of the time series are in phase.

The combined effects of intercomparing frequency autospectra and coherence and phase functions for the pressure gauge array on Harvest Platform provide clear indications of faulty or suspect data. When such conditions are detected in a collection, frequency-direction spectra are not computed. Such rigorous examination of the data ensures that only high-quality time series are used in directional estimation.

## Frequency-Direction Spectra

Estimates of frequency-direction spectra are made using the iterative maximum likelihood estimator (IMLE) developed by Pawka (1983). The first step in this method is a computation of the maximum likelihood estimate (MLE) described by Davis and Regier (1977). All estimates determine directional distribution functions on a frequency-by-frequency basis. At a given frequency, a directional distribution function  $D(f_n, \theta_m)$  is related to its corresponding frequency-direction spectrum  $S(f_n, \theta_m)$  by

$$D(f_n, \theta_m) = \frac{S(f_n, \theta_m)}{S(f_n)} \quad (7)$$

where  $\theta_m$  is a discrete angle indicating the direction from which wave energy arrives, measured counterclockwise from true north, as indicated in Figure 2. The direction index  $m$  ranges from  $m = 1$  to  $m = M = 181$ , while direction ranges from  $\theta_1 = -180$  deg to  $\theta_{181} = 180$  deg in steps of  $d\theta = 2$  deg. The normalizing term in the denominator on the right-hand side of Equation 7 is the sea surface displacement variance spectral density. Because the integral with respect to direction of  $S(f_n, \theta_m)$  is identically  $S(f_n)$ , the directional distribution function has the property

$$\sum_{m=1}^M D(f_n, \theta_m) d\theta = 1 \quad (8)$$

for all  $f_n$ .

The lowest order estimate is the MLE, which takes the form

$$D_0(f_n, \theta_m) = \frac{a_0}{d\theta \sum_{i=1}^I \sum_{j=1}^I M_{ij}^{-1}(f_n) e^{i\bar{k}_n(\theta_m) \cdot (\bar{x}_i - \bar{x}_j)}} \quad (9)$$

where  $a_0$  is a factor of order 1 that is used to ensure Equation 8 is satisfied,  $I$  is the number of gauges, the  $M_{ij}^{-1}(f_n)$  are elements of the inverse of the dimensionless cross-spectral matrix defined by Equation 1,  $\bar{k}_n(\theta_m)$  is the wave number vector, and  $\bar{x}_i$  and  $\bar{x}_j$  are coordinate position vectors of gauges  $i$  and  $j$ , respectively. The wave number vector  $\bar{k}_n(\theta_m)$  is a function of both frequency and direction, being defined as

$$\bar{k}_n(\theta_m) = k_n \cos \theta_m \hat{e}_x + k_n \sin \theta_m \hat{e}_y \quad (10)$$

where  $\hat{e}_x$  and  $\hat{e}_y$  are spatial coordinate unit vectors in the  $x$ - and  $y$ -directions, respectively, and  $k_n$  is wave number vector magnitude, which is related with gravitational acceleration  $g$  to frequency  $f_n$  and water depth  $d$  through the linear wave dispersion relation

$$4\pi^2 f_n^2 = g k_n \tanh k_n d \quad (11)$$

The need for the iterative part of the estimator arises because the zeroth order estimate of Equation 9 can be shown to produce directional distributions that are too directionally broad relative to true directional distributions. An IMLE result is achieved in several computational steps. At the  $r^{\text{th}}$  iteration step, an estimate  $'M_{ij}(f_n)$  of the observed cross-spectral matrix  $M_{ij}(f_n)$  is computed from the previous directional distribution function estimate  $D_{r-1}(f_n, \theta_m)$  by

$$'M_{ij}(f_n) = \sum_{m=1}^M D_{r-1}(f_n, \theta_m) e^{i\bar{k}_n(\theta_m) \cdot (\bar{x}_i - \bar{x}_j)} d\theta \quad (12)$$

A new intermediate directional distribution function estimate  $D'_r(f_n, \theta_m)$  is computed using the cross-spectral matrix of Equation 12 by

$$D'_r(f_n, \theta_m) = \frac{a_r}{d\theta \sum_{i=1}^I \sum_{j=1}^I 'M_{ij}^{-1}(f_n) e^{i\bar{k}_n(\theta_m) \cdot (\bar{x}_i - \bar{x}_j)}} \quad (13)$$

where  $a_r$ , like  $a_0$ , is adjusted so that Equation 8 is satisfied for  $D'_r(f_n, \theta_m)$ . A correction is computed for  $D'_r(f_n, \theta_m)$  by first computing

$$\lambda_r(f_n, \theta_m) = 1 - \frac{D'_r(f_n, \theta_m)}{D_0(f_n, \theta_m)} \quad (14)$$

and then finding a new directional distribution function estimate  $D_r(f_n, \theta_m)$  from

$$D_r(f_n, \theta_m) = D'_r(f_n, \theta_m) \left[ 1 + \frac{|\lambda_r(f_n, \theta_m)|^{\beta+1}}{\gamma \lambda_r(f_n, \theta_m)} \right] \quad (15)$$

The parameters  $\beta$  and  $\gamma$  in Equation 15 control the rate of convergence of the estimator. As used by Pawka (1983), the values  $\beta = 1$  and  $\gamma = 5$  were used for all estimates discussed in this report.

An objective of the iterative technique is to try to make estimates of the cross spectrum computed with Equation 12 as close as possible to the measured cross spectrum of Equation 1. In each iterative loop, a convergence check  $\epsilon_r$  is computed as the sum of the squared magnitudes of the differences of the two cross spectra. This takes the form

$$\epsilon_r = \sum_{i=1}^I \sum_{j=1}^I |M_{ij}(f_n) - M'_{ij}(f_n)|^2 \quad (16)$$

Iteration continues as long as  $\epsilon_r$  decreases between successive iterations, or until an upper limit  $R$  of iterations has been completed. In computations reported herein,  $R = 30$  because tests with synthetic data have indicated that very little increase in accuracy is generally obtained if a higher iteration limit is used.

Equations 9 to 16 form the basis of the IMLE technique. For a given frequency, and for the iteration  $r$  that satisfies the convergence check, the dimensional directional distribution of energy is formed from

$$S(f_n, \theta_m) = S(f_n) D_r(f_n, \theta_m) \quad (17)$$

When evaluated for all frequencies in the wind wave pass band, the resulting entity is the frequency-direction spectrum for a given collection. An example of such a spectrum is illustrated in Figure 3. The upper graph is a three-dimensional plot of  $S(f_n, \theta_m)$ , and the lower right graph is a contour plot of the spectrum. The right panel in the three-dimensional plot is a linear graph

of the discrete frequency spectrum  $S(f_n)$ , which is related to the frequency-direction spectrum by

$$S(f_n) = \sum_{m=1}^M S(f_n, \theta_m) d\theta \quad (18)$$

The left panel in the three-dimensional plot is a linear graph of the direction spectrum  $S(\theta_m)$ , which is the directional analog of the frequency spectrum, defined by

$$S(\theta_m) = \sum_{n=1}^N S(f_n, \theta_m) df \quad (19)$$

Figure 3 illustrates a case having a moderate amount of energy, with a low-frequency peak of wave energy arriving from slightly west of south, and a second mode of energy having greater spread in both frequency and direction arriving from the northwest quadrant. To classify this spectrum, as well as all the spectra in the 1993 year of observations at Harvest Platform, a set of characterizing parameters is defined in Chapter 4. The behavior and relationships among those parameters, discussed in subsequent chapters, then reveal some of the directional characteristics at this site.

## 4 Characterizing Parameters

---

Two groups of parameters are used to characterize the members of the set of frequency-direction spectra used in this study. One set, called *bulk parameters*, attempts to characterize whole spectra (like the three-dimensional plot in Figure 3) so that common features and correlations among various properties can be identified. The other set of parameters characterizes components of frequency-direction spectra on a frequency-by-frequency basis. Called *frequency-dependent parameters*, they characterize directional properties that can be identified with low-, medium-, and high-frequency parts of the observed spectra. This chapter defines the parameters used. Parametric behavior is described in Chapters 5 and 6.

### Bulk Parameters

A set of nine parameters, along with total water depth and modal analyses of both frequency and direction spectra, are defined to help characterize complete frequency-direction spectra. The nine parameters are characteristic wave height, peak frequency, two measures of characteristic direction, two measures of directional spread, two measures of asymmetry of directionally distributed wave energy, and a measure of kurtosis of directional distributions. This section establishes the mathematical definitions of these parameters.

#### Wave height

In this report, the conventional definition of characteristic wave height based on 4 times sea surface displacement variance is used. Denoted  $H_{mo}$ , it can be defined in terms of the full frequency-direction spectrum, the frequency spectrum defined by Equation 18, or the direction spectrum defined by Equation 19. A definition that relates all of these entities is

$$\frac{H_{mo}^2}{16} = \sum_{m=1}^M \sum_{n=1}^N S(f_n, \theta_m) df d\theta = \sum_{n=1}^N S(f_n) df = \sum_{m=1}^M S(\theta_m) d\theta \quad (20)$$

## Peak frequency

Peak frequency  $f_p$  is defined as the discrete frequency at which the frequency spectrum  $S(f_n)$  is maximum. This definition is also conventional, in that it is the usual characteristic frequency defined for nondirectional gauges. It represents the frequency that has the most overall wave energy, and is subject to less statistical estimation uncertainty than the most logical alternative peak frequency definition, which is the frequency at which  $S(f_n, \theta_m)$  is maximum.

## Peak direction

There are several ways to designate a characteristic direction for a distribution of energy. Two ways are used in this report. One is based on a circular moment of the distribution, and is defined in the following section. A simpler one, but one that is subject to considerable statistical uncertainty, is a point of maximum variance density in a directional distribution. In this report, a peak direction  $\theta_p$  is defined as the direction of maximum variance density in the directional distribution associated with the peak frequency. In symbols,  $\theta_p$  is the direction at which  $S(f_p, \theta_m)$  is a maximum. It is interpreted as the direction of the most energetic waves at the frequency containing the greatest overall energy.

## Parameters from circular moments

A set of parameters that define a characteristic mean direction, as well as measures of directional spread, skewness, and kurtosis was proposed by Kuik, van Vledder, and Holthuijsen (1988) based on theoretical and analogical arguments by Borgman (1969) and Mardia (1972) involving circular moments. Though derived for directional distributions at individual frequencies, the definitions can be applied to any directional distribution function. For the purposes of characterizing a frequency-direction spectrum as a whole, the directional spectrum  $S(\theta_m)$ , as defined by Equation 19, can be used because it represents total wave energy in any given direction arc.

To define a proper directional distribution function (one that integrates to unit area),  $S(\theta_m)$  must be normalized by its own area. By Equation 20, this area is identically  $\frac{1}{16} H_{m0}^2$ , so the appropriate directional distribution function is

$$D(\theta_m) = \frac{16}{H_{m0}^2} S(\theta_m) \quad m = 1, 2, \dots, M \quad (21)$$

Discrete approximations of the circular moments defined by Kuik, van Vledder, and Holthuijsen (1988) in terms of  $D(\theta_m)$  take the forms



$$m_1 = \sum_{m=1}^M \cos(\theta_m - \theta_0) D(\theta_m) d\theta \quad (22)$$

$$n_1 = \sum_{m=1}^M \sin(\theta_m - \theta_0) D(\theta_m) d\theta \quad (23)$$

$$m_2 = \sum_{m=1}^M \cos(2\theta_m - 2\theta_0) D(\theta_m) d\theta \quad (24)$$

$$n_2 = \sum_{m=1}^M \sin(2\theta_m - 2\theta_0) D(\theta_m) d\theta \quad (25)$$

where  $\theta_0$  is a characteristic direction called the *mean direction* defined by requiring  $n_1 = 0$ . With this constraint, Equation 23 can be solved for mean direction with the result

$$\theta_0 = \tan^{-1} \left[ \frac{\sum_{m=1}^M \sin \theta_m D(\theta_m) d\theta}{\sum_{m=1}^M \cos \theta_m D(\theta_m) d\theta} \right] \quad (26)$$

With  $\theta_0$  determined by Equation 26, the remaining circular moments  $m_1$ ,  $m_2$ , and  $n_2$  can be computed from Equations 22, 24, and 25, respectively.

Kuik, van Vledder, and Holthuijsen (1988) then define a measure of directional spread called the *circular width*  $\sigma$  as

$$\sigma = (2 - 2m_1)^{1/2} \quad (27)$$

as well as a measure of asymmetry of a directional distribution called the *circular skewness*  $\gamma$ , given by

$$\gamma = \frac{-n_2}{\left(\frac{1}{2} - \frac{1}{2}m_2\right)^{3/2}} \quad (28)$$

and a measure of the flatness of a directional distribution called *circular kurtosis*  $\delta$ , which is

$$\delta = \frac{6 - 8m_1 + 2m_2}{(2 - 2m_1)^2} \quad (29)$$

The circular parameters  $\theta_0$ ,  $\sigma$ ,  $\gamma$ , and  $\delta$  are intended to be directional analogs of parameters derived from moments of linear functions like the frequency spectrum. Kuik, van Vledder, and Holthuijsen (1988) found the analogy to be quite good for narrow directional distributions of wave energy, and reasonable for a variety of broader distributions.

### Quartile parameters

Two parameters that are modestly more intuitive than the corresponding circular parameters, and are also useful for characterizing spread and asymmetry in directional distribution functions are the *quartile spread*  $\Delta\theta$  and *quartile asymmetry*  $A$  used by Long and Oltman-Shay (1991). The concept is based on the fact that any directional distribution function integrates across all directions to unity, and, for the Harvest Platform array, spans a full 360-deg viewing arc. An integral of the discrete distribution function from the direction of minimum energy  $\theta_{m_{min}}$  (where  $m_{min}$  is the discrete direction index at which the energy minimum occurs) to any arbitrary angle creates a function  $I(\theta_m - \theta_{m_{min}})$  that increases monotonically from zero to an upper limit of unity. The directions at which this integral (interpolated as necessary from discrete data) has the values  $\frac{1}{4}$ ,  $\frac{1}{2}$ , and  $\frac{3}{4}$  are the first quartile, median, and third quartile directions of the directional distribution, respectively. Differences among these directions then provide information about the spread and asymmetry of the distribution.

For bulk parameterization, the direction spectrum  $D(\theta_m)$  is used as a representative distribution function. The integral function is defined by

$$I(\theta_m - \theta_{m_{min}}) = \sum_{l=m_{min}}^m D(\theta_l) d\theta \quad (30)$$

and the quartile directions satisfy the equations

$$I(\theta_{25\%} - \theta_{m_{min}}) = 0.25 \quad (31)$$

$$I(\theta_{50\%} - \theta_{m_{min}}) = 0.50 \quad (32)$$

and

$$I(\theta_{75\%} - \theta_{m_{min}}) = 0.75 \quad (33)$$

where, if necessary, a distribution is treated as cyclic because the direction axis covers a complete circle.

A measure of directional spread  $\Delta\theta$  is

$$\Delta\theta = \theta_{75\%} - \theta_{25\%} \quad (34)$$

Because the range of directions in Equation 34 spans the two middle quartiles, this definition of directional spread has the specific interpretation that it is the arc subtending the central 50 percent of the energy distribution.

A measure of asymmetry of a distribution is the ratio of the directional width of the third quartile to that of the second quartile. By taking the natural logarithm of this ratio, a symmetric distribution has an asymmetry parameter  $A$  near zero, and that for a skewed distribution acquires a positive or negative sign if the skewness is toward larger or smaller angles, respectively. The asymmetry parameter is thus defined as

$$A = \ln \left[ \frac{\theta_{75\%} - \theta_{50\%}}{\theta_{50\%} - \theta_{25\%}} \right] \quad (35)$$

### Modal analysis

The number and intensity of energy peaks, or modes, indicate the number and relative importance of various wave source processes. For bulk characterization of observed spectra, a modal analysis is done both for directional modes, using  $D(\theta_m)$  as a characterizing function, and for frequency modes, using the normalized frequency spectrum  $16 S(f_n)/H_{mo}^2$  as a characterizing function.

Usually, a mode is distinguished as a local maximum in a distribution with modal boundaries identified as the adjacent minimal points. However, because the IMLE method can generate modestly spurious maxima, especially in the estimation of broad, flat true distributions, a governing condition must be imposed to ensure the distinction of true modes. In this report, a modal edge is defined as a minimum point for which a directional distribution has a value that is no greater than half the value of the lesser of the adjacent maximum points. For consistency, the same definition is used to analyze normalized frequency spectra. In both types of analysis, the number of modes is one less than the number of modal edges found in a distribution.

The area of a distribution between modal edges is a fraction less than or equal to unity, which, when multiplied by 100 percent, indicates the percent of total energy represented by that mode. By recording the percentage of energy in the modes of a distribution, it can be determined if secondary and higher modes contain significant amounts of energy, or are just relatively minor fluctuations in the low-energy tails of a distribution. In both direction and frequency modal analyses, percentages of energy in all modes are computed.

## Frequency-Dependent Parameters

Seven parameters are used to characterize directional distribution functions at each frequency for each collection. The parametric definitions are essentially the same as those used for bulk analysis except directional distribution functions  $D(f_n, \theta_m)$  at each frequency  $f_n$  are used as basis functions. In addition, a modal analysis is done for each distribution. This section introduces notation and provides definitions of these parameters. Note that because the basic analysis results in 13 discrete frequency bands, there are 13 frequency-dependent parameters derived from each collection.

### Peak direction

Using  $n$  in subscript form to denote the index of a discrete frequency  $f_n$ , the peak direction  $\theta_{pn}$  of a directional distribution function at that frequency  $D(f_n, \theta_m)$  is defined as the direction at which  $D(f_n, \theta_m)$  is a maximum.

### Parameters from circular moments

As in bulk characterization, there are parameters defining mean direction, circular width, circular skewness, and circular kurtosis for each of the 13 directional distributions in a collection. The forms of the definitions of these parameters are the same as for bulk parameters, but the basis distributions are different, and the notation is adapted to the fact that there is a set of parameters for each frequency.

The four basic circular moments at the  $n^{\text{th}}$  frequency  $f_n$  are

$$m_{1n} = \sum_{m=1}^M \cos(\theta_m - \theta_{0n}) D(f_n, \theta_m) d\theta \quad (36)$$

$$n_{1n} = \sum_{m=1}^M \sin(\theta_m - \theta_{0n}) D(f_n, \theta_m) d\theta \quad (37)$$

$$m_{2n} = \sum_{m=1}^M \cos(2\theta_m - 2\theta_{0n}) D(f_n, \theta_m) d\theta \quad (38)$$

$$n_{2n} = \sum_{m=1}^M \sin(2\theta_m - 2\theta_{0n}) D(f_n, \theta_m) d\theta \quad (39)$$

where  $\theta_{0n}$  is the mean direction at frequency  $f_n$  defined by requiring  $n_{1n} = 0$ . Solving for  $\theta_{0n}$  using Equation 37 leads to

$$\theta_{0n} = \tan^{-1} \left[ \frac{\sum_{m=1}^M \sin\theta_m D(f_n, \theta_m) d\theta}{\sum_{m=1}^M \cos\theta_m D(f_n, \theta_m) d\theta} \right] \quad (40)$$

which can be used in Equations 36, 38, and 39 to solve for  $m_{1n}$ ,  $m_{2n}$ , and  $n_{2n}$ , respectively.

Again following the work by Kuik, van Vledder, and Holthuijsen (1988), a frequency-dependent circular width  $\sigma_n$  is

$$\sigma_n = (2 - 2m_{1n})^{1/2} \quad (41)$$

a circular skewness  $\gamma_n$  is

$$\gamma_n = \frac{-n_{2n}}{\left(\frac{1}{2} - \frac{1}{2}m_{2n}\right)^{3/2}} \quad (42)$$

and a circular kurtosis  $\delta_n$  is

$$\delta_n = \frac{6 - 8m_{1n} + 2m_{2n}}{(2 - 2m_{1n})^2} \quad (43)$$

It is noted that the parameters  $\theta_{0n}$ ,  $\sigma_n$ ,  $\gamma_n$ , and  $\delta_n$  derived from directional distributions at individual frequencies are the types discussed by Kuik, van Vledder, and Holthuijsen (1988) in their work, so these frequency-dependent parameters may be more comparable to their results than the corresponding bulk parameters defined in the previous section.

## Quartile parameters

As with bulk parameters, frequency-dependent parameters for quartile spread  $\Delta\theta_n$  and quartile asymmetry  $A_n$  are useful in characterizing the directional distributions  $D(f_n, \theta_m)$ . The forms of their definitions follow Equations 30 to 35, and their meaning and interpretation are the same. For each frequency, an integral function  $I_n(\theta_m - \theta_{m_{min}})$  can be defined as

$$I_n(\theta_m - \theta_{m_{min}}) = \sum_{l=m_{min}}^m D(f_n, \theta_l) d\theta \quad (44)$$

where  $m_{min}$  is understood to be the direction index of the minimum of  $D(f_n, \theta_m)$  at the  $n^{th}$  frequency. Quartile directions satisfy

$$I_n(\theta_{25\%,n} - \theta_{m_{min}}) = 0.25 \quad (45)$$

$$I_n(\theta_{50\%,n} - \theta_{m_{min}}) = 0.50 \quad (46)$$

$$I_n(\theta_{75\%,n} - \theta_{m_{min}}) = 0.75 \quad (47)$$

The frequency-dependent quartile directions  $\theta_{25\%,n}$ ,  $\theta_{50\%,n}$ , and  $\theta_{75\%,n}$  determined from Equations 45, 46, and 47, respectively, are used to define directional spread

$$\Delta\theta_n = \theta_{75\%,n} - \theta_{25\%,n} \quad (48)$$

and asymmetry

$$A_n = \ln \left[ \frac{\theta_{75\%,n} - \theta_{50\%,n}}{\theta_{50\%,n} - \theta_{25\%,n}} \right] \quad (49)$$

for each frequency.

## Modal analysis

Modal analysis is also performed on  $D(f_n, \theta_m)$  for each frequency to determine the number and relative intensities of directional peaks. The reasoning and method are the same for the frequency-dependent analysis as was discussed for bulk modal analysis. The intent is to gain a more detailed description of modal structure as it may vary with frequency, and to get a more

quantitative understanding of modal character based on individual frequencies rather than that obtained from the somewhat smoothed integrated direction spectrum  $D(\theta_m)$ .

## Summary of Parameters

Frequency-direction spectra observed at Harvest Platform are characterized using a set of bulk parameters to describe whole spectra, and a set of frequency-dependent parameters to obtain more detail of directional energy distributions at individual frequencies. In addition to numbers and relative intensities of directional and frequency modes for the spectra as whole units, nine bulk parameters ( $H_{m0}$ ,  $f_p$ ,  $\theta_p$ ,  $\theta_0$ ,  $\sigma$ ,  $\gamma$ ,  $\delta$ ,  $\Delta\theta$ ,  $A$ ) yield considerable insight for general wind wave energy distribution. A more refined examination of these spectra is characterization of directional distributions frequency by frequency. Seven parameters ( $\theta_{pn}$ ,  $\theta_{0n}$ ,  $\sigma_n$ ,  $\gamma_n$ ,  $\delta_n$ ,  $\Delta\theta_n$ ,  $A_n$ ), as well as an analysis of directional modes, are used in this study.

Distributions, behavior, and interactions of the bulk spectral characteristics are shown and discussed in Chapter 5. Detailed, frequency-by-frequency characteristics are examined in Chapter 6. Some insight into the accuracy of the parameters derived from the present data set is given in Chapter 10.

## 5 Bulk Parametric Behavior

---

A way to examine the 1-year set of directional spectra observed at Harvest Platform is through the behavior of the characterizing bulk parameters. In this chapter, a wave climatology is discussed briefly based on time series of the bulk parameters illustrated in Appendix A. Statistical distributions of these parameters are also shown and discussed in this chapter to quantify ranges, typical values, and most common conditions. In the third part of this chapter, correlations among various bulk parameters are illustrated to see if, for example, there is a typical parametric behavior under high- or low-energy conditions.

### Time Series of Bulk Parameters

To show general spectral behavior in a climatological way, time series graphs of characterizing parameters are shown in Appendix A. Parameters are plotted in two groups for each month in the year of observations, with one group on each of two facing pages. Left-hand pages illustrate  $H_{mo}$ ,  $f_p$ ,  $\theta_p$ ,  $\theta_0$ ,  $\Delta\theta$ , and  $\sigma$ . Right-hand pages show  $d$ ,  $A$ ,  $\gamma$ ,  $\delta$ , percent of wave energy in each of up to three directional modes, and percent of wave energy in each of up to three frequency modes. As is shown in the following section, three is the maximum number of modes found in any of the  $S(\theta_m)$  or  $S(f_n)$  examined in this report.

### Wave height

Characteristic wave height  $H_{mo}$ , being derived from total sea surface displacement variance, indicates, among other conditions, the occurrence of high-energy events that are of concern to those concerned with shore protection. Data from Harvest Platform indicate a persistent, somewhat energetic wave climate with heights commonly in the range 1-2 m (3.3-6.6 ft). High-energy events occur in late fall, winter, and spring. Numerous events with wave heights between 3 and 4 m (9.8 and 13.1 ft) occurred in January, February, March, and April, with the annual cycle beginning again in November and December. The extreme event of the year occurred on 2 April with characteristic wave heights in excess of 5 m (16.4 ft). The lowest energy condition occurred on 1 October, where wave heights fell to about 0.6 m (2.0 ft).



## Peak frequency

Frequencies  $f_p$  representing peak energy levels in the observed frequency spectra cover the full range of discrete frequencies used to define the spectra. High peak frequencies occur in the initial stages of storm events. Very low peak frequencies tend to occur when the spectrum is dominated by waves from distant sources. Intermediate frequencies occur for all other wave conditions, with common values of 0.06 to 0.10 Hz. This behavior is consistent with conventional observations of wind sea and swell (Kinsman 1984), and so is not surprising.

## Characteristic directions

Two parameters, peak direction  $\theta_p$  and mean direction  $\theta_0$  have been defined to yield single characteristic directions for observed frequency-direction spectra. As shown in Appendix A,  $\theta_p$  tends mostly to lie in the range 50 to 70 deg west of north (following the direction convention shown in Figure 2), indicating that a common source of energetic waves is west-northwest of Harvest Platform. This region is the open North Pacific Ocean to which Harvest Platform is well-exposed. Variations in  $\theta_p$  during January, February, and March appear to be associated with some high-energy events that are also characterized by high peak frequencies, suggesting the presence of local storms. In the summer months of July, August, and September,  $\theta_p$  occasionally shifts abruptly to directions near  $\pm 180$  deg, and is associated with low peak frequencies. This behavior suggests dominance of the wave field by *southern swell*, which consists of waves generated in the South Pacific Ocean during the southern winter.

Mean direction  $\theta_0$  generally follows the pattern of  $\theta_p$ , but has a smaller magnitude of large fluctuations, and tends to vary more smoothly than  $\theta_p$ . The reason for these differences is that  $\theta_p$  is defined as the peak of the directional distribution at  $f_p$ , whereas  $\theta_0$  is based on integrals of  $D(\theta_m)$  (Equation 26), which tends to smooth the result, and  $D(\theta_m)$  is itself based on an integral of  $S(f_n, \theta_m)$  (Equations 19 and 21), which provides further smoothing. As a consequence, behavior of these two parameters must be interpreted carefully. For example, in a spectrum with both local wind sea and a dominant southern swell,  $\theta_p$  will (within the accuracy of the IMLE method) be the southern swell direction. Because of the smoothing effect of the integrals defining mean direction,  $\theta_0$  will be neither the southern swell direction nor the local wind sea direction (unless they are codirectional), but some direction in between. The two characteristic directions are more likely to agree if only southern swell is present, or if only local wind sea is present. There is also likely to be greater variation in estimates of  $\theta_p$  because it is based on a single point in  $S(f_n, \theta_m)$ , and so has fewer degrees of freedom than an integrated parameter like  $\theta_0$ .

To illustrate how they are related, Figure 5 shows the correlation of  $\theta_p$  and  $\theta_0$  based on the data shown in Appendix A. For this figure, data were recast along axes ranging from 0 to 270 deg instead of -180 to 180 deg by adding 360 deg to any negative parameter. This procedure clarified the relationship among parameters near  $\pm 180$  deg, and did not change the meaning of any data. Figure 5 shows only three quadrants because none of the characteristic directions were detected in the northeast quadrant, which is a range of directions with very short fetches from the continental land mass, and from which little wave energy is expected.

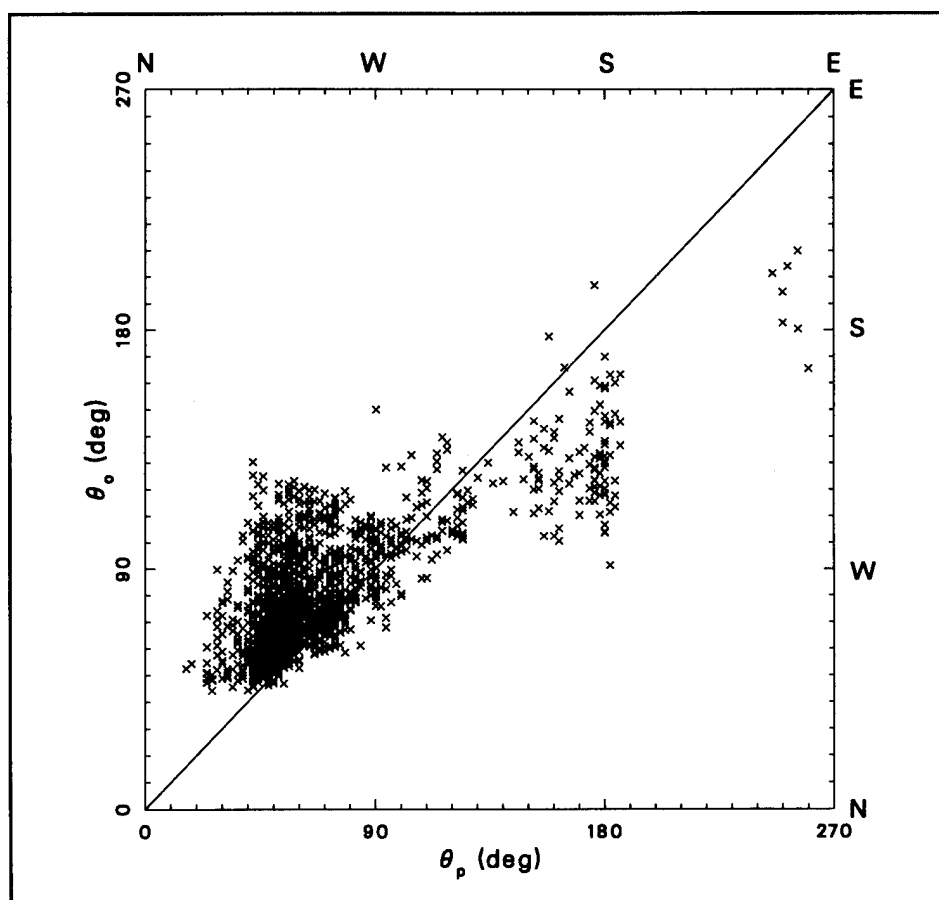


Figure 5. Correlation of characteristic direction parameters

Considerable scatter is seen in Figure 5, as well as the fact that the overall range of  $\theta_0$  is less than that of  $\theta_p$ . An extreme example of scatter occurs for  $\theta_0$  near 90 deg;  $\theta_p$  ranges from about 20 deg to more than 180 deg. The interpretation of this behavior is that numerous directional spectra have centroids represented by  $\theta_0$  in a small range near 90 deg, but extreme values that cover a broad range because some distributions are broad or multimodal, and  $\theta_p$  is a direction well displaced from the distribution centroid. Some scatter is also accounted for by less statistical reliability in estimates of  $\theta_p$ , and a slower

response of  $\theta_0$  to changing spectral conditions. A user of these data must use some caution in choice of either of these characteristic directions. The two directions have different meanings, and, in complex wave conditions, there may not be a single direction that represents any spectrum well.

### Directional spread parameters

Two parameters have been defined in this report that characterize angular spread of observations of  $D(\theta_m)$ . Time series of circular width  $\sigma$  and quartile spread  $\Delta\theta$  plotted in Appendix A show quite similar behaviors, though their numerical values differ. Using  $\Delta\theta$  as a representative descriptor, directional spreads appear to have a persistent background range of values between 20 and 60 deg with occasional excursions to a range of rather large values between 90 and 120 deg. Excursion events appear to be associated with some increases in wave energy as shown for the months of January, February, and March, and also during southern swell or storm events scattered from late July to late November. At times (e.g., in July and August), there are increases in spread parameters without corresponding shifts in  $\theta_p$  or  $\theta_0$ . This condition simply suggests that there may be multiple modes of energy, but the storm or southern swell event does not dominate.

Because  $\sigma$  and  $\Delta\theta$  appear to correspond well in the graphs in Appendix A, a scatter diagram has been constructed to indicate their correlation. As shown in Figure 6, the two parameters seem well correlated for high spreads ( $\Delta\theta$  greater than 90 deg), and less correlated at low spreads ( $\Delta\theta$  less than about 60 deg). Data points cluster in these two spread ranges, which crudely quantifies the dual regimes discussed in the previous paragraph. Because the correlation is reasonably good in Figure 6, it appears that one can estimate reasonably well one of these parameters given the other, especially at higher spreads.

It is noted that Kuik, van Vledder, and Holthuijsen (1988) multiply their  $\sigma$  by  $180/\pi$  to estimate a spreading angle in degrees, using an analogy with linear (vice circular) moments. Such an estimate is more exact for small spread, and appears reasonable for  $\sigma = 0.5$ , for which their spread estimate is approximately 29 deg, and  $\Delta\theta$  is in the range 20 to 40 deg based on Figure 6. However, for  $\sigma = 1$ , their spread estimate is about 57 deg, but Figure 6 indicates that  $\Delta\theta$  is in the range 120 to 140 deg, which is quite different. Though the numerical values are different, the reasonable correlation suggested by Figure 6 indicates that  $\sigma$  and  $\Delta\theta$  detect similar properties of a distribution. This subject should be pursued further because a meaningful, universally understandable measure of directional spread has yet to be defined.

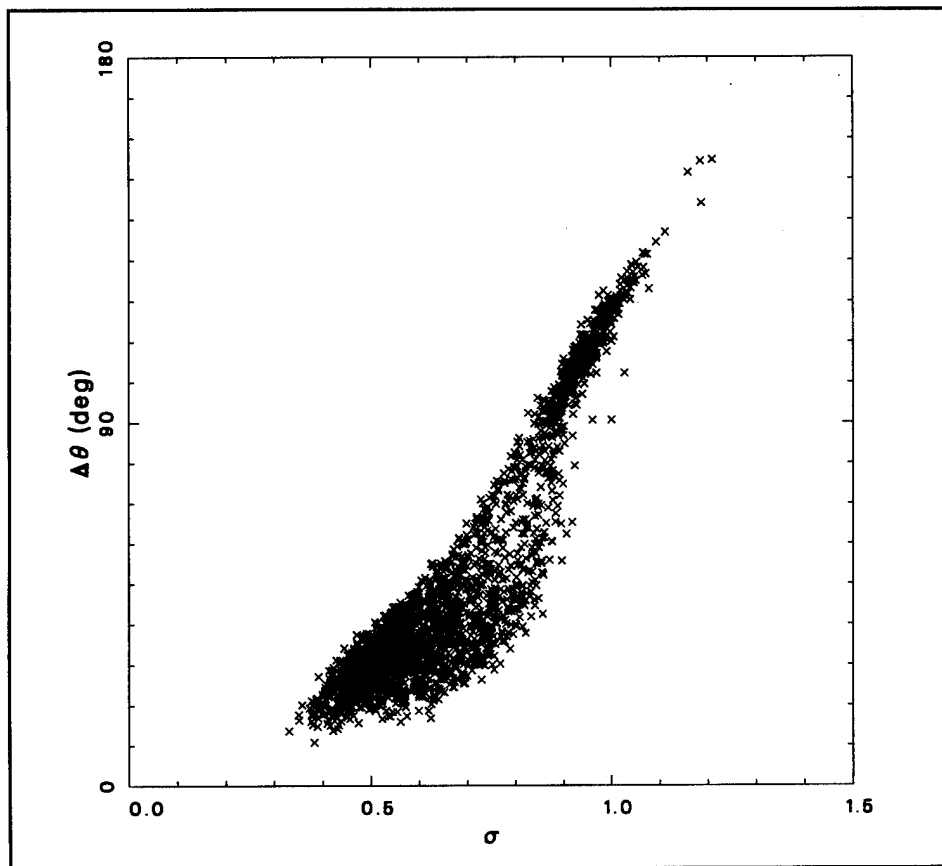


Figure 6. Correlation of directional spread parameters

### Depth

Time series plots of water depth  $d$  are included in Appendix A for general information. Total water depth does not vary enough to have a significant effect on directional-spectral estimates. However, even though strongly filtered by sample averaging of 2-hr 16-min records, the figures in Appendix A give an indication of tide stage, tide range, and the occurrence of spring and neap tides. Such information may be of use to modelers and climatologists interested in this study site.

### Asymmetry parameters

There are two parameters defined in this report that indicate skewness or asymmetry of a directional distribution of wave energy. They are circular skewness  $\gamma$  and quartile asymmetry  $A$ . They are important parameters because they indicate the presence of significant side lobes of energy in a distribution that may not be evident in mean direction or directional spread parameters. For a symmetric distribution in the sense of these parameters, both  $A$  and  $\gamma$  are zero. The general background levels of these parameters as shown in Appendix A tend not to be zero, but are slightly positive with  $A$  varying typically from 0 to 1, and  $\gamma$  ranging from 0 to 2. Large changes in

asymmetry do not appear to be highly correlated with energetic events, as evidenced by the persistent (with some exceptions) background levels in the energetic months of January through April.

Asymmetry changes markedly during events associated with peak directions indicating strong waves from the south, as seen most clearly in time series plots for August and September. Due either to storms or southern swell, such events impose a lobe of energy to one side of a pre-existing energy distribution, leading to a strong asymmetry indication. This is especially true for  $A$  if the side lobe is at a large azimuthal separation from the main lobe. Such behavior suggests there may be two main regimes for asymmetry parameters: one for conditions where all waves are from a single source leading to a narrow range of relatively small asymmetry scales, and another where multiple wave sources are involved leading to another range of large asymmetry parameters.

The two parameters  $A$  and  $\gamma$  show evidence of some correlation in the time series plots, but there are frequent deviations. Figure 7 is a scatter plot of the two parameters, and shows that there is a coarse relationship between the two. When one is large, the other tends to be large, but there is no clear relationship. The dark cluster of points near  $\gamma = 1$  and  $A = 0.5$  illustrates the persistent background conditions noted previously. A second banding of points for which  $A$  ranges between 1 and 2 where  $\gamma = 1$  is indicative of bimodality or secondary lobe conditions. Because the correlation in general is not strong, the two parameters must be sensitive to different aspects of skewed energy distributions, and so should be interpreted separately.

## Kurtosis

Time series of circular kurtosis  $\delta$  derived from  $D(\theta_m)$ , and shown in Appendix A, range from near 1 to about 14. Values in the upper part of this range appear to be common. Values in the lower part of this range occur when there is large  $\Delta\theta$ . This behavior is qualitatively consistent with the usual interpretation of kurtosis. A normal or Gaussian distribution has  $\delta = 3$ . Distributions with  $\delta > 3$  are considered to be more peaked than a Gaussian curve, and those with  $\delta < 3$  tend to be flatter than a Gaussian curve. The tendency for  $\delta$  to be commonly above 3 indicates that many directional distributions have sharper peaks than a normal distribution. The occurrence of low  $\delta$  with large  $\Delta\theta$ , which also corresponds generally with  $\theta_p$  near  $\pm 180$  deg, is consistent with multiple sources of wave energy from divergent directions. This condition leads to flatter (in the kurtosis sense) distributions than a normal distribution because there may be several widely separated peaks of about the same amplitude in  $D(\theta_m)$ . If the peaks or modes were analyzed separately, each would likely have a higher kurtosis.

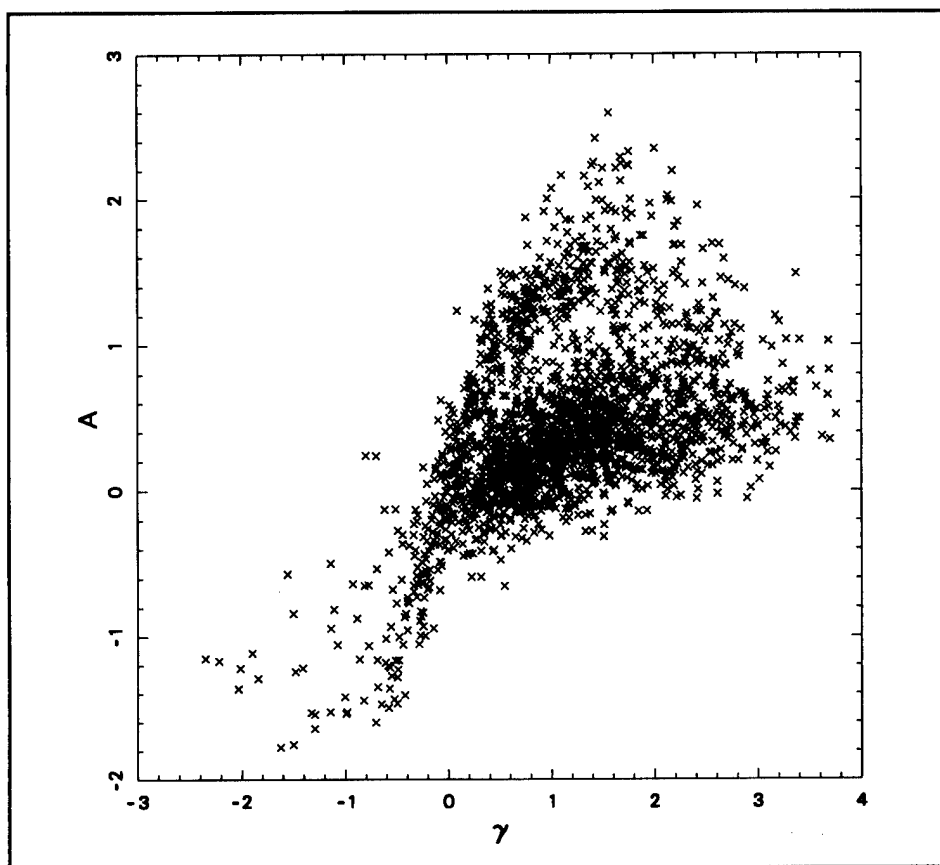


Figure 7. Correlation of asymmetry parameters

### Modal analysis

The final sets of parameters shown in Appendix A are time series of percentages of wave energy in the modes of the direction spectra  $D(\theta_m)$  and the normalized frequency spectra  $16S(f_n)/H_{mo}^2$ . Such curves give an indication of the number and relative intensity of the energy modes in these distributions. The maximum number of modes found in any of these distributions was three. One or two modes was far more common than three. As modes were isolated in analysis described in the previous chapter, they were ordered by size, with the most energetic mode (the mode having the highest fraction of total energy) being called the primary mode, and subsequent modes being called secondary and tertiary, respectively.

Among the directional modal curves labelled  $\theta$ -modal energy in Appendix A, there were long periods when most of the directional distributions were unimodal, i.e., having 100 percent of wave energy in a single mode. These periods occurred in January, February, March, April, and toward the end of the year in December. In all the other months, there were frequent occurrences of bimodal directional distributions. Among these, there were many with significant amounts of energy contained in the secondary mode. These conditions indicate multiple sources of energy, and account for much of the variation in other bulk parameters discussed previously.

Numerous multimodal conditions also occur in frequency spectra, where the modal percentage curves are labelled  $f$ -modal energy in Appendix A. Though occurring throughout the year, multimodal frequency spectra are most common in spring, summer, and fall. There is a high coincidence of multimodal frequency spectra and multimodal direction spectra in the months of June, July, August, and September. This behavior is consistent with the existence of southern swell, where modal peaks occur not only at different directions, but also at different frequencies. Multimodal frequency spectra in spring and fall are likely due to storm events, which build new seas on existing swell. In most of the occurrences of multimodal frequency spectra, a significant fraction of total wave energy is contained in the secondary mode.

## Bulk Parameter Probability Densities

To gain insight as to ranges and probable values of the set of bulk parameters discussed in the last section, bar charts of probability density functions are presented and discussed in this section. Being based on the whole data set of 2,339 observed frequency-direction spectra, the distributions are somewhat coarse, without distinction of seasonal or finer time scale variations. Nonetheless, they give a broad view of conditions found at Harvest Platform.

### Wave height, peak frequency, and peak direction

Figure 8 shows the probability density of  $H_{m0}$  in terms of percent of total number of observations in bins of 0.2-m (0.66-ft) width. The most frequently occurring characteristic wave height is approximately 1.6 m (5.2 ft). There are no observations of wave heights less than 0.5 m (1.6 ft), and only about 2 percent of the cases had heights below the 1-m (3.3-ft) bin. Extreme characteristic wave heights were approximately 5 m (16.4 ft). The considerable amount of wave energy passing Harvest Platform is seen by noting that about 15 percent of observations had wave heights in excess of 3 m (9.8 ft), as determined by adding the percentages in all bins at and above 3 m (9.8 ft).

Figure 9 illustrates the distribution of  $f_p$ . The most common peak frequency is approximately 0.07 Hz, which corresponds to peak periods of about 14 sec. Such periods are characteristic of swell or well-developed storm waves. Because of the bounds on analyzed frequencies discussed in Chapter 2, analyses were not done for frequencies less than 0.04 Hz or greater than 0.16 Hz. Consequently, Figure 9 is based on frequencies between 0.04 and 0.16 Hz, so that true peak frequencies outside this range were not detected and are not shown. Figure 9 shows that very few cases had peak frequencies near 0.04 Hz, indicating dominance by very low-frequency swell, and fewer than 1 percent had peak frequencies near 0.16 Hz, which typically occur briefly in the initial stages of storms.

The distribution of  $\theta_p$  is shown in Figure 10. It is immediately obvious that the bulk of energetic peaks originate to the northwest and west of Harvest

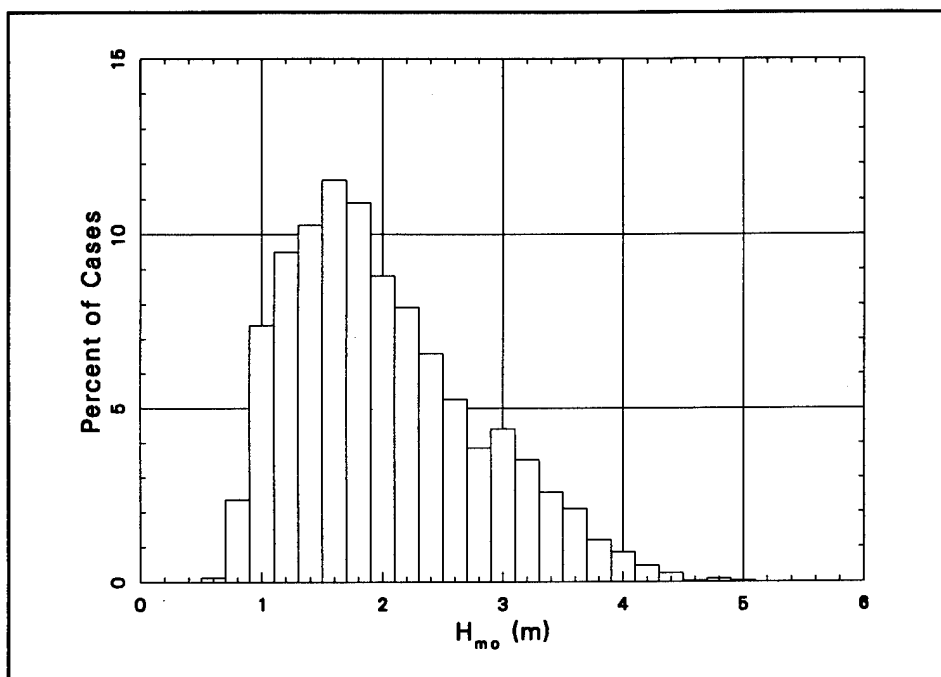


Figure 8. Distribution of characteristic wave height

Platform, which is the open north Pacific Ocean and Gulf of Alaska, a region of notable wave-generating capacity. There is a range of peak directions from the south-southwest to the south-southeast wherein about 4 percent of observations occur. These are typical approach directions for southern swell. The

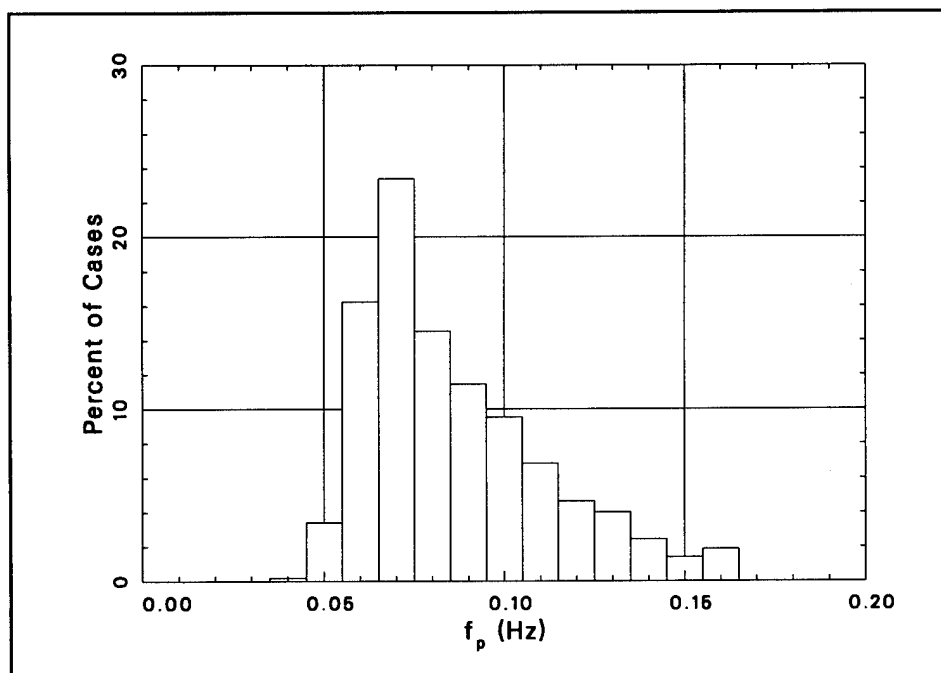


Figure 9. Distribution of peak frequency



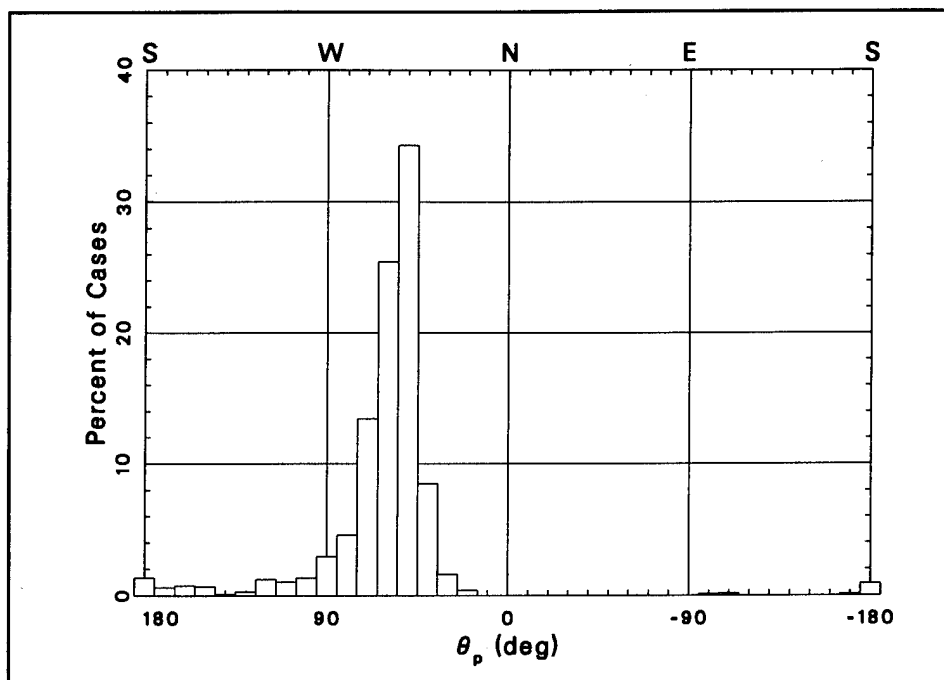


Figure 10. Distribution of peak direction

small percentage of cases in this range of directions does not mean that southern swell is present in only 4 percent of observations, but rather that it is the most energetic direction in 4 percent of observations. There is also a very small number of cases where peak direction is east-southeast. This is the direction of Santa Barbara Channel, which has enough fetch for local storms occasionally to induce peak waves in this quadrant.

### Circular moment parameters

Parameters  $\theta_0$ ,  $\sigma$ ,  $\gamma$ , and  $\delta$  derived from circular moments of  $D(\theta_m)$  reveal additional spectral properties when considered as statistical distributions. Figure 11 shows the distribution of  $\theta_0$ . As a characteristic wave direction,  $\theta_0$  has most of its values in the northwest quadrant (e.g.,  $\theta_p$  in Figure 10). However, unlike  $\theta_p$ , the most common direction is more to the west, and the influence of waves from the south only moves the mean direction into the west side of the southwest quadrant. This behavior occurs because mean direction is a centroid of the distribution, whereas peak direction is the extreme of the distribution. Equal modes of energy from the northwest and south then result in  $\theta_0$  at some intermediate angle, as evidenced in Figure 11.

The distribution of circular width  $\sigma$  is shown in Figure 12. This parameter ranges from values near 0.35 to about 1.20. There appear to be two peaks in the distribution: one near 0.55, and another, lesser one between 0.90 and 1.00. The low-valued peak represents narrow directional spreads, and by being the most populous, indicates the most common width in this data set.

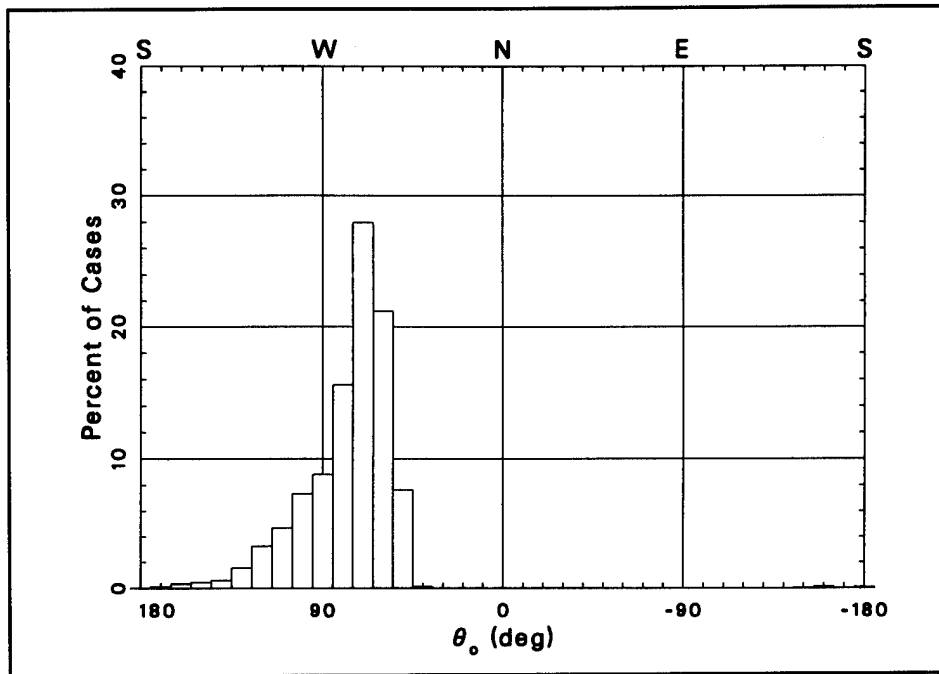


Figure 11. Distribution of mean direction

The high valued peak represents broad directional spreads, and is evidently the result of multimodal distributions of energy from widely divergent sources. Because a reasonable correlation between  $\sigma$  and the quartile spread  $\Delta\theta$

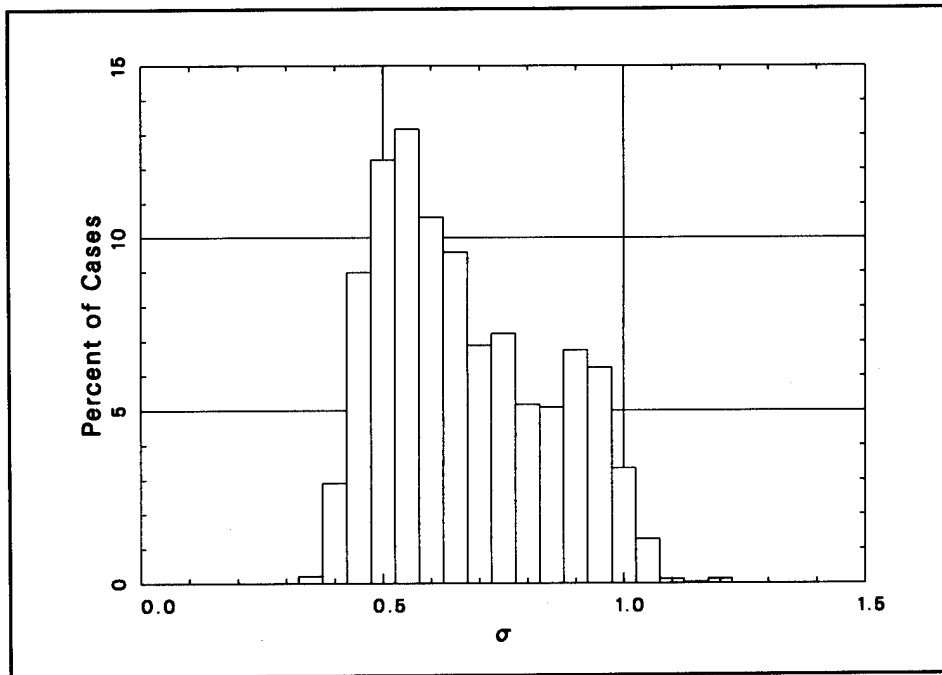


Figure 12. Distribution of circular width

was seen in Figure 6, it is possible to assign some angular measure of spread to the two modal peaks in Figure 12. Specifically, Figure 6 indicates that for  $\sigma \approx 0.55$ , a spread angle of 20 to 40 deg is common. For  $\sigma$  between 0.90 and 1.00, a spread angle of roughly 90 to 120 deg may be expected.

Circular skewness  $\gamma$  has a distribution shown in Figure 13, which indicates a range of -2.5 to 3.8. The peak probability of skewness occurs for  $\gamma \approx 0.8$ , and most of the observations have positive skewness. Only about 10 percent of the observations have  $\gamma \leq 0$ . As defined in this report, positive skewness means that distributions have tail regions or side lobes at positive angles (relative to  $\theta_0$ ) that are not balanced by similar features at negative angles. Because  $\theta_0$  resides mostly in the northwest quadrant, positive skewness suggests additional wave energy from the west or southwest. This behavior is consistent with secondary source regions for wave energy at Harvest Platform in the central and south Pacific Ocean, the most likely alternative source regions to those in the northwest.

The distribution of bulk circular kurtosis  $\delta$  is shown in Figure 14. There is a broad region of nearly equal probability densities for  $\delta$  in the range 1.5 to 5.5, and a tail region of higher values that extends to about 13.5. As discussed previously, kurtosis values greater than 3 indicate distributions that are more peaked than Gaussian curves, i.e., they have more pointed peak regions and broader bases than standard normal distributions. For wave energy distributions, this behavior suggests that distributions with large  $\delta$  are dominated by waves from a single direction with little spread near the distri-

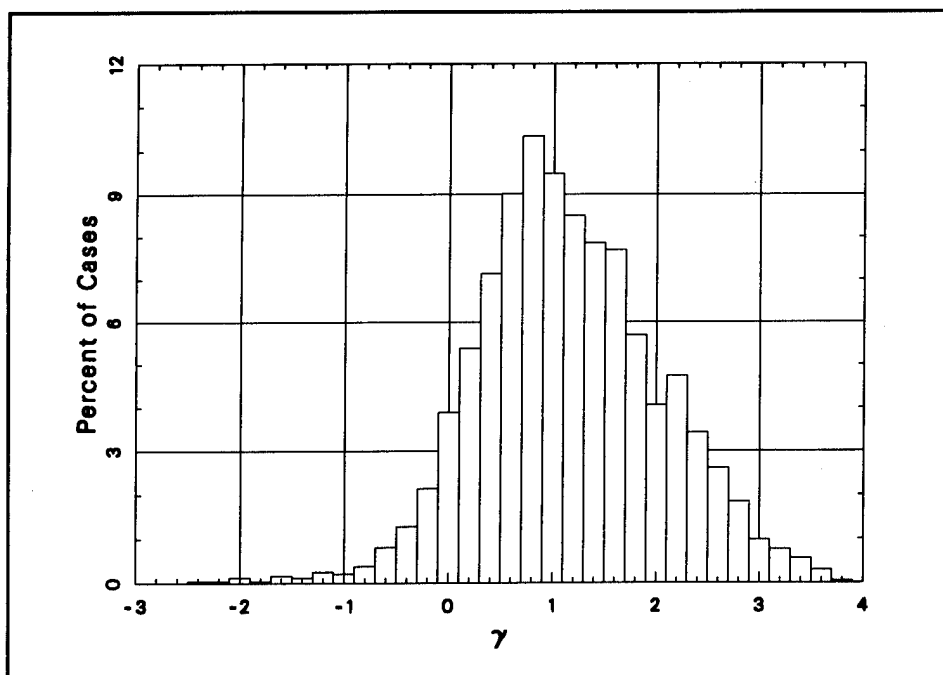


Figure 13. Distribution of circular skewness

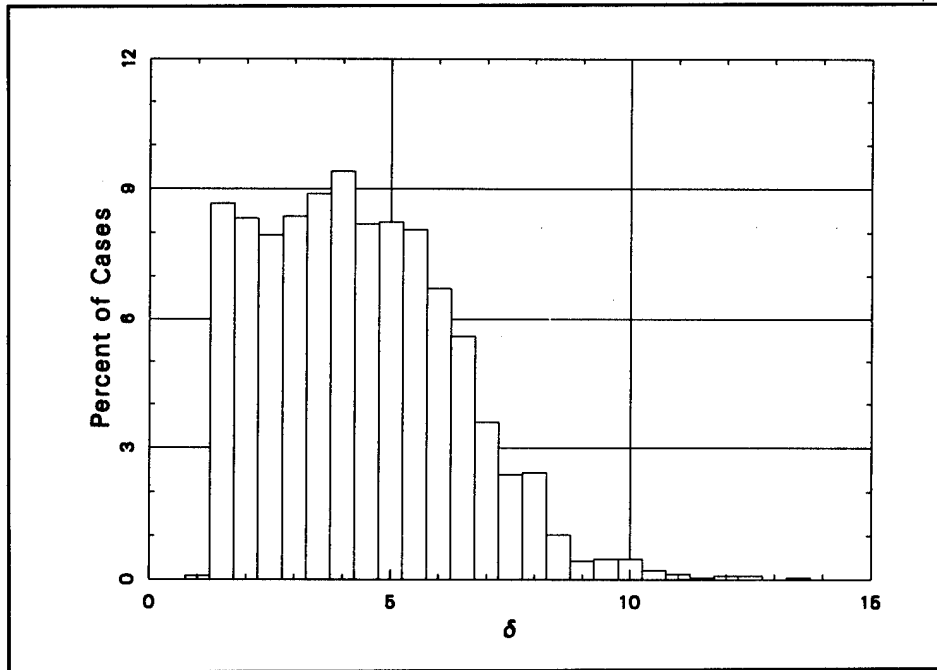


Figure 14. Distribution of circular kurtosis

bution peaks. Kurtosis values less than 3 indicate broad peak regions with abrupt drops in energy at the outer edges. This behavior is consistent with broad directional distributions of wave energy, as occurs when several source regions are active at the same time. The sudden drop in probability density of  $\delta$  for values near 1.5 indicates a characteristic behavior that is seldom exceeded. In this set of data, it is probably the coexistence of southern swell and local wind sea from the northwest, which occurs frequently and in a rather fixed pattern.

### Quartile parameters

The probability density of quartile spread  $\Delta\theta$  is shown in Figure 15. Overall, the spread parameter covers a very broad range from about 15 deg to values near 155 deg. The distribution has two clear peaks: one at about 30 deg, and a second at about 105 deg. As suggested by the circular width parameter  $\sigma$  in Figure 12, but more clearly in Figure 15, the narrower spreads are likely due to unimodal energy distributions, and the broader spreads arise because of waves travelling from directionally divergent sources. Figure 15 suggests that unimodal directional distributions have  $\Delta\theta$  in the range 15 deg to approximately 70 deg, with higher  $\Delta\theta$  due to multimodal distributions. This anticipated behavior is examined further in Chapter 8.

Probability density of the quartile measure of distribution asymmetry  $A$  is illustrated in Figure 16. Like circular skewness  $\gamma$  in Figure 13,  $A$  shows a propensity for slightly positive values, with peak probability density for

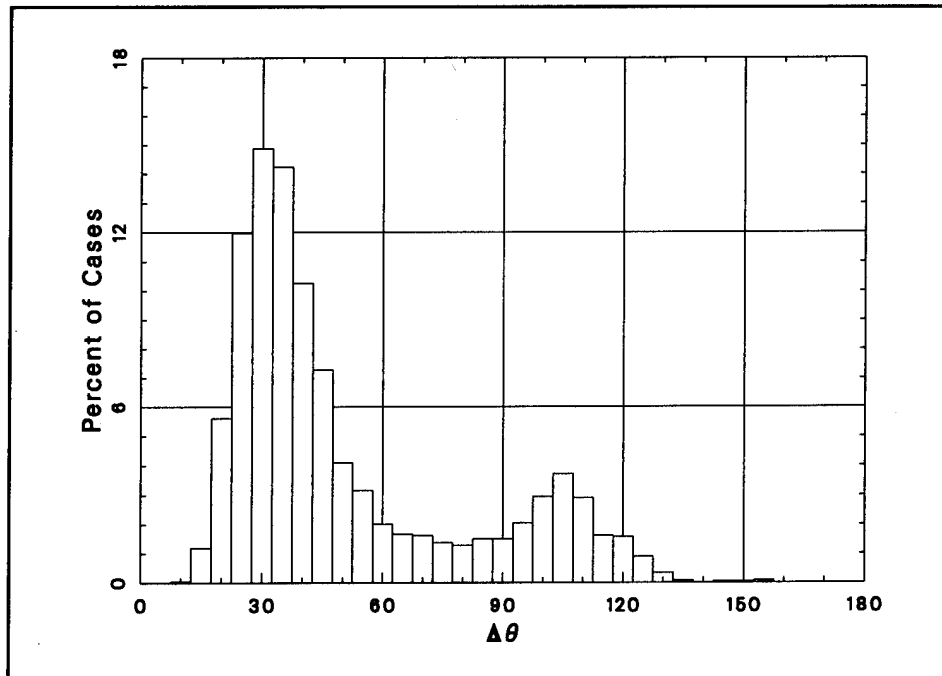


Figure 15. Distribution of quartile spread

$A \approx 0.2$ , and about 75 percent of cases with  $A$  greater than zero. This behavior supports the interpretation of Figure 13, which was that positive asymmetry occurs because of dominant waves from the northwest and simultaneous secondary waves from the west and south. As with  $\Delta\theta$ , the verity of this interpretation is shown in Chapter 8.

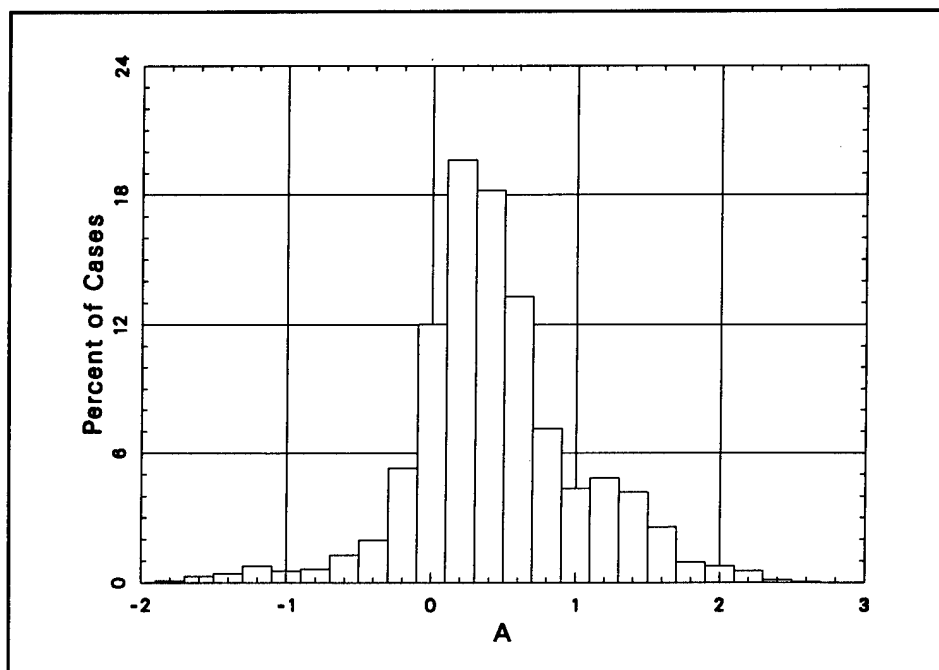


Figure 16. Distribution of quartile asymmetry

## Modal analysis

Distributions of modal parameters based on  $D(\theta_m)$  and normalized frequency spectra are shown in Figures 17 and 18, respectively. In Figure 17, the probability density of number of directional modes is shown on the left-hand side. A maximum of 3 modes was found in any of the  $D(\theta_m)$  analyzed, and that condition occurred in only about 1 percent of the cases. The most common number of modes is 2, which occurred in approximately 60 percent of the observations. The remaining cases, about 39 percent, were unimodal in direction. Because of the highly constrained definition of modal separation as described in Chapter 4, the bimodal distributions discerned in this study are quite distinct, and suggest clear, directionally deviate sources of wave energy.

The right-hand side of Figure 17 shows the probability density of percent of wave energy in the primary, or most energetic, mode. This computation was done because there could be a strong indication of bimodal spectra, but the secondary modes could all have very low energy, and consequently be of little interest. Figure 17 indicates that approximately 45 percent of all cases had between 97.5 and 100 percent in the primary mode. This bin has more cases (45 percent) than the number of unimodal cases (39 percent) because some secondary modes (roughly, 6 percent of cases) had less than 2.5 percent of the energy in a distribution, and so were included in the 95-to-100-percent bin. Slightly less than 10 percent of all cases had 92.5 to 97.5 percent of total energy in the primary mode, indicating 2.5 to 7.5 percent of energy was in a secondary mode. By adding adjacent bin percentages, it can be seen that approximately 25 percent of observations had secondary modes with 17.5 to 50 percent of total energy. This result means the amount of energy in secondary modes is often of considerable importance.

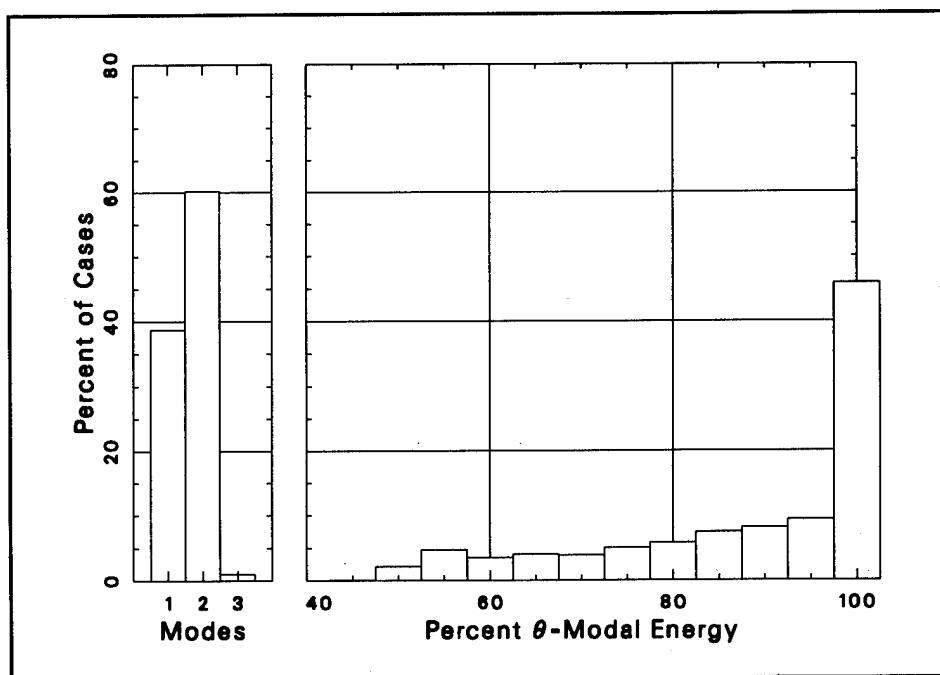


Figure 17. Distribution of directional modes

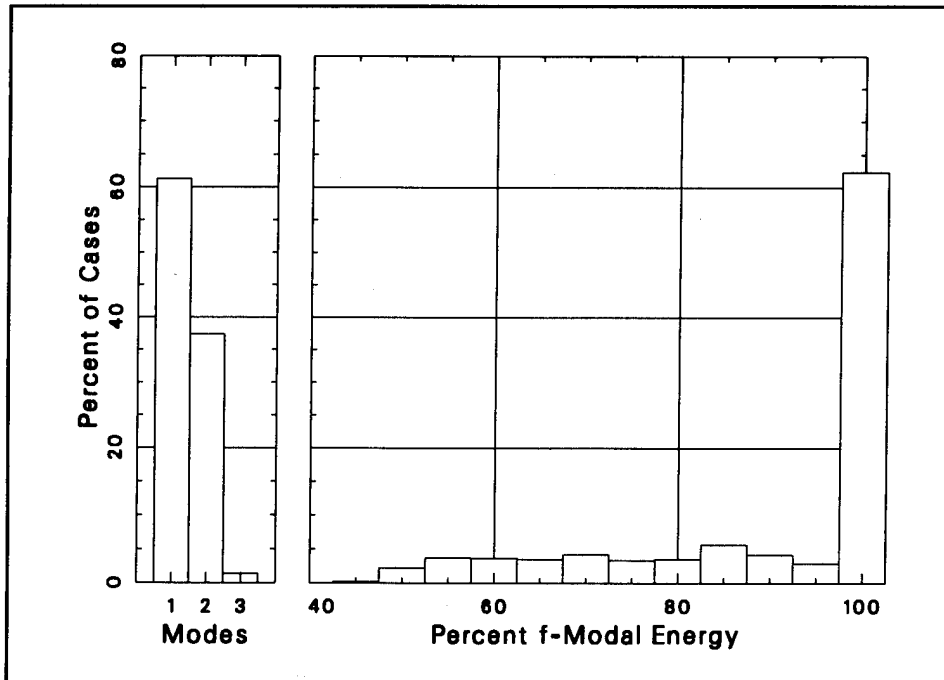


Figure 18. Distribution of frequency modes

Figure 18 illustrates results of modal analysis for normalized frequency spectra  $16S(f_n)/H_{mo}^2$ . A maximum of three modes was found, with approximately 1 percent of cases having three modes, 37 percent of cases having two modes, and 62 percent of cases being unimodal. Note that the percentage of unimodal frequency spectra need not be the same as the percentage of unimodal direction spectra because two directional modes can occur at the same frequency, or two frequency modes can occur in the same direction. Figure 18 shows that approximately 62 percent of all cases have between 97.5 and 100 percent of wave energy in the primary mode. About 25 percent of all cases have between 17.5 and 47.5 percent of wave energy in secondary and tertiary modes, again making secondary modes important. It is likely that some of the secondary frequency modes are the same as the secondary direction modes in cases where southern swell propagates through a local wind sea.

## Parameter Correlations with Wave Height

Of considerable interest is characterization of the wave field at Harvest Platform in high-energy conditions. High-energy waves, as indicated by large  $H_{mo}$ , passing this site from the open Pacific Ocean are directed toward the California coast, and it is typically for these waves that a coastal engineer must design shore protection structures or beach renourishment projects. A reasonable description of wave fields in high-energy conditions can be achieved by correlating bulk spectral parameters with  $H_{mo}$  to determine ranges of these parameters that apply in extreme conditions.

## Peak frequency and peak direction

Figure 19 relates  $f_p$  and  $H_{mo}$ . There are a total of 13 smooth frequency bands in all frequency related spectra discussed in this report. Figure 19 shows that all bands contain spectral peaks for some observations. At low energy, for which  $H_{mo} \approx 1$  m (3.3 ft),  $f_p$  ranges from 0.05 to 0.16 Hz. At intermediate energy, with  $H_{mo} \approx 3$  m (9.8 ft), peak frequency appears in the lowest frequency band (0.04 Hz), but only ranges to about 0.12 Hz, probably because it is normal for peak frequency to move to lower values in growing wind-driven seas. At the highest energies [ $H_{mo} > 4$  m (13.1 ft)], peak frequency typically resides in a narrow range from 0.05 to 0.08 Hz.

Figure 20 shows the correlation of  $\theta_p$  with  $H_{mo}$ . Clearly, the bulk of cases have peak directions in the northwest to west, and this property holds even for the highest waves. Dominance of the spectrum by southern energy sources occurs only for lower energy conditions. Rare events provide intermediate energy levels with peak directions from the southwest or east-southeast.

## Circular moment parameters

Correlation of  $H_{mo}$  with mean direction  $\theta_0$  derived from circular moment  $n_1$  is shown in Figure 21. The gross pattern of points in Figure 21 is like the

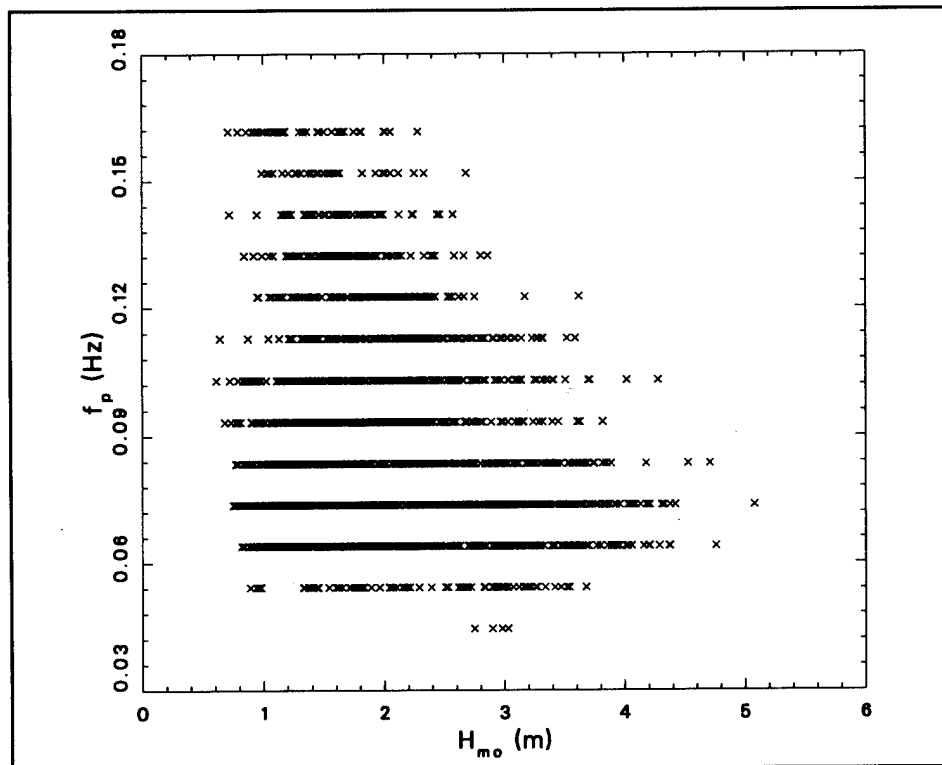


Figure 19. Correlation of wave height with peak frequency



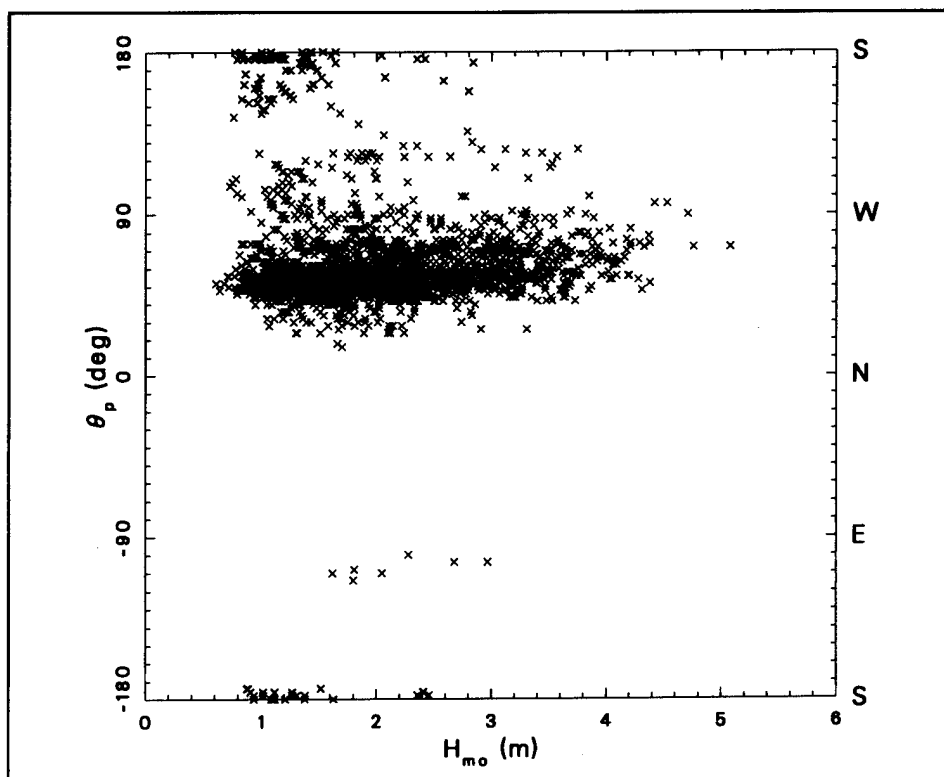


Figure 20. Correlation of wave height with peak direction

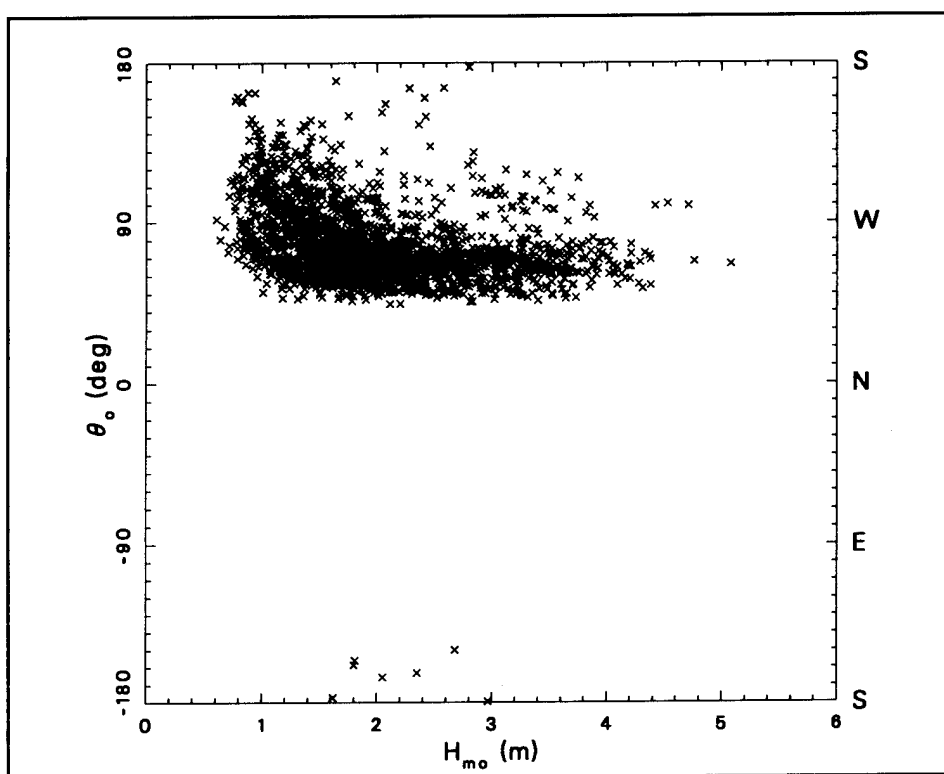


Figure 21. Correlation of wave height and mean direction

pattern for peak direction shown in Figure 20. The bulk of points in Figure 21 are in the northwest to west directions at intermediate to high  $H_{mo}$ . For low wave heights, there is a deviation in mean direction to the southwest. This behavior is likely due to the averaging effect on wind sea from the northwest quadrant and southern wave sources in the computation of  $\theta_0$ ; for two distinct modes of energy, mean direction will fall between the modal peak directions. Of note is the fact that mean and peak directions are approximately equal (to within  $\pm 5$  deg) in high-energy conditions for which  $H_{mo} > 4$  m (13.1 ft). This behavior suggests that directional distributions are naturally narrow and symmetric in these conditions.

The suggested narrowness of directional distributions at high energy is verified in Figure 22, which is a correlation of  $H_{mo}$  with circular width  $\sigma$ . The broad swath of points indicates generally large  $\sigma$  for small  $H_{mo}$ , and small  $\sigma$  for large  $H_{mo}$ . For high energy [ $H_{mo} > 4$  m (13.1 ft)],  $\sigma$  is in the range 0.3 to 0.5, which clearly includes the smallest observed circular widths. Based on the correlation shown in Figure 6, this range of  $\sigma$  occurs for quartile spreads  $\Delta\theta$  in the range 10 to 40 deg, which are rather narrow.

Evidently, the small directional spreads at high energy are indicative of moderately low values of circular skewness  $\gamma$ , as shown in Figure 23. Though there is a large scatter of points in Figure 23, the grouping tightens

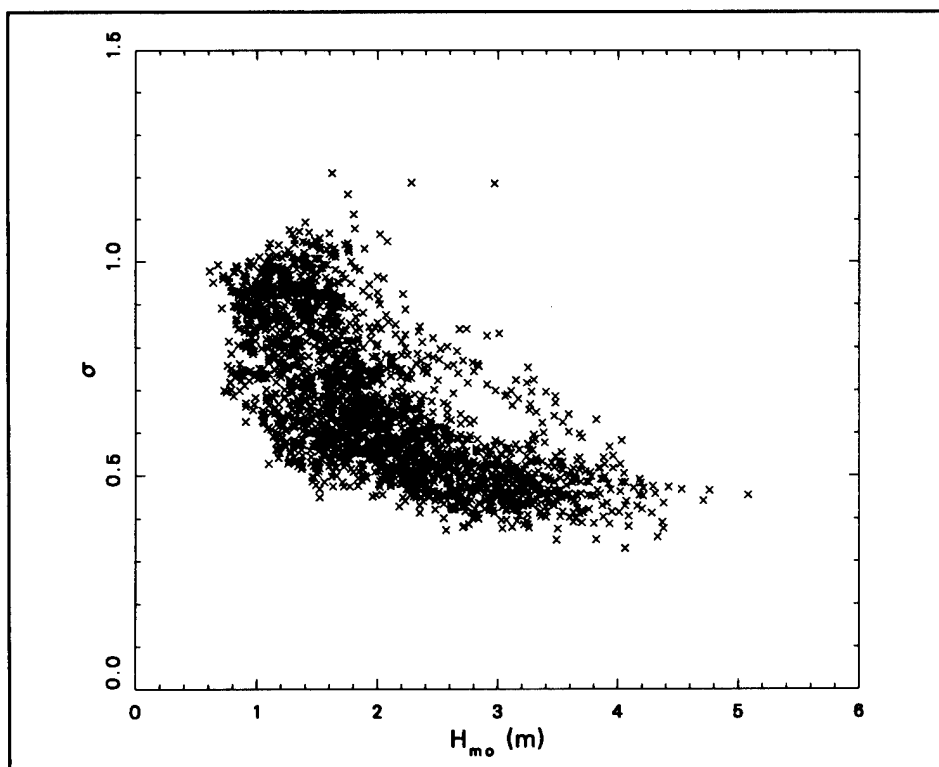


Figure 22. Correlation of wave height with circular width

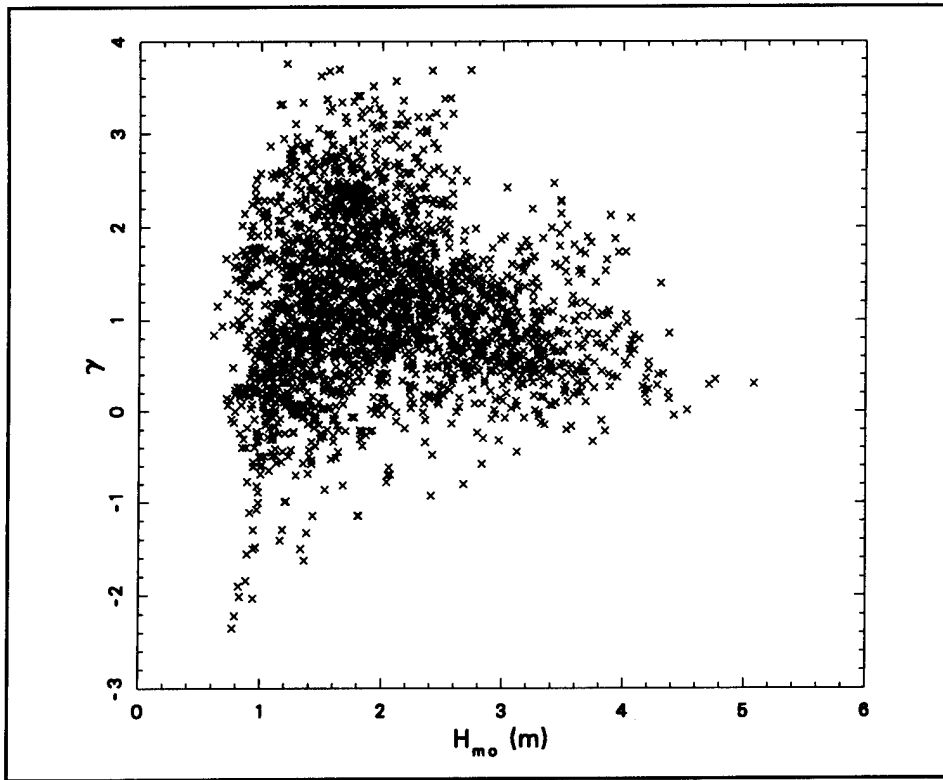


Figure 23. Correlation of wave height with circular skewness

somewhat for high  $H_{mo}$ . For  $H_{mo} > 4$  m (13.1 ft),  $\gamma$  is in the range -0.2 to 2.2, which is considerably narrower than the range of -2.5 to 3.8 indicated for  $H_{mo}$  near 1 m (3.3 ft). Furthermore, because the high-energy spectra have small directional spreads, side lobes of energy that cause a non-zero  $\gamma$  may not be greatly removed from the main energy peaks. Consequently, high-energy spectra may appear relatively unskewed. These properties will be examined further in Chapter 8 where characteristic directional distributions are discussed.

Figure 24 shows how circular kurtosis  $\delta$  is related to  $H_{mo}$ . The main cluster of points indicates a gross tendency for  $\delta$  to increase with increasing  $H_{mo}$ , being less than 4 for the smallest wave heights, but ranging approximately between 4 and 9 for  $H_{mo} > 4$  m (13.1 ft). Kurtosis greater than 3 indicates that maxima of the directional distributions are more peaked than a Gaussian curve. This property of high-energy directional distributions seems consistent with narrowly spread curves of small to moderate skewness.

#### Quartile spread and asymmetry

Figures 25 and 26 illustrate the correlation of  $H_{mo}$  with quartile spread  $\Delta\theta$  and quartile asymmetry  $A$ , respectively, as derived from  $D(\theta_m)$ . Quartile

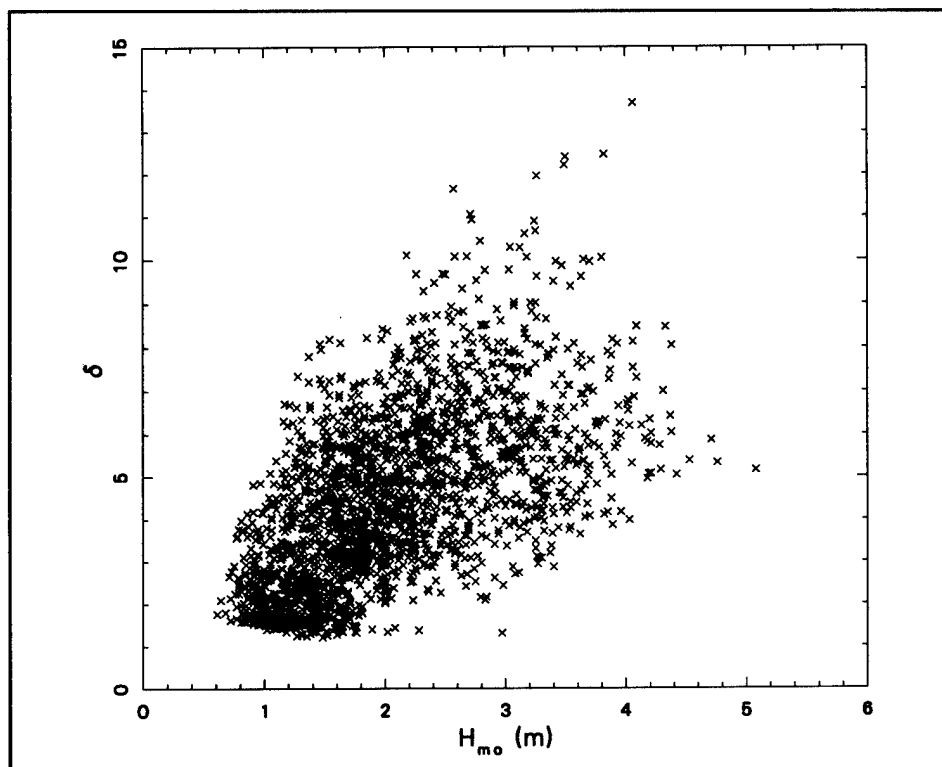


Figure 24. Correlation of wave height with circular kurtosis

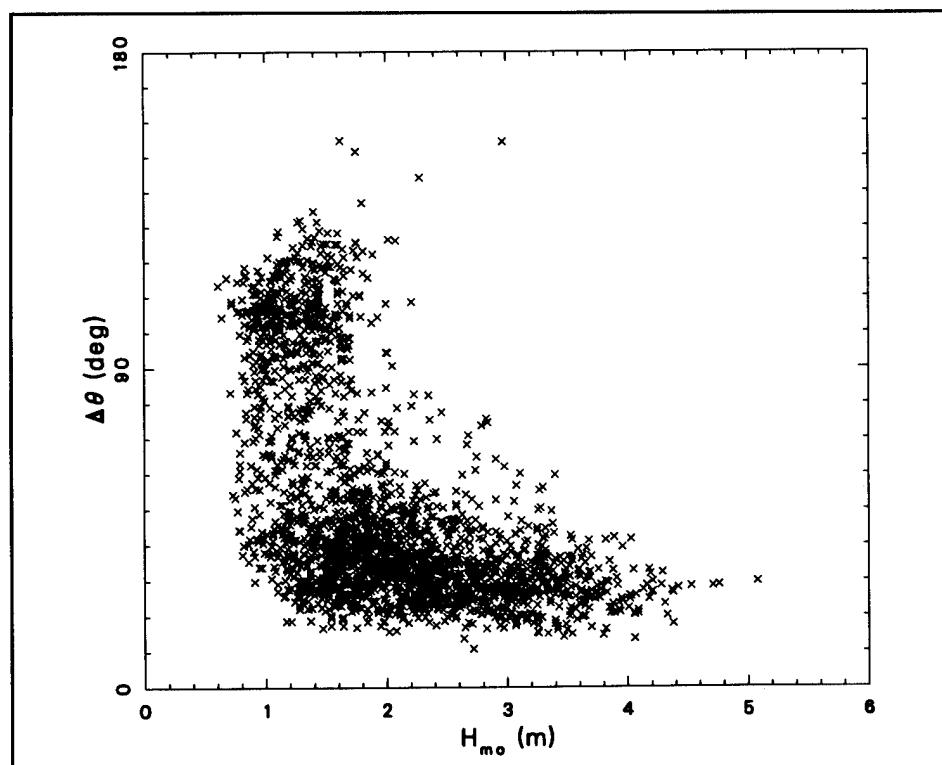


Figure 25. Correlation of wave height with quartile spread

spread spans a very large range for low-energy distributions, but narrows in range and becomes moderately small for  $H_{mo} > 4$  m (13.1 ft). There appear to be two clusters of  $\Delta\theta$  for  $H_{mo}$  between 1 and 2 m (3.3 and 6.6 ft). The largest group, having a  $\Delta\theta$  range of 20 to approximately 70 deg, is associated with wind seas and swell from a single direction. The smaller group, with  $\Delta\theta > 90$  deg, is attributed to wave trains from multiple source directions. For high-energy spectra,  $\Delta\theta$  is confined to the range 15 to 45 deg. For the extreme high  $H_{mo}$ ,  $\Delta\theta = 30$  deg, which happens to be the most common spread as shown in Figure 15.

Quartile asymmetry also shows a wide range for low  $H_{mo}$  and a narrow range for high  $H_{mo}$ , as shown in Figure 26. The reasons for this behavior are the same as for the behavior of  $\Delta\theta$ ; multiple wave sources with varying intensities induce large apparent asymmetries in the total directional distributions, whereas intense single sources lead to more nearly symmetric distributions. For the extreme high  $H_{mo}$  in Figure 26,  $A$  is nearly zero (i.e., symmetric in the sense of the definition of  $A$ ). For  $H_{mo} > 4$  m (13.1 ft),  $A$  is roughly in the range -0.6 to 0.6, and so is nearly symmetric.

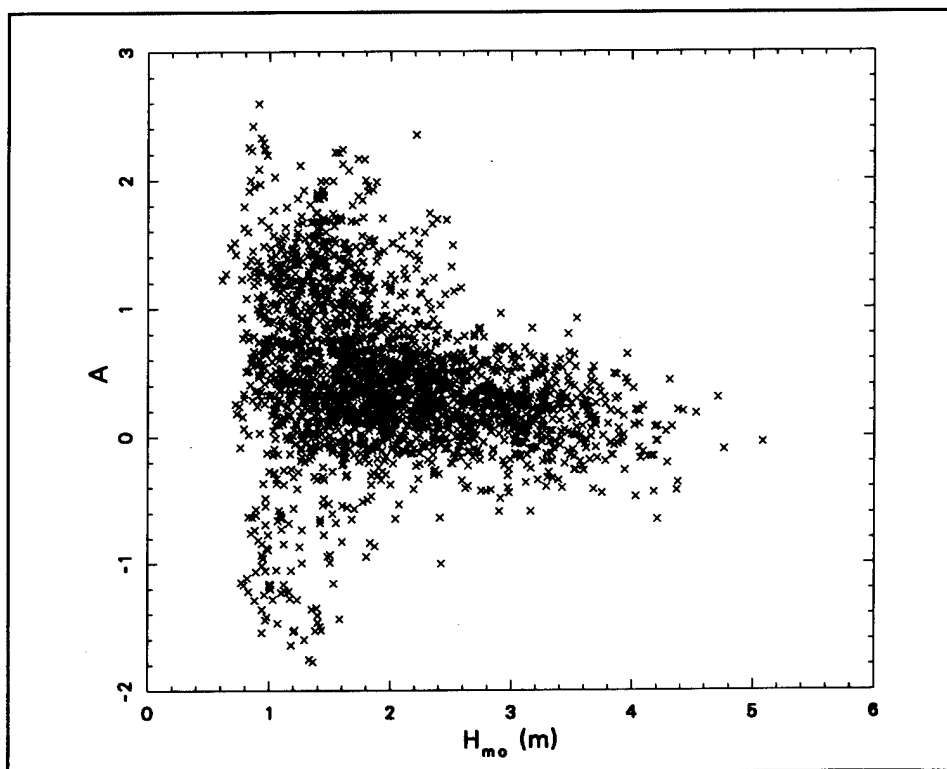


Figure 26. Correlation of wave height with quartile asymmetry

## Summary of Bulk Parameters

In this chapter, parameters characterizing integrated direction spectra  $D(\theta_m)$  and normalized frequency spectra  $16S(f_n)/H_{m0}^2$  have been examined in several ways to deduce some of the directional behavior of waves at Harvest Platform. Time series graphs in Appendix A show timing, duration, and seasonal variation of these parameters as a gross characterization of the wave climate. Statistical distributions of individual parameters in probability density form indicate ranges and most common values of these parameters, and suggest ways that groups of parameters are affected in various wave regimes. Correlations of bulk parameters with characteristic wave height reveal ranges and groupings of parameters at various energy levels, especially in conditions of high energy.

Table 1 contains a summary of some of the indicator statistics described in this chapter. A distinction is made between all observations and a subset called high energy, which has been defined arbitrarily as any condition in which the characteristic wave height exceeds 4 m (13.1 ft). Minimum and maximum values are listed for each of the nine bulk parameters discussed in this chapter for each of the two data groupings. The column labeled mode in the grouping for all data is the most common value of each parameter as deduced from the maximum probability density shown in the set of figures in the second part of this chapter. Bulk parameters discussed in this chapter are gross indicators of frequency-direction spectral structure, but may be indicative of greater detail. Details of spectral structure are examined more closely in subsequent chapters, using bulk parameters for general categorization.

<b>Table 1</b> <b>Summary of Bulk Parameter Statistics</b>					
Parameter	All Data			High Energy ( $H_{m0} > 4$ m)	
	Minimum	Mode	Maximum	Minimum	Maximum
$H_{m0}$ (m)	0.61	1.60	5.08	4.00	5.08
$f_p$ (Hz)	0.04	0.07	0.16	0.05	0.08
$\theta_p$ (deg)	-180	50	180	45	100
$\theta_0$ (deg)	-180	70	177	49	105
$\sigma$	0.33	0.55	1.21	0.38	0.58
$\gamma$	-2.35	0.80	3.76	-0.10	2.15
$\delta$	1.22	4.00	13.68	4.90	8.70
$\Delta\theta$ (deg)	11	30	155	13	43
$A$	-1.77	0.20	2.59	-0.67	0.49

## 6 Frequency-Dependent Parameters

---

More detail about frequency-direction spectral structure is obtained by examining parameters derived from directional distribution functions  $D(f_n, \theta_m)$  on a frequency-by-frequency basis. At this level, properties of directional distributions  $D(\theta_m)$  based on integrated frequency-direction spectra can be explained in terms of contributions from the various frequency bands that are the basis of integration. For example, large directional spreads or asymmetries may be due to influences from a limited range of frequencies, which, in turn, may be of local or more general importance to students of wave generation and propagation if the influential frequencies are low or high.

In this chapter, statistical distributions of nine frequency-dependent properties are examined. Spectral density  $S(f_n)$  and peak direction  $\theta_{pn}$  are two of them, and indicate energy levels and dominant direction of wave propagation. The subscript  $n$  remains an index of discrete frequency, and is useful for distinguishing frequency-dependent properties from bulk parameters. The four circular moment parameters defined by Kuik, van Vledder, and Holthuijsen (1988) are included to indicate moment properties of distributions. These four parameters are mean direction  $\theta_{0n}$ , circular width  $\sigma_n$ , circular skewness  $\gamma_n$ , and circular kurtosis  $\delta_n$ . Use of these parameters at the frequency level is more appropriate to the intent of the paper by Kuik, van Vledder, and Holthuijsen (1988), though these parameters in bulk form were quite useful in analyzing  $D(\theta_m)$  in the previous chapter of this report. Quartile spread  $\Delta\theta_n$  and quartile asymmetry  $A_n$  are used to augment interpretation of circular width and skewness, respectively. Finally, a modal analysis is done for the set of directional distributions at each frequency.

### Spectral Density and Peak Direction

Figure 27 shows statistical distributions of frequency spectral densities at each frequency in the form of probability density functions. The intent is to determine which frequencies have the highest wave energy, ranges of wave energy observed at each frequency, and most probable wave energies at each

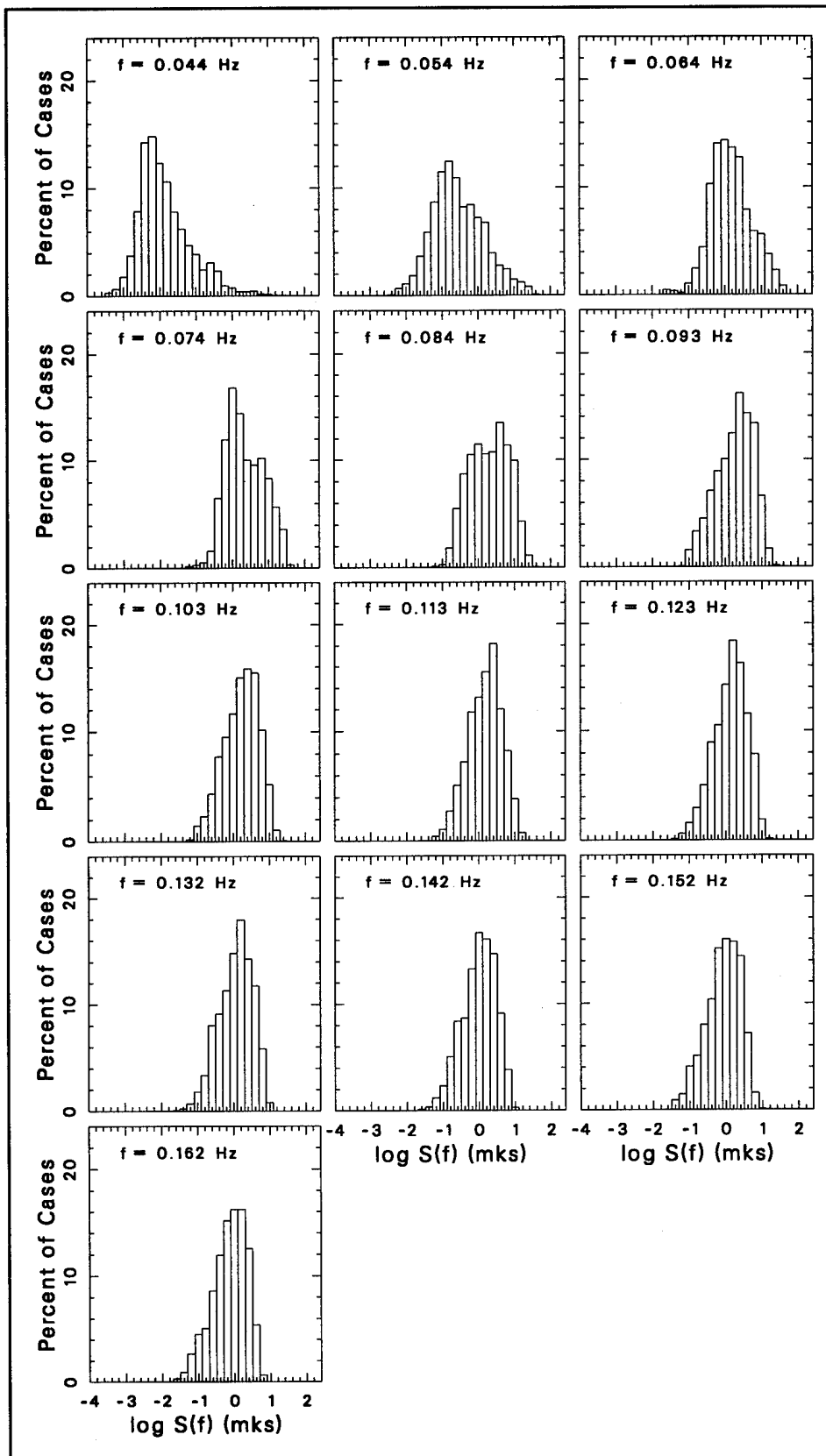


Figure 27. Distributions of frequency spectral density



frequency. Note that the abscissas in Figure 27 are logarithmic scales so that each numeral represents a power of 10. Because resolution bandwidths are constant at approximately 0.01 Hz, sea surface displacement variances represented on the abscissas include values from  $10^{-6}$  to  $1 \text{ m}^2$  ( $10^{-4.97}$  to  $10^{1.03} \text{ ft}^2$ ), a rather large range. Note also that the order of the subplots is such that frequency increases in raster fashion, across the page, and then down.

There is a clear distinction of spectral content among groups of frequencies shown in Figure 27. At the lowest frequency, energy density tends to be lower than at any of the other frequencies, with a most common variance density of  $10^{-2} \text{ m}^2/\text{Hz}$  ( $10^{-0.97} \text{ ft}^2/\text{Hz}$ ), and a maximum near  $10 \text{ m}^2/\text{Hz}$  ( $10^{2.03} \text{ ft}^2/\text{Hz}$ ). For the next three frequencies,  $f = 0.054, 0.064$ , and  $0.074 \text{ Hz}$ , the modal variance density increases in orderly fashion to about  $10^{-0.8} \text{ m}^2/\text{Hz}$  ( $10^{0.23} \text{ ft}^2/\text{Hz}$ ), and then to  $1 \text{ m}^2/\text{Hz}$  ( $10^{1.03} \text{ ft}^2/\text{Hz}$ ). These three frequencies are distinguished by having variance densities up to  $10^{1.6} \text{ m}^2/\text{Hz}$  ( $10^{2.63} \text{ ft}^2/\text{Hz}$ ), higher than any other frequencies. This behavior is consistent with spectral peak frequencies equalling one of these frequencies in the high-energy conditions shown in Figure 19. At  $f = 0.084 \text{ Hz}$ , variance density is nearly uniformly distributed between  $10^{-1}$  and  $10 \text{ m}^2/\text{Hz}$  ( $10^{0.03}$  and  $10^{2.03} \text{ ft}^2/\text{Hz}$ ). For  $f \geq 0.093 \text{ Hz}$ , the distributions are rather uniform in shape, ranging roughly from  $10^{-1}$  to  $10 \text{ m}^2/\text{Hz}$  ( $10^{0.03}$  to  $10^{2.03} \text{ ft}^2/\text{Hz}$ ), with modal values from  $1$  to  $10^{0.4} \text{ m}^2/\text{Hz}$  ( $10^{1.03}$  to  $10^{1.43} \text{ ft}^2/\text{Hz}$ ). The similarity in the distributions of the high-frequency wave energy is interesting because it means that each of these frequencies has a given energy level roughly the same fraction of the time.

Distributions of frequency-dependent peak direction are shown in Figure 28. It is readily seen that all frequencies have significant contributions of  $\theta_{pn}$  from the northwest quadrant, with such conditions being dominant for  $f \geq 0.074 \text{ Hz}$ . Wave fields with peak directions in the southwest and south have comparable or dominant percentages for the three lowest frequencies. As illustrated in Figure 20, distributions with bulk peak directions in the southwest and south are of primarily low and occasionally intermediate energy (as represented by  $H_{mo}$ ). The same range of energy is represented in Figure 20 by peak waves from the west to southwest, which appear in Figure 28 to have larger, though not dominant, percentages in the upper half of the overall frequency band. Though difficult to see in Figure 28, the intermediate-energy waves from the east-southeast shown in Figure 20 appear to be represented in distributions of  $\theta_{pn}$  at the three highest frequencies in Figure 28.

Note that parameters shown in Figures 20 and 28 differ in that Figure 20 shows bulk peak direction based on an integration of the frequency-direction spectra over all frequencies. Figure 28 shows distributions of directional peaks at individual frequencies. Because the two figures agree qualitatively in content, it can be deduced that waves at frequencies away from  $f_p$  tend to align with  $\theta_p$  (i.e.,  $\theta_{pn} \approx \theta_p$ ), in a given frequency-direction spectrum. This behavior is consistent with the idea that waves at different frequencies from a given source all tend to have the same characteristic direction.

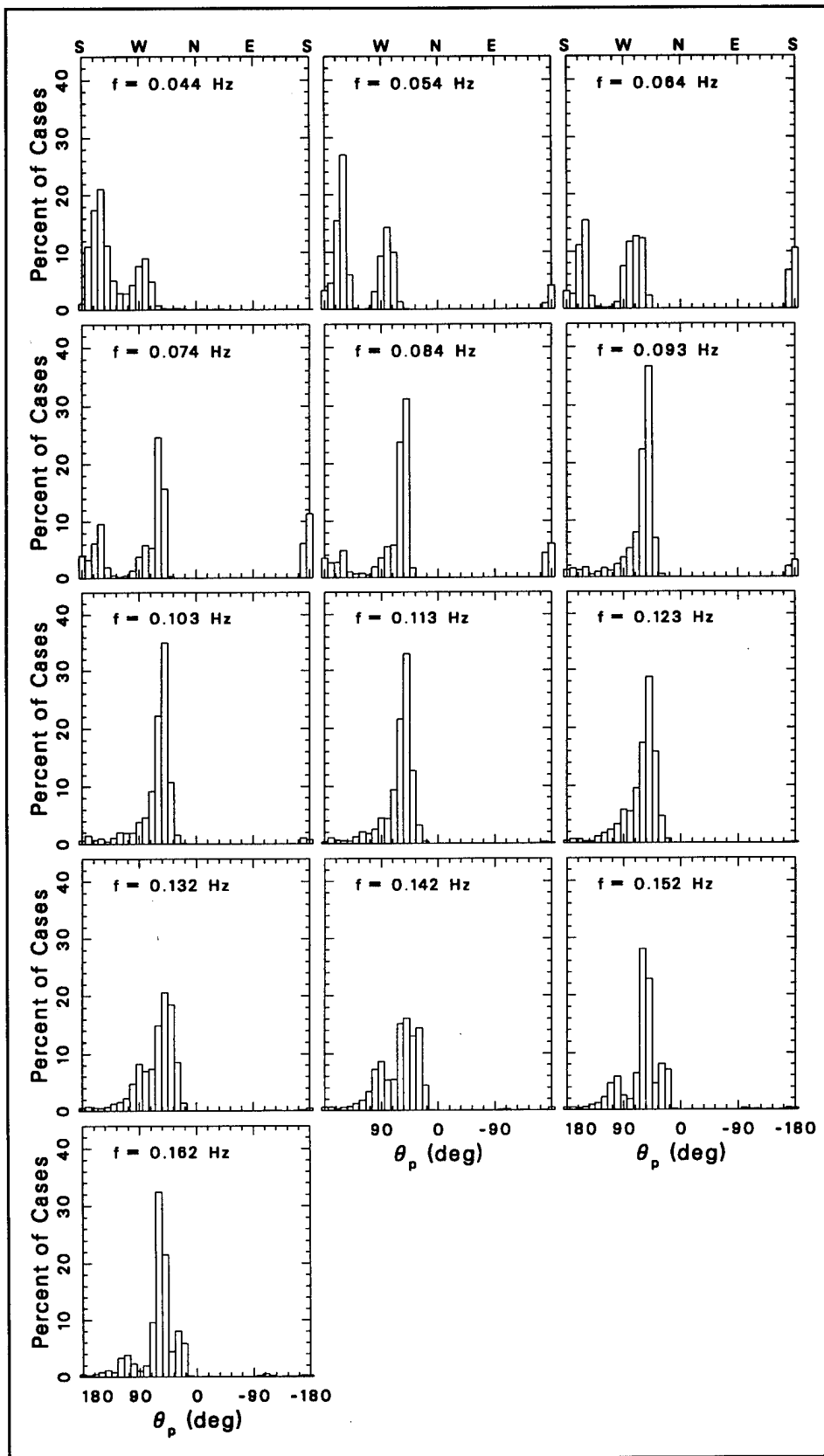


Figure 28. Distributions of peak direction for all frequencies

## Circular Moment Parameters

Distributions of frequency-dependent mean direction  $\theta_{0n}$  are shown in Figure 29, which indicates that mean directions have distributions that are qualitatively similar to peak directions (Figure 28) at corresponding frequencies. However, it is noted that distributions of mean direction are smoother and have fewer contributors at extreme directions than those of peak directions. This relative behavior of frequency-dependent peak and mean directions exists for the same reasons given for the relation between bulk peak and mean directions discussed in Chapter 5; where directional distributions are broad or have multiple, directionally divergent modes, peak direction will be the maximum of the dominant mode, whereas mean direction will be some direction intermediate between the modes because of the smoothing nature of its integral definition (Equation 40).

Consequently, when there are directional modes from both southern swell and western storms, peak direction will indicate either west or south, depending on the peak of the dominant mode, and mean direction will indicate somewhere in the southwest, depending on the areas under the two modes. This behavior is quite evident at the lowest three frequencies in Figures 28 and 29; peak direction has a significant fraction of cases from due south, and mean direction has very few. The behavior of and distinction between these two parameters is important in modeling efforts. Neither represents bimodal spectra very well (analysis of individual modes is required for this). Models of coastally propagating waves, which are extremely direction-sensitive (O'Reilly and Guza 1991, 1993), will yield different results for unimodal directional distributions if one or the other of these parameters is used as characteristic direction, and can yield quite incorrect results in bimodal situations if either parameter is used.

Figure 30 shows distributions of direction-dependent circular width  $\sigma_n$ . Extreme widths are seen at the lowest frequency, which is likely due to a combination of waves from widely divergent sources and analysis noise. Analysis noise is more noticeable at the lowest frequency because wave energy levels are typically small, as shown in Figure 27. For most frequencies, the most common  $\sigma$  is near 0.5. There are larger percentages of high-width cases for  $f$  in the range 0.064 to 0.093 Hz. These frequencies are common to both wind seas and southern swell, and, further, are often energetic so that large circular widths are likely due to multiple-source waves. The narrowest distributions, with  $\sigma \approx 0.3$ , occur at low and intermediate frequencies and are likely due to unimodal swell and well-developed, isolated seas created by steady winds.

Distributions of frequency-dependent circular skewness  $\gamma_n$  are shown in Figure 31. The lowest-frequency energy distributions have a narrow range of skewness with dominant values zero or slightly negative, suggesting a balance of wave energy distributions about the mean directions for this frequency. The widest ranges of skewness occur at intermediate and lower frequencies.

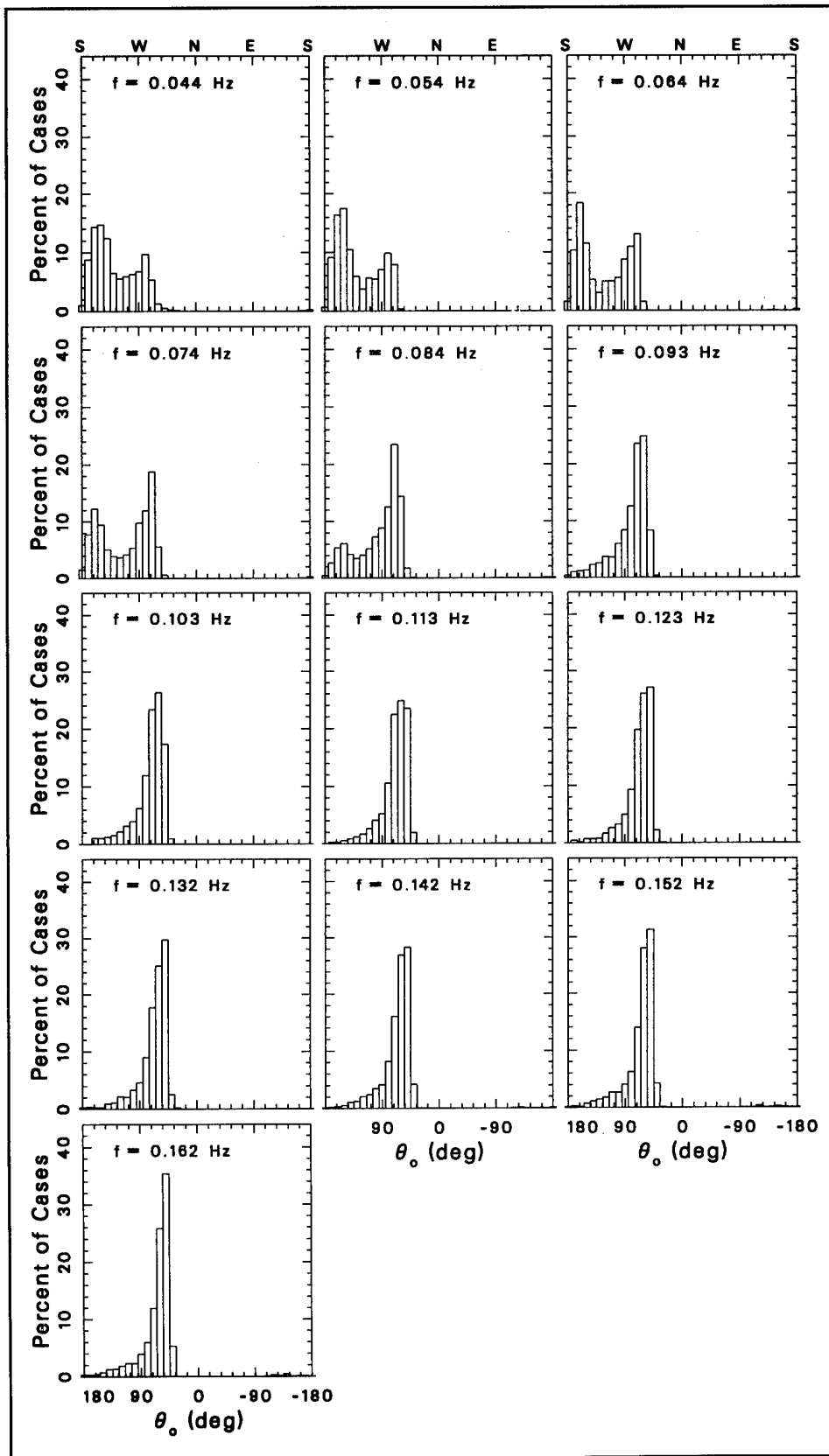


Figure 29. Distributions of mean direction for all frequencies

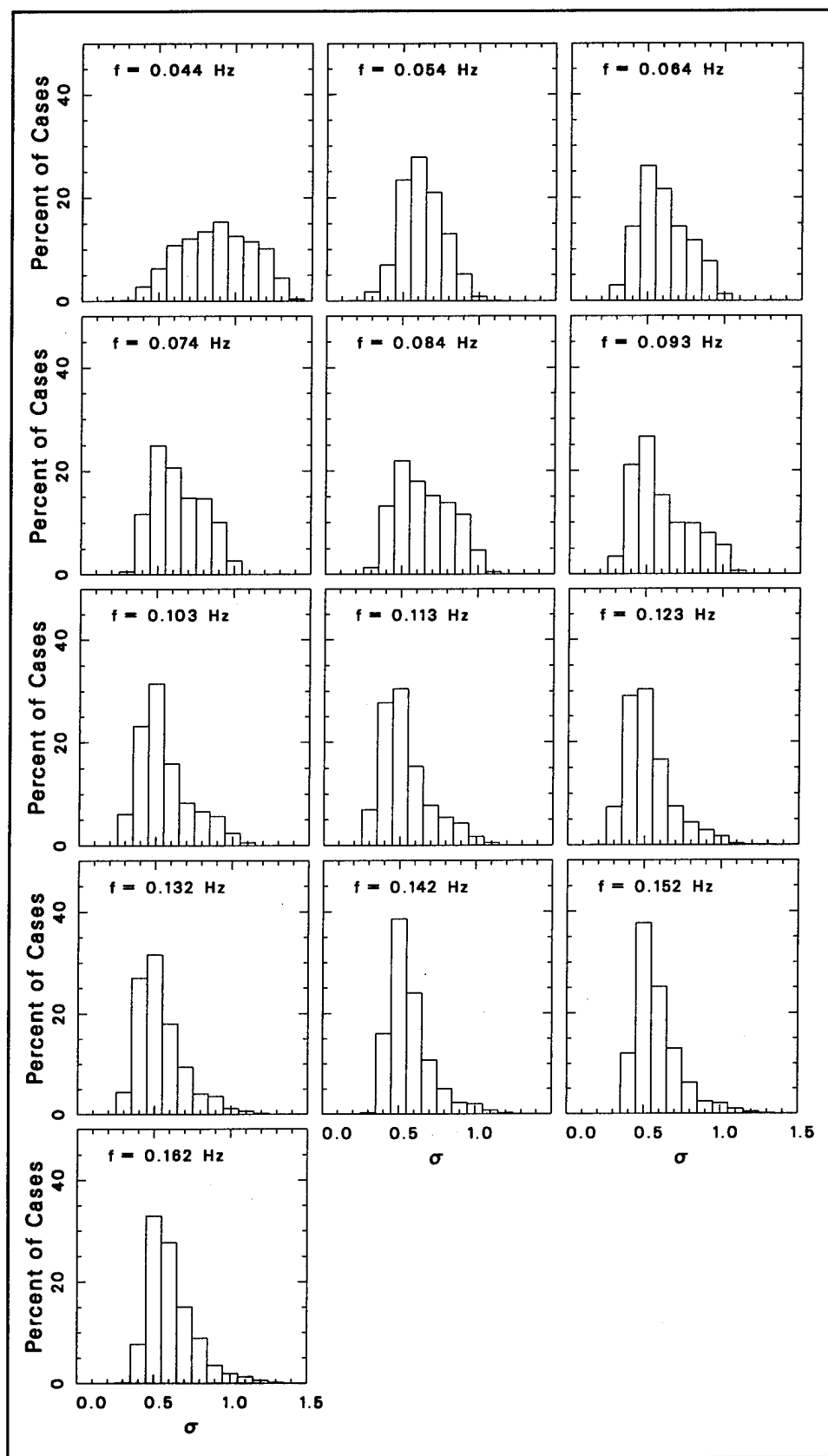


Figure 30. Distributions of circular width for all frequencies

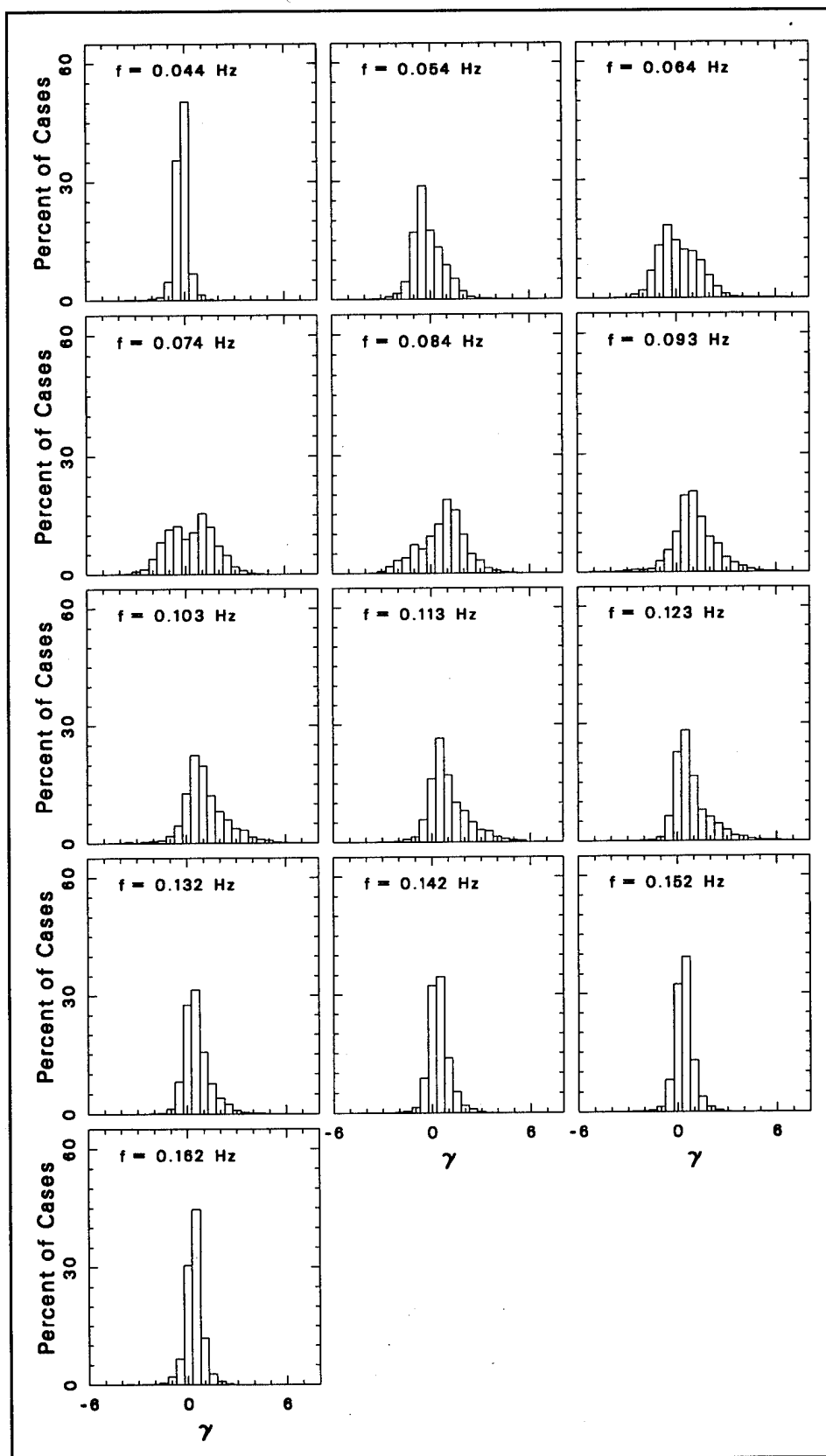


Figure 31. Distributions of circular skewness for all frequencies

The modal, or most common, values shift from slightly negative at lower frequencies to slightly positive at higher frequencies. Negative skewness indicates side lobes at positive angles from the mean direction. In the coordinate system used in this report, negative skewness is consistent with mixed western wind seas and southern swell, with the wind sea energy dominating. When southern swell energy dominates, skewness becomes positive. Figure 31 shows this latter case to occur often at the lower frequencies. At the highest frequencies, ranges of skewness are small, with most common values zero or slightly positive, suggesting nearly symmetric energy distributions.

Circular kurtosis  $\delta_n$  distributions are shown in Figure 32. As discussed in Chapter 5 for bulk parameters, kurtosis is a measure of flatness or peakedness of a distribution, with  $\delta = 3$ , the kurtosis of a Gaussian distribution, being a standard comparator. In Figure 32, the distribution of  $\delta$  at the lowest frequency is predominantly at values less than 3, indicating that most of the distributions are relatively flat. For the highest seven frequencies, the distributions of kurtosis range from about 1 to as high as 20, with modal values typically between 4 and 6. These high-frequency distributions indicate that typical directional energy distributions are more peaked than Gaussian curves. For the lower frequencies (except the lowest), the distributions are rather uniform for  $\delta$  in the range 2 to 6, with a significant fraction of cases having  $\delta > 6$ . These low-frequency results indicate a mix of distributions with some very peaked curves, suggesting well-directed waves with single direction modes, and some very flat curves, indicating waves from directionally diverse sources.

## Quartile Spread and Asymmetry

Directional spread  $\Delta\theta_n$  and asymmetry  $A_n$  parameters based on quartile directions of energy distributions at each frequency can be compared to frequency-dependent circular width  $\sigma_n$  and skewness  $\gamma_n$ , respectively, to augment interpretation. Figure 33 shows distributions of directional spread deduced from the set of observations. At the lowest frequency, there is a broad range of spread parameter, like the circular width at this frequency in Figure 30, but there is a most common value of about 25 deg, suggesting the frequent occurrence of very narrow directional distributions. For frequencies higher than 0.054 Hz, there appear to be two modes in  $\Delta\theta$  distributions. With a boundary between these two modes at roughly 60 to 80 deg, directional spreads in the high-spread mode can be as high as 100 to 140 deg, which suggests the presence of multiple wave sources. The low-spread modes in Figure 33 indicate  $\Delta\theta$  generally in the range 10 to 60 deg, which are typical of unimodal seas from single sources in various stages of development (Long and Oltman-Shay 1991).

Figure 34 shows distributions of quartile asymmetry. The shapes of several of the distributions in Figure 34 look very much like the distributions of circular skewness shown in Figure 31. This observation applies to the distri-

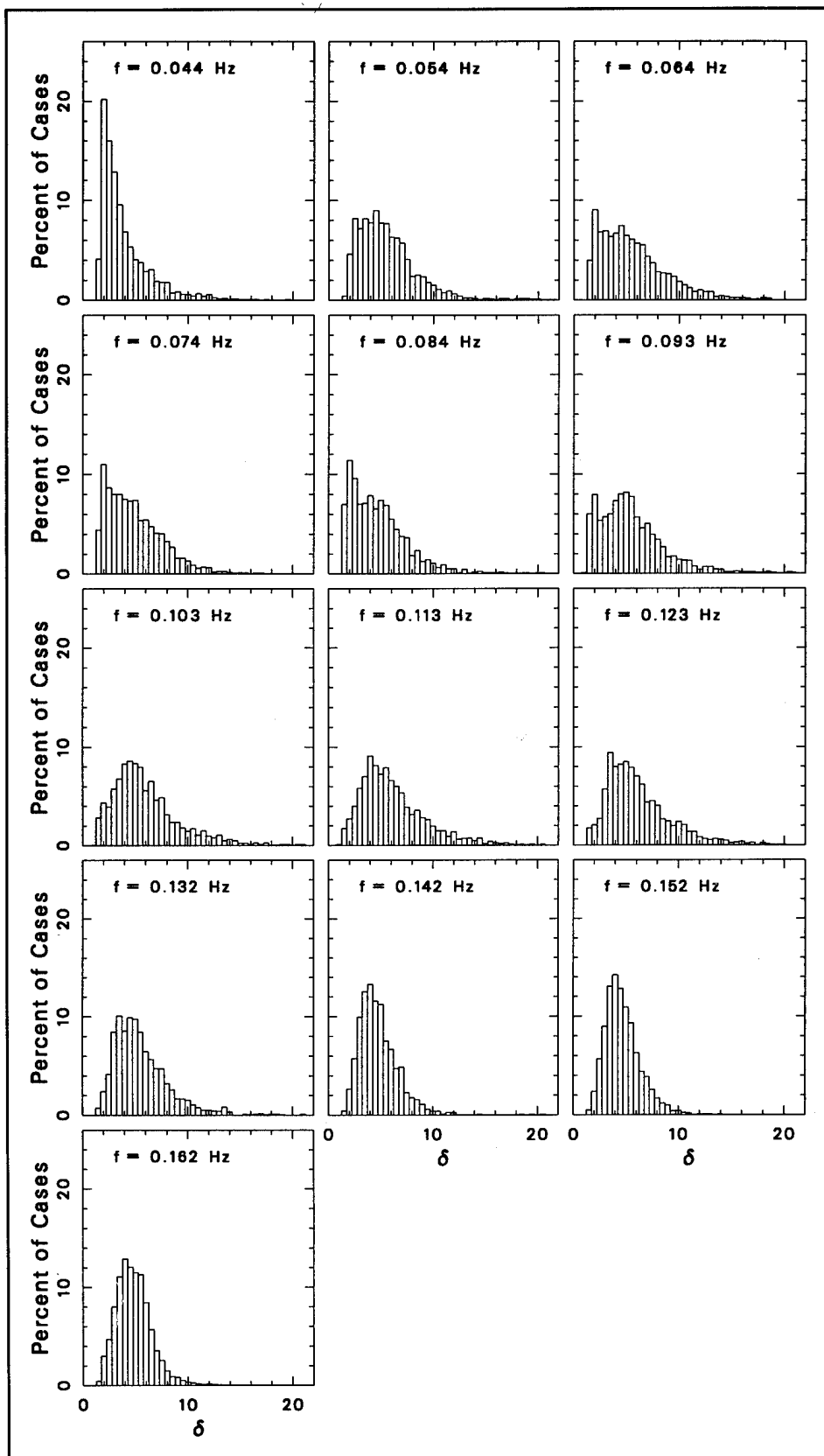


Figure 32. Distributions of circular kurtosis for all frequencies



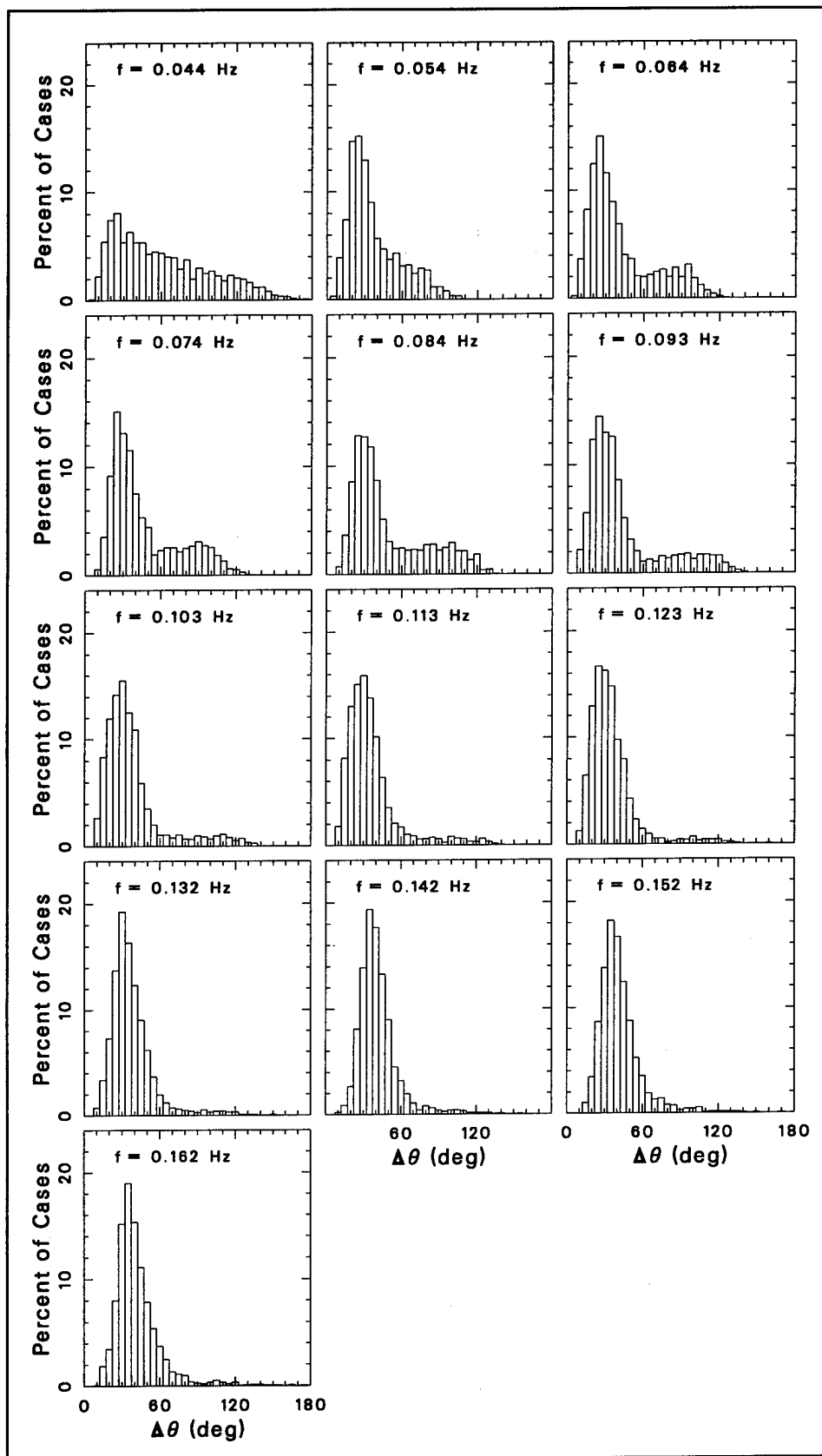


Figure 33. Distributions of quartile spread for all frequencies

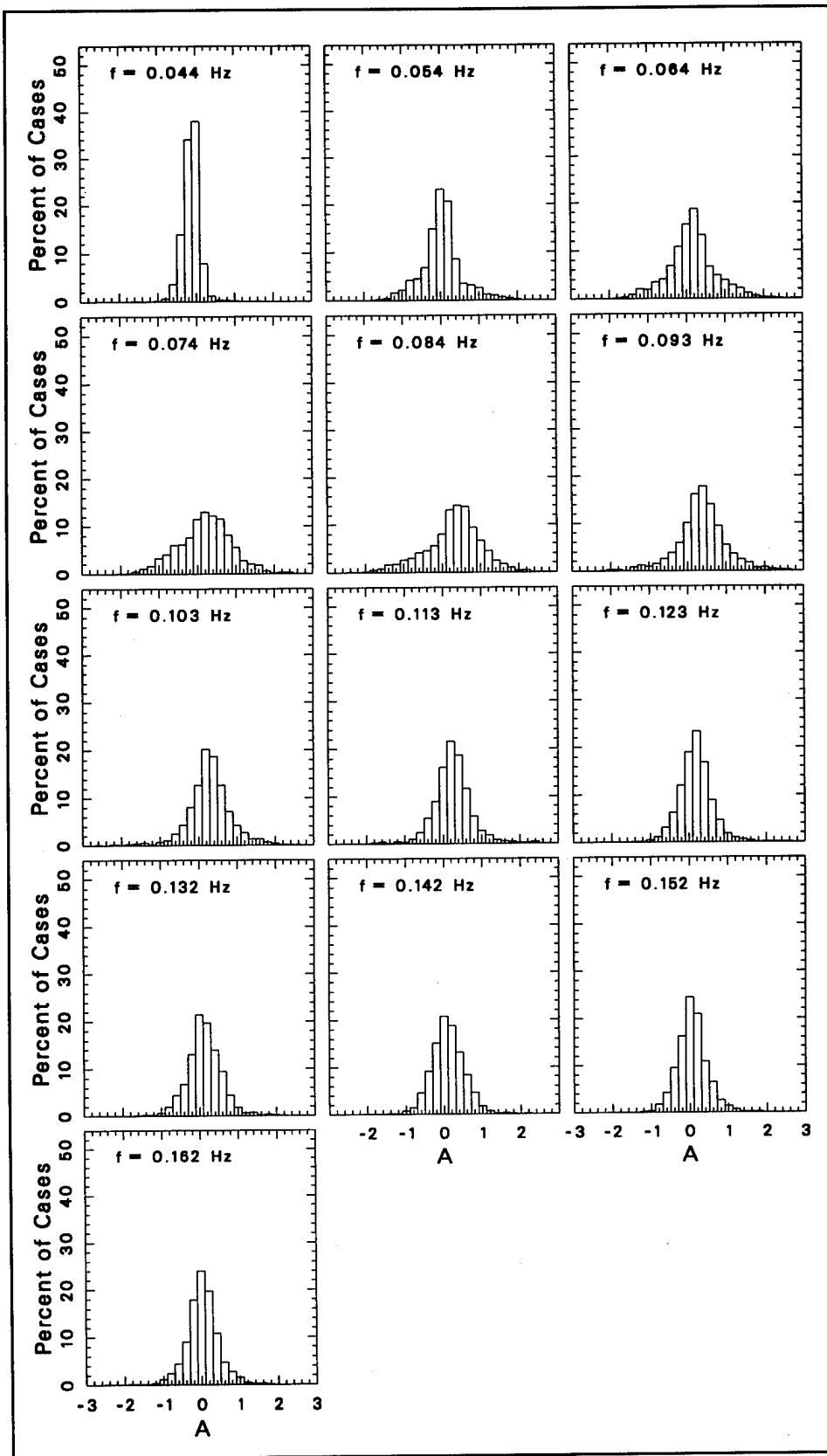


Figure 34. Distributions of quartile asymmetry for all frequencies

butions at  $f = 0.044, 0.084, 0.093,$  and  $0.103$  Hz, which suggests that  $\gamma$  and  $A$  are measures of the same property. At other frequencies, there are subtle differences in the distributions shown in Figures 31 and 34 that suggest the two parameters are more remotely related. For example, at frequencies  $0.054$  and  $0.064$  Hz, the modes in distributions of  $\gamma$  are slightly negative, whereas modes in distributions of  $A$  are slightly positive. For these two frequencies,  $\gamma$  indicates common skewness with mild secondary lobes at directions smaller than the mean directions, whereas  $A$ , if interpreted as a skewness, indicates the opposite. Additionally, at the highest four frequencies,  $A$  indicates higher percentages of negative values than does  $\gamma$ . However, for all  $f \geq 0.074$  Hz, the most common values of both parameters are slightly positive. The general indication is that the two parameters are closely related so that either can indicate distribution asymmetry.

## Modal Analysis

Within a frequency-direction spectrum, the directional distribution at any given frequency can have several modes, or peaks, depending on the directional separation and strength of sources of waves at that frequency, as well as low-level peaks that are due to fluctuations in background noise levels. Modal analysis discussed in Chapter 5 was based on the normalized, integrated direction spectrum  $D(\theta_m)$ . By virtue of its integration over all frequencies, such a directional distribution is smoother (i.e., has fewer modes) in general than the frequency-dependent directional distributions that contributed to the integral. Consequently, it is useful to examine the statistical distributions of numbers and relative importance of modes at each frequency.

Figure 35 is the result of such an analysis. For each frequency, there is a probability density function for the number of modes, and another probability density for the percentage of wave energy in the primary, or largest, mode. As many as five modes were found in some frequency-dependent distributions, whereas a maximum of three modes were found in the bulk parameterization shown in Figure 17. The lowest frequency shown in Figure 35 is the easiest to evaluate. Approximately 96 percent of all directional distributions were unimodal, and approximately 96 percent of all distributions had 97.5 to 100 percent of energy in the primary mode.

For the following three low frequencies ( $f = 0.054, 0.064,$  and  $0.074$  Hz), there were four or five modes represented by significant fractions of observations. At these frequencies, fewer than 40 percent of observations had 97.5 to 100 percent of energy in the primary modes, and fewer than 60 percent of observations had 92.5 to 100 percent of energy in the primary modes. This result means a significant fraction of cases had 7.5 to 50 percent of energy distributed among secondary modes. This is important because two of these frequencies are peak frequencies in conditions of highest energy (Figure 19), and are also common frequencies for southern swell (Figure 28).

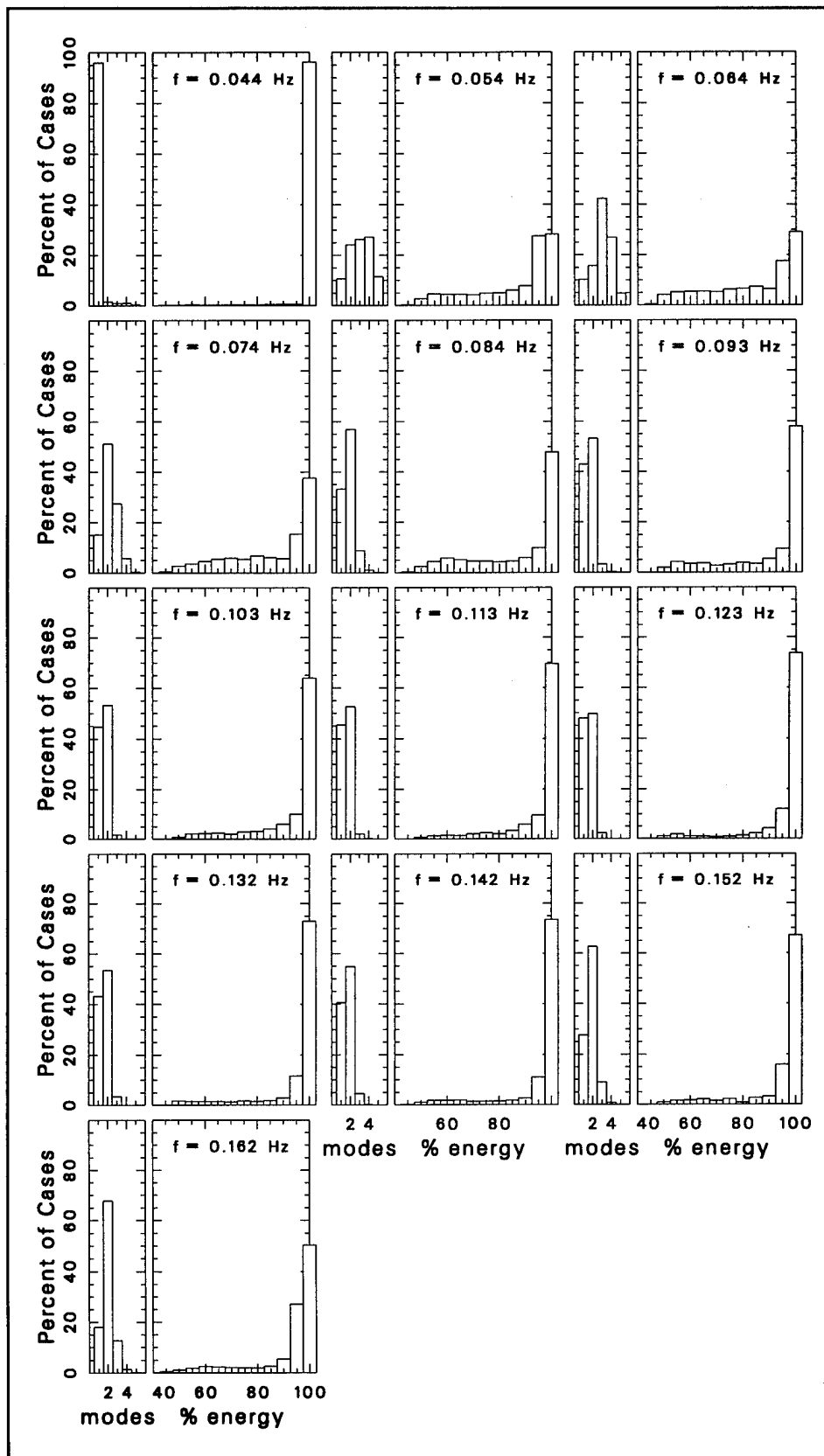


Figure 35. Modal analysis for each frequency

For  $f \geq 0.093$  Hz, most of the distributions are described by one or two modes, with bimodal distributions being most common. Between 50 and 74 percent of observations had 97.5 to 100 percent of wave energy in the primary mode, and 73 to 88 percent of observations had 87.5 to 100 percent of wave energy in the primary mode. Thus, 12 to 27 percent of cases had 12.5 to 50 percent of energy in secondary modes. This indicates that although most of the high-frequency observations were bimodal, not a lot of the secondary modes were energetic.

## Summary of Frequency-Dependent Parameters

This chapter contains a detailed examination of statistical distributions of spectral properties and parameters associated with individual frequency bands. These properties include spectral density, peak direction, mean direction, higher circular moments (width, skewness, and kurtosis), quartile directional spread and asymmetry, and analysis of directional modes. As illustrated in Figures 27 to 35, there are generally significant differences in these properties over the full range of frequencies examined. Furthermore, parametric behavior at the frequency level does not necessarily parallel bulk parametric distributions. Knowledge of parametric behavior at the frequency level enables classification of directional distribution functions for further display and analysis, which is done in subsequent chapters of this report.

## 7 Examples of Spectra

---

Part of the purpose of this report is to characterize frequency-direction spectral observations from Harvest Platform by illustration. This is a somewhat daunting task because there are more than 2,000 observations in the data set, and, as indicated by the bulk and frequency-dependent parameters discussed in Chapters 5 and 6, there is a very broad variety in energy distributions. Space does not allow picturing all the spectra, so a subset of representative spectra was identified for illustration.

To define a representative subset, each member of the whole set of observations was classified in terms of its quartile spread  $\Delta\theta$  and asymmetry  $A$ . These two bulk parameters give indications of the directional arcs over which wave energy is distributed, and the existence and relative importance of side lobes and modes in the distributions. Observations were grouped in classes of  $\Delta\theta$  that were 10 deg wide, and centered at 10-deg intervals, starting at 10 deg. The narrowest spread class thus included observations with  $\Delta\theta$  in the range 5 to 15 deg. Sixteen spread classes were employed, so the broadest spread class satisfied  $155 \text{ deg} < \Delta\theta \leq 165 \text{ deg}$ . Within each spread class, observations were further grouped by  $A$  in 11 bins of width 0.4, starting at  $A = -1.8$ , and extending to  $A = 2.6$ . The most symmetric distributions were thus in the asymmetry class for which  $-0.2 < A \leq 0.2$ .

By counting the number of observations in each of the classification cells, the most common conditions (within the definition used here) could be identified. Example spectra were chosen from 24 of the most populous cells. Because there is much interest in high-energy conditions, 24 examples were chosen based on the case with the highest  $H_{m0}$  in each of the populous cells. In three of the populous cells with  $\Delta\theta$  near 100 deg, additional cases with low or intermediate energy were included for intercomparison.

A total of 28 examples are shown in this report. One of them is Figure 3, discussed in conjunction with primary data analysis in Chapter 3. The remainder are shown in Appendix B. Table 2 is a listing of the sample cases, and includes for each case the figure where it is graphed as well as its set of characterizing bulk parameters. In Appendix B, graphs are drawn three per page in order of low to high  $\Delta\theta$  for each  $A$  ranging from most negative to most positive. The most populous classification cells were in two groups: low to moderate  $\Delta\theta$  with low to moderate  $A$ , and high  $\Delta\theta$  with moderate to

**Table 2**  
**Parameters for Example Spectra**

Figure	$H_{mo}$ m	$f_p$ Hz	$\theta_p$ deg	$\theta_o$ deg	$\sigma$	$\gamma$	$\delta$	$\Delta\theta$ deg	$A$
3	1.41	0.064	44	72	0.895	1.25	2.16	103	1.50
B1t <sup>1</sup>	4.37	0.064	78	71	0.391	0.21	6.42	27	-0.43
B1m	3.53	0.083	118	97	0.555	-0.20	3.75	43	-0.26
B1b	4.06	0.064	64	66	0.485	2.10	8.13	20	0.10
B2t	4.53	0.083	96	101	0.468	0.01	5.38	28	0.18
B2m	3.85	0.083	100	99	0.518	-0.21	4.16	35	-0.07
B2b	3.18	0.083	62	87	0.560	0.46	3.70	45	0.13
B3t	2.26	0.113	70	95	0.654	0.09	2.78	56	0.09
B3m	3.86	0.064	68	74	0.492	1.65	7.27	21	0.29
B3b	4.71	0.083	90	99	0.441	0.29	5.86	28	0.30
B4t	3.40	0.083	54	60	0.498	0.46	4.12	36	0.29
B4m	3.38	0.074	88	102	0.600	0.30	3.37	46	0.54
B4b	3.30	0.083	92	96	0.724	-0.05	3.09	56	0.23
B5t	3.96	0.064	66	73	0.518	1.74	5.94	24	0.64
B5m	3.47	0.064	88	98	0.639	1.80	4.91	30	0.80
B5b	3.54	0.064	84	97	0.625	1.41	4.27	37	0.92
B6t	3.01	0.074	60	81	0.832	1.90	3.38	48	0.64
B6m	3.40	0.093	52	83	0.695	0.83	2.88	60	0.60
B6b	1.67	0.083	52	97	0.847	0.65	1.91	96	0.93
B7t	2.24	0.083	52	72	0.677	1.73	3.85	43	1.12
B7m	2.52	0.074	64	82	0.796	1.95	3.40	47	1.13
B7b	1.45	0.083	58	92	0.858	1.06	2.21	94	1.24
B8t	0.81	0.093	58	92	0.896	1.22	2.31	88	1.08
B8m	2.00	0.064	58	74	0.927	1.22	2.29	94	1.26
B8b	1.68	0.113	40	83	0.915	1.21	2.22	99	1.02
B9t	1.58	0.113	44	84	0.927	1.16	2.04	105	1.26
B9m	0.61	0.103	52	92	0.978	0.84	1.77	113	1.22
B9b <sup>1</sup>	1.62	0.132	40	74	0.920	1.53	2.32	99	1.50

<sup>1</sup>The letters t, m, and b indicate top, middle, and bottom graphs, respectively, in figures in Appendix B.

high  $A$ . Consequently, the graphs in Appendix B appear somewhat scattered. However, the figures presented and discussed in this chapter are for illustrative rather than analytic purposes, so the apparent lack of system in their order is not detrimental.

The example spectra illustrate many properties described parametrically in Chapters 5 and 6. For instance, all examples indicate significant amounts of wave energy arriving from the northwest (wave directions between 0 and 90 deg in the figures) as indicated in Figure 10 for statistical distributions of  $\theta_p$  and in Figure 20 for correlations of  $\theta_p$  and  $H_{mo}$ . Example cases with  $H_{mo} > 4$  m (13.1 ft) (Figures B1t, B1b, B2t, and B3b, where t, m, and b indicate top, middle, and bottom graphs, respectively, in the figures in Appendix B) all have  $\Delta\theta$  between 20 and 30 deg as indicated in Figure 25, and thus give a graphic image of narrowly spread, high-energy spectra.

Directionally broad examples (Figures 3, B6b, B7b, and all graphs in Figures B8 and B9) are characteristically wind seas from the northwest on which are superimposed peaks of energy from the south. The added effect of these southern energy peaks is to increase dramatically estimates of  $\Delta\theta$ . This can be seen qualitatively by comparing Figures B3b and B8b, where the wind sea (from the northwest) parts of the spectra have roughly the same features, but Figure B8b shows other peaks of energy from the south and at low frequency. For Figure B3b,  $\Delta\theta = 28$  deg, which is a reasonable estimate for the wind sea part of Figure B8b. However, Figure B8b has a bulk  $\Delta\theta$  of 99 deg, which must be mostly due to the secondary energy mode from the south.

There can be substantive differences in detailed spectral structure within classes characterized by ranges of  $\Delta\theta$  and  $A$ . For example, Figures B9t ( $\Delta\theta = 105$  deg,  $A = 1.26$ ) and B9m ( $\Delta\theta = 113$  deg,  $A = 1.22$ ) are from the same class cell, the two having been included in the example set for comparison of contrasting energy levels; the spectrum of Figure B9t represents more than six times the energy of the spectrum in Figure B9m. Figure B9m indicates greater directional energy spread at high frequencies and greater frequency distribution of energy in the southern source mode than the case shown in Figure B9t. However, the integrated direction spectra  $D(\theta_m)$  shown in the left rear panels of these graphs, and from which the classifying bulk parameters are derived, have comparable structural shapes. Subtleties in spectral structure are not all energy-related. Figures 3 and B9b are from the same class cell, and have nearly the same set of parameters throughout, except for peak frequency. Visually, it appears that the structure of the wind sea mode of energy from the northwest is substantially narrower in Figure B9b than in Figure 3. Many of these subtleties can be resolved by analyzing and characterizing separately each energy mode in a spectrum. Though beyond the scope of the initial investigation reported here, such analysis clearly can yield a more detailed and uniform characterization of these spectra.

Disregarding minor differences, the example spectra provide images of energy distributions as they are identified through the classifying parameters. Spectra with narrow directional spreads tend to be unimodal with small to



moderate asymmetries. Cases in the high-energy regime tend to have the narrowest directional spreads. Cases with large directional spreads tend to be multimodal with varying contributions of energy from southern sources to extant wind seas. Though there exist many additional spectra, some with more deviate energy distributions, the examples used in this chapter are from populous directional spread and asymmetry classes, and so are representative of much of the data set.

## 8 Characteristic Directional Distribution Functions

---

A way to gain further insight in the way wave energy is directionally distributed in observations from Harvest Platform is to examine the distribution functions from all frequencies from all observed frequency-direction spectra. Each of the 2,339 frequency-direction spectra considered in this report has 13 frequency bands so that from the normalized frequency-direction spectra  $D(f_n, \theta_m)$  defined by Equation 7 there are a total of 30,407 individual directional distribution functions. These functions can be classified, grouped, and averaged within groups to define characteristic directional distribution functions. Because normalized distributions are used, any effect of energy content is removed in this type of analysis. Because all distribution functions are averaged without regard to source wave frequency, any knowledge of frequency effects, such as high-frequency versus low-frequency processes, is lost. This is acceptable at the level of analysis done here because the objective is to define general characteristic shapes, along with some knowledge of frequency of occurrence of these shapes.

### Classification Algorithms

In this report, directional distribution functions are classified and grouped based on three frequency-dependent parameters  $\theta_{0n}$ ,  $\Delta\theta_n$ , and  $A_n$  defined in Chapter 4. For each frequency  $f_n$  in a normalized frequency-direction spectrum  $D(f_n, \theta_m)$ , the directional distribution function is translated on the direction axis by its mean direction  $\theta_{0n}$ , classified as being in a particular range of directional spread  $\Delta\theta_n$  and asymmetry  $A_n$ , and stored in a classification buffer function  $D_{ijk}(\theta_m - \theta_0)$ . Mathematically, this process is expressed

$$D_{ijk}(\theta_m - \theta_0) = D(f_n, \theta_m - \theta_{0n}) \quad m = 1, 2, \dots, M \quad (50)$$

Index  $i$  in Equation 50 is an index designating a range of directional spread, and is defined as the nearest integer to  $\Delta\theta_n/10$  so that the  $i^{\text{th}}$  range includes directional spreads from  $10i - 5$  deg to  $10i + 5$  deg. Most of the

observations were classifiable when twelve spread ranges were used so that  $i$  assumes values from 1 to 12. Index  $j$  in Equation 50 designates a range of quartile asymmetry, and is defined as the nearest integer to  $A_n/0.4$  so that the  $j^{th}$  range includes asymmetries from  $0.4j - 0.2$  to  $0.4j + 0.2$ . The bulk of observations had asymmetries in the overall range of -2.2 to 2.2 so that  $j$  assumes values from -5 to 5, with the class for which  $j = 0$  being the most symmetric. Index  $k$  in Equation 50 is a case index to distinguish among the contributing distribution functions in the accumulation buffer. The upper limit for  $k$  in each spread-asymmetry classification cell is  $K_{ij}$ , which indicates the total number of contributors to cell  $ij$ . The argument  $\theta_0$  on the left-hand side of Equation 50 is a generic notation that indicates all contributors to the accumulation buffer are centered on their mean directions.

In this classification scheme, 30,044 directional distributions out of a possible 30,407 distributions fit, with only 363 distributions (1.2 percent) exceeding the indicated ranges of spread or asymmetry. Furthermore, as will be seen, not all of the classification cells had contributions. Nevertheless, 98.8 percent of all observations are accounted for, and the classification cells defined here form a regular grid in the spread-asymmetry plane.

Characteristic distribution functions are defined as averages (at each discrete direction) of contributing distributions in each classification cell. A measure of variability of the members within a cell is found by computing standard deviations of contributing distributions. Such statistics require a minimum number of contributions in each cell. In this study, no statistics were computed for any cell in which  $K_{ij} < 3$ . In cells for which  $K_{ij} \geq 3$ , sums were computed of the value and the square of each contributing member in the accumulation buffer for each discrete direction. The mathematical expressions for these processes are

$$s_{1ij}(\theta_m - \theta_0) = \sum_{k=1}^{K_{ij}} D_{ijk}(\theta_m - \theta_0) \quad m = 1, 2, \dots, M \quad (51)$$

and

$$s_{2ij}(\theta_m - \theta_0) = \sum_{k=1}^{K_{ij}} D_{ijk}^2(\theta_m - \theta_0) \quad m = 1, 2, \dots, M \quad (52)$$

A characteristic mean distribution function  $\bar{D}_{ij}(\theta_m - \theta_0)$  is then defined as

$$\bar{D}_{ij}(\theta_m - \theta_0) = \frac{s_{1ij}(\theta_m - \theta_0)}{K_{ij}} \quad m = 1, 2, \dots, M \quad (53)$$

and a standard deviation  $D_{\sigma ij}(\theta_m - \theta_0)$  of contributing distributions about the mean is computed from

$$D_{\sigma ij}(\theta_m - \theta_0) = \sqrt{\frac{s_{2ij}(\theta_m - \theta_0) - K_{ij} \bar{D}_{ij}^2(\theta_m - \theta_0)}{K_{ij} - 1}} \quad m = 1, 2, \dots, M \quad (54)$$

Equation 53 provides the essential definition for the set of characterizing distribution functions. Equation 54 provides a measure of how well contributing distributions agree in structural form. If standard deviation values are small relative to means, it is an indication that contributing shapes are quite similar. If standard deviations are large, there is considerable variability in the forms of contributing distributions.

## Resulting Distributions

Characteristic distributions resulting from these computations are illustrated in Appendix C. There is a graph representing each spread-asymmetry class, with a page of graphs for each class of directional spread, and each page shows all the asymmetry classes for the indicated directional spread class.

Each graph shows  $\bar{D}_{ij}(\theta_m - \theta_0)$  as a solid line. Dashed lines show standard deviations in the forms  $\bar{D}_{ij} + D_{\sigma ij}$  and  $\bar{D}_{ij} - D_{\sigma ij}$ . Each graph also indicates the number of contributing distributions used in the computations. If a cell had too few contributions ( $K_{ij} < 3$ ), the number of cell members is shown, but no curves are drawn.

Shapes of the mean curves, relative values of standard deviation curves, and numbers of contributing distributions are all relevant to interpreting these graphs. Characteristic distributions with small to moderate spreads and small to neutral asymmetry shown as graphs near page centers in Figures C1 to C4 tend to have simple shapes with a strong primary peak and either no or a very slight side lobe of energy. Characteristic curves with broad spreads and small to neutral asymmetries, as in Figures C10 and C11, appear to be composed of two or more main lobes of comparable energy content. Curves with the largest asymmetries, which do not appear in the narrowest classes, but begin with Figure C5, all have well-displaced (in direction) secondary lobes of moderate relative intensity. The classification scheme appears to preserve distribution symmetry; within a spread class, curves in asymmetry classes of the same magnitude but of opposite sign appear qualitatively to be mirror images of each other. This property holds true even though there tends to be a great many more members in classes with positive asymmetry than with negative.

Quality of the characterizing nature of these curves appears to be higher for distributions in classes with small to moderate spreads than for those with large spreads. In Figures C1 to C3, standard deviations are small relative to mean values near distribution peaks. This condition suggests that all

contributing distributions have nearly the same shape. In contrast, Figures C10 to C12 show distributions with standard deviations that are larger percentages of peak values, suggesting considerable variability in contributing shapes.

However, a pattern seems evident in the largest spread classes shown in Figures C10 to C12. Most of the mean distributions appear to be bimodal, and, with careful examination, it can be seen that modal separation increases as spread classification parameter increases. This result suggests that distributions assigned to the higher spread classes are products of wave conditions having multiple sources (as indicated by examples in Chapter 7) so that spread classification is controlled by directional separation of source processes rather than energy distributions within individual modes. In fact, if modes are separated at minimum points in the high-asymmetry distributions in Figures C10 to C12, it appears that individual modes would be classifiable within the low-to moderate-spread classes of Figures C1 to C5. Though clearly a valuable topic for future research, such modal separation is not done in this study because it is important to retain complete distributions for overall data characterization, and for estimation accuracy presented in Chapter 9.

Not so obvious in the figures in Appendix C is the relative importance of some classes over others. All classes are shown, which suggests equal weighting, but some classes are much more populous than others, and so are more representative of common or typical conditions at Harvest Platform. The single most populous class is the neutrally symmetric cell with spreads near 30 deg (Figure C3). With 3,295 contributing distributions, this one class represents approximately 10.8 percent of all distributions. In contrast, the classes with spreads of 100 deg or greater (Figures C10 to C12) have only between 5 and 124 cases, or 0.02 to 0.41 percent of all observations.

Clearly, the classes with small to intermediate spreads (Figures C1 to C5) and near-neutral asymmetry are dominant. For the group of classes with  $\Delta\theta < 55$  deg and  $-0.2 < A < 0.2$ , 9,582 distributions or 31.5 percent of all distributions are represented. If the first asymmetry cells on either side of the neutral asymmetry cells are included (i.e.,  $-0.6 < A < 0.6$ ) in the group with  $\Delta\theta < 55$  deg, the number of distributions rises to 20,312, or 66.8 percent of all cases, clearly a dominant group of classes. Much less dominant are the high-spread classes. The whole set of classes with  $\Delta\theta > 65$  deg (all cases in Figures C7 through C12) contains only 4,198 cases or 13.8 percent of observations. Note that if individual modes are analyzed separately, as mentioned previously, many members of the high-spread classes would add to the low-spread, low-asymmetry classes.

Some contributions to the high-spread classes may be less due to wave signal than to background system noise. Included in the classification set are all distributions from the lowest analyzed frequency (0.044 Hz). As indicated in Figure 27, the lowest wave frequency is dominated by very low wave energy. In low-energy conditions, collection and analysis noise become more important. A signature of noisy conditions in directional analysis is very

broad distributions. Because only 13 resolution frequency bands were analyzed, a significant part of one-thirteenth (7.7 percent) of contributing distributions could be affected by noise. This condition could be eliminated in future analysis by constraining contributing distributions to be from spectral densities above a certain minimum level. The main results of the present work are not seriously affected by a small percentage of potentially noisy results, however, because such results reside in classes with low populations.

The characteristic directional distribution functions shown in Appendix C and discussed in this chapter are elucidative in that they reveal some of the variety of common shapes of energy distributions observed at Harvest Platform. The more common shapes are readily identified by populations within the various classification cells. These characteristic shapes are also extremely useful in evaluating the resolving ability of the Harvest Platform directional wave gauge, as presented in the following chapter.

## 9 Accuracy of Directional Distribution Estimates

---

Central to any gauging device is the accuracy with which it resolves an input signal. This is especially true in high-resolution directional wave gauging because, in the application used here, an array of separate pressure gauges is employed, and the computational algorithm is complicated. The IMLE method is nonlinear, which complicates error estimates relative to linear systems, where errors can often be described analytically. The IMLE method is also data adaptive, which means results are quite sensitive to input conditions. At present, the only known way to estimate directional resolving ability with this method is to make computations, basing input on known directional distributions and comparing IMLE output estimates to these known conditions. Clearly, the choice of input conditions is important, and should be closely related to conditions at a given observation site. For the Harvest Platform data set discussed in this report, reasonable test conditions are the characteristic distribution functions described in Chapter 8. The present chapter describes test methodology and resulting estimates of uncertainty for these test conditions.

### Test Method

If a discrete directional distribution function  $D(f_n, \theta_m)$  at a given frequency  $f_n$  is known, an exact (to discretization accuracy) normalized cross-spectral matrix  $M_{ij}(f_n)$  can be computed as a basis for input for IMLE estimation. The mathematical expression is like Equation 12, taking the form

$$M_{ij}(f_n) = \sum_{m=1}^M D(f_n, \theta_m) e^{i\vec{k}_n(\theta_m) \cdot (\vec{x}_i - \vec{x}_j)} d\theta \quad (55)$$

where element indexes  $i$  and  $j$  range from 1 to  $I$ , the number of gauges in the test array. If the left-hand side of Equation 55 is used in place of the data-derived cross-spectral matrix used in Equation 9, then the set of Equations 9 to 15 can be used to make an IMLE estimate of  $D(f_n, \theta_m)$ , and the two distribution functions can be compared.

This procedure is correct, and is often used, but is somewhat unrealistic in that it overlooks the natural variability of a sea surface. Displacement of a natural sea surface is commonly treated as a Gaussian random process, which means there is expected to be noise in any cross spectrum that represents real wave signals. Consequently, noise must be added to the exact cross spectrum of Equation 55 to simulate natural variability.

In tests reported here, noise was added to exact cross spectra using the method of Brennan and Mallett (1976). In their method, the  $M_{ij}(f_n)$  of Equation 55 are elements of the  $I \times I$  Hermitian matrix  $M$ , which is decomposed using standard matrix procedures as

$$M = U \Lambda U^{-1} \quad (56)$$

where  $U$  is an  $I \times I$  matrix with each column holding one eigenvector of  $M$ ,  $\Lambda$  is a diagonal matrix containing the  $I$  eigenvalues of  $M$ , and the superscript  $-1$  indicates the matrix inverse. In the following expressions, use is made of the facts that the eigenvector matrix satisfies

$$U^{-1} = U_T^* \quad (57)$$

where the asterisk indicates complex conjugation, and the subscript  $T$  denotes matrix transpose, and, for a Hermitian matrix, eigenvalues of  $M$  are all real. Using these relationships, the right-hand side of Equation 56 can be rewritten as

$$\begin{aligned} M &= U \Lambda^{1/2} \Lambda^{1/2} U^{-1} \\ &= U \Lambda^{1/2} \Lambda^{1/2} U_T^* \\ &= V^* V_T \end{aligned} \quad (58)$$

where

$$V = U^* \Lambda^{1/2} \quad (59)$$

The advantage of this manipulation is that noise can be introduced by multiplying the matrix  $V$  by a column vector  $Z$  of  $I$  complex random deviates from a Gaussian distribution with zero mean and variance  $\frac{1}{2}$  to form a matrix with noise  $\tilde{V}$  in the form

$$\begin{aligned} \tilde{V} &= VZ \\ &= U^* \Lambda^{1/2} Z \end{aligned} \quad (60)$$



Equation 60 can be substituted into the right-hand side of the last equality of Equation 58 to form a cross-spectral matrix with noise as

$$\begin{aligned}\tilde{M} &= \tilde{V}^* \tilde{V}_T \\ &= U \Lambda^{1/2} Z^* Z_T \Lambda^{1/2} U_T^*\end{aligned}\tag{61}$$

where it will be remembered that matrix product order is reversed on transposition for the second triplet of terms in the second equality of Equation 61.

Equation 61 has two desired properties associated with adding noise to a cross-spectral matrix. One property is that, on average,  $\tilde{M}$  is equal to  $M$ , which can be shown by finding the expected value (the average over a large number of observations) of Equation 61. Because the eigenvalue and eigenvector matrices are constant for a given simulation, the expectation operation can be written

$$\begin{aligned}E[\tilde{M}] &= E[U \Lambda^{1/2} Z^* Z_T \Lambda^{1/2} U_T^*] \\ &= U \Lambda^{1/2} E[Z^* Z_T] \Lambda^{1/2} U_T^* \\ &= U \Lambda^{1/2} I \Lambda^{1/2} U_T^* \\ &= U \Lambda^{1/2} \Lambda^{1/2} U_T^* \\ &= M\end{aligned}\tag{62}$$

where  $E[ ]$  is the expectation operator, and  $I$  is the identity matrix. The expected value of  $Z^* Z_T$  becomes identity because, as written, each of the complex random numbers in  $Z$  is multiplied by its own conjugate, forming the sum of the squares of two Gaussian random deviates. Each of the squared values has an expected value of  $\frac{1}{2}$ , so they sum to form an expected value of unity. The other desired property is that the noise is distributed throughout the matrix elements in exactly the same way that cross-spectral estimates are distributed when computed from raw Fourier coefficients of data from the  $I$  gauges of the test array.

The cross spectrum with noise computed from Equation 61 is appropriate for raw cross-spectral estimates, and has two degrees of freedom. To simulate results from a data collection, results from Equation 61 must be computed, accumulated, and averaged a number of times corresponding to the product of the number of ensembles used and the number of frequency bands averaged in an actual data collection. In collections analyzed for this report, data were analyzed using eight contiguous ensembles with frequency smoothing over ten frequency bands. Consequently, an average of 80 computations of Equation 61, each with new random numbers, was required to simulate the 160 degrees of freedom obtained in prototype data collections.

If the elements  $\tilde{M}_{ij}(f_n)$  of the resulting cross spectrum with noise are used as the source cross spectrum at a given test frequency in Equations 9 to 15, the resulting IMLE directional distribution function estimate  $\tilde{D}_k(f_n, \theta_m)$  is but one of a large number (indexed by subscript  $k$ ) of possible results as a consequence of the added noise. To find an expected result from these possible results, the procedure outlined above for finding one estimate is repeated a large number of times, and the results are accumulated and averaged. For the tests reported here, experimentation revealed that reasonably stable statistics were obtained if 500 estimates were computed. An expected distribution  $\bar{D}(f_n, \theta_m)$  and standard deviation from the expected distribution  $D_o(f_n, \theta_m)$  for a given test case were found by first computing the sums

$$\tilde{s}_1(f_n, \theta_m) = \sum_{k=1}^{500} \tilde{D}_k(f_n, \theta_m) \quad m = 1, 2, \dots, M \quad (63)$$

and

$$\tilde{s}_2(f_n, \theta_m) = \sum_{k=1}^{500} \tilde{D}_k^2(f_n, \theta_m) \quad m = 1, 2, \dots, M \quad (64)$$

and then computing

$$\bar{D}(f_n, \theta_m) = \frac{\tilde{s}_1(f_n, \theta_m)}{500} \quad m = 1, 2, \dots, M \quad (65)$$

and

$$D_o(f_n, \theta_m) = \sqrt{\frac{\tilde{s}_2(f_n, \theta_m) - 500\bar{D}^2(f_n, \theta_m)}{499}} \quad m = 1, 2, \dots, M \quad (66)$$

It is noted that the statistics computed using Equations 63 to 66 are strictly legitimate only for MLE results, where variance estimates in each direction  $\theta_m$  are independent of each other. In IMLE, the constraints of Equations 8 and 16 result in some coupling of results across all directions. Consequently, mean and standard deviation distributions from Equations 65 and 66, respectively, are good indicators of estimator accuracy but are not completely defensible from first principles.

## Test Distributions

To examine resolvability of some of the variety of directional distributions that occur at Harvest Platform, the mean characteristic distributions discussed

in Chapter 8 and illustrated in Appendix C were used as test distributions. These distributions have the advantages that they are representative of prototype conditions, being derived as averages of such conditions, and they are of reasonable number. This last feature is important because it takes a significant amount of computer time to run a test condition through the test procedure outlined in the previous section. Testing a great number of cases then becomes somewhat impractical. Within the directional spread-asymmetry cells shown in Appendix C, there are 110 cells for which mean distributions are shown. These 110 mean distributions constitute the basic test set.

The 110 test distributions were defined by averaging individual distributions without regard to the frequencies at which the individual distributions were observed. However, resolving ability of a fixed array of gauges is a function of the wavelengths of incident waves, which are related to frequencies by virtue of the dispersion relation (Equation 11). To conduct a more complete set of tests, each of the test distributions was run for three frequencies. These frequencies were 0.05, 0.10, and 0.15 Hz to represent low-, medium-, and high-frequency regions, respectively, in observed spectra. With 110 test shapes run at each of three frequencies, there were a total of 330 test conditions.

## Test Results

Test results discussed in the present chapter are illustrated in Appendix D. Results varied reasonably smoothly through the set of test conditions so that some space is saved by illustrating a subset of test cases. Shown in Appendix D are 19 figures, each representing one of the 110 test distributions. Each figure shows results for all three of the test frequencies. Represented are tests based on characteristic distributions from directional spread classes centered at 10 deg (the narrowest class), 20, 30, and 40 deg (the most populous classes), 60 and 100 deg (intermediate classes), and 120 deg (the broadest class). Within each directional spread class except the narrowest, illustrated cases include neutral asymmetry as well as an extreme positive asymmetry and an extreme negative asymmetry. Only the neutral asymmetry case is shown for the narrowest spread class.

Each figure contains three graphs, one for each frequency. The test frequency is shown in the upper right-hand corner of each graph, along with the wavelength for waves of that frequency in water depth of 200 m. All graphs within a figure are drawn to the same scale, but scales change from figure to figure. Each graph contains three curves. A solid line, called the true distribution, is the test distribution obtained from the characteristic distribution illustrated in Appendix C for the ranges of  $\Delta\theta$  and  $A$  indicated at the tops of the figures in Appendix D. Dotted lines are expected, or mean, distributions based on 500 estimates as expressed by Equation 65. Ideally, expected and true distributions are identical. When they are not identical, differences indicate the amount of estimator bias. Dashed lines show standard deviation

distributions as computed using Equation 66, and provide a measure of the variability of the set of estimates from the expected distribution.

The set of figures in Appendix D indicate that the best results are obtained for distributions with narrow spread and near-neutral asymmetry in medium- to high-frequency wave conditions. Figures D1, D3, and D6 all illustrate very small differences between true and expected distributions for test frequencies of 0.10 and 0.15 Hz. For low-frequency waves at test frequency 0.05 Hz, there are differences of approximately 5 to 10 percent between the peaks of the true and expected distributions. Low-frequency waves are typically more difficult to resolve in IMLE because their wavelengths (approximately 600 m in these examples) are much larger than the maximum size of the array (approximately 60 m, as shown in Figure 2) so that phase differences due to small changes in wave direction are more difficult to resolve than for shorter waves. Note that because the total areas under directional distribution functions are constrained to be unity by Equation 8, regions where expected distributions are lower than true distributions must be compensated by regions at other directions where expected distributions exceed true distributions. Thus, where the peak expected curve is lower than the true curve for the lowest frequency in Figure D1, the shoulders of the expected curve have higher values than the true distribution.

Standard deviation curves appear uniformly maximum in the regions of the maxima of the true curves. In the regions of these maxima, standard deviations are approximately 10 to 20 percent of the true distribution values. This behavior indicates that in a single estimate using data from real waves, a variation of the maximum by 10 to 20 percent is not uncommon. At directions different from true spectral maxima, the standard deviation curves become smaller, though it appears there are increases in percentages of true spectral values represented by the standard deviation curves. For example, at the lowest frequency illustrated in Figure D1, the standard deviations in the directions near 20 deg and -20 deg appear to be about half, or 50 percent, of the true distribution values. The figures suggest that these higher percentages occur in regions away from spectral peaks, and so may be less dire errors.

Test distributions with moderate to large asymmetry and large spread are slightly less well-resolved than are the narrow, neutrally symmetric cases. The magnitude of asymmetry does not necessarily indicate poorer results, however. For example, expected distributions for low and intermediate frequencies in the narrow, moderately asymmetric example of Figure D2 show a 5- to 10-deg bias of peak values toward the high-energy tail of the distribution, along with small variations in the resolution of the high-energy tail. In contrast, Figure D16 illustrates a case with spread of approximately 100 deg and quartile asymmetry of about 2.0, yet has about the same magnitude bias toward its high-energy tail, and likewise small variations in resolution of the tail region.

The poorest representation of true distribution by expected distribution is shown in Figure D18, which is a case having neutral symmetry, but extreme spread with  $\Delta\theta$  near 120 deg. Both true and expected distributions have

curiously undulating values in the regions of their broad peaks. At none of the test frequencies are the agreements exceptional; expected peak directions deviate from true peak directions by 15 to 30 deg. A reason for this behavior is that the IMLE algorithm was derived to try to isolate narrowly distributed wave signals from background noise (Davis and Regier 1977), which it does quite well as shown in the example of Figure D1. In broadly distributed wave signals like those of Figure D18, the algorithm tends to produce spurious peaks, which can be seen as central maxima for the two higher frequencies in Figure D18. Qualitatively, the agreement of true and expected distributions in Figure D18 is quite good. The main features of the true distribution (broad, rather uniform high-energy region, and nearly constant background region) are reasonably well-represented, but not as well as in narrower examples.

It is noted that all the test distributions taken from the characteristic shapes of Appendix C have mean directions near 0 deg. This means that the centroid directions are those of waves propagating from the north, and so only propagate through one orientation of the array geometry shown in Figure 2. In more complete tests, true distributions would be shifted so their centroids were at several places around the horizon, and thus test array response to varied wave angle of attack. This was impractical because it would add another dimension to an already computationally intensive test program.

However, there are indications in the present test set that varying wave angle of attack does not substantially change array response. In all of the asymmetric examples in Appendix D for  $\Delta\theta > 35$  deg (Figures D8, D10, D11, D13, D14, D16, D17, and D19), there are clear indications of side lobes having substantial fractions of total energy. Existence of these side lobes causes distribution mean directions to shift away from distribution peaks so that peak energy conditions are not at 0 deg, but deviate by as much as 35 deg (Figures D17 and D19). Secondary lobes deviate from 0 deg by as much as 110 deg (Figure D14). Because distributions with both positive and negative asymmetries were tested, and test results were nearly symmetric (compare Figures D14 and D16, for example), one can conclude that directional response is generally uniform for all waves coming from the northeast and northwest quadrants. By symmetry, responses to waves coming from the southeast and southwest quadrants will be the same because their orientation to the array geometry is the same as for waves from the two northern quadrants. Thus, these tests suggest that array response is reasonably uniform for all wave approach directions.

It can be argued that test conditions were somewhat biased because observations from the Harvest Platform array were used to test array response, and it is reasonable to expect such a device to be able to resolve its own output quite well. However, in no test case was an exact array result used as a test condition; all test conditions were derived from averages of several array results. Because the standard deviations of the characteristic distributions of Appendix C were finite, it is unlikely that any average distribution was an exact replication of any single result. Furthermore, the addition of synthetic statistical noise ensured that no two input conditions were identical. Finally, because the expected distributions were very much like the true conditions for

all of the most populous characteristic distributions tested (Figures D2 to D10), it is likely that the characteristic distributions used for these tests were largely representative of actual wave conditions at Harvest Platform.

These tests indicate that the directional wave response of the Harvest Platform array is quite good for any application that can tolerate slight biases in peak energy levels and occasional errors in peak direction of up to 10 deg. Results from the array may only be qualitatively useful for highly direction-sensitive models like the one described by O'Reilly and Guza (1993). However, these results should be excellent ground truth for such applications as deep ocean wave modeling, remote sensing by air- and spacecraft, and field comparisons of low-resolution directional wave gauges. Further indications of the quality of array response are provided by examination of the behavior of directional parameters that characterize these data. Such an examination is done in Chapter 10.

# 10 Accuracy of Directional Parameters

---

Characterizing parameters of directional distributions of wave energy rather than the distributions themselves is a common practice in engineering and modeling efforts. A set of seven frequency-dependent parameters that describe various features of directional distributions were introduced in Chapter 4 of this report, and discussed in statistical form in Chapter 6. These parameters are distribution peak direction  $\theta_{pn}$ , the circular moment parameters describing mean direction  $\theta_{0n}$ , circular width  $\sigma_n$ , skewness  $\gamma_n$ , and kurtosis  $\delta_n$ , and the quartile parameters describing directional spread  $\Delta\theta_n$ , and asymmetry  $A_n$ . To determine how well these parameters can be resolved in typical wave conditions with the Harvest Platform array, statistics were accumulated during the directional distribution tests described in Chapter 9. Summary statistics of these parameters are displayed and discussed here.

Statistical descriptors were simply the means and standard deviations of each of the parameters during the 500 iterative runs of the 110 test distributions for each of the three test frequencies. The parameter mean value indicates its expected value from any arbitrary test sample, and can be compared to the parameter true value to investigate biases. Standard deviations give a measure of variability of test results, and indicate a nominal confidence range for a parameter in a given test condition.

## Peak Direction

Figure 36 illustrates results of these tests for peak direction. There is one graph for each of the three test frequencies. Each graph is in the form of a correlation of true  $\theta_p$  with mean test  $\theta_p$  (the subscript  $n$ , which indicates a frequency-dependent parameter, is dropped in subsequent discussion because frequency is shown explicitly in each graph). Superimposed on each mean  $\theta_p$  point is the standard deviation of the test set in the form of vertical error bars that extend above and below the mean point by one standard deviation. Symbols, identified at the top of Figure 36, indicate the directional spread class of the test distributions, and correspond with the spread classes of the characteristic distributions shown in Appendix C. For each symbol, there is a data

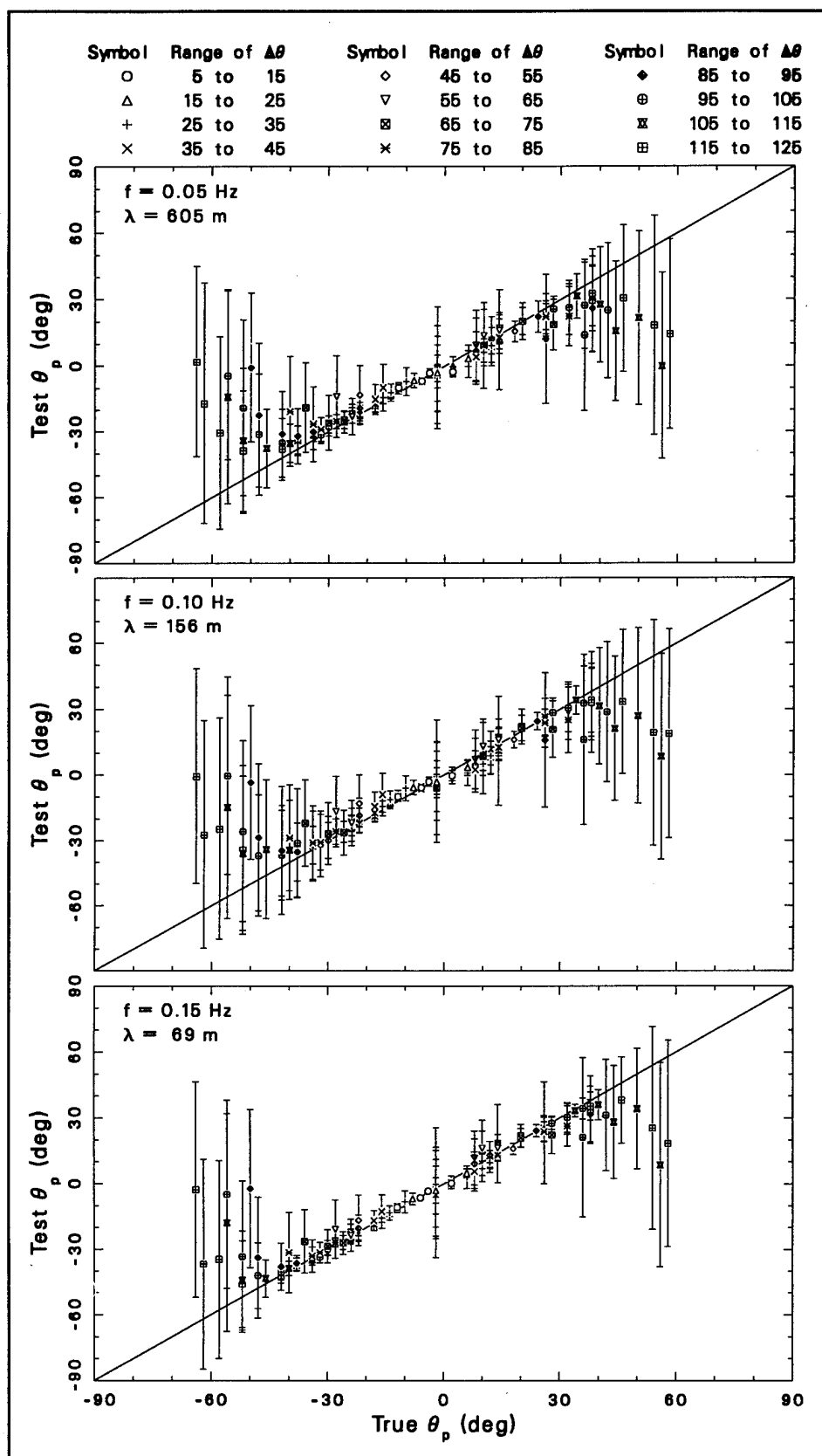


Figure 36. Test results for peak direction



point for each of the asymmetry classes associated with a given spread class in Appendix C. For example, circles represent the narrowest spread class in the test set, and there are four circles in each graph in Figure 36 because there are only four asymmetry classes shown in Figure C1 for this spread class.

Distinction of symbols is important because the eye is drawn to the large error bars in Figure 36, yet the large error bars do not represent the most common cases in the observed data. Close examination of Figure 36 indicates that the cases with greatest standard deviations are mostly from classes with large spreads and large  $\theta_p$ . Mean results for these cases are also biased toward small peak directions, in some cases by more than 60 deg. Curiously, this is a desired result. Examination of the test distributions for cases with extreme spread (Figure C12) shows that peak directions are extreme for the cases with near-neutral asymmetry. Because such distributions have broad, rather flat peaks, minor variations in distributions from the test cases can be detected as distribution peaks scattered over a wide range of directions. On average, one would expect such a distribution to fall near the centers of the broad flat regions, yielding peak directions near 0 deg. In the extreme cases of Figure 36, this is exactly what happens, yielding what appear to be large biases, and very large standard deviations. The three cases of extreme  $\theta_p$  from each of the four broadest cases (diamond-plus, circle-plus, double-triangle, and box-plus symbols) all exhibit this behavior for all test frequencies shown in Figure 36. Another large-error group of cases centered near 0 deg is from classes of intermediate spread with near-neutral asymmetry that also have considerable uncertainty in location of peak direction, but for which peaks of test spectra are near 0 deg.

If these extreme cases are eliminated from Figure 36, much tighter groupings of points emerge. The group with the smallest variations is the set of narrowest cases (open-circle symbols), for which the standard deviation indications are about the same size as the plotted symbol (approximately 1 or 2 deg). The next broader group (base-down-triangle symbols) has slightly larger scatter (approximately 3 to 4 deg), and an occasional bias of about the same size. Note that none of these narrow cases extends to very large  $\theta_p$ , and so are clustered within 10 to 20 deg of 0 deg.

A general interpretation of Figure 36 is that errors in peak direction are small for narrow distributions or broader distributions with well-defined, narrow modal peaks. When modal peaks become broad and flat, peak direction varies dramatically due to minor output fluctuations that vary with different combinations of statistical noise. Comparison of the three graphs in Figure 36 indicates somewhat smaller ranges of error bar lengths for cases with narrow and intermediate spreads at the highest frequency. This is a consequence of improved IMLE resolution of high-frequency distributions as discussed in Chapter 9.

## Circular Moment Parameters

Peak direction might be expected to be noisy because it is a single-point parameter, relying on directional estimates in a particular direction to be stable in the presence of naturally varying input conditions. Moment-based parameters are expected to be less noisy because moments are weighted sums of contributions from all directions in a distribution, a process that acts as a stabilizing filter. In this section, the behaviors of the four frequency-dependent parameters based on distribution circular moments are examined.

### Mean direction

Tests of mean direction reported here are somewhat limited because all the characteristic distributions of Appendix C that were used for testing were centered on their mean directions. Thus, results from all statistical tests should ideally yield the same result. Figure 37 shows the means and standard deviations of all test cases of  $\theta_0$  plotted not as functions of true  $\theta_0$ , which should be constant, but rather as functions of true asymmetry parameter  $A$ , which may reveal sensitivity to irregular energy distributions. As with peak direction, Figure 37 contains three graphs, one for each test frequency. Symbols, defined at the top of the figure, denote directional spread classes of test distributions shown in Appendix C. Horizontal lines through each graph show the value of true  $\theta_0$  for all the test cases. Due to an indexing error in an analysis program, all test distributions were centered one direction bin too high, so that true  $\theta_0 = -2$  deg instead of 0 deg. Note that this error has no effect on any other tests or discussion in this report, and only shifts the reference lines in Figure 37 to -2 deg instead of 0 deg.

For a given spread and asymmetry class shown in Figure 37, the smallest errors occur at the highest test frequency, and increase modestly for the two lower test frequencies. For a given asymmetry class, error bars are smallest for the narrowest test cases and increase with increasing spread range. For example, for the cases at which  $f = 0.15$  Hz, and  $A \approx 0$ , the standard deviation is less than 1 deg for the narrowest spread class (open-circle symbol), but is more than 6 deg for the broadest spread class (box-plus symbol). Error bars are roughly the same size for all asymmetries in a given spread class and at a particular frequency.

At the highest frequency shown in Figure 37, there is very little bias in the mean test  $\theta_0$ . The symbols tend to be within  $\pm 1$  deg of the reference line at this frequency. For the middle frequency, there is a slight bias that appears correlated with asymmetry. This bias is about -3 deg for the largest negative asymmetry, is near 0 deg at neutral asymmetry, and becomes positive by about 2 deg for the largest positive asymmetry. A similar, but stronger pattern is seen in the graph for the lowest frequency, where the bias ranges from about -5 deg at extreme negative asymmetry to about 3 deg at extreme positive asymmetry. The bias is due to the fact that, at low frequencies, there is a

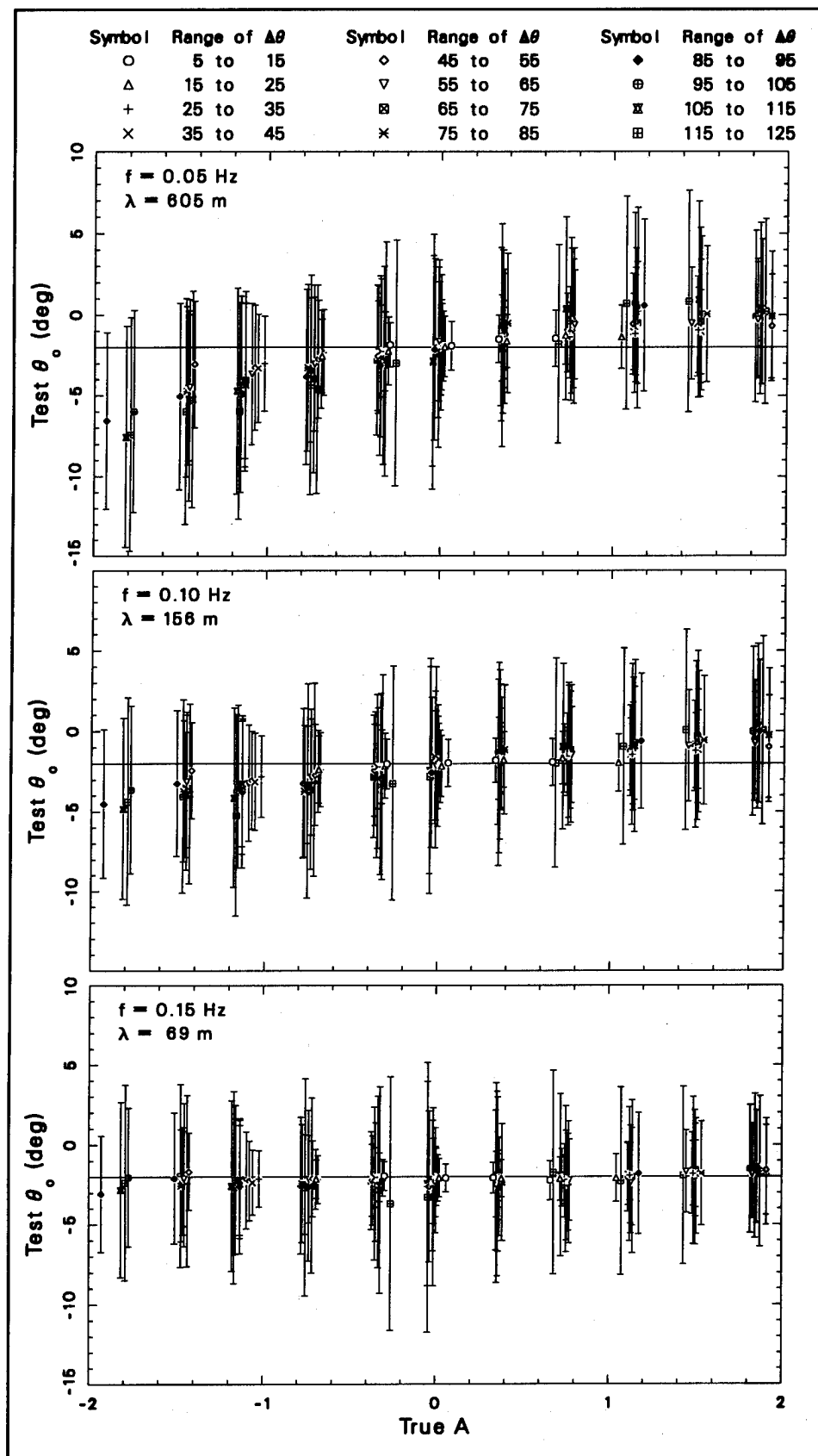


Figure 37. Test results for mean direction

tendency for IMLE to yield too little energy under a true distribution peak, and consequently, too much energy in the tails. When weighted by the trigonometric functions in its definition (Equation 40), the resulting  $\theta_0$  is shifted away from the peak and toward the high-energy tail. This behavior makes it correlate with asymmetry, for which the high-energy tail changes sides as asymmetry changes sign.

An overall characterization of mean direction accuracy is represented by the graph of the center frequency in Figure 37. A nominal standard deviation is  $\pm 5$  deg. A nominal bias is 2 to 3 deg, depending on asymmetry. If more exact characterization of error is necessary, the information plotted in Figure 37 can be used.

### Circular width

Means and standard deviations of the sets of  $\sigma$  estimates are shown as functions of true circular width in Figure 38, following the same class identification patterns used in Figures 36 and 37. Figure 38 shows  $\sigma$  to be relatively robust, with no strong biases evident, and reasonably uniform standard deviations within each test frequency group. Though errors are modestly smaller for the highest test frequency, it is relatively straightforward to assign a nominal uncertainty of  $\pm 0.05$  to estimates of  $\sigma$ .

### Circular skewness

Like the circular width parameter, circular skewness  $\gamma$  is reasonably well-behaved. Figure 39 illustrates the correlation of estimated mean skewness with true skewness, along with vertical error bars to show standard deviations of estimates. For each test frequency, the standard deviations are nominally the same, with slight reductions in the vicinity of  $\gamma = 0$ . As usual, errors are least at high frequencies, and increase with decreasing frequency. Nominal standard deviations are  $\pm 0.4$  for  $f = 0.15$  Hz, and  $\pm 0.5$  for the other two test frequencies. Biases are evident in the results at extreme values of  $\gamma$ , with the bias directions being toward smaller  $\gamma$ . For  $\gamma \approx 4$ , a nominal bias of -0.3 can be associated with the lowest test frequency, -0.2 with the center test frequency and less than -0.1 for the high-frequency test. Biases are very small near  $\gamma = 0$ , and are largest for the narrowest classes of test cases (open-circle, base-down-triangle, +, and x symbols), suggesting sensitivity to minor variations in skewed, but closely grouped distributions of high-energy points. This parameter is better resolved for directionally broad, highly asymmetric distributions than for any of the narrow, moderately asymmetric distributions.

### Circular kurtosis

Test results for circular kurtosis  $\delta$  are shown in Figure 40. Standard deviations of results tend to increase with increasing  $\delta$ . A nominal estimate

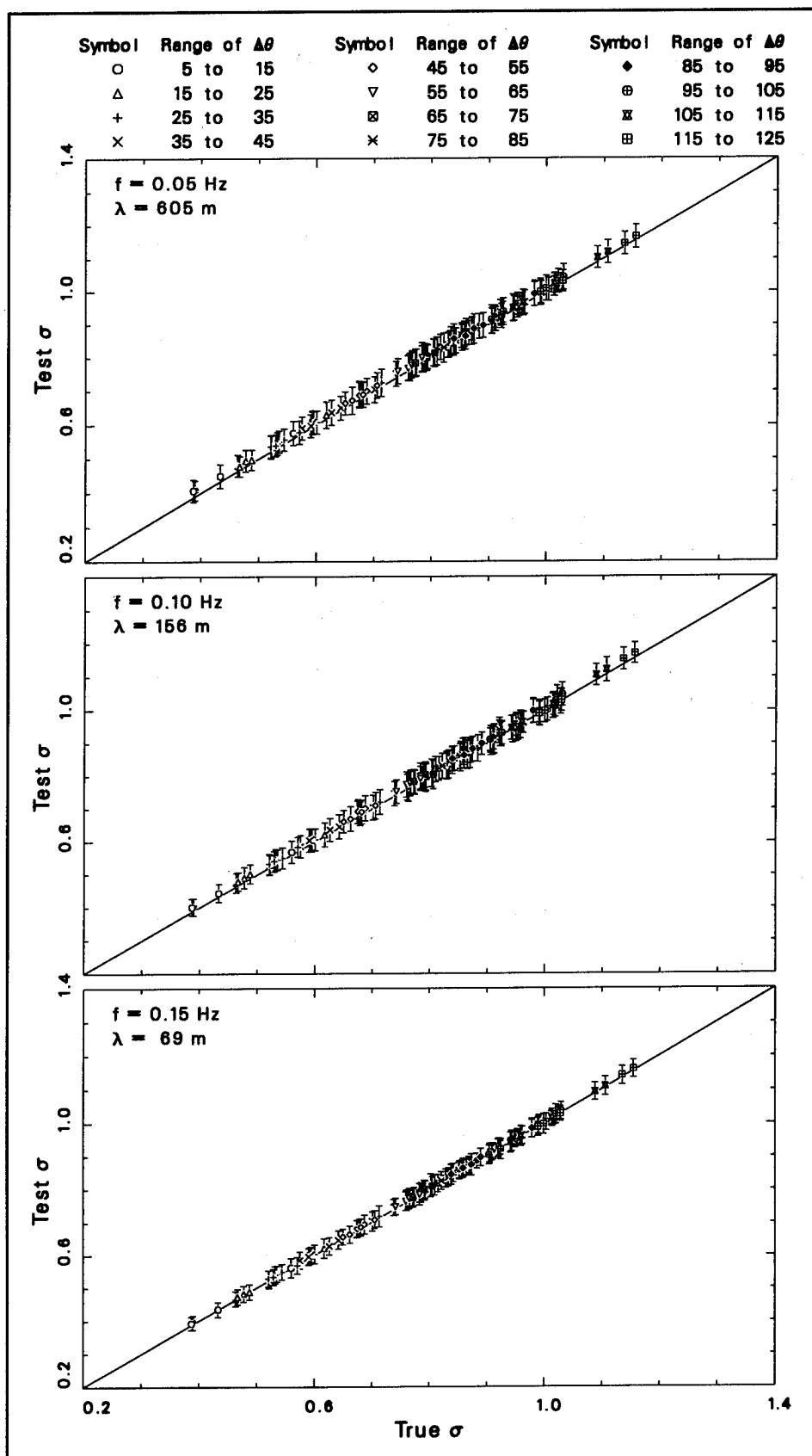


Figure 38. Test results for circular width

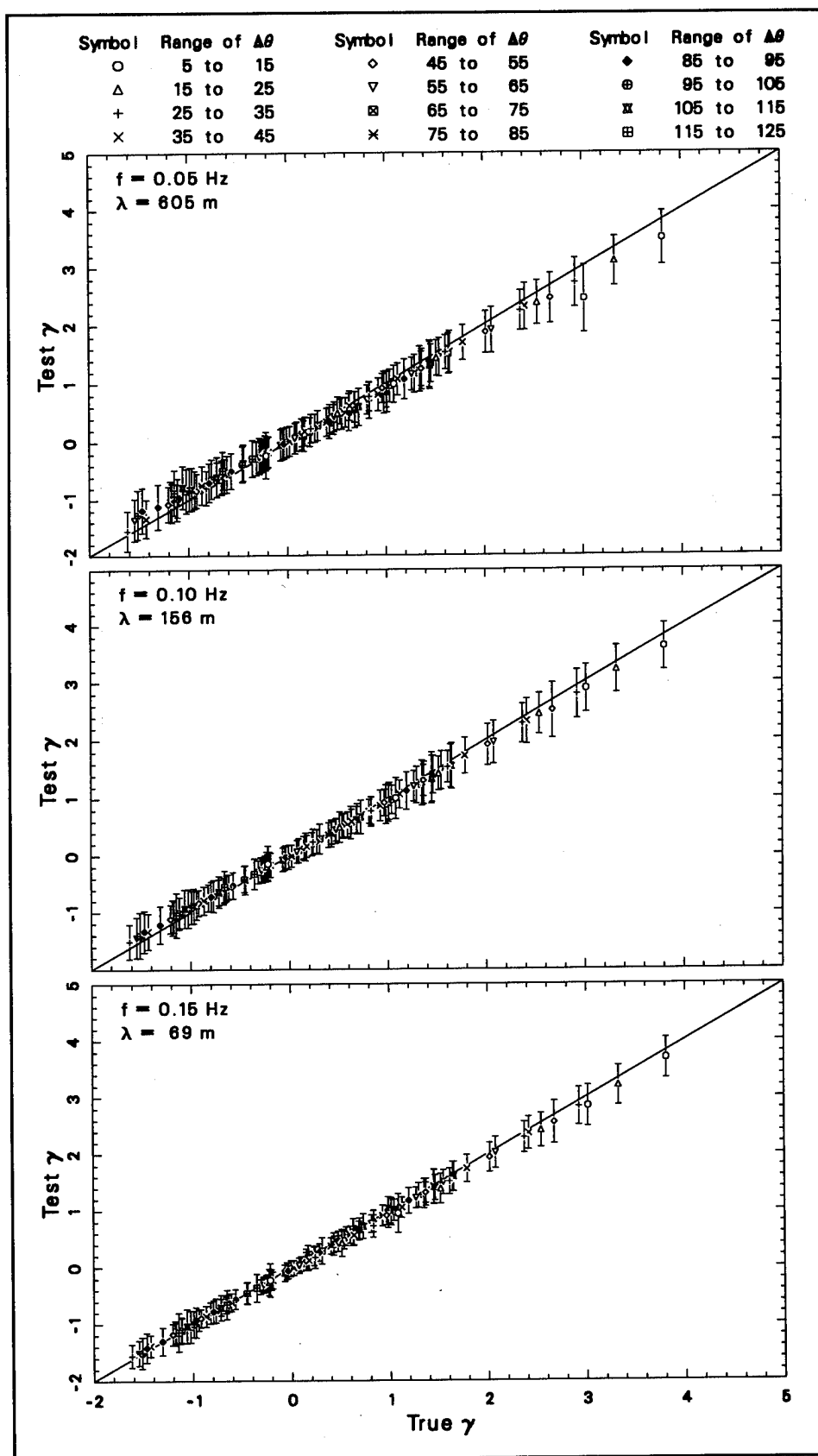


Figure 39. Test results for circular skewness

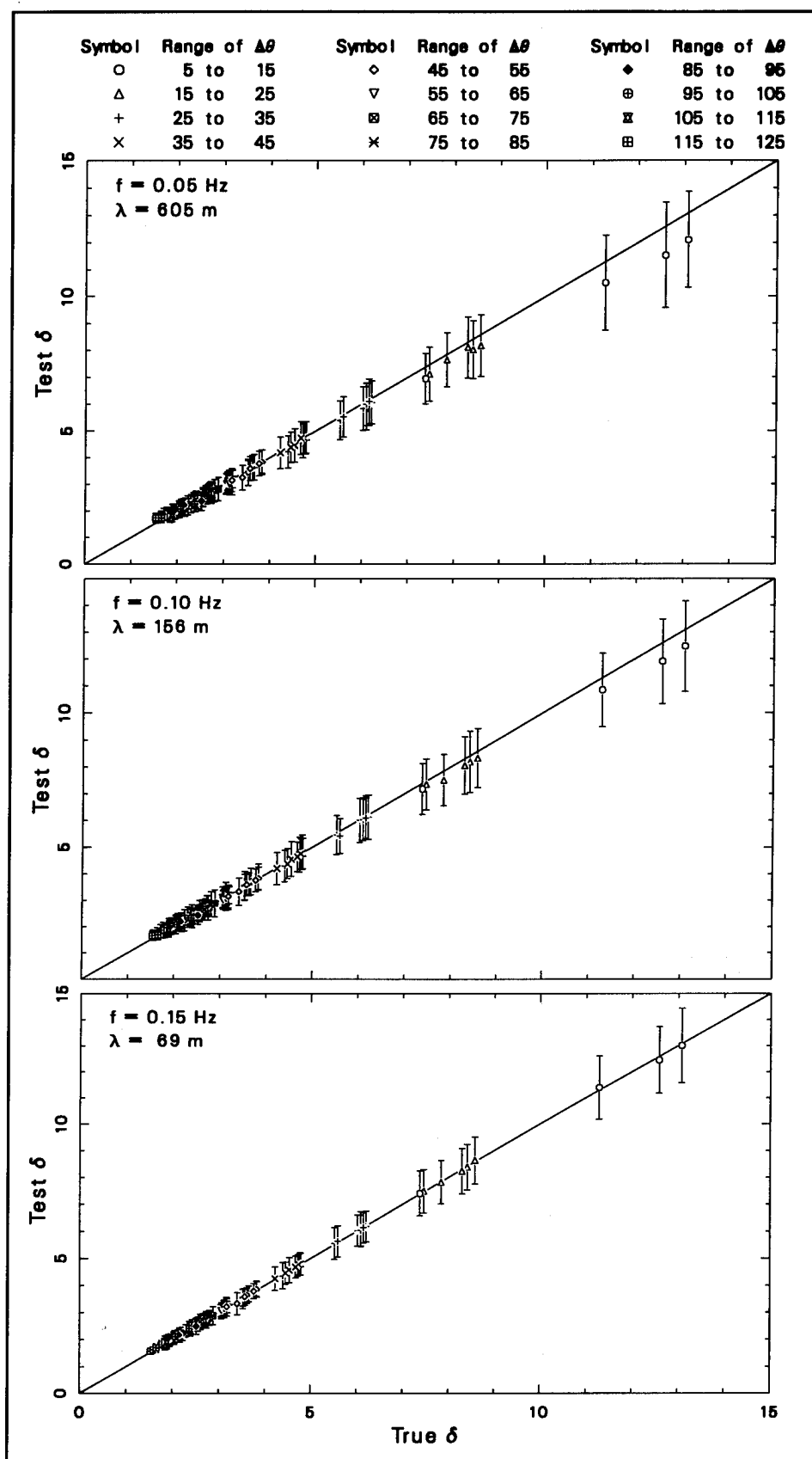


Figure 40. Test results for circular kurtosis

of standard deviation based on Figure 40 is 15 percent of  $\delta$ . Errors are somewhat smaller at the highest test frequency. Biases are also evident in Figure 40 for the intermediate and low test frequencies. Biases are low by approximately 8 percent for  $f = 0.05$  Hz, and 5 percent for  $f = 0.10$  Hz. As with skewness, the largest errors are associated with the narrowest classes of test distributions. These distributions have high kurtosis, meaning they are more peaked than Gaussian curves, and have increased scatter in their kurtosis estimation because kurtosis is a higher moment of a distribution, and the energetic parts of these distributions are defined by a small number of points. Higher moments are typically more difficult to resolve than lower moments like mean direction and circular width. Absolute errors are smallest for low kurtosis distributions, which are from the very broad spread classes.

## Quartile Parameters

Two additional parameters tested are quartile spread  $\Delta\theta$  and asymmetry  $A$ , which are based on quartile directions of distribution functions. Because quartile points are determined through integration of a distribution function (Equation 44), these parameters are expected to have stabilities comparable to those of circular moment parameters.

### Quartile spread

Figure 41 shows correlations of mean test  $\Delta\theta$  with distribution true  $\Delta\theta$ , along with vertical error bars showing standard deviations of test spread parameters. Because these graphs are of  $\Delta\theta$ , it is pointless to classify results by spread grouping, so symbols are employed to represent asymmetry classes, and are defined at the top of Figure 41. Error bars tend to be small for small spreads, being less than 3 deg for the narrowest spread class at all test frequencies. Error bars increase with increasing  $\Delta\theta$ , reaching nominal values of 5 to 15 deg for  $\Delta\theta$  near 60 deg, and then are approximately constant for higher  $\Delta\theta$ . High-frequency distributions tend to have smaller errors, with nominal values of  $\pm 5$  deg for large  $\Delta\theta$ , than the two lower-frequency groups.

There is a slight bias toward smaller spreads evident in the intermediate- and low-frequency test sets, being approximately 5 deg at the highest  $\Delta\theta$ . This bias is due to the tendency for IMLE to shift estimates of modal peaks in bimodal distributions such that the peaks move closer together. This has the effect of compressing the distribution along the direction axis, resulting in lower estimates of  $\Delta\theta$ .

A nominal value for uncertainty in  $\Delta\theta$  is  $\pm 10$  deg based on the data set as a whole, though this is clearly an overestimate of the errors for small  $\Delta\theta$ . Note that this nominal uncertainty is qualitatively consistent with uncertainty in circular width  $\sigma$ , which is also a measure of directional spread. Based on the general slope of the correlation curve of Figure 6 relating bulk estimates



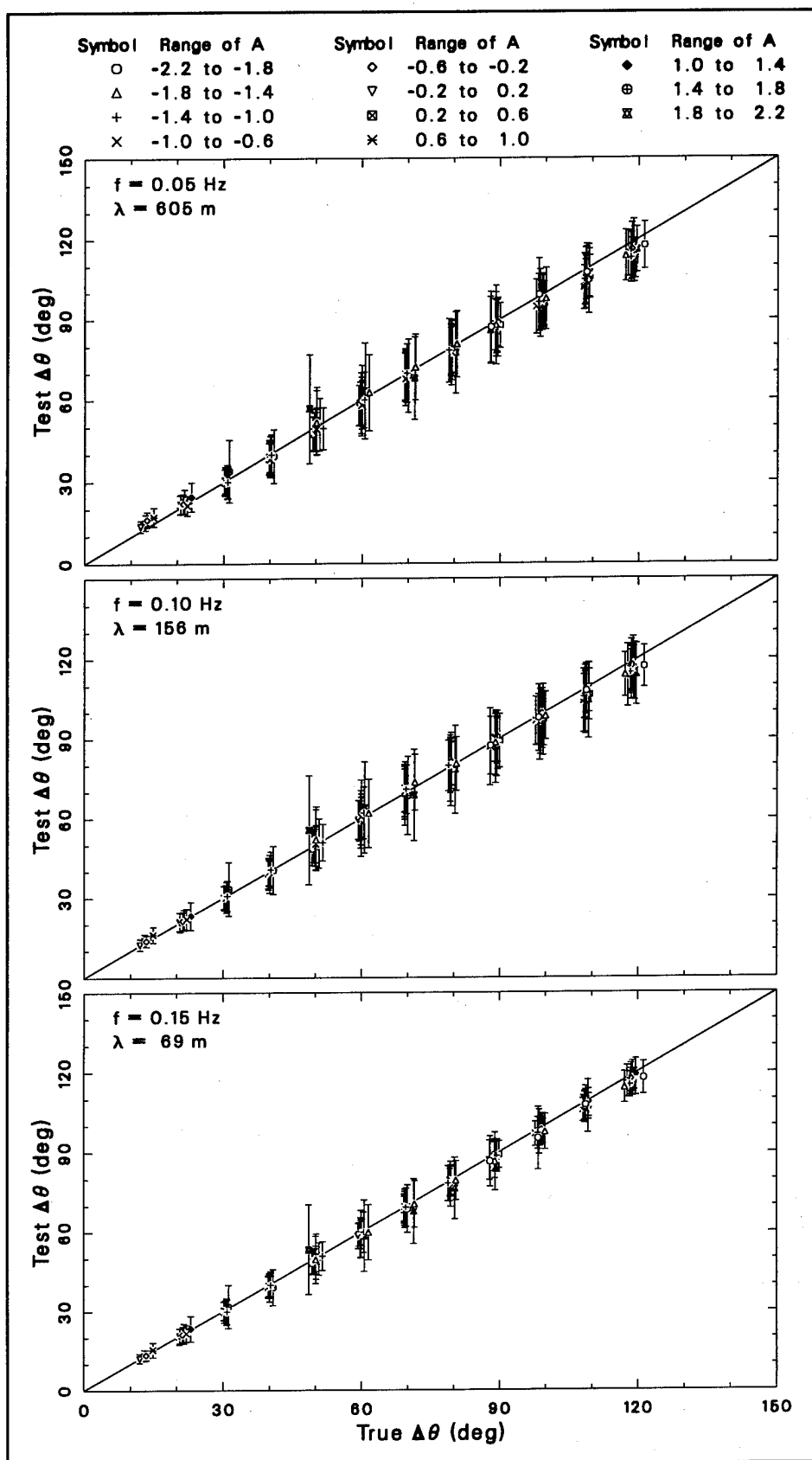


Figure 41. Test results for quartile spread

of these parameters, a variation of  $\pm 0.05$  in  $\sigma$  is approximately equivalent to a variation of  $\pm 10$  deg in  $\Delta\theta$ .

### Quartile asymmetry

The final parameter examined in these tests is quartile asymmetry  $A$ , for which test results are illustrated in Figure 42. Correlations of test  $A$  with true  $A$  are shown for three test frequencies, and symbols denote spread classes. Error bars, denoting standard deviations of test  $A$ , seem of reasonably uniform size within each graph. Nominal standard deviation values are 0.3, 0.4, and 0.5 for  $f = 0.15$ , 0.10, and 0.05 Hz, respectively. The middle- and low-frequency results reveal biases at large  $A$  toward smaller values. The reason for these biases is that the IMLE tendency to underestimate peak values in wide, bimodal distributions has the effect of making estimated distributions more uniform along the direction axis, thereby reducing their asymmetry.

## Summary of Parameter Accuracy

Table 3 is a summary listing of nominal parameter accuracies and bias ranges for the circular and quartile parameters based on information shown in Figures 37 to 42. The intent of Table 3 is to provide citable accuracies that represent the bulk of typical observations at Harvest Platform. Clearly, the table is not complete because many of the parameters have greater or lesser variability than the cited numbers as can be seen by examining the test result figures. Of note is the fact that tests of mean direction were extremely limited, having been conducted for only a single test direction. Results cited in Table 3 are based on that single test direction, but may not be representative of the broader suite of mean directions from which waves arrive at this gauge.

<b>Table 3</b> <b>Accuracies and Biases of Characterizing Parameters</b>			
Parameter	Test Range	Nominal Accuracy	Nominal Bias Range
$\theta_0$	-2 deg <sup>1</sup>	$\pm 5$ deg	-5 deg to 3 deg
$\sigma$	0.38 to 1.17	$\pm 0.05$	None
$\gamma$	-1.6 to 3.8	$\pm 0.5$	-0.3 to 0.1
$\delta$	1.4 to 13	$\pm 15$ percent	-8 percent to None
$\Delta\theta$	12 deg to 120 deg	$\pm 10$ deg	-5 deg to None
$A$	-2.0 to 2.0	$\pm 0.4$	-0.3 to 0.3
<sup>1</sup> All tests were run with a constant mean direction			

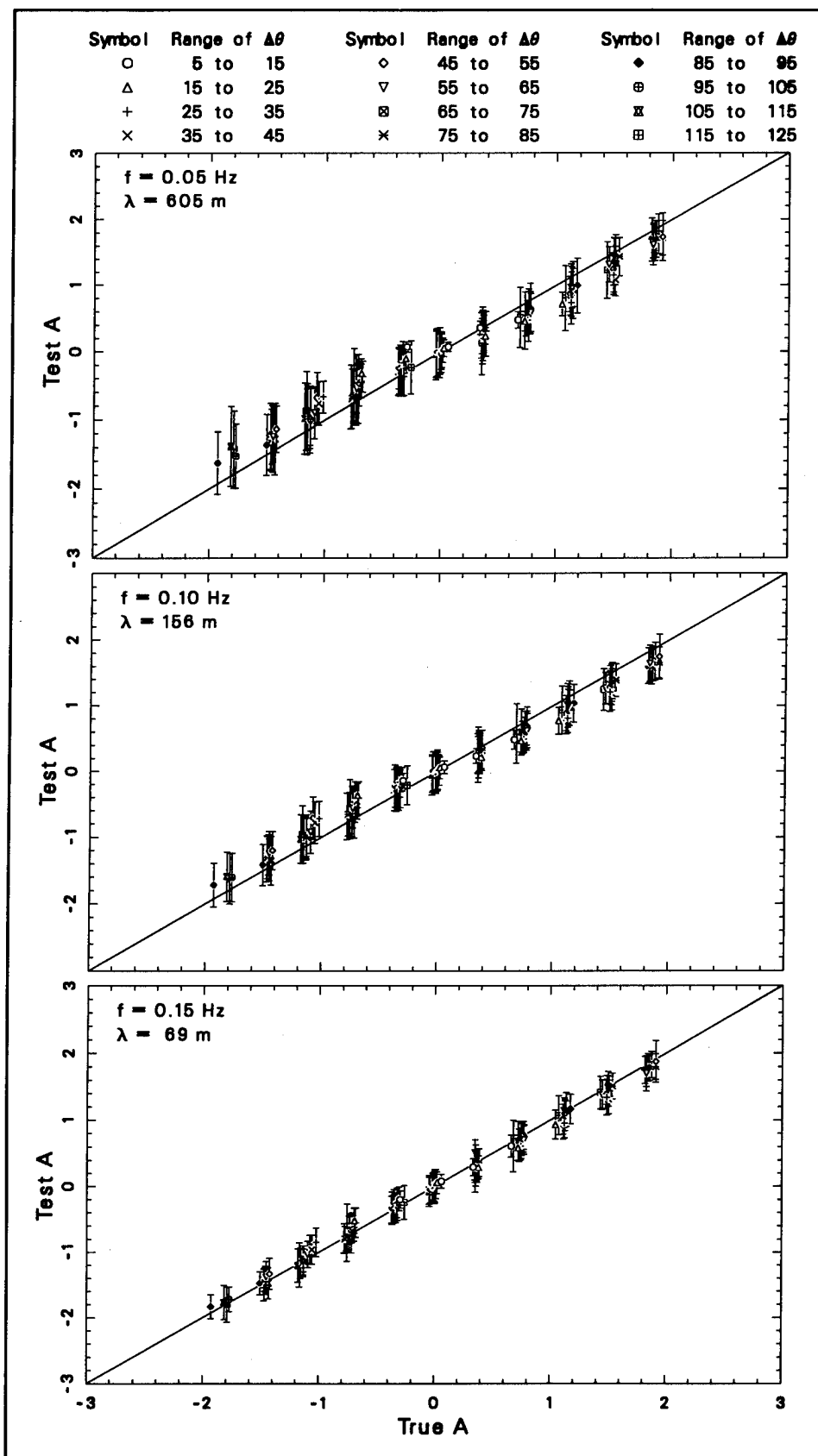


Figure 42. Test results for quartile asymmetry

Missing from Table 3 are characterizing accuracy and biases for peak direction. This parameter was omitted because test results were highly variable, and could not be represented well by single numbers. Figure 36 must be used to estimate accuracy and bias for peak direction.

It should be remembered that the test results presented here are based on the addition of synthetic Gaussian noise to IMLE input cross-spectra derived from characteristic directional distributions. The noise was theoretically appropriate for 160 degrees of freedom, which matches the degrees of freedom claimed in the basic directional analysis described in Chapter 3. Results using longer or shorter data records than those used in this report would have greater or fewer degrees of freedom, and consequent differences in parameter resolution.

An advantage of evaluating accuracies and biases of directional parameters is that it allows a quantification of the ability of an array to resolve directional distributions of wave energy, which are difficult otherwise to evaluate. In combination with distribution test results discussed in Chapter 9, the parametric evaluation in the present chapter indicates the extent to which the Harvest Platform array can resolve directional distributions, and reasons for inaccuracies and biases. With this knowledge, a user can then decide if reported results are adequate for a given purpose. Because there are no other long-term, deepwater, high-resolution directional wave gauges (as of this writing), the present results are the best in existence. They should add immensely to understanding deep ocean wave conditions, which will allow better definitions of seaward boundary conditions for applied models of shoreward propagating wave energy. Furthermore, the existence of the Harvest Platform gauge (or, at least, the use at other sites of the technical principles described in this report) should allow better understanding of results from commonly used low-resolution directional gauges, and improved ground truth for tests of applied remote sensing techniques.

# 11 Summary

---

A high-resolution directional wave gauge has been installed on the Texaco Oil Company Harvest Platform to initiate long-term monitoring of the directional wind wave climate at a deepwater site that can be used to represent open ocean conditions for waves approaching the coast of southern California. In addition to wind wave climatology, results from this gauge can be used for seaward boundary conditions in coastal wave propagation models, studies of ocean wave evolution, comparison studies with locally deployed low-resolution directional wave gauges, and ground truth in remote sensing research and tests. This report describes various attributes of the directional wave gauge, and, in some detail, a summary of results from one year of operation.

## Gauge and Basic Data Set

Harvest Platform is located approximately 20 km (10.8 n.m.) west of Point Conception, California, at about the 200-m (656-ft) water depth. The directional gauge is an array of six pressure gauges mounted on the Harvest Platform structure at a nominal depth of 16 m (53 ft). Utilizing the maximum available horizontal extent of the platform structure, the array is rectangular in shape with outside dimensions approximately 23 by 59 m (75.5 by 193.6 ft). Data are acquired eight times daily in collections of time series having durations equal to 2 hr 16 min, with all six gauges sampled simultaneously at 1 Hz. Data quality is assured by intercomparing frequency spectra from all six gauges, and further by intercomparing frequency cross spectra over redundant lag spacings within the array. Data that passed these quality checks were further processed into frequency-direction spectra using the iterative maximum likelihood estimation method derived and described by Pawka (1983). This report is based on all results from calendar year 1993, from which 2,339 satisfactory collections were processed from a total of 2,920 possible collections.

## Bulk Parameters

A set of characterizing parameters were defined and used to reduce the substantial information in the frequency-direction spectra to manageable form. In addition to characteristic wave height and peak frequency normally defined for wave data, a set of direction-dependent parameters were computed both for bulk integrated direction spectra (directional analogs of frequency spectra), and for directional distributions at individual frequencies. The parameter set included peak direction, four moment parameters defined by Kuik, van Vledder, and Holthuijsen (1988), and two quartile parameters defined by Long and Oltman-Shay (1991). The four moment parameters were mean direction, circular width, skewness, and kurtosis. The two quartile parameters were directional spread and asymmetry. Additionally, directional and frequency modes were analyzed to obtain number and relative importance of peaks in uni- and multimodal distributions.

Bulk parameters were used to characterize the general behavior of frequency-direction spectra as whole units. Time series of these parameters, illustrated in Appendix A, indicated wave climatology for the collection year. Statistical distributions of parameters indicated common and extreme values that were observed. Characteristic wave heights ranged from 0.6 m (2.0 ft) to more than 5 m (16.4 ft) with common values between 1 and 2 m (3.3 and 6.6 ft). Most common peak frequency was 0.07 Hz, suggesting a predominance of swell, but all frequency bands were occasionally most energetic, indicating the occurrence of initial and well-developed stages of local storms as well as long-travelled waves from distant sources. Peak directions were mostly due to waves from the northwest, but about 5 percent of observations were from the south, suggesting occasional dominance of the spectra by southern swell. Mean direction demonstrated a similar pattern, but, being an integral parameter, was only shifted slightly toward the south, indicating a common coexistence of local wind seas and southern swell.

Circular width and directional spread both showed two main groupings of cases. A narrow group with circular width commonly 0.55 and directional spread 30 deg was associated with unimodal spectra from single sources. A broad group with circular width peaking between 0.9 and 1.0, and directional spread having a maximum near 100 deg was attributed to multimodal seas from directionally divergent sources. Circular skewness and asymmetry parameters both showed common positive values, indicating that energy distributions were not symmetric, but had energetic tail regions preferentially counterclockwise from main energy peaks. Circular kurtosis was dominated by values greater than 3, indicating distribution shapes sharper or more peaked than Gaussian curves. Approximately 24 percent of kurtosis values were less than 3, suggestive of flattening that would occur either in broad unimodal distributions or multimodal sources widely separated in direction.

Most of the bulk distributions were either uni- or bimodal. Frequency spectra were approximately 61 percent unimodal and 38 percent bimodal. Directional spectra were only 39 percent unimodal, and 60 percent bimodal.

Secondary modes were not inconsequential. Approximately 25 percent of directional distributions had 25 percent of total energy in second modes.

Correlations of bulk parameters with characteristic wave height gave indications of spectral behavior in various wave conditions, especially in energetic conditions that may be of concern to coastal interests. High-energy waves typically had peak frequencies in the range 0.07 to 0.09 Hz, and both peak and mean directions in the west-northwest. Directional spectra of energetic waves were narrow with circular widths between 0.35 and 0.50, and directional spreads from 15 to 45 deg. Circular skewness and asymmetry were both near zero, with a tendency toward slightly positive values. Circular kurtosis achieved some of its highest values in high-energy conditions, indicating very peaked energy distributions.

## Frequency-Dependent Parameters

More detailed information is obtained by examining statistical distributions of characterizing parameters on a frequency-by-frequency basis. This type of analysis avoids the smoothing effect of integration across all frequencies required for definition of the directional spectrum from which the bulk parameters were derived. At the frequency level, there appear three groupings with common features: very low frequencies, identified by the single band at 0.044 Hz, low frequencies in the range 0.054 to 0.093 Hz, and middle to high frequencies, which extend to 0.16 Hz, the highest frequency examined.

Very low-frequency distributions typically have very low energy, with peak and mean directions in the west-northwest, and across much of the southwest quadrant. Circular width and directional spread extend over broad ranges, with  $\sigma$  having common values from 0.5 to 1.2, and  $\Delta\theta$  ranging from less than 20 deg to more than 100 deg. Asymmetry and circular skewness parameters indicate such distributions to be highly symmetric, and kurtosis is commonly equal to 2.0, suggesting broad, flat distributions. Approximately 96 percent of all such distributions are unimodal. Because energy levels are low, distributions at this frequency are likely to be mostly noise, which tends to be directionally white.

Low-frequency distributions contain broad ranges of energy, including the highest energies of any group of frequencies. Mean and peak directions have two common groupings: one from the northwest quadrant, and another, with about equal commonality, from the south. This behavior is indicative of the interplay between well-developed western storm waves and swell from distant southern sources. Circular width shows broad ranges of common values from 0.4 to 0.9, and directional spread is not only widely distributed, but also shows two main groupings for this range of frequencies. One group, from 10 to 60 deg in spread, suggests unimodal, locally generated seas. The other group, with spreads from 60 to 120 deg, indicates multimodal distributions with energy from widely separated directions. Skewness and asymmetry both show a gradual shift of common values from near zero to slightly positive as

frequency increases through this band. Kurtosis has a wide range of common values from 2 to 6 for these frequencies, again suggesting a variety of distribution shapes from broad to peaky. This range of frequencies is noted for its high number of directional modes, as many as six, with secondary modes commonly energetic because 90 percent or more of total energy is contained in the primary mode for only 50 to 70 percent of the observations.

High-frequency distributions tend to be more regular, with intermediate levels of energy, peak and mean directions primarily centered in the northwest quadrant, and modest angular distributions, with  $\sigma$  typically 0.4 to 0.7, and  $\Delta\theta$  in the range 10 to 60 deg, peaking near 30 to 40 deg. These distributions tend to be neutrally to slightly positively skewed, though there are modest ranges of these parameters with  $\gamma$  between -1 and 3, and  $A$  between -1.0 and 1.5. Kurtosis ranges from 2 to 18 at these frequencies, but has common values of 4 to 5, indicating relatively peaked shapes. The most common number of directional modes for these distributions is two, but the effect of the secondary modes is less than for the low frequencies because approximately 80 percent of all observations have 90 percent of energy in primary modes.

## Representative Results

To illustrate the appearance of observed frequency-direction spectra, 27 examples are shown in Appendix B. These examples are primarily high-energy cases because such cases are typically of most interest, though a few low- and intermediate-energy cases are shown for comparison. The examples were chosen as representative of various bulk directional spreads and asymmetries by which the entire observation set was classified. Examples shown are mostly the highest-energy case from each of the most populous classification cells.

Of the 30,407 individual directional distribution functions observed during 1993, 110 characteristic distributions were defined to illustrate variety and frequency of occurrence of typical shapes. All individual distributions were classified and grouped in cells defined by ranges of quartile spread and asymmetry. All members of each cell were then averaged, without regard to source wave frequency, to determine characteristic shapes. Standard deviations of each cell population were also computed to indicate shape variability within a class. Illustrated in Appendix C, the most common classes by far were those with narrow to moderate spreads and small to neutral asymmetries. Broad distributions with multiple modes were not common. This behavior suggests that where a frequency-direction spectrum can be considered multimodal, the cause is a series of mostly unimodal distributions at different frequencies, such as local wind sea from the northwest at intermediate frequencies coupled with southern swell at low frequencies.



## Gauge Accuracy

To investigate the directional resolving ability of the Harvest Platform array and its analysis algorithm, a number of tests were run using characteristic distributions as basic test elements. Ideal cross spectra were computed for these test cases, and then synthetic, Gaussian noise appropriate to the computational degrees of freedom was added to the cross spectra. When used as input to the IMLE method, a cross spectrum with noise resulted in an output distribution that represented one possible result from a natural sea. This process was repeated 500 times for each test case so that statistics could be computed from a population of 500 results. All 110 of the characteristic distributions were treated this way, and, because results are frequency-sensitive, all distributions were tested for three representative frequencies: 0.05, 0.10, and 0.15 Hz.

From the 500-member population of test results for each case and each test frequency, mean and standard deviation distributions were computed to determine an expected result and a measure of variability of results. Some of the test results are illustrated in Appendix D, where it is seen that results are excellent for high-frequency waves having distributions with low to moderate spreads with any asymmetry. Results degraded somewhat with decreasing frequency for the low- to moderate-spread cases. Directionally broad distributions with large asymmetries were well-resolved, but had a tendency to bias distribution peaks toward high-energy distribution tails. Results were worst, but still qualitatively good, for broad distributions with small asymmetries. Evaluations of test distributions are necessarily qualitative because there are many distribution shapes that represent the full suite of observations, and no single quantitative statistic can represent directional resolution in much detail.

However, quantitative estimates of error can be ascribed to the set of directional parameters that represent the test distributions. For the 500 sample runs of the 110 test cases at each of the three test frequencies, means and standard deviations were computed for peak direction, mean direction, circular width, skewness, kurtosis, directional spread, and asymmetry. When ordered by directional spread and asymmetry classes, these means and standard deviations give quantitative measures of directional resolving ability of the Harvest Platform array. Results varied widely from parameter to parameter, and the reader is referred to Table 3 and Figures 36 to 42 in Chapter 10 for specific numerical values. Essentially, these tests quantify and substantiate observations deduced from the directional distribution tests discussed in Chapter 9.

## Closing Comment

It should be noted that the Harvest Platform array is the only long-term, deepwater, high-resolution directional wave gauge in existence. Tests discussed in this report indicate that the gauge is reliable, and gives generally excellent results for the most common frequency-direction spectra observed at this site. Though the array makes optimum use of the space available in the

platform structure, it still has quite limited spatial coverage, and so is less able to resolve detailed directional distributions of low-frequency wind waves, i.e., those with long wavelengths. This property may make the array less than ideal for use in numerical models having extreme directional sensitivity. Nonetheless, observations made with this array are more than adequate for a multitude of other purposes, among them general directional wind wave climate, deepwater directional spectral evolution during storms, intercomparison tests with and development of commonly used low-resolution directional gauges, and ground truth in remote sensing applications. Resulting improved knowledge of deep ocean wind wave conditions can only enhance abilities to model the physics of open ocean wave processes, and the consequent near-shore wave climate required in coastal engineering computations as such waves propagate landward.

# References

---

- Bendat, J. S., and Piersol, A. G. (1971). *Random data: Analysis and measurement procedures*. Wiley-Interscience, New York.
- Borgman, L. E. (1969). "Directional spectra models for design use." *Proceedings of the Offshore Technology Conference*. American Institute of Mining, Metallurgical, and Petroleum Engineering, Houston, 721-746.
- Brennan, L. E., and Mallett, J. D. (1976). "Efficient simulation of external noise incident on arrays." *IEEE Transactions on Antennas and Propagation*. AP-23, 740-741.
- Coastal Data Information Program, *Monthly Reports*, University of California San Diego, Scripps Institution of Oceanography, La Jolla, CA.
- Davis, R. E., and Regier, L. A. (1977). "Methods for estimating directional wave spectra from multi-element arrays." *Journal of Marine Research* 35, 453-477.
- Dean, R. G., and Dalrymple, R. A. (1984). *Water wave mechanics for engineers and scientists*. Prentice-Hall, Englewood Cliffs, New Jersey.
- Kinsman, B. (1984). *Wind waves*. Dover, New York.
- Kuik, A. J., van Vledder, G. Ph., and Holthuijsen, L. H. (1988). "A method for the routine analysis of pitch-and-roll buoy wave data." *Journal of Physical Oceanography* 18, 1020-1034.
- Long, C. E., and Oltman-Shay, J. M. (1991). "Directional characteristics of waves in shallow water," Technical Report CERC-91-1, U.S. Army Engineer Waterways Experiment Station, Vicksburg, MS.
- Mardia, K. V. (1972). *Statistics of directional data*. Academic Press, New York.
- O'Reilly, W. C., and Guza, R. T. (1991). "Comparison of spectral refraction and refraction-diffraction wave models." *Journal of Waterway, Port, Coastal, and Ocean Engineering* 117, 199-215.

- O'Reilly, W. C., and Guza, R. T. (1993). "A comparison of two spectral wave models in the Southern California Bight." *Coastal Engineering* 19, 263-282.
- Pawka, S. S. (1983). "Island shadows in wave directional spectra." *Journal of Geophysical Research* 88, 2579-2591.
- Shore Protection Manual*. (1984). 4<sup>th</sup> Edition, 2 Vols, U.S. Army Engineer Waterways Experiment Station, Coastal Engineering Research Center, U.S. Government Printing Office, Washington, DC.
- Welch, P. D. (1967). "The use of fast Fourier transform for the estimation of power spectra: A method based on time averaging over short, modified periodograms." *IEEE Transactions on Audio and Electroacoustics*. AU-15, 70-73.

# **Appendix A**

## **Time Series Graphs of Bulk Parameters**

---

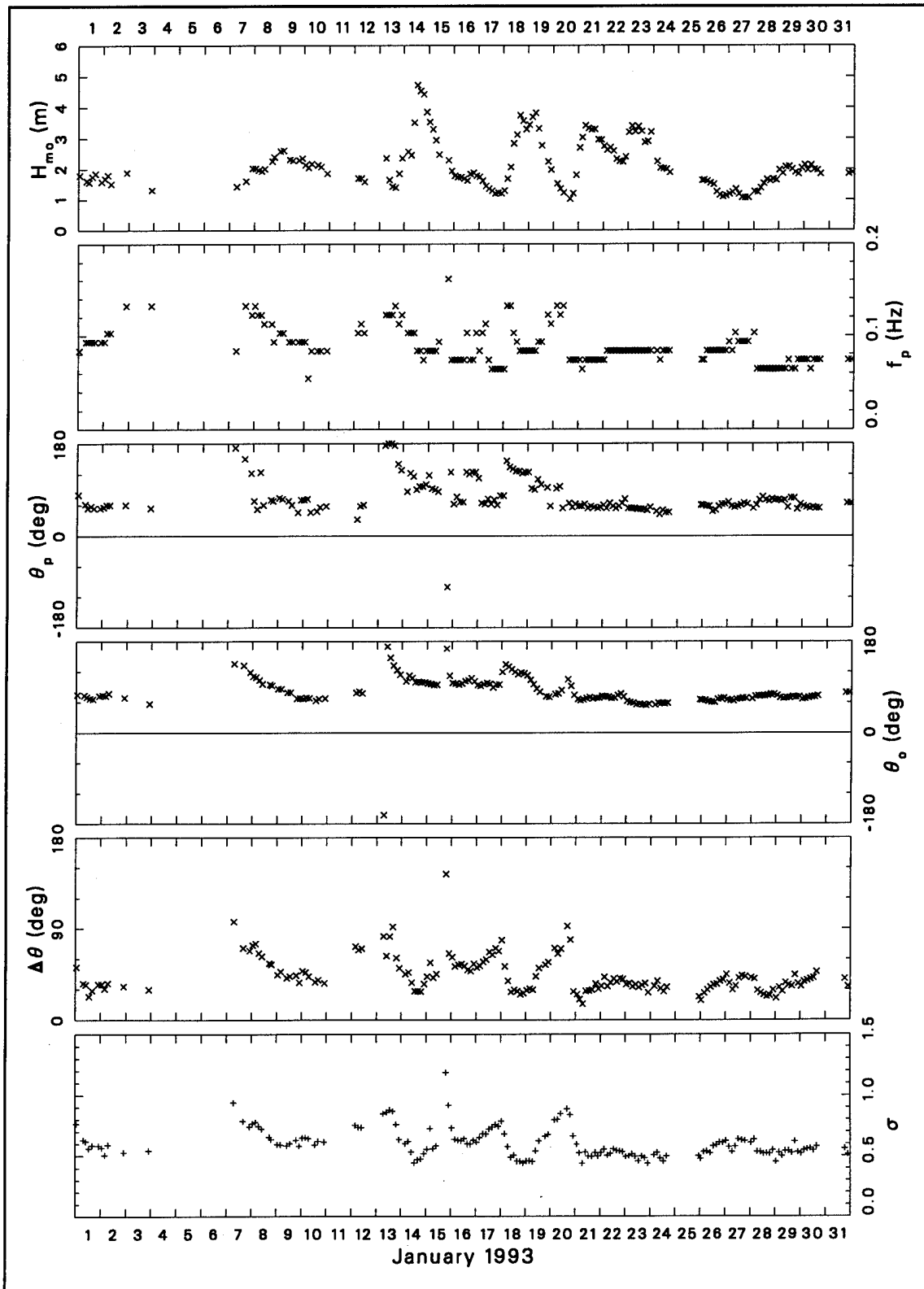


Figure A1. Bulk data for January 1993 (Continued)

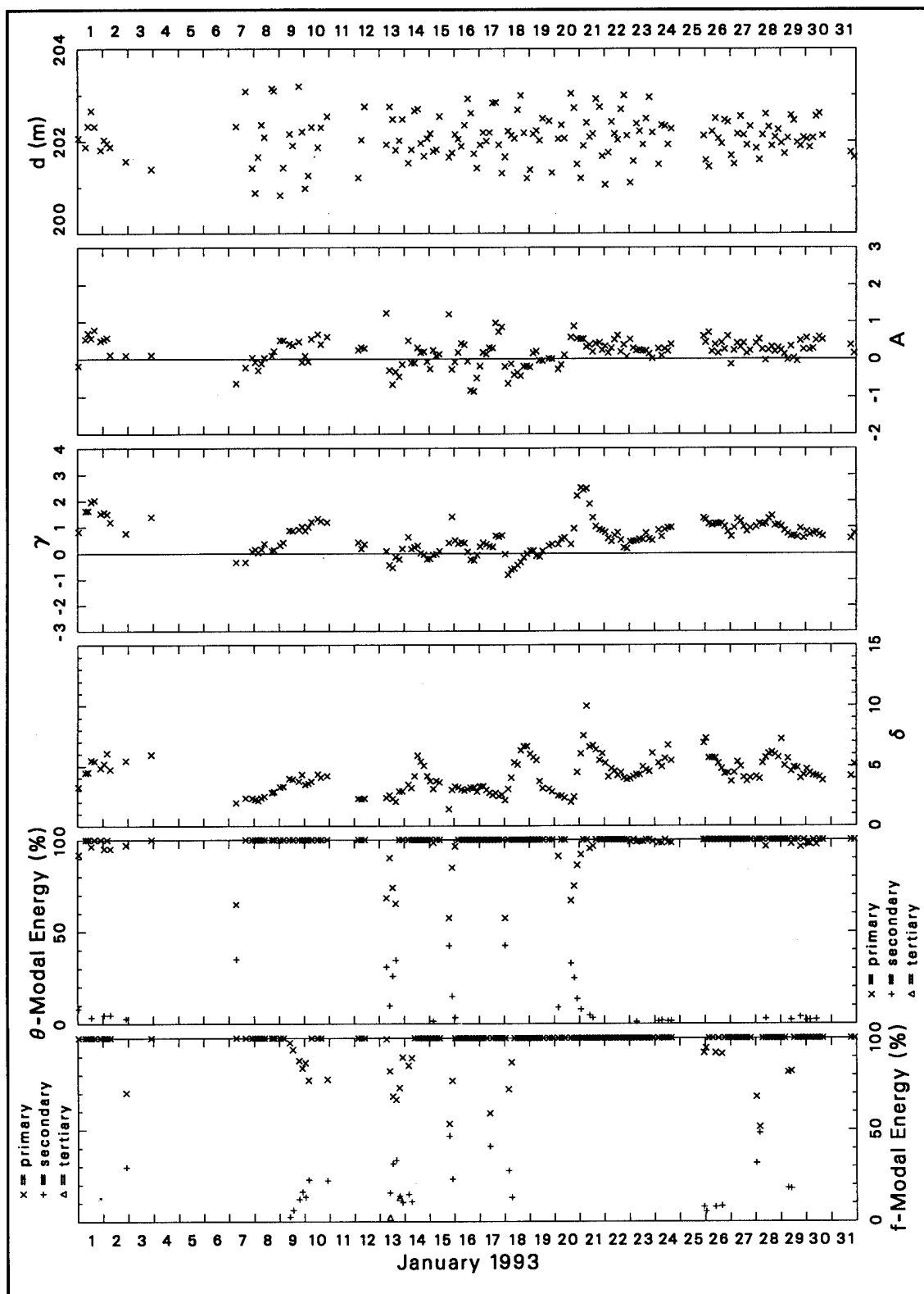


Figure A1. (Concluded)

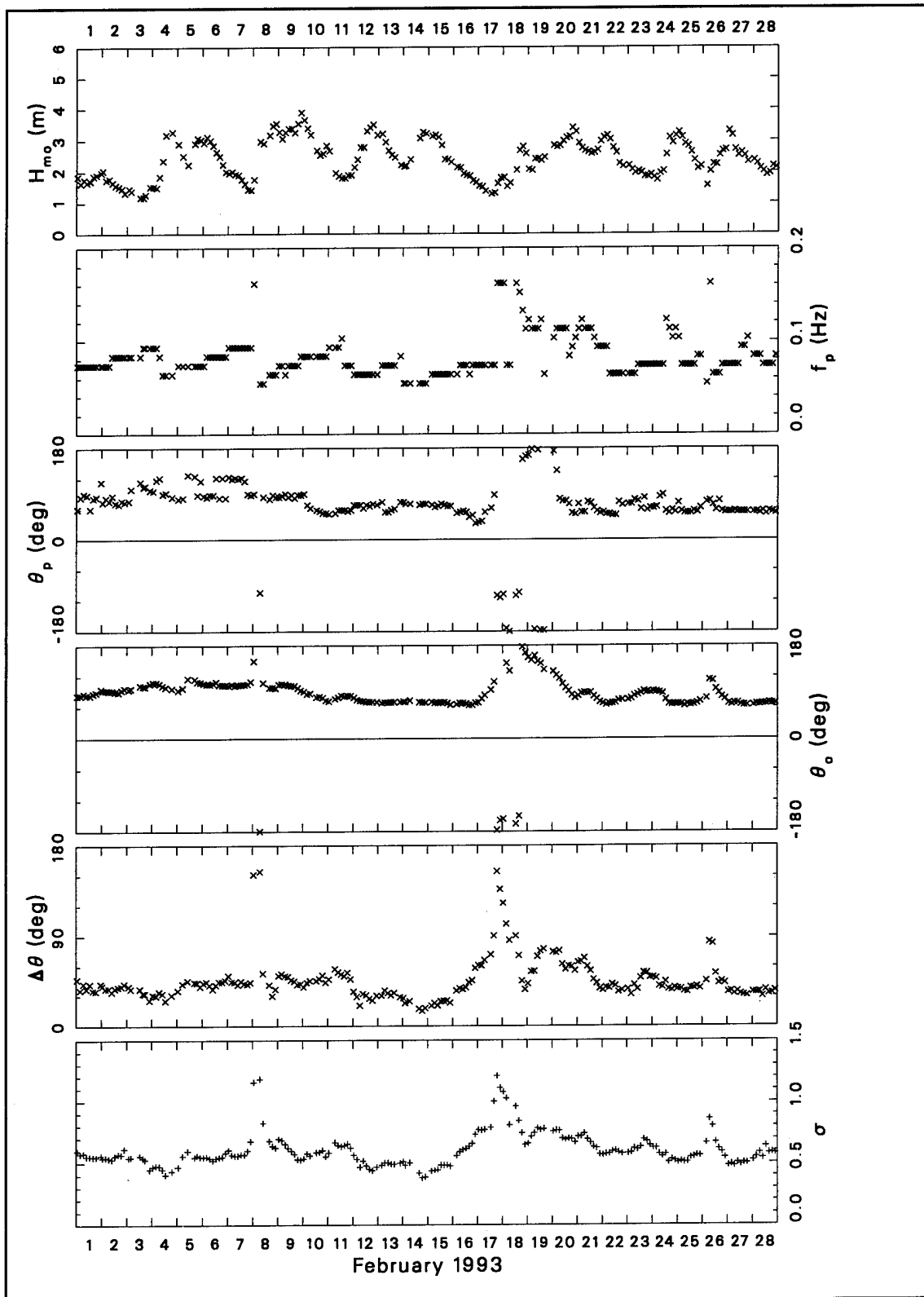


Figure A2. Bulk data for February 1993 (Continued)



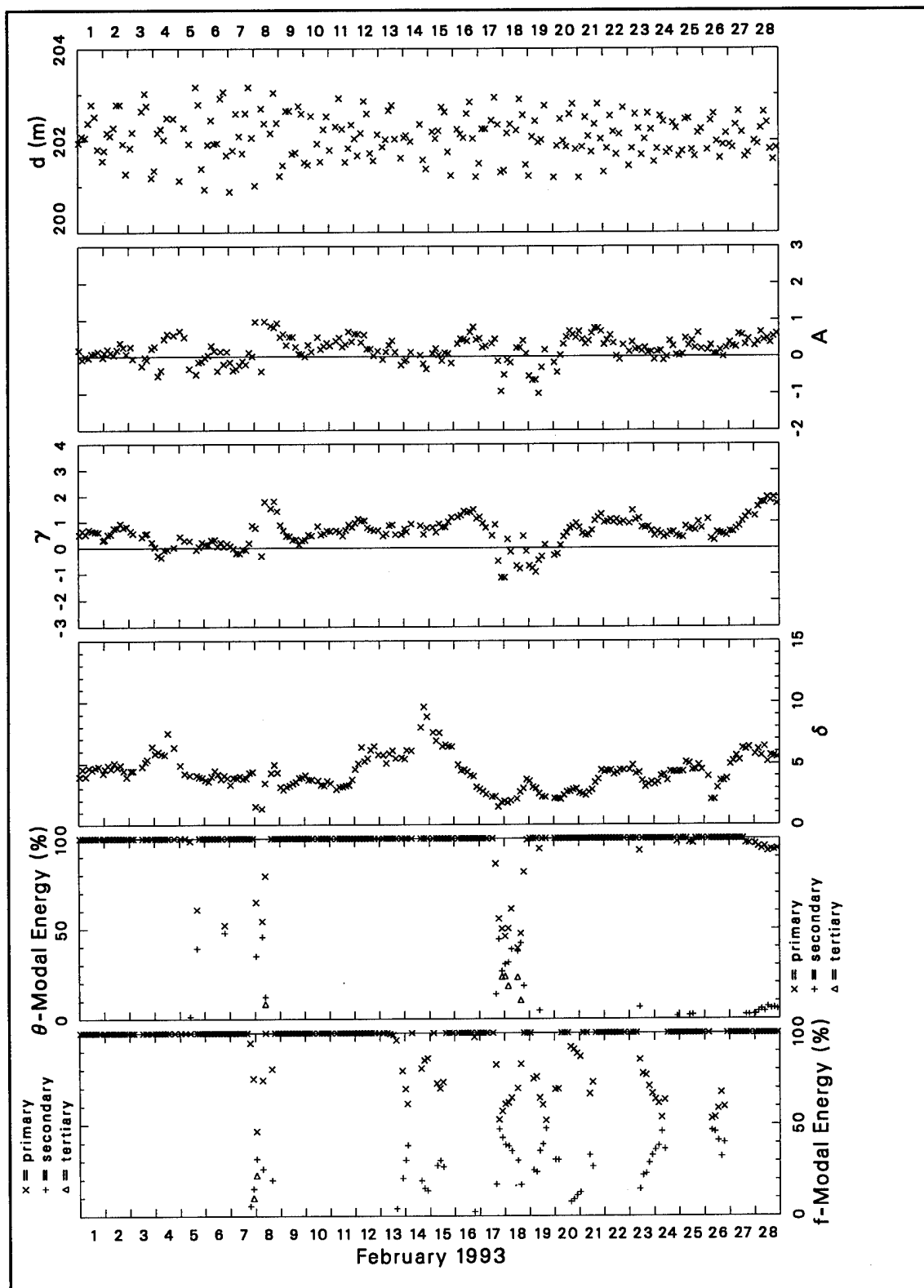


Figure A2. (Concluded)

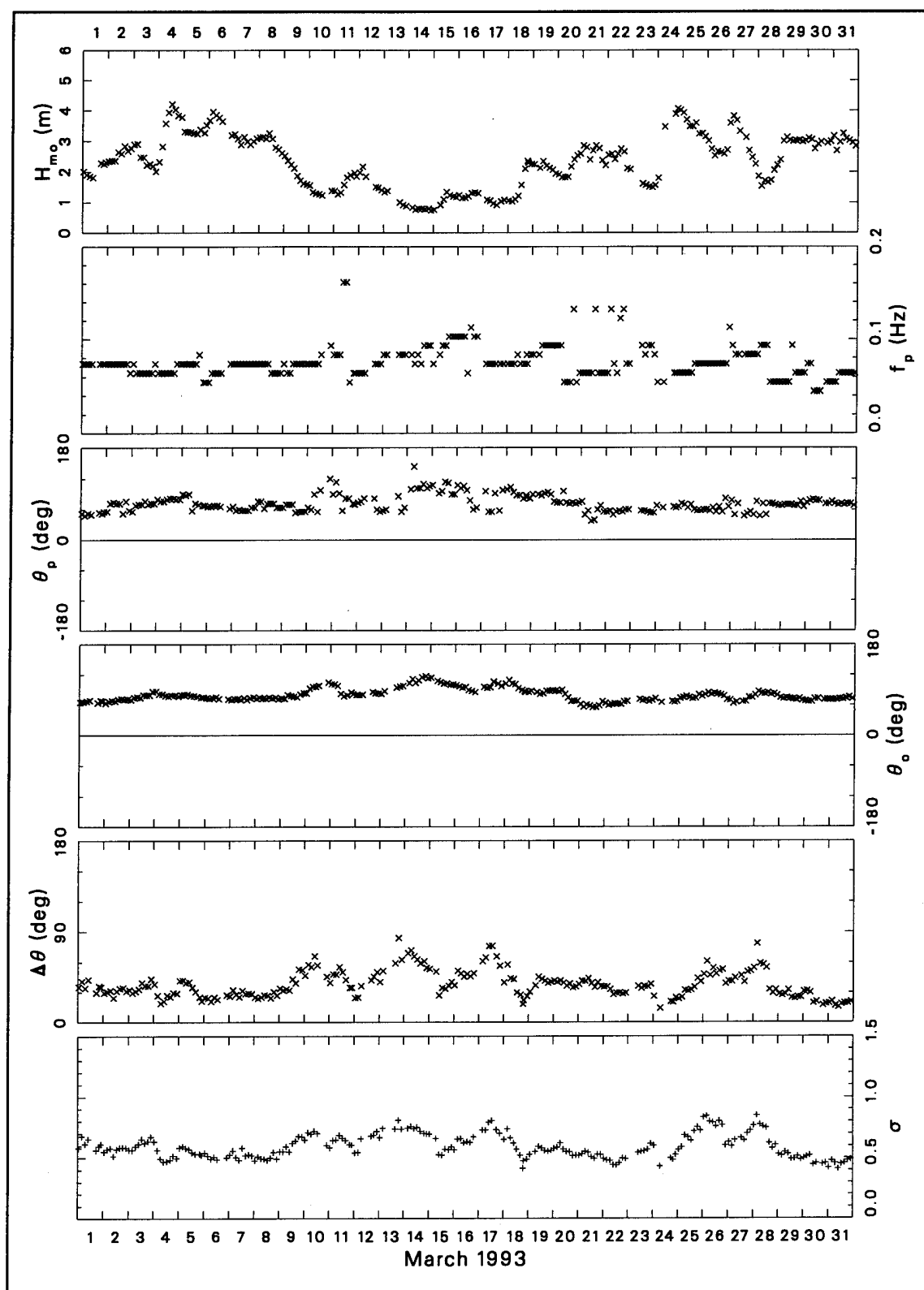


Figure A3. Bulk data for March 1993 (Continued)

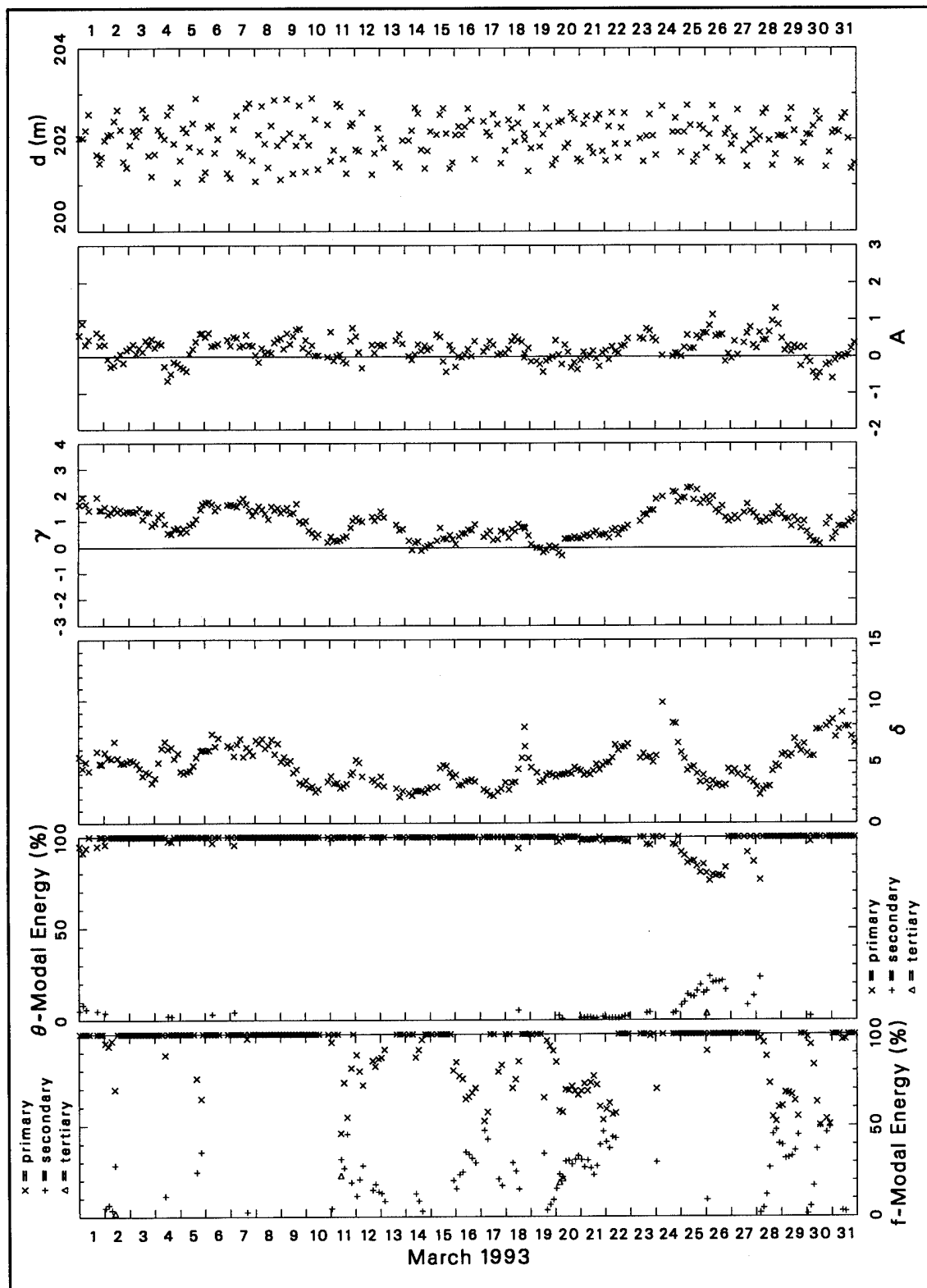


Figure A3. (Concluded)

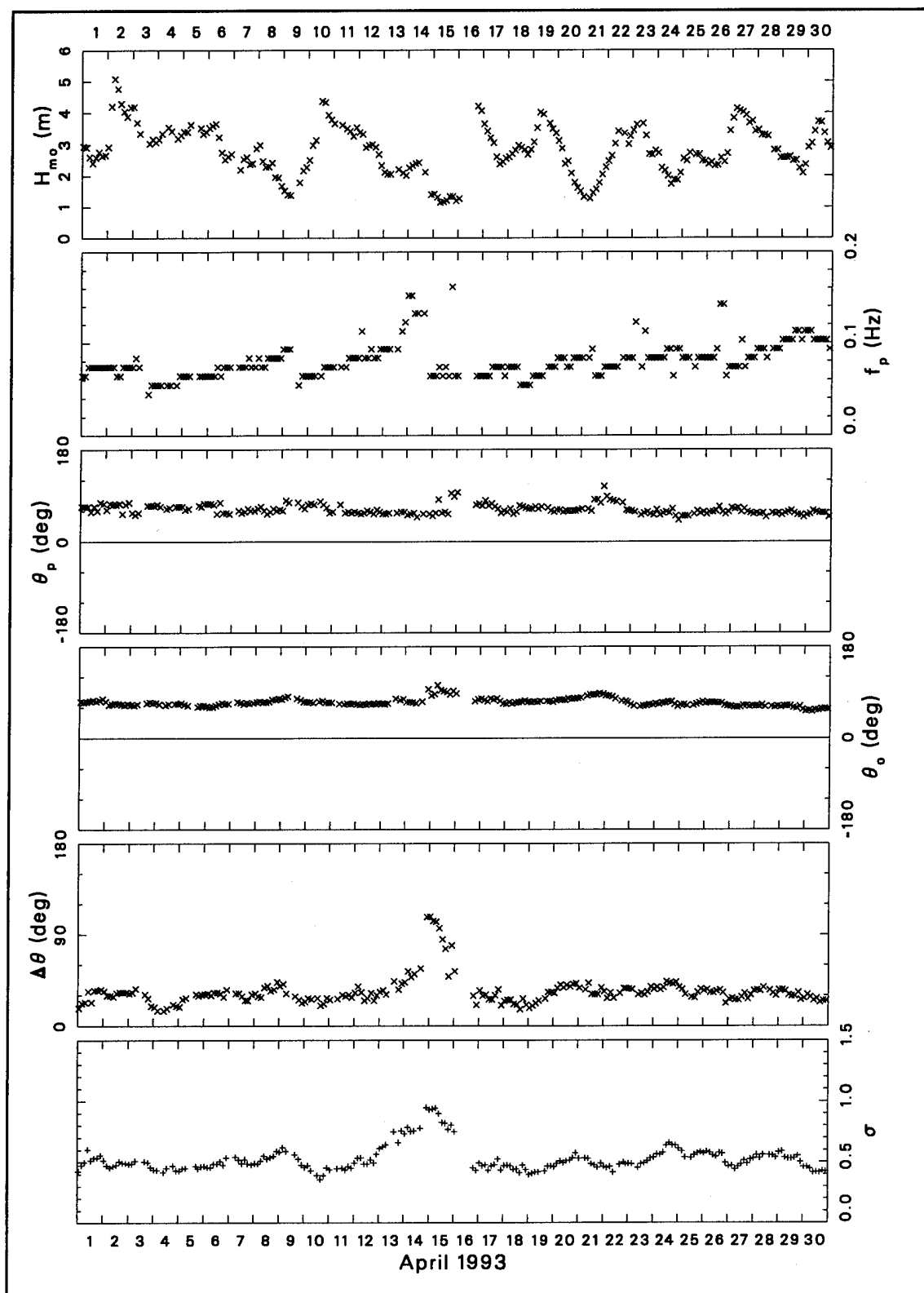


Figure A4. Bulk data for April 1993 (Continued)

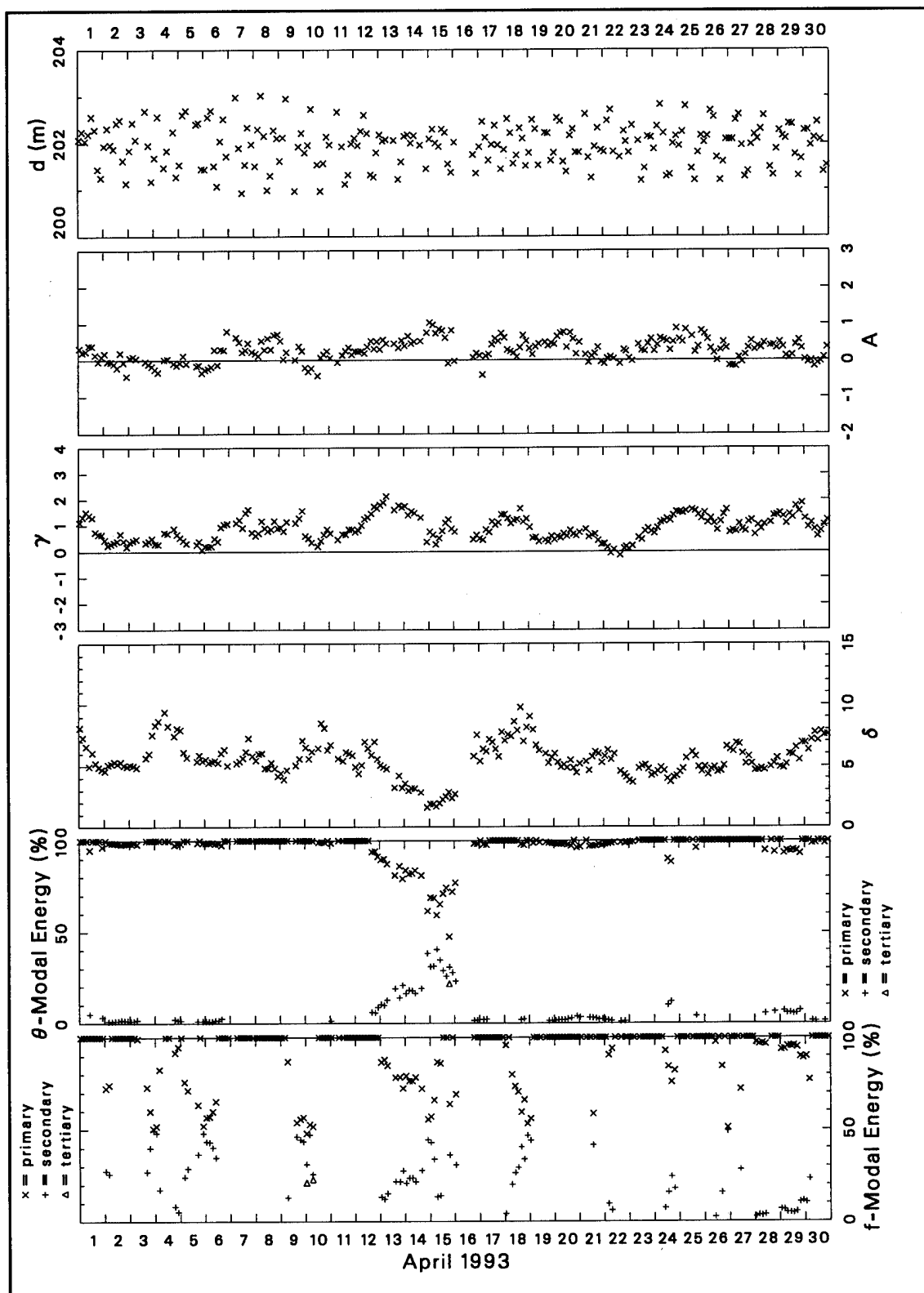


Figure A4. (Concluded)

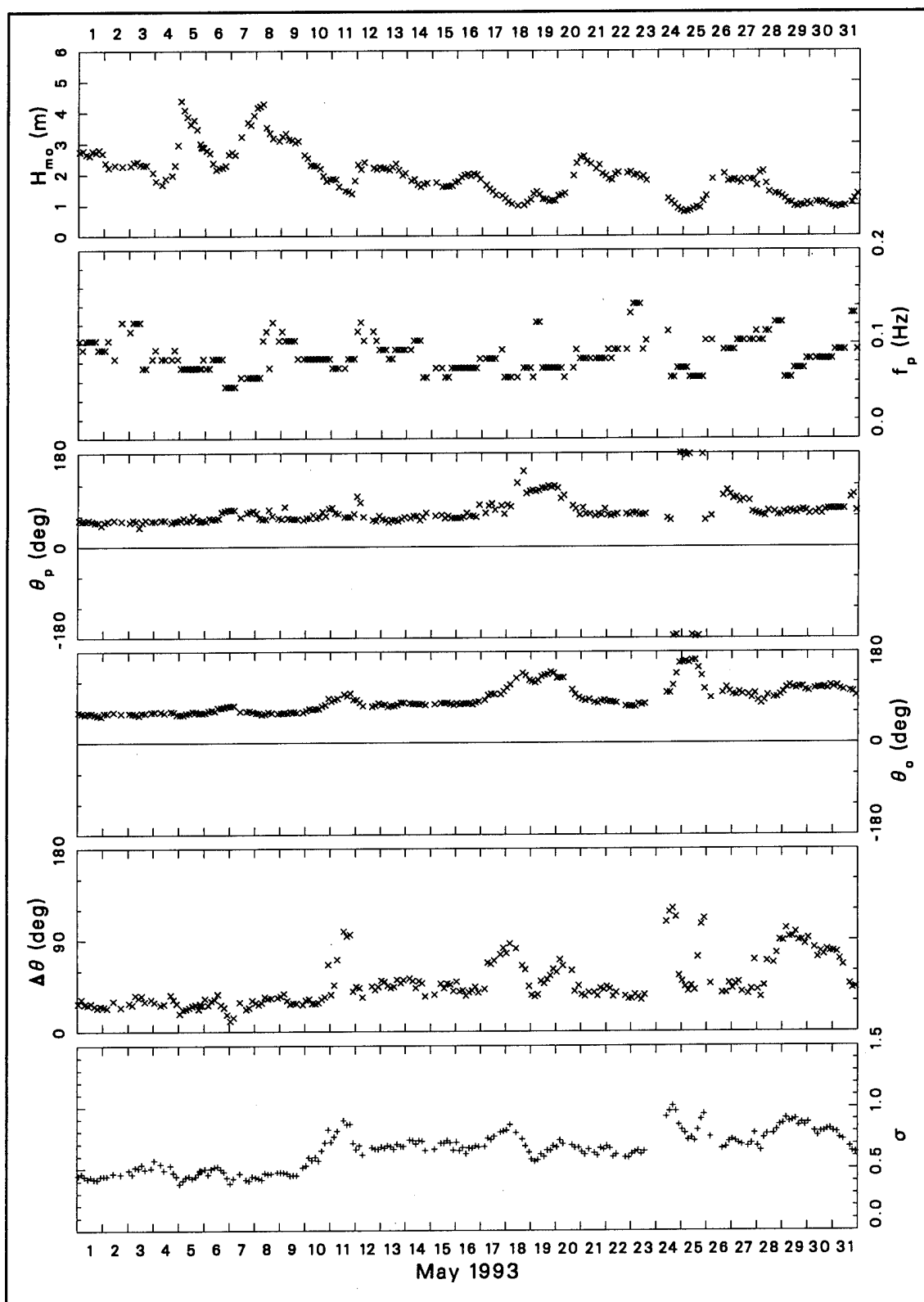


Figure A5. Bulk data for May 1993 (Continued)

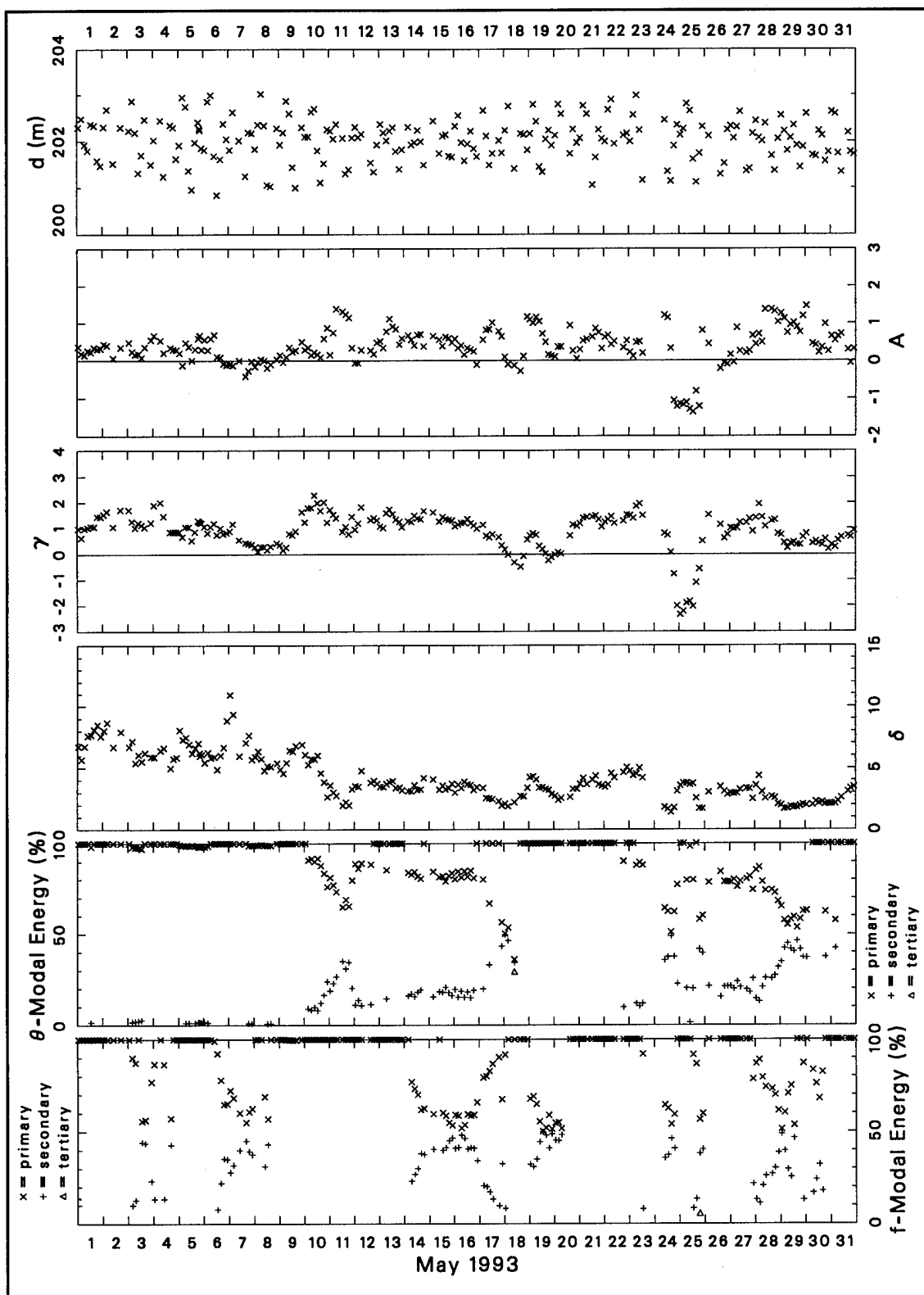


Figure A5. (Concluded)

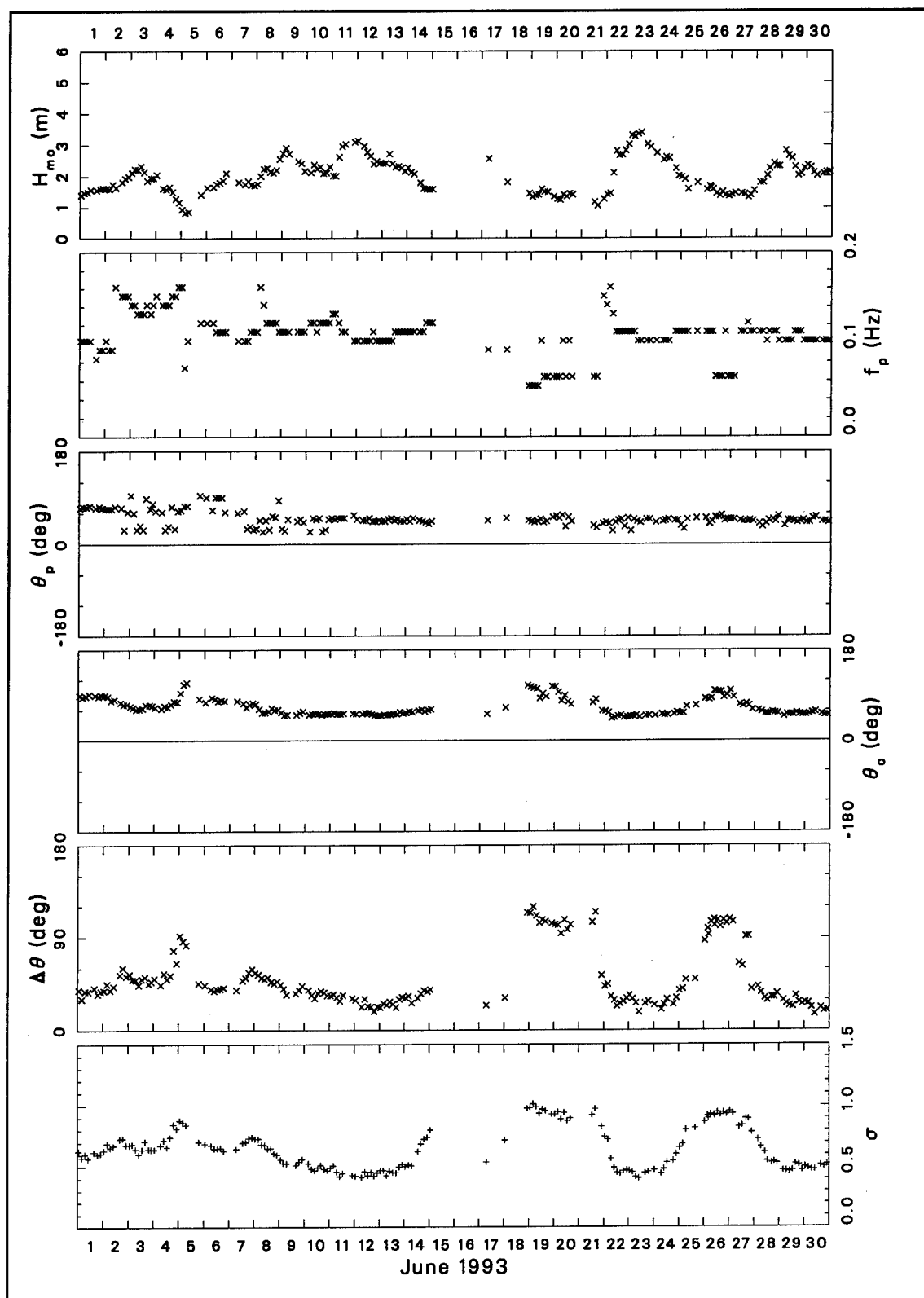


Figure A6. Bulk data for June 1993 (Continued)



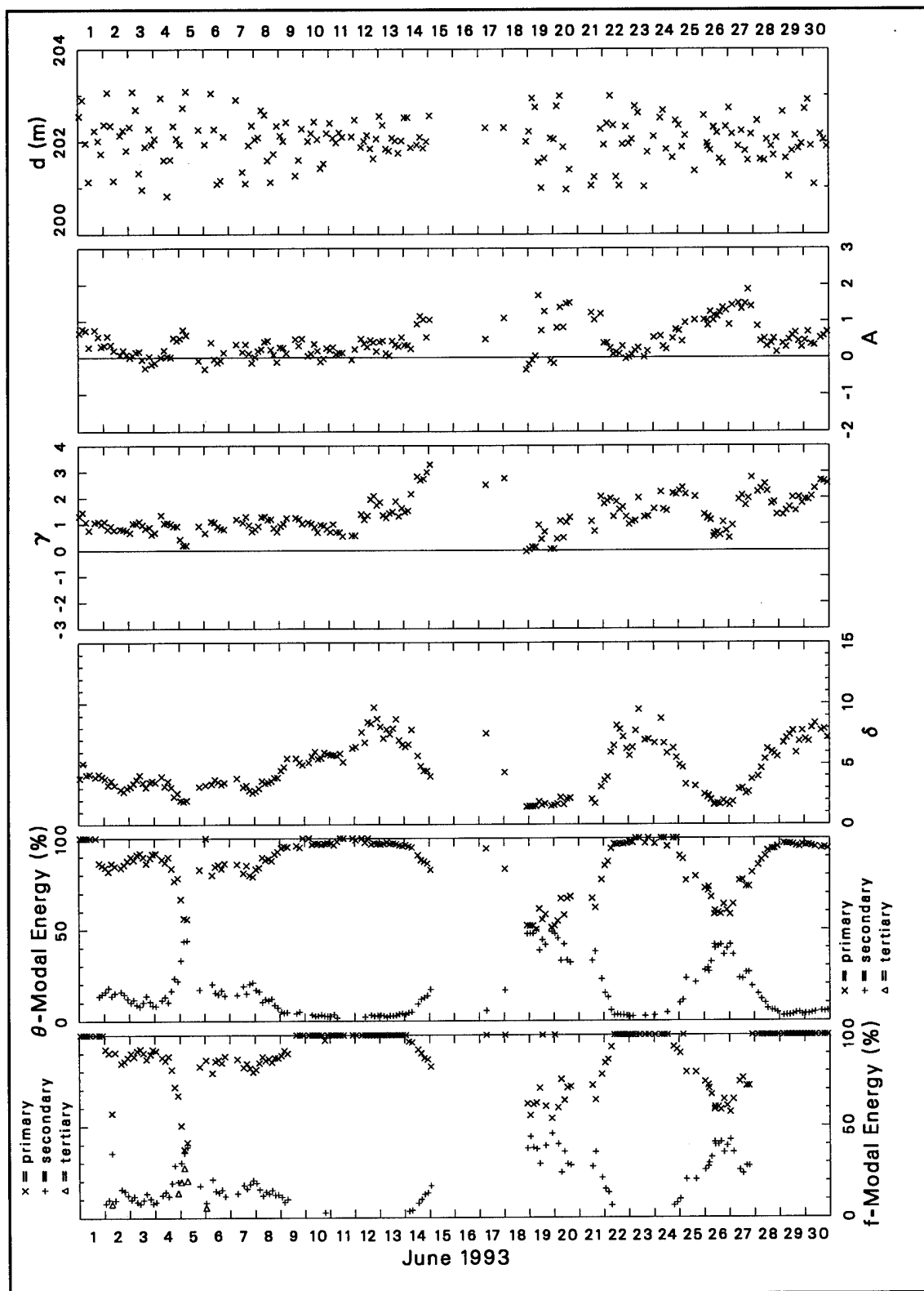


Figure A6. (Concluded)

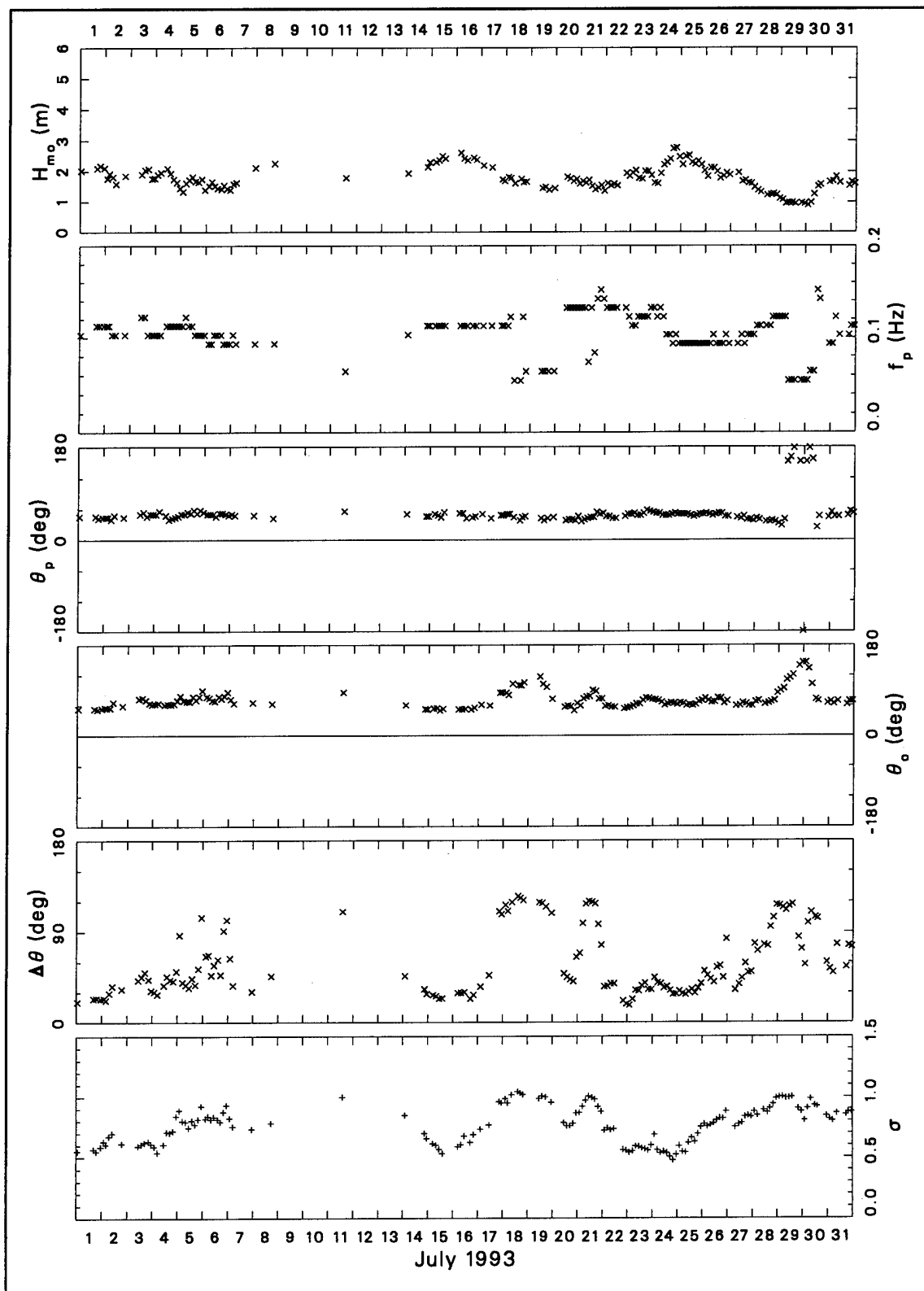


Figure A7. Bulk data for July 1993 (Continued)

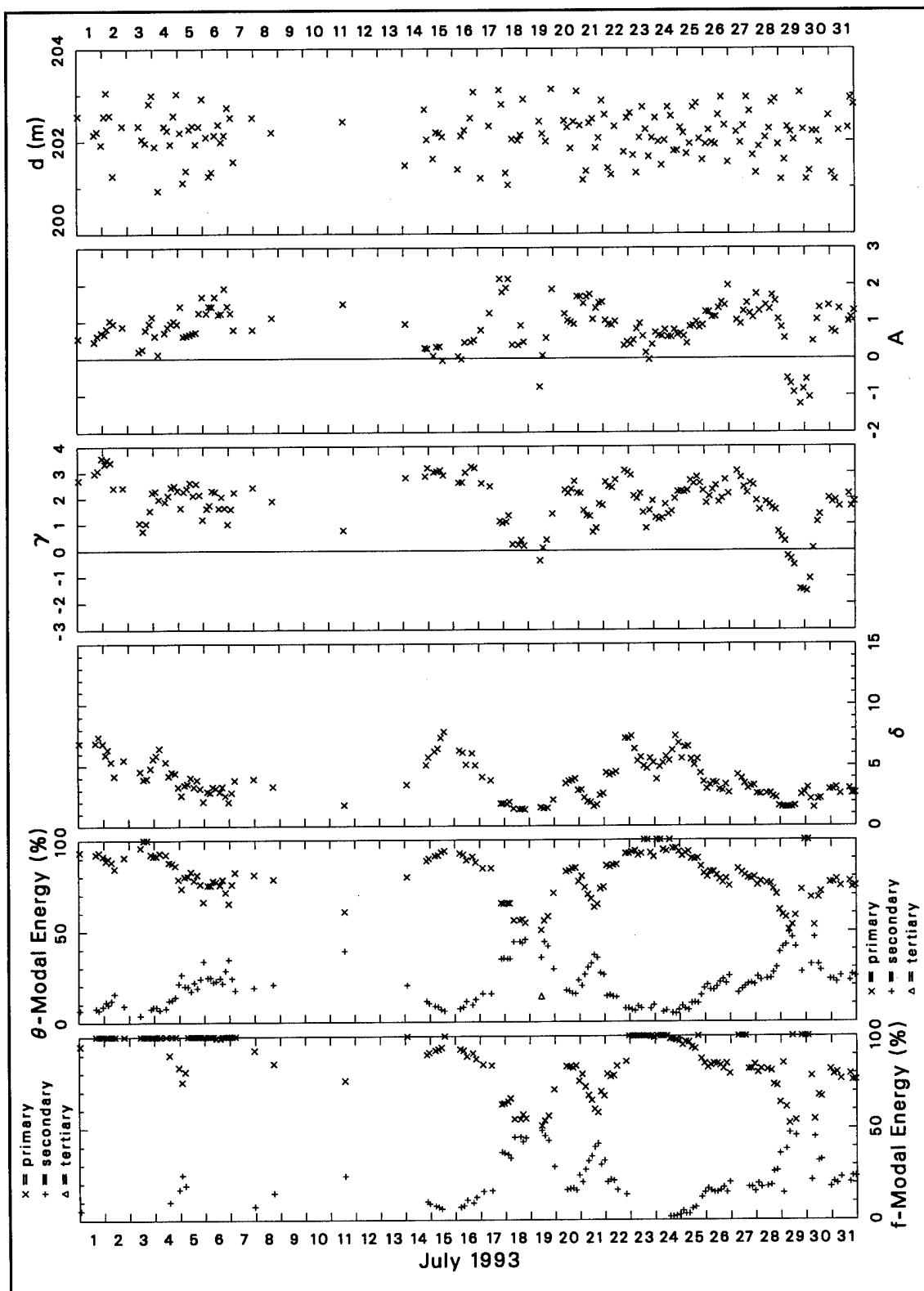


Figure A7. (Concluded)

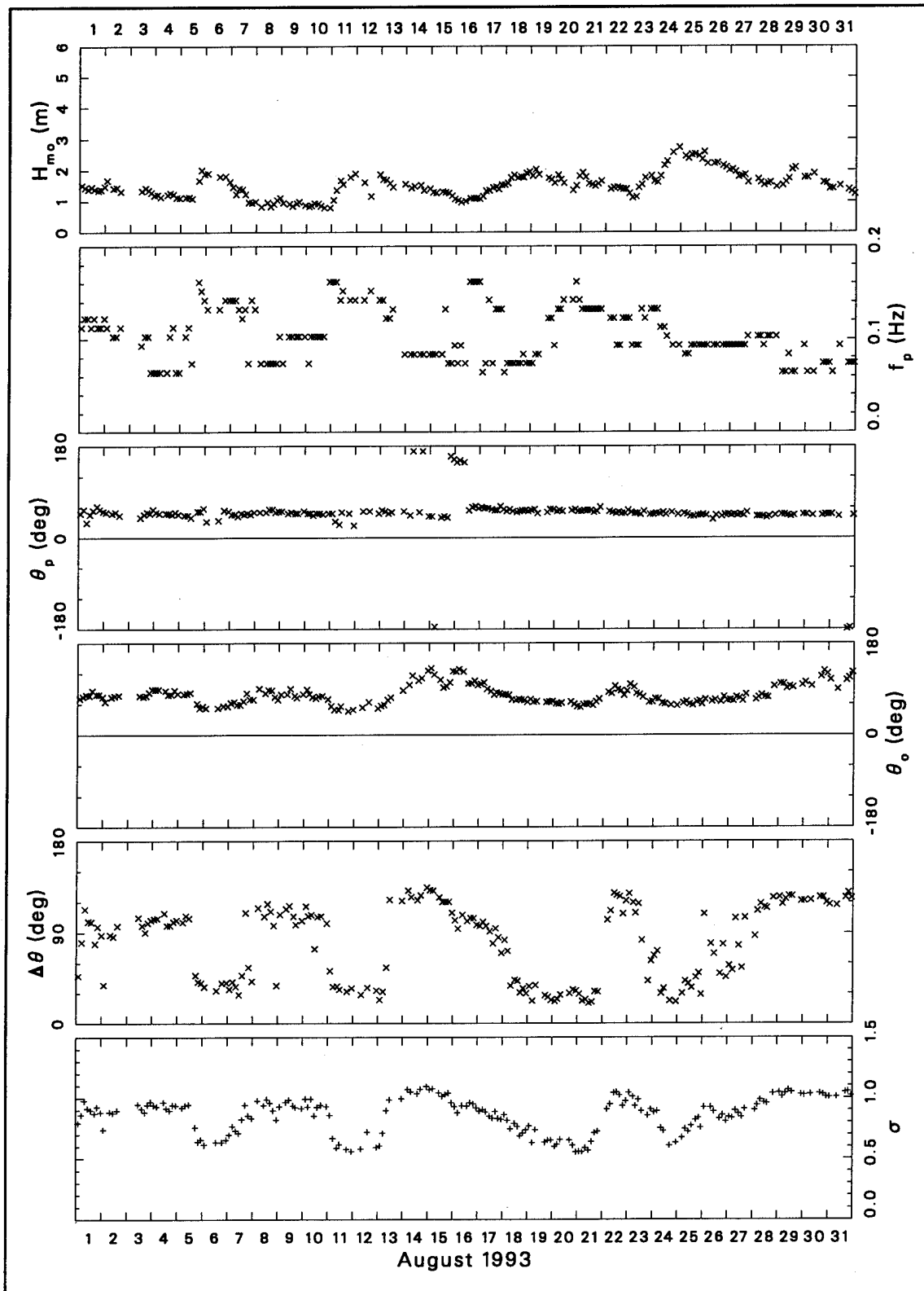


Figure A8. Bulk data for August 1993 (Continued)

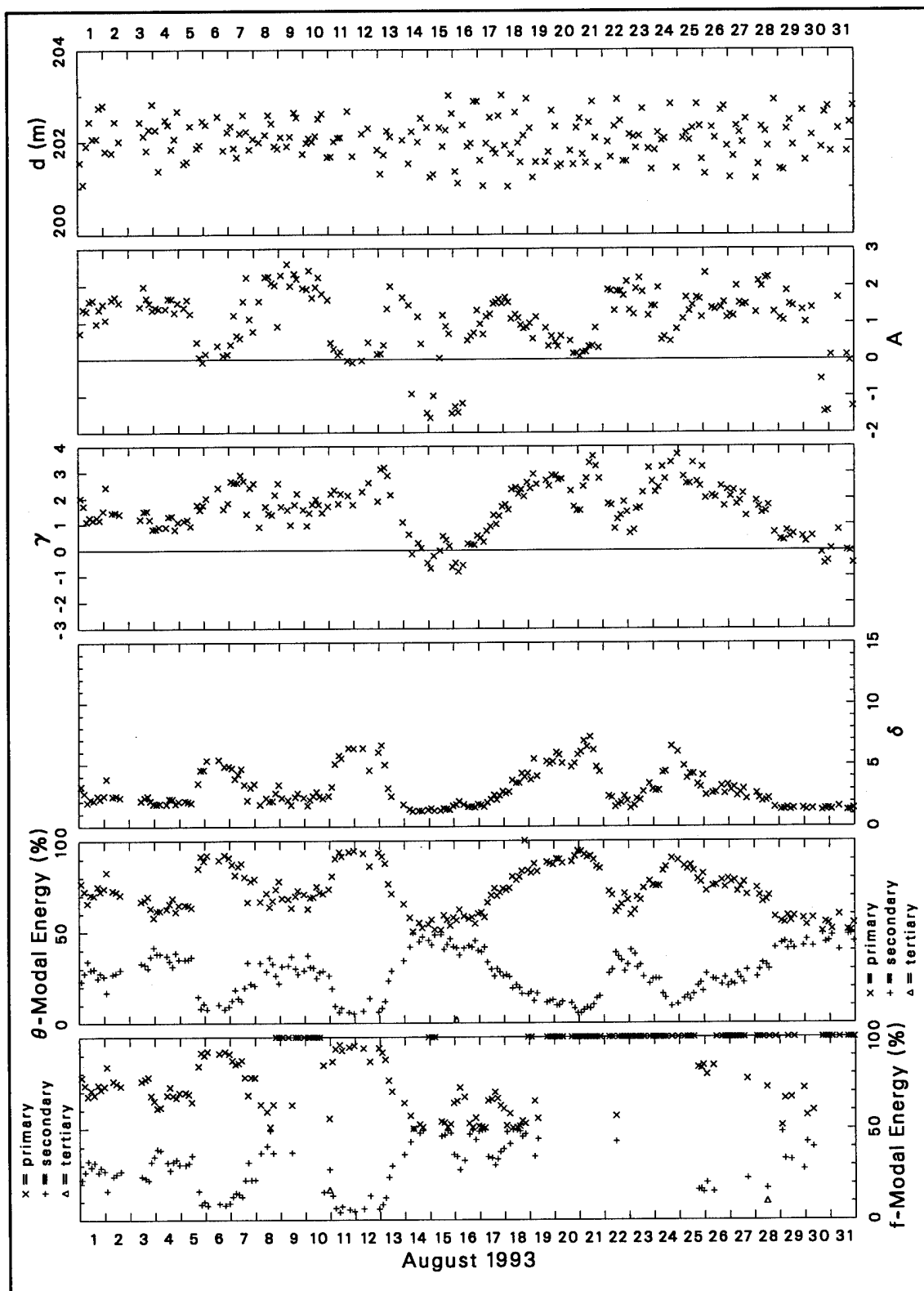


Figure A8. (Concluded)

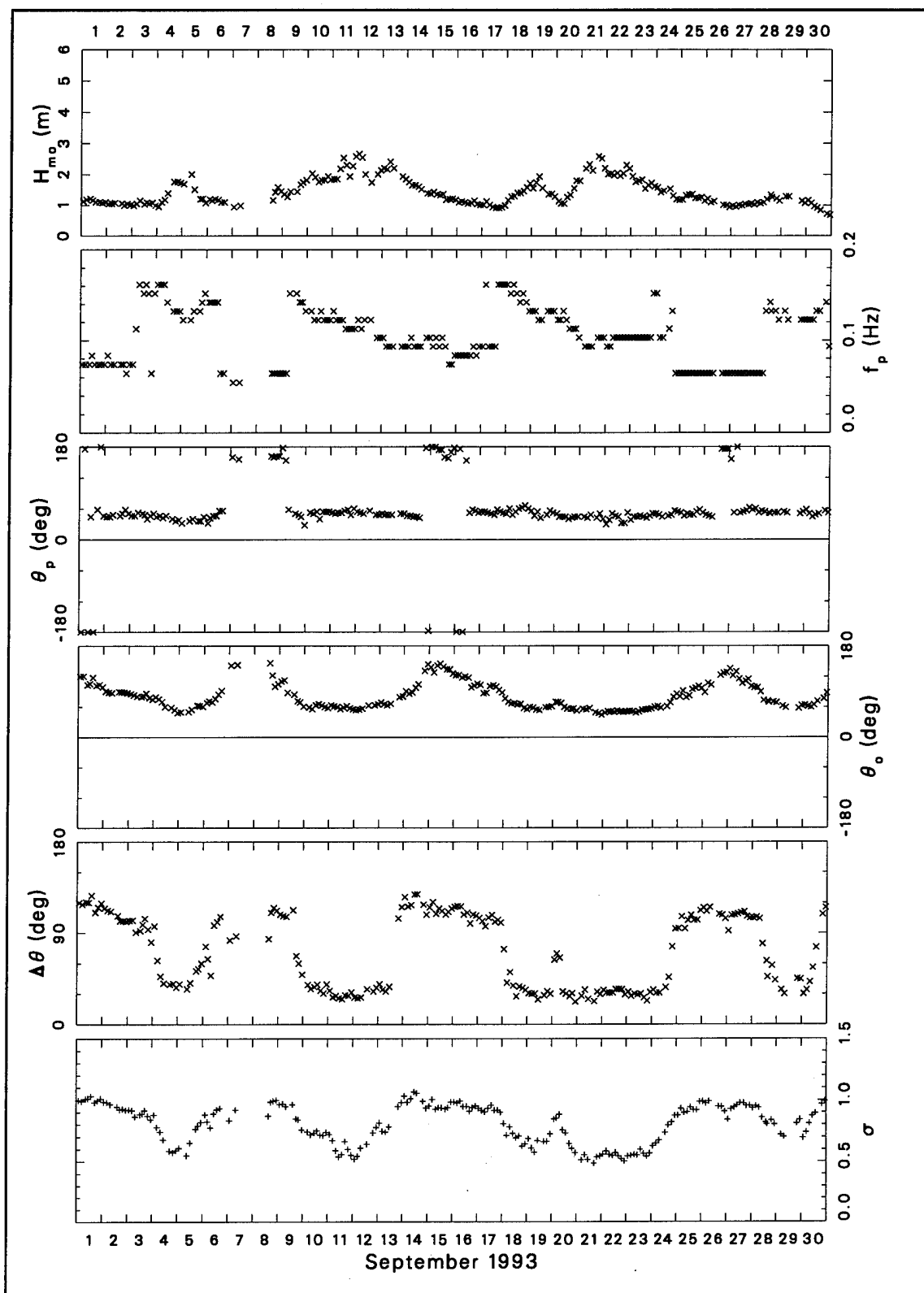


Figure A9. Bulk data for September 1993 (Continued)

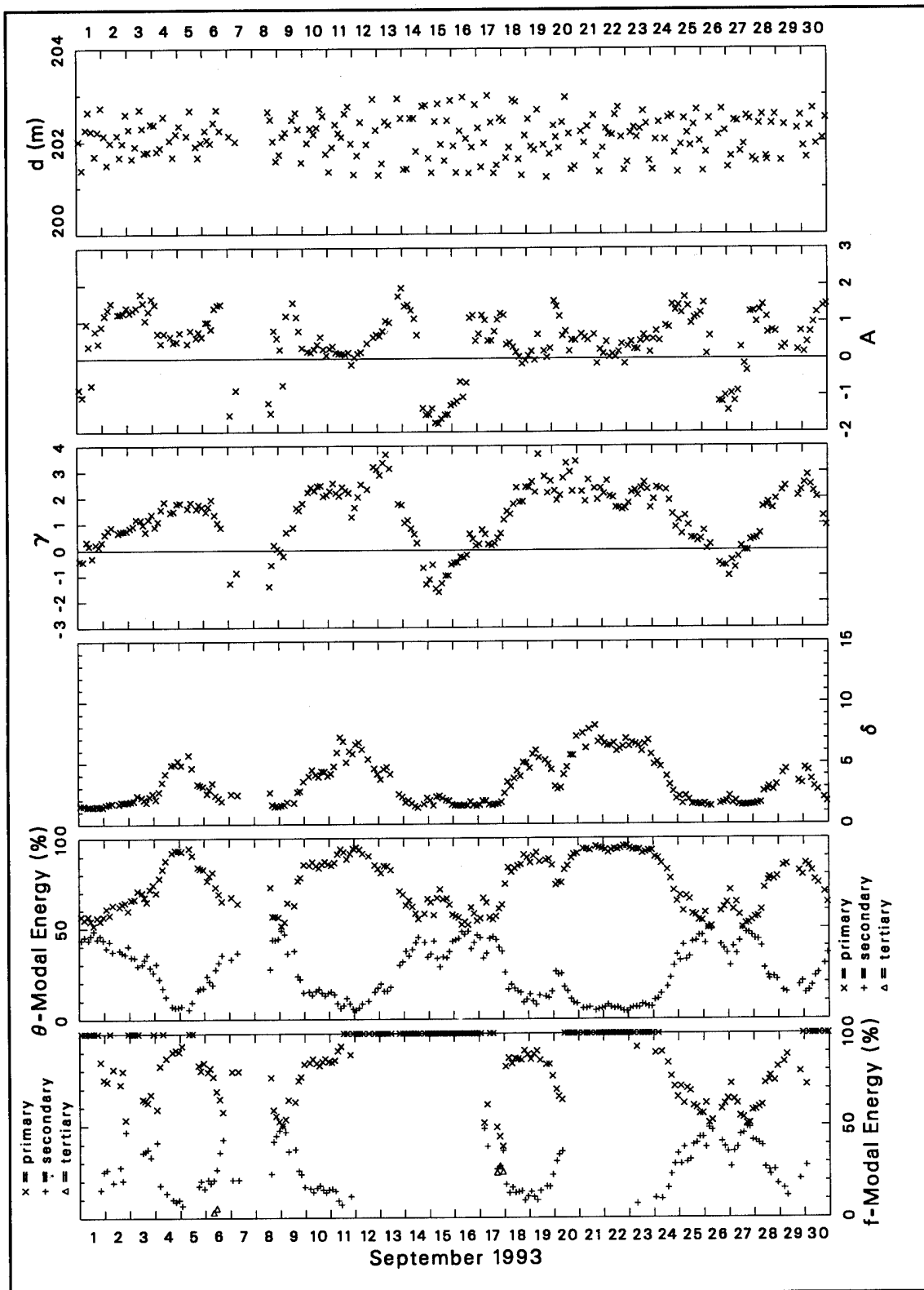


Figure A9. (Concluded)

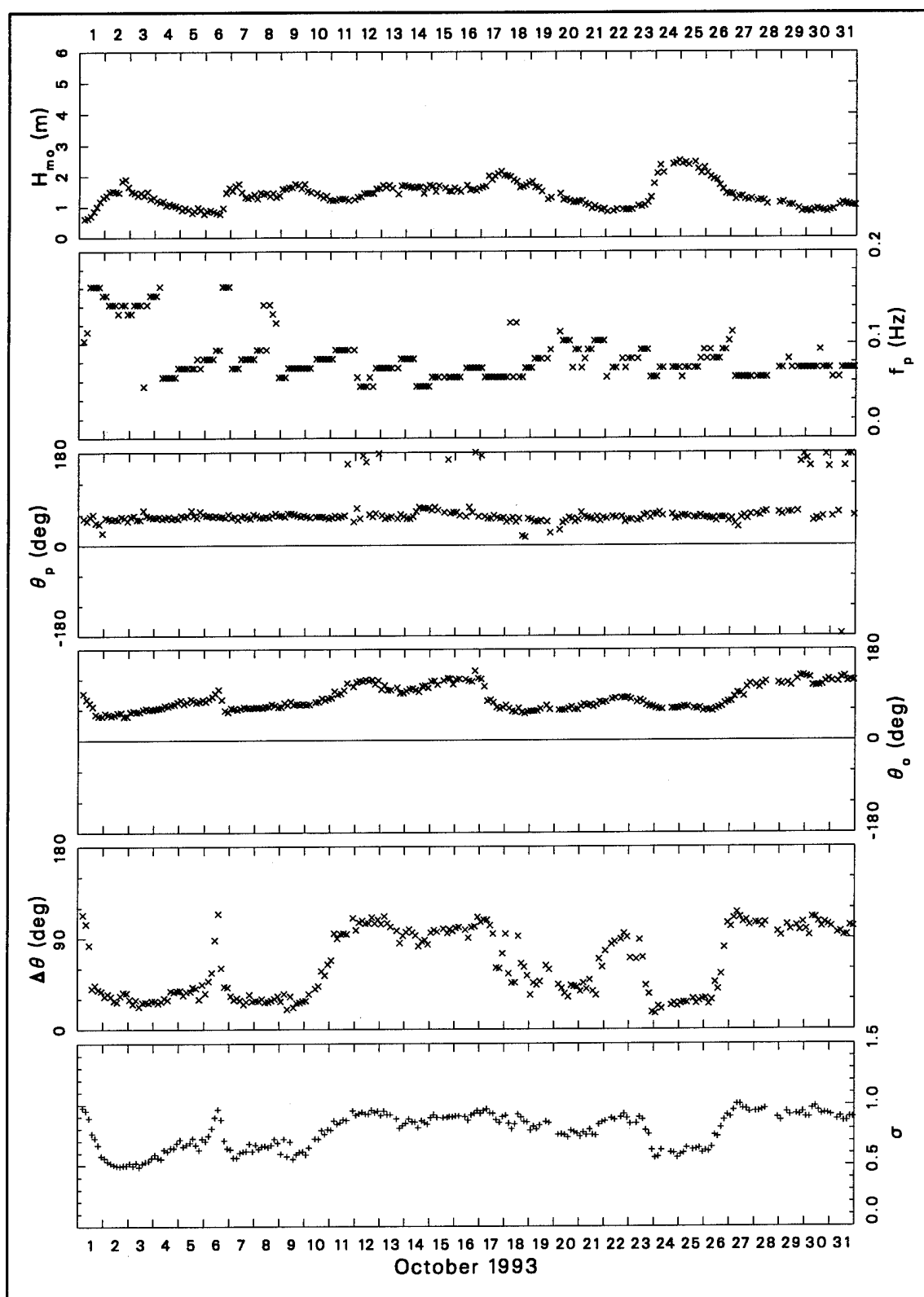


Figure A10. Bulk data for October 1993 (Continued)



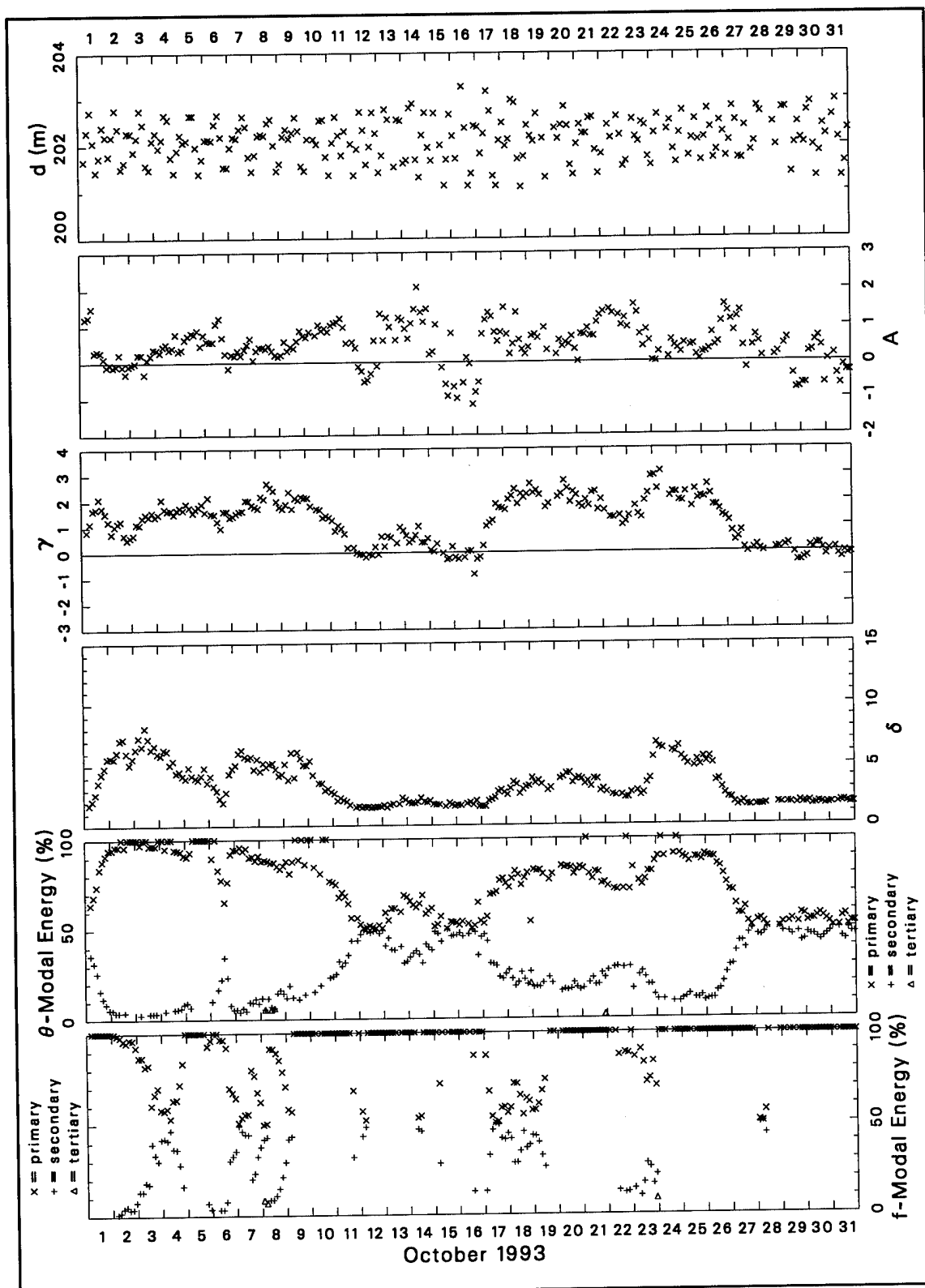


Figure A10. (Concluded)

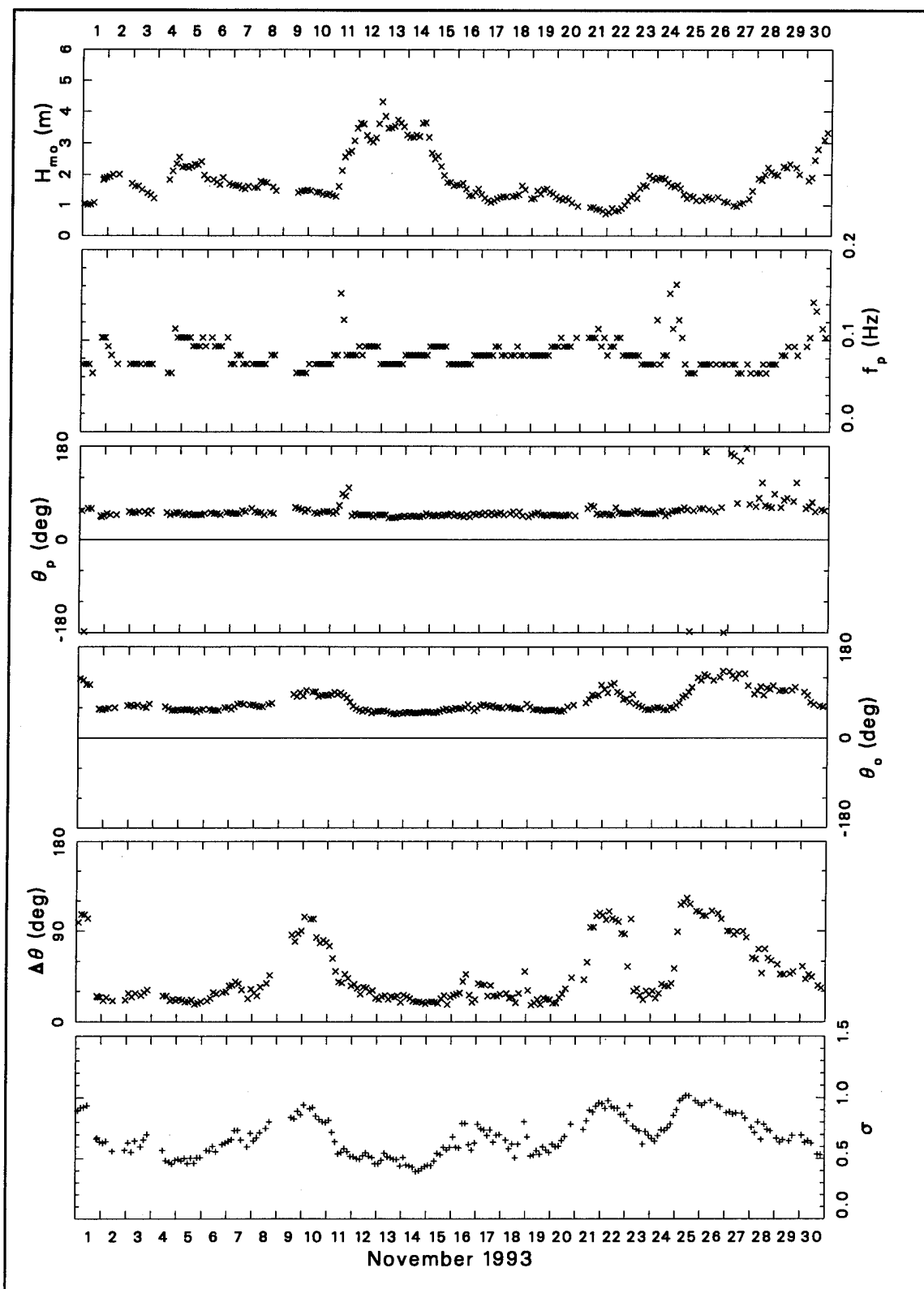


Figure A11. Bulk data for November 1993 (Continued)

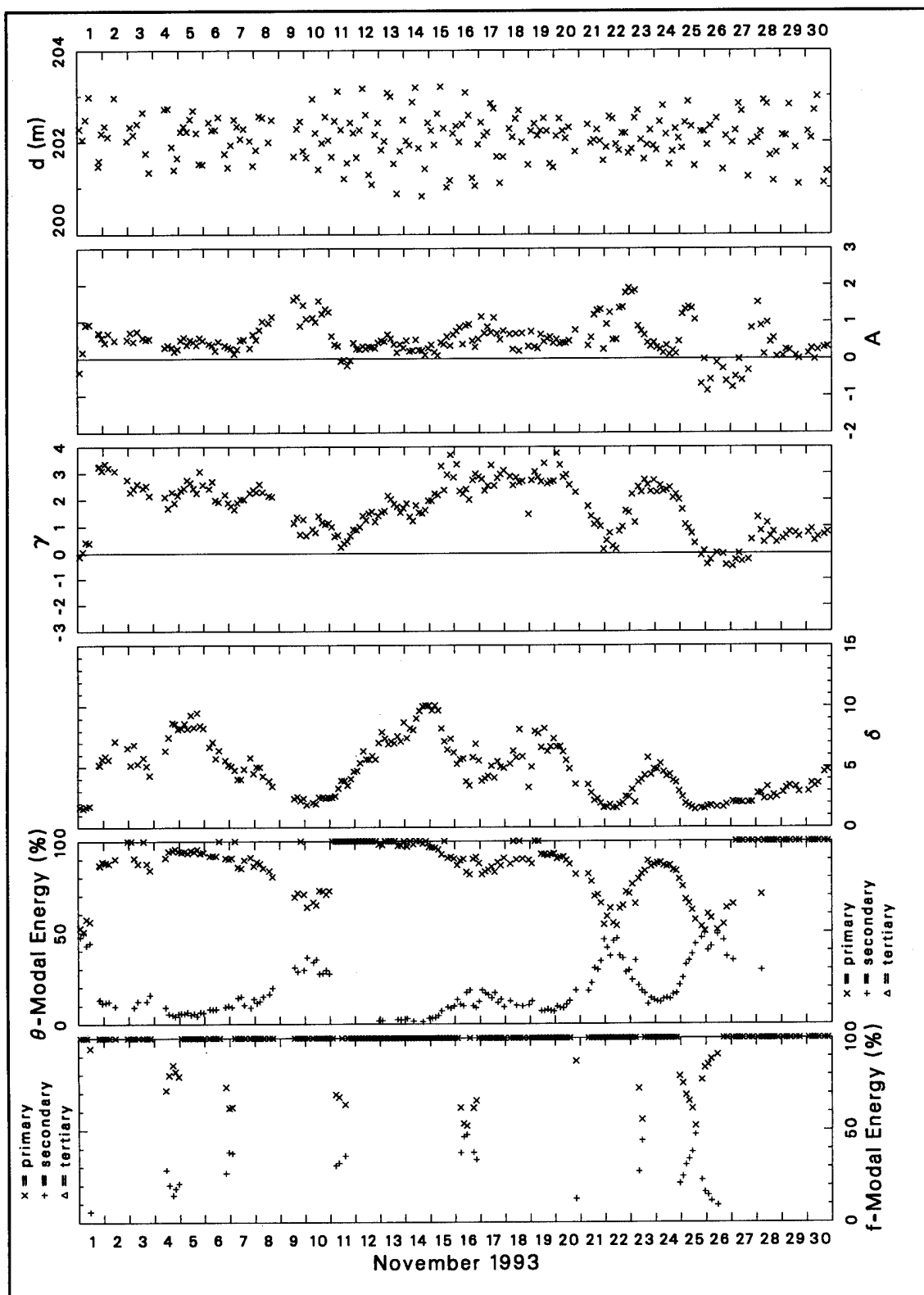


Figure A11. (Concluded)

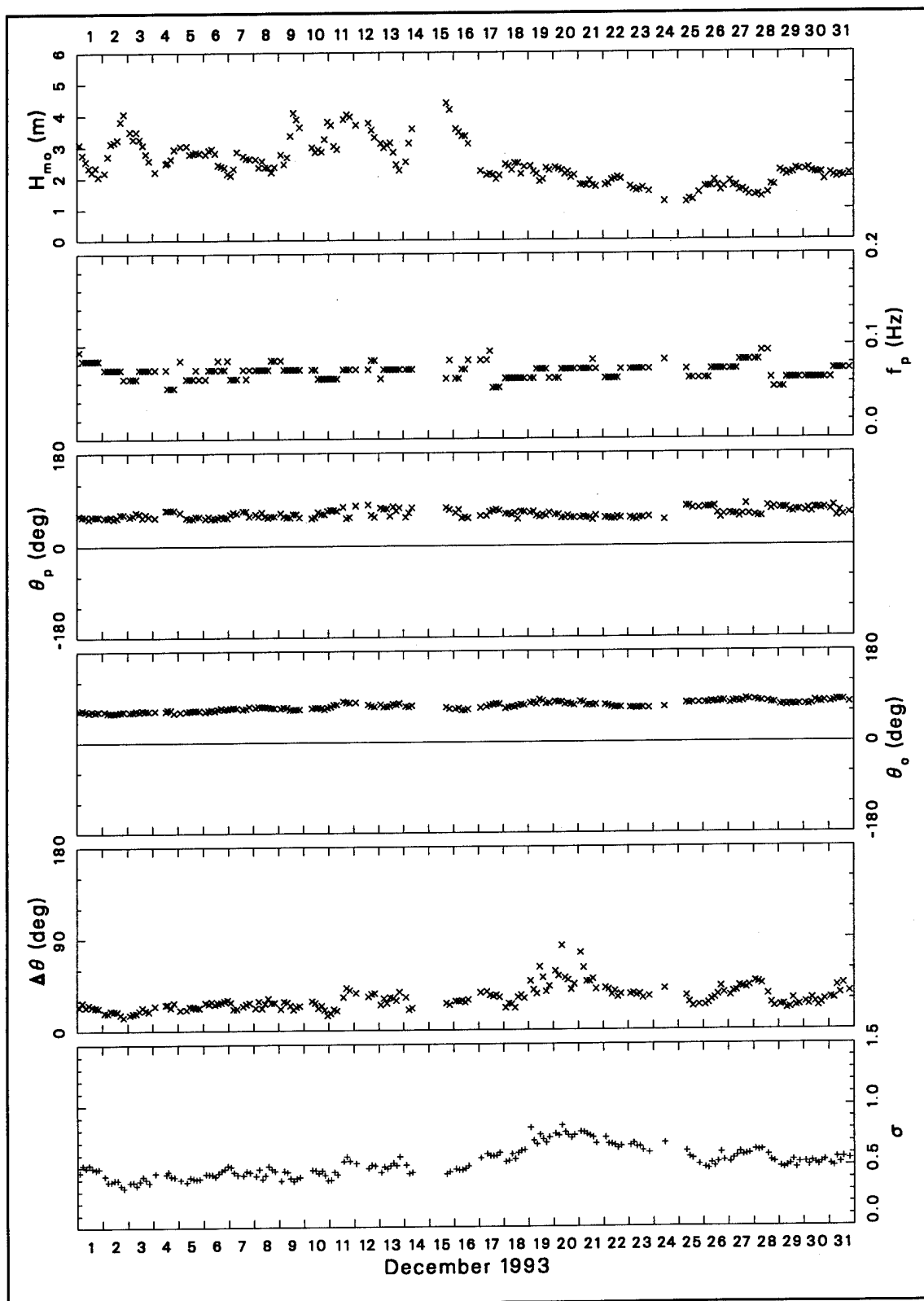


Figure A12. Bulk data for December 1993 (Continued)

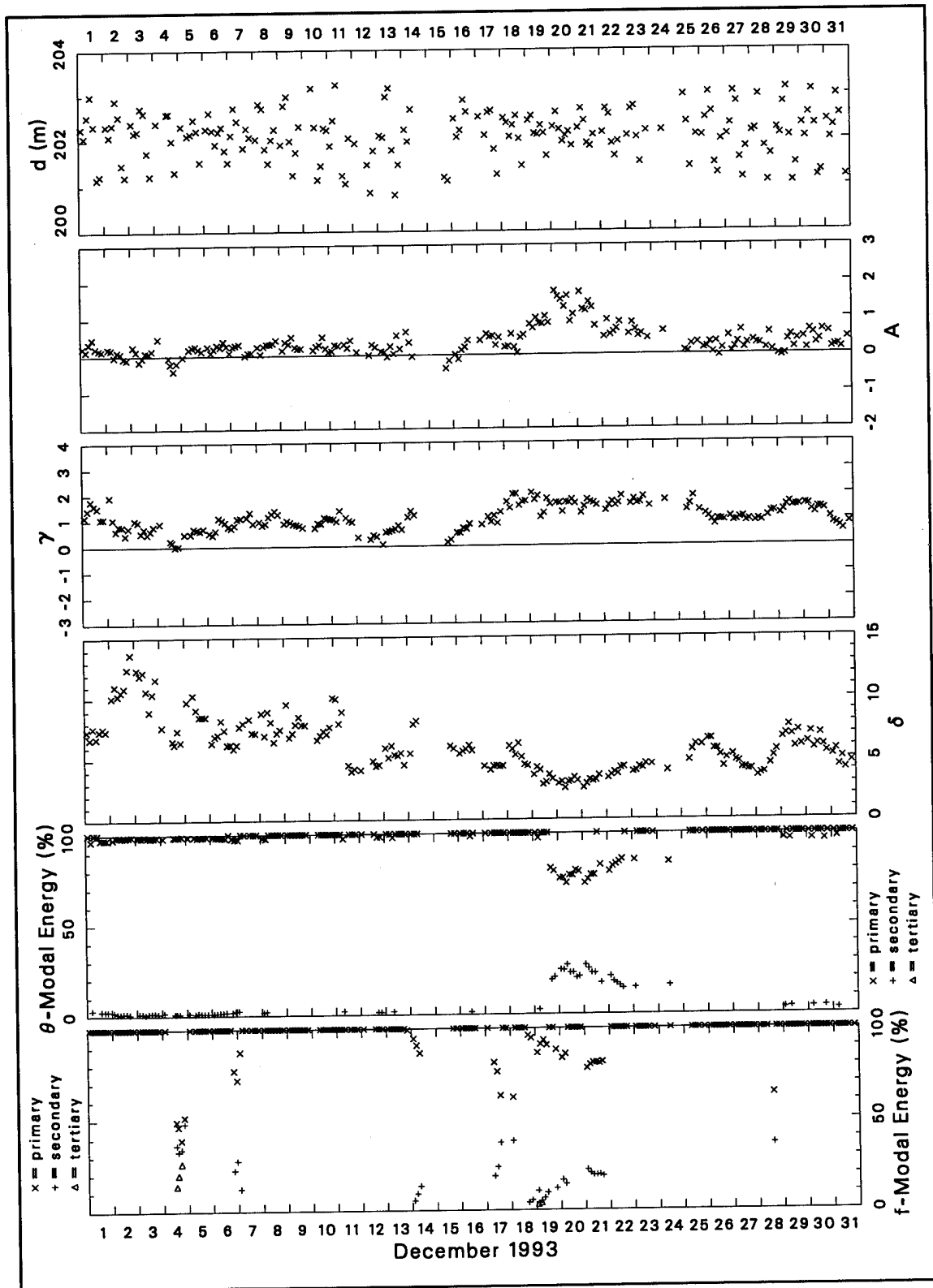


Figure A12. (Concluded)

# **Appendix B**

## **Graphs of Example Spectra**

---

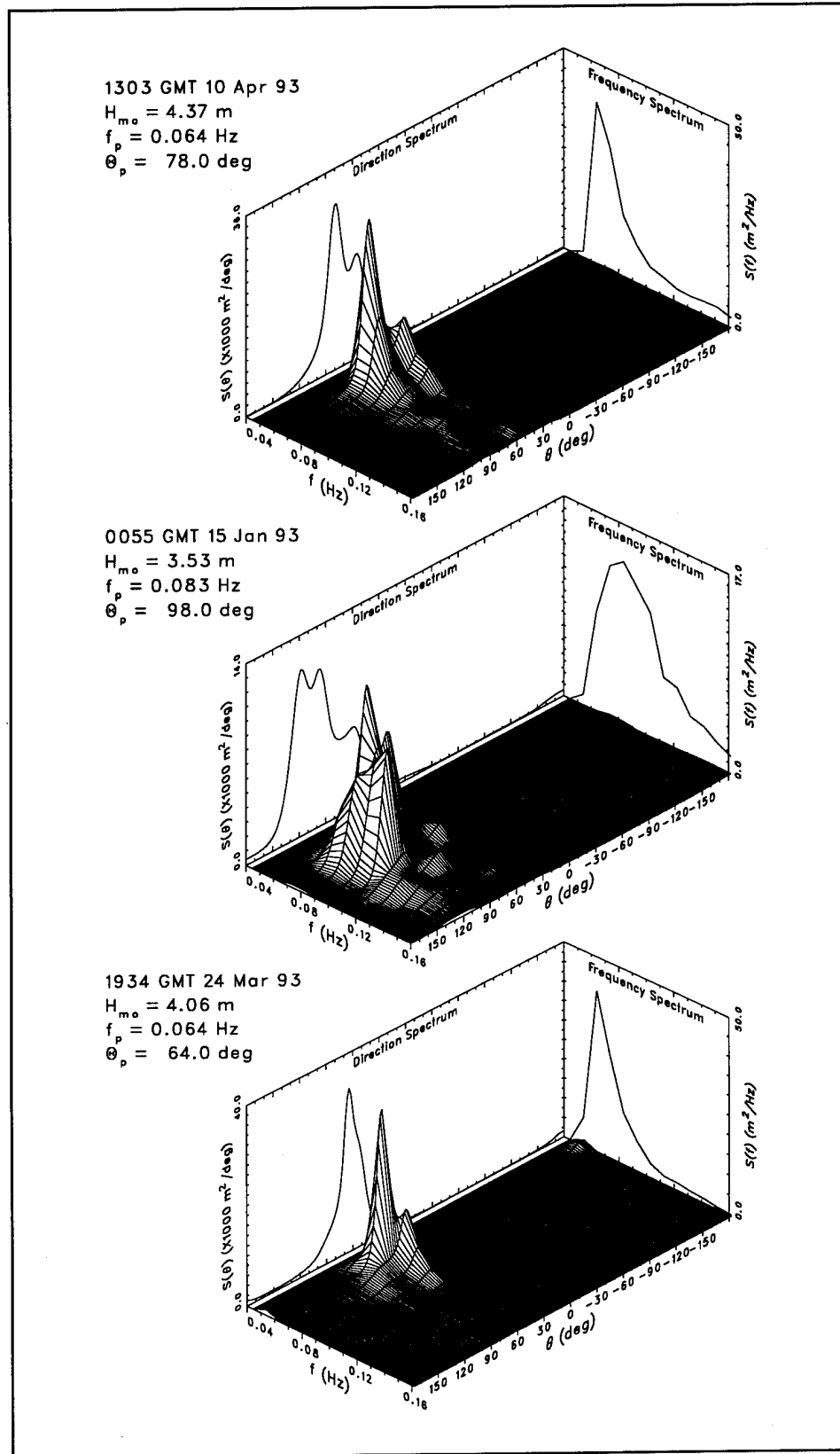


Figure B1. Spectra, top to bottom:  $\Delta\theta = 27^\circ$ ,  $A = -0.43$ ;  $\Delta\theta = 43^\circ$ ,  $A = -0.26$ ; and  $\Delta\theta = 20^\circ$ ,  $A = 0.10$

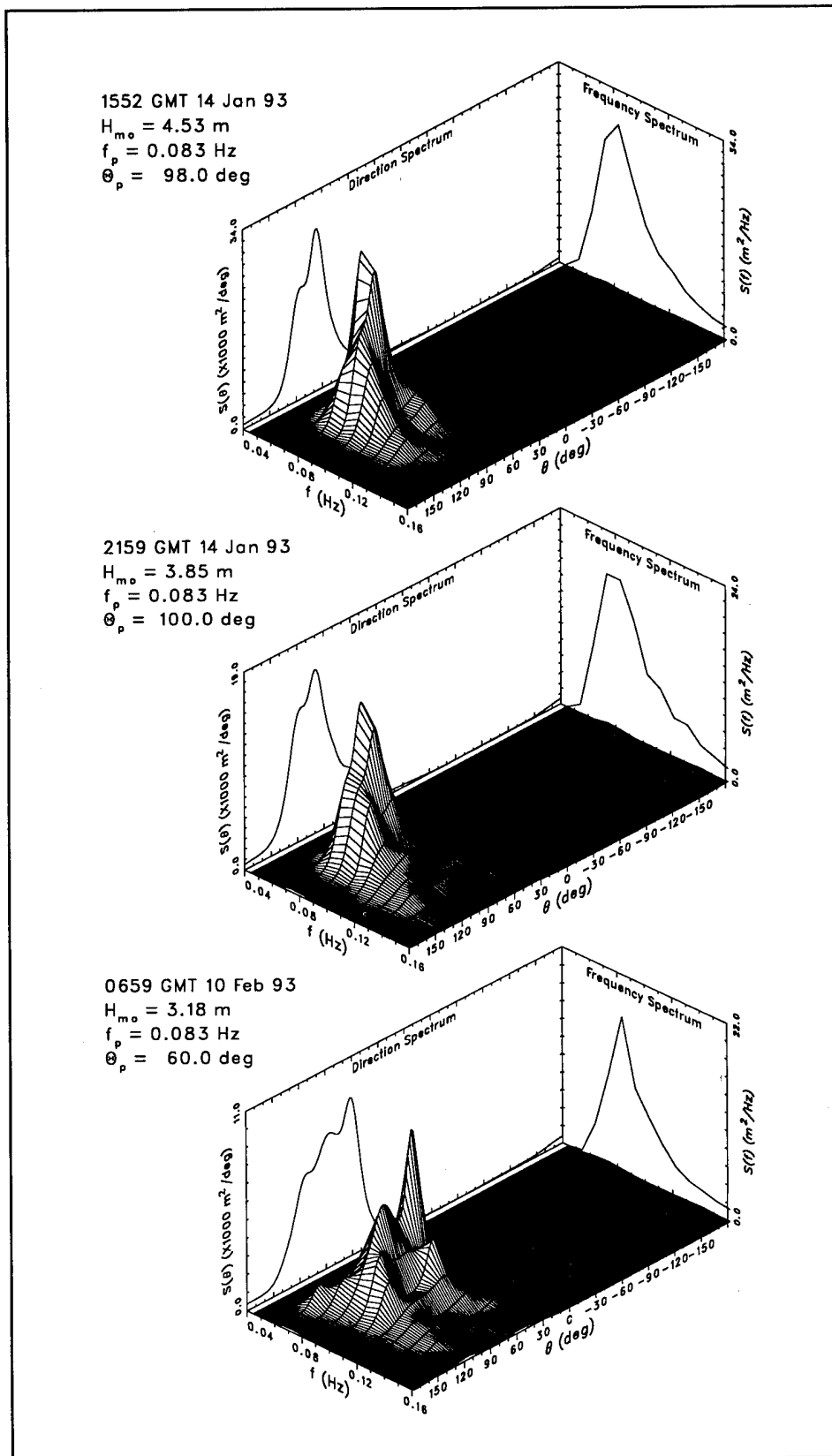


Figure B2. Spectra, top to bottom:  $\Delta\theta = 28^\circ$ ,  $A = 0.18$ ;  $\Delta\theta = 35^\circ$ ,  $A = -0.07$ ; and  $\Delta\theta = 45^\circ$ ,  $A = 0.13$



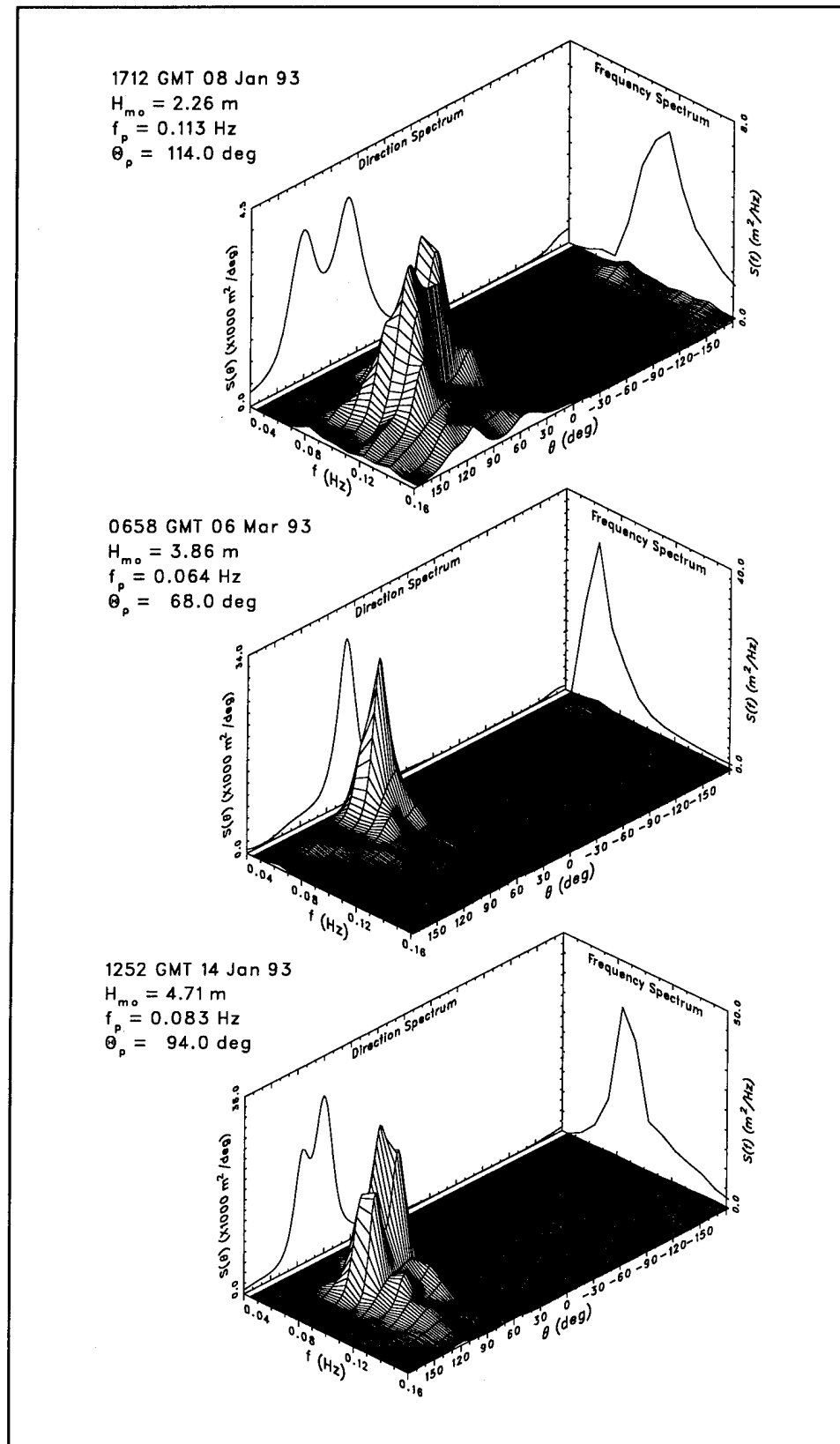


Figure B3. Spectra, top to bottom:  $\Delta\theta = 56^\circ$ ,  $A = 0.09$ ;  $\Delta\theta = 21^\circ$ ,  $A = 0.29$ ; and  $\Delta\theta = 28^\circ$ ,  $A = 0.30$

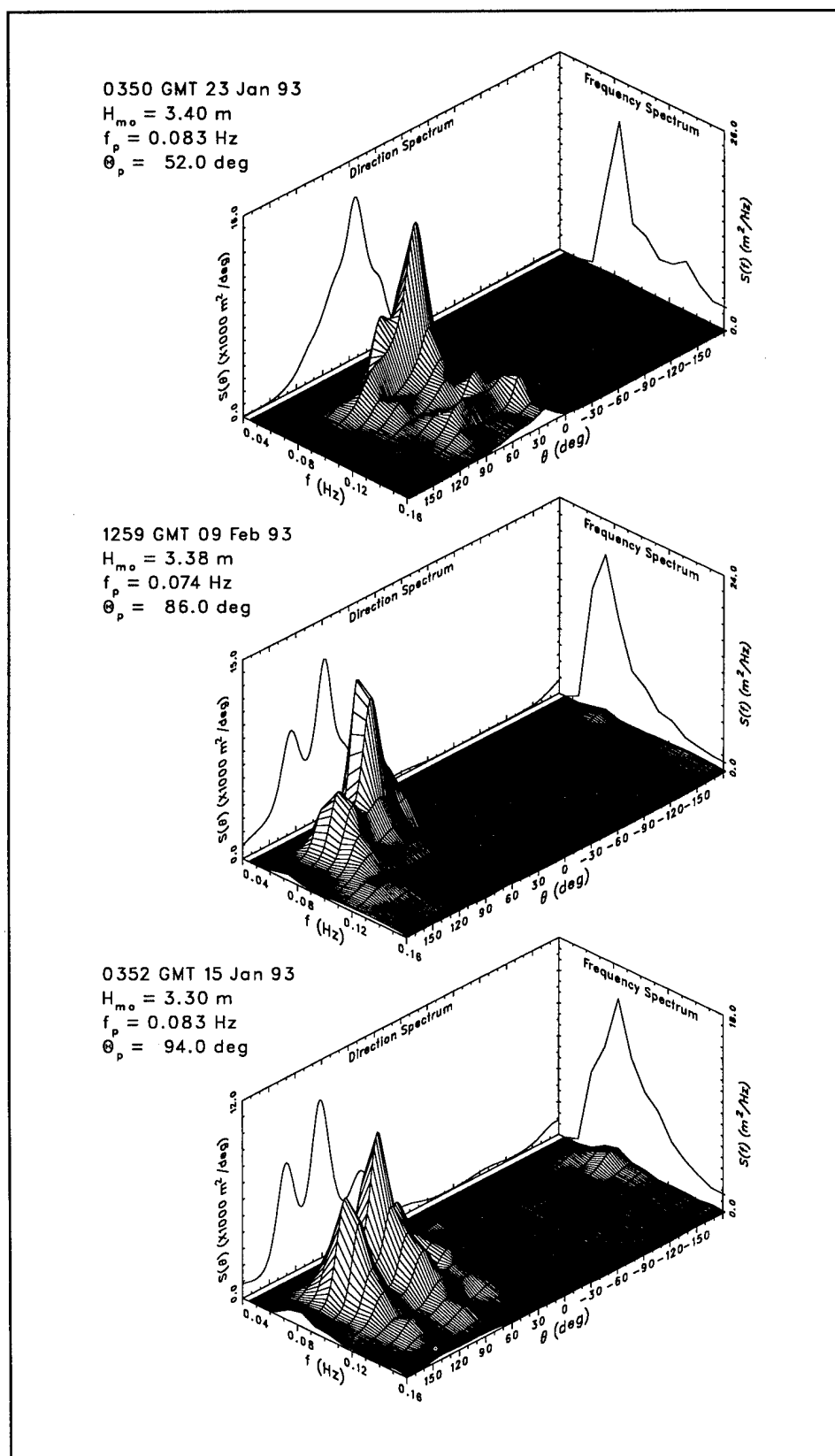


Figure B4. Spectra, top to bottom:  $\Delta\theta = 36^\circ$ ,  $A = 0.29$ ;  $\Delta\theta = 46^\circ$ ,  $A = 0.54$ ; and  $\Delta\theta = 56^\circ$ ,  $A = 0.23$

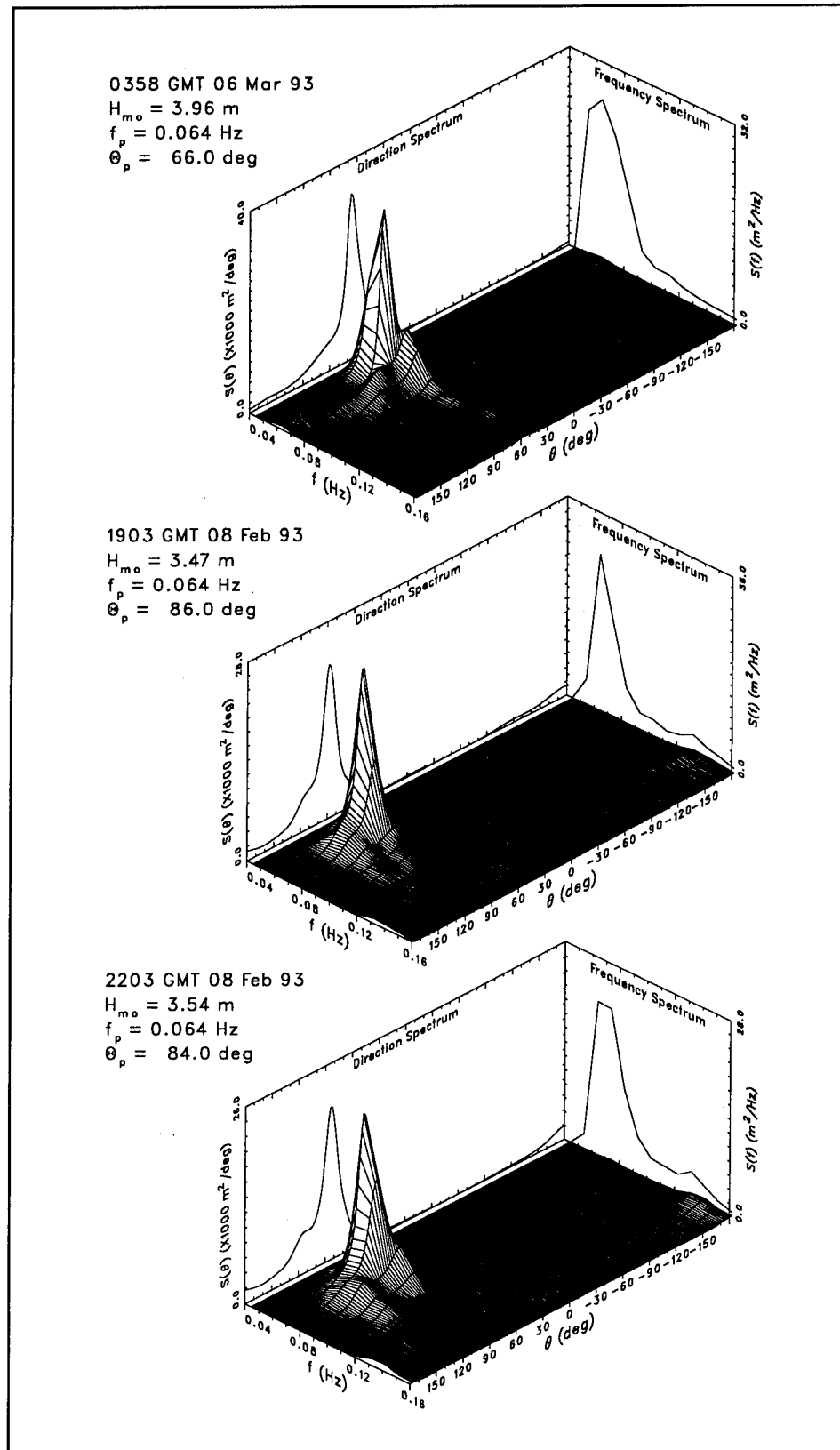


Figure B5. Spectra, top to bottom:  $\Delta\theta = 24^\circ$ ,  $A = 0.64$ ;  $\Delta\theta = 30^\circ$ ,  $A = 0.80$ ; and  $\Delta\theta = 37^\circ$ ,  $A = 0.92$

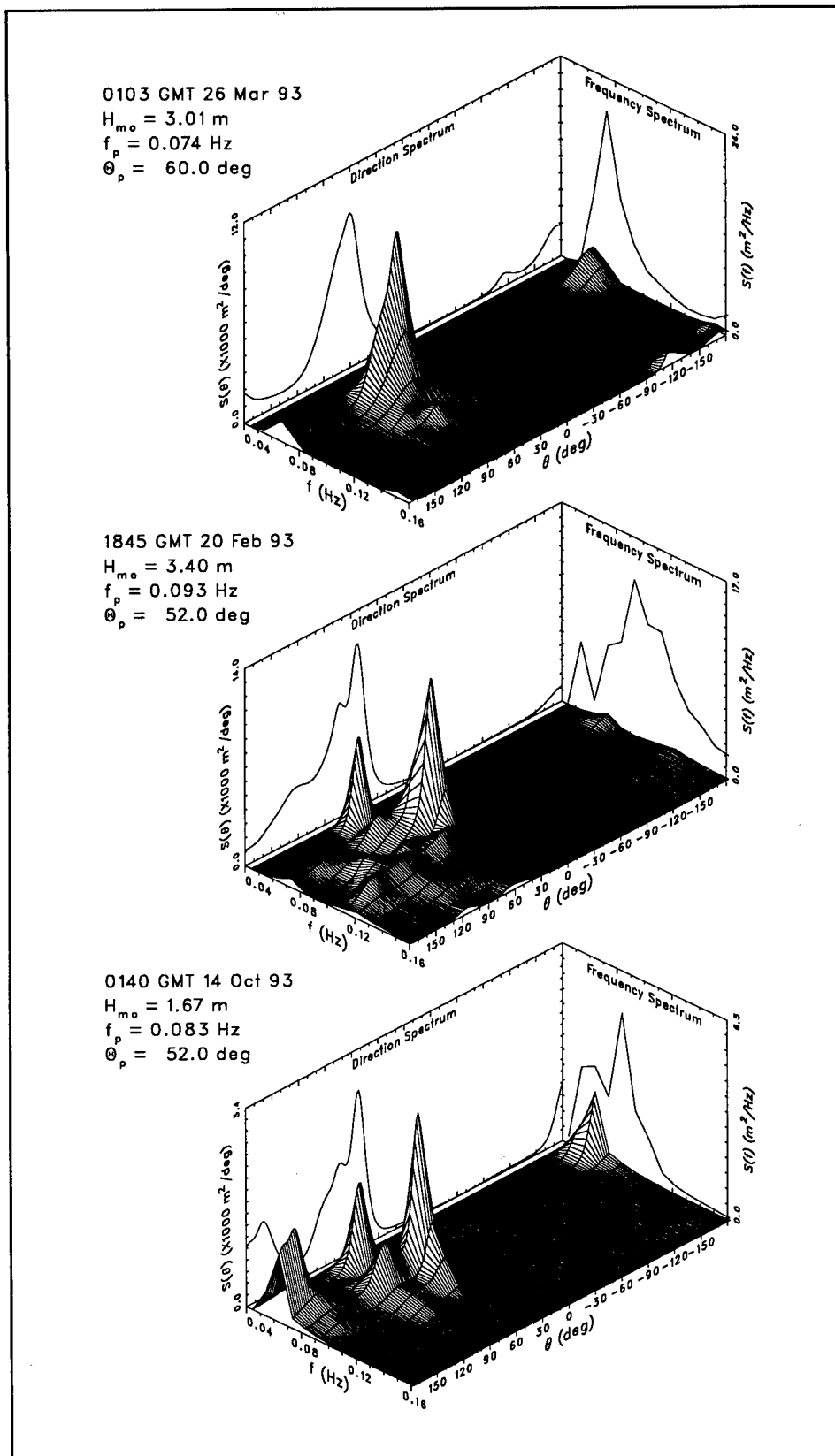


Figure B6. Spectra, top to bottom:  $\Delta\theta = 48^\circ$ ,  $A = 0.64$ ;  $\Delta\theta = 60^\circ$ ,  $A = 0.60$ ; and  $\Delta\theta = 96^\circ$ ,  $A = 0.93$

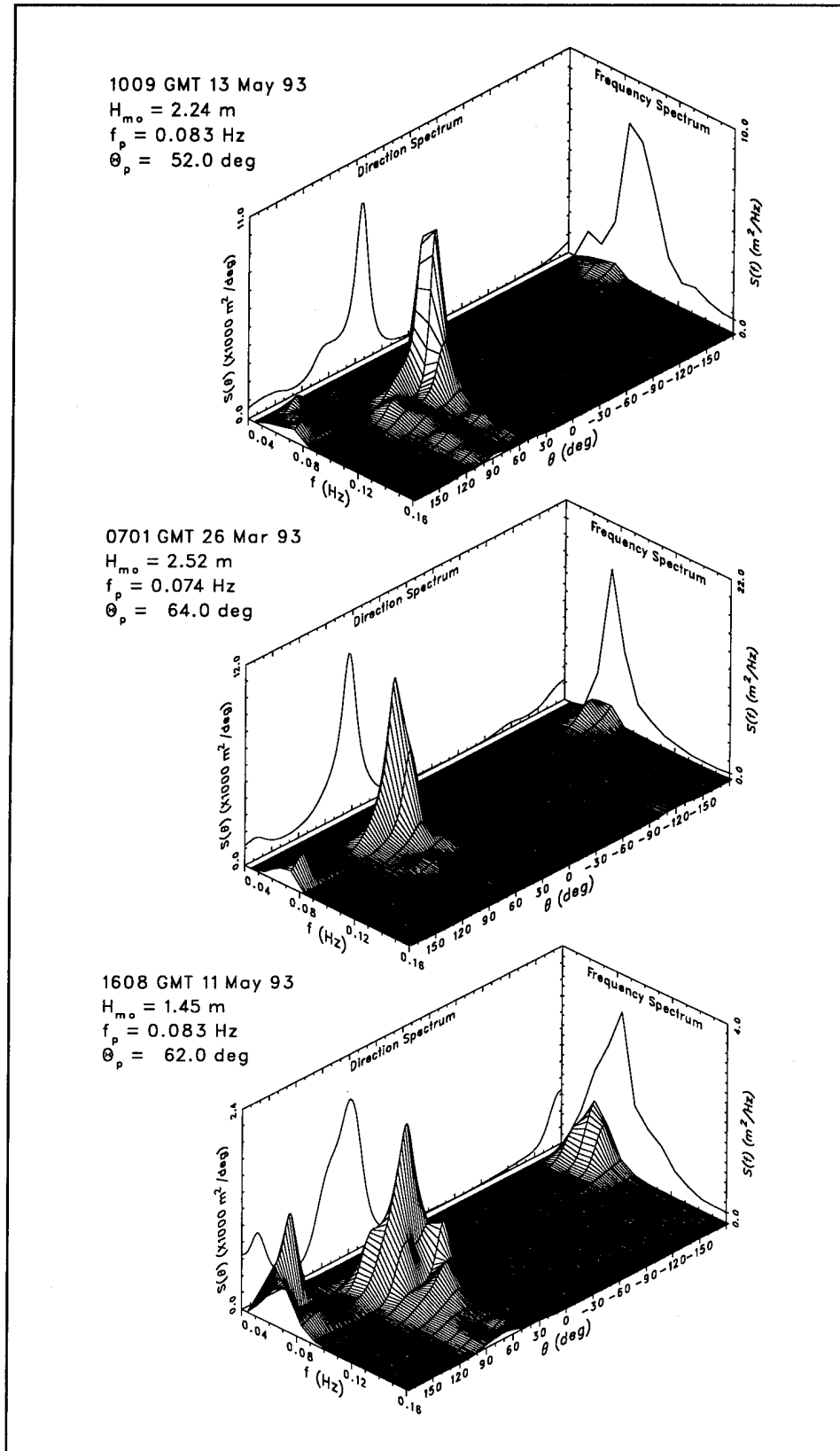


Figure B7. Spectra, top to bottom:  $\Delta\theta = 43^\circ$ ,  $A = 1.12$ ;  $\Delta\theta = 47^\circ$ ,  $A = 1.13$ ; and  $\Delta\theta = 94^\circ$ ,  $A = 1.24$

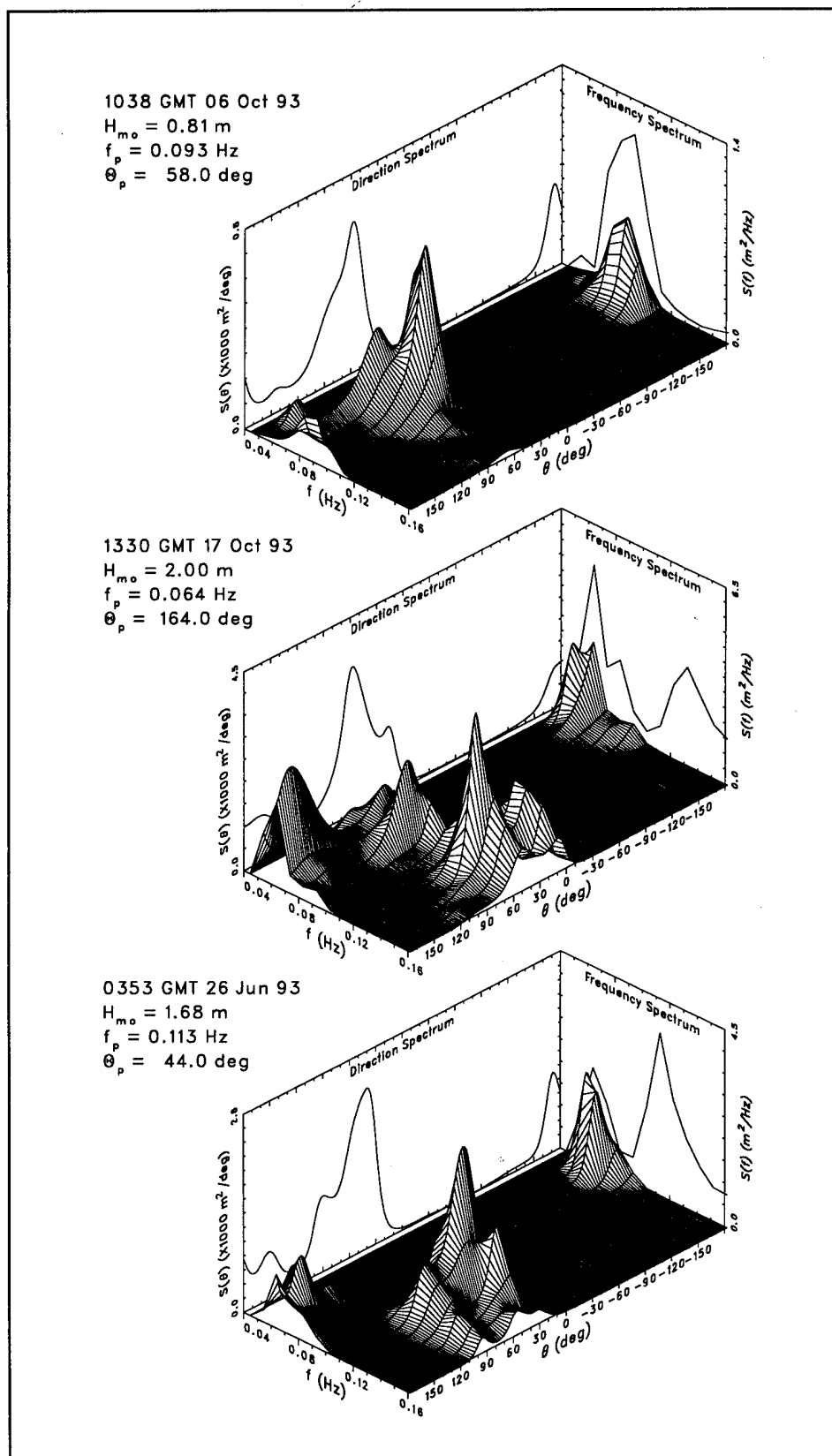


Figure B8. Spectra, top to bottom:  $\Delta\theta = 88^\circ$ ,  $A = 1.08$ ;  $\Delta\theta = 94^\circ$ ,  $A = 1.26$ ; and  $\Delta\theta = 99^\circ$ ,  $A = 1.02$

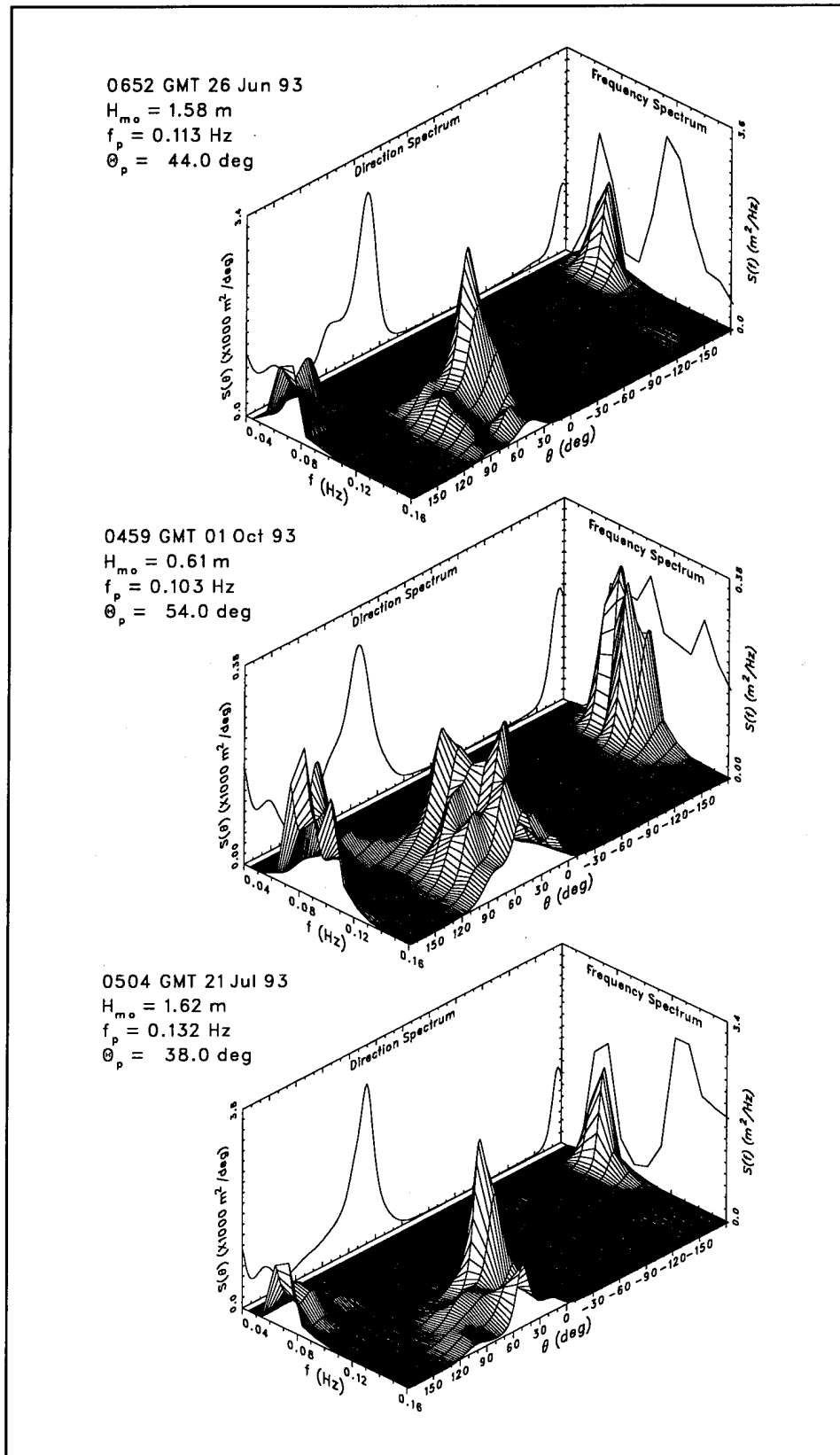


Figure B9. Spectra, top to bottom:  $\Delta\theta = 105^\circ$ ,  $A = 1.26$ ;  
 $\Delta\theta = 113^\circ$ ,  $A = 1.22$ ; and  $\Delta\theta = 99^\circ$ ,  $A = 1.50$

# **Appendix C**

## **Graphs of Characteristic Directional Distributions**

---



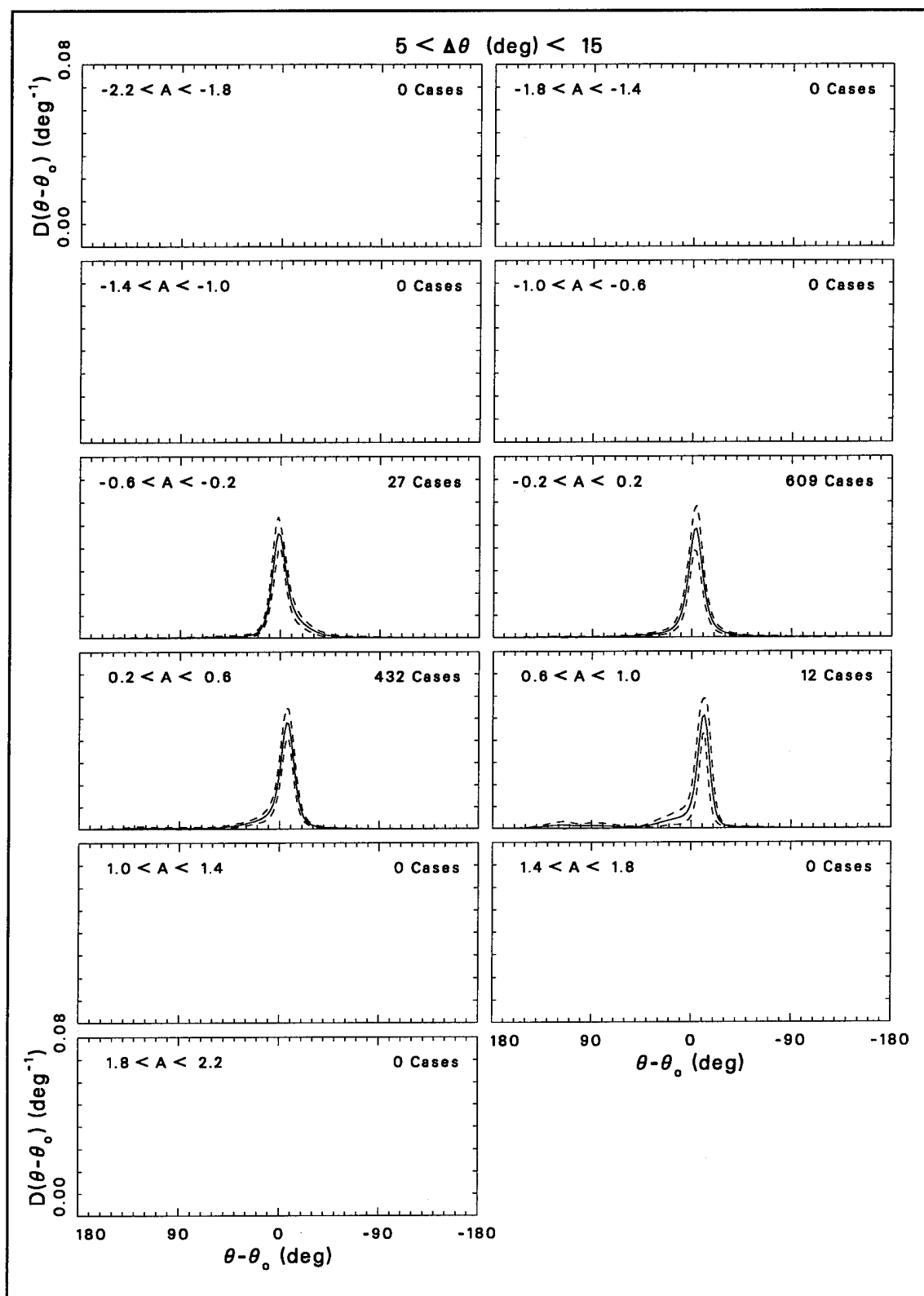


Figure C1. Distribution functions with  $\Delta\theta$  in the range 5 to 15 deg

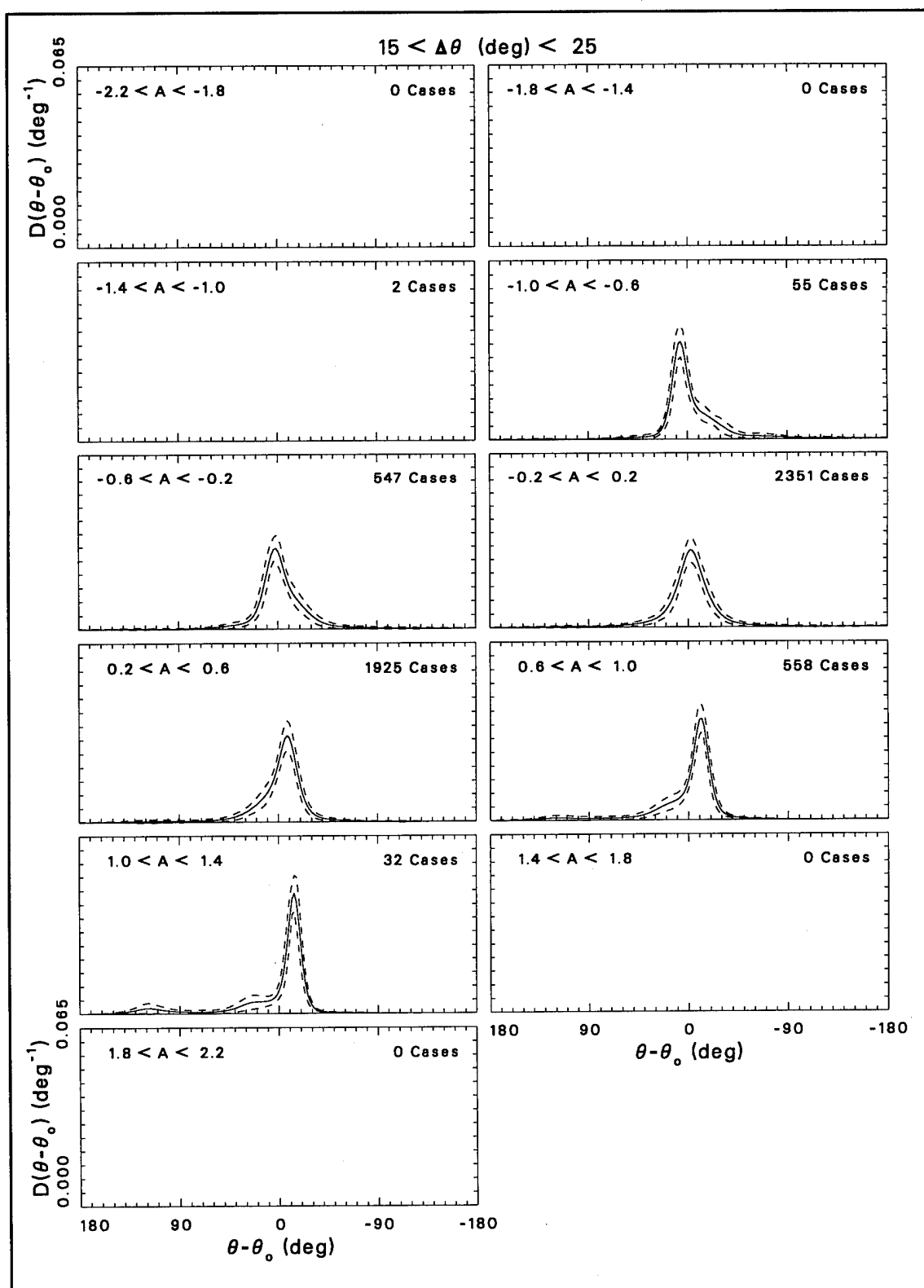


Figure C2. Distribution functions with  $\Delta\theta$  in the range 15 to 25 deg

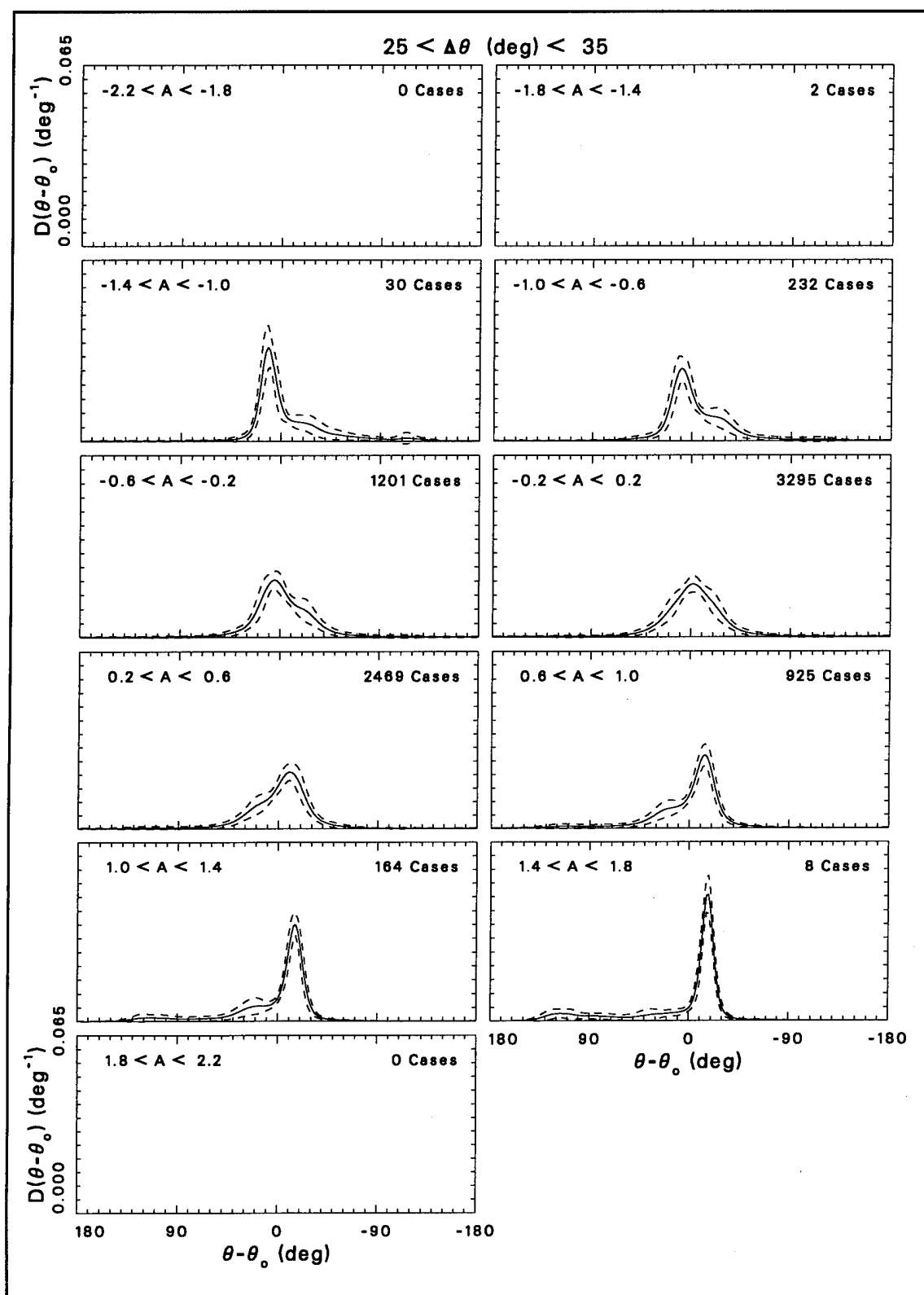


Figure C3. Distribution functions with  $\Delta\theta$  in the range 25 to 35 deg

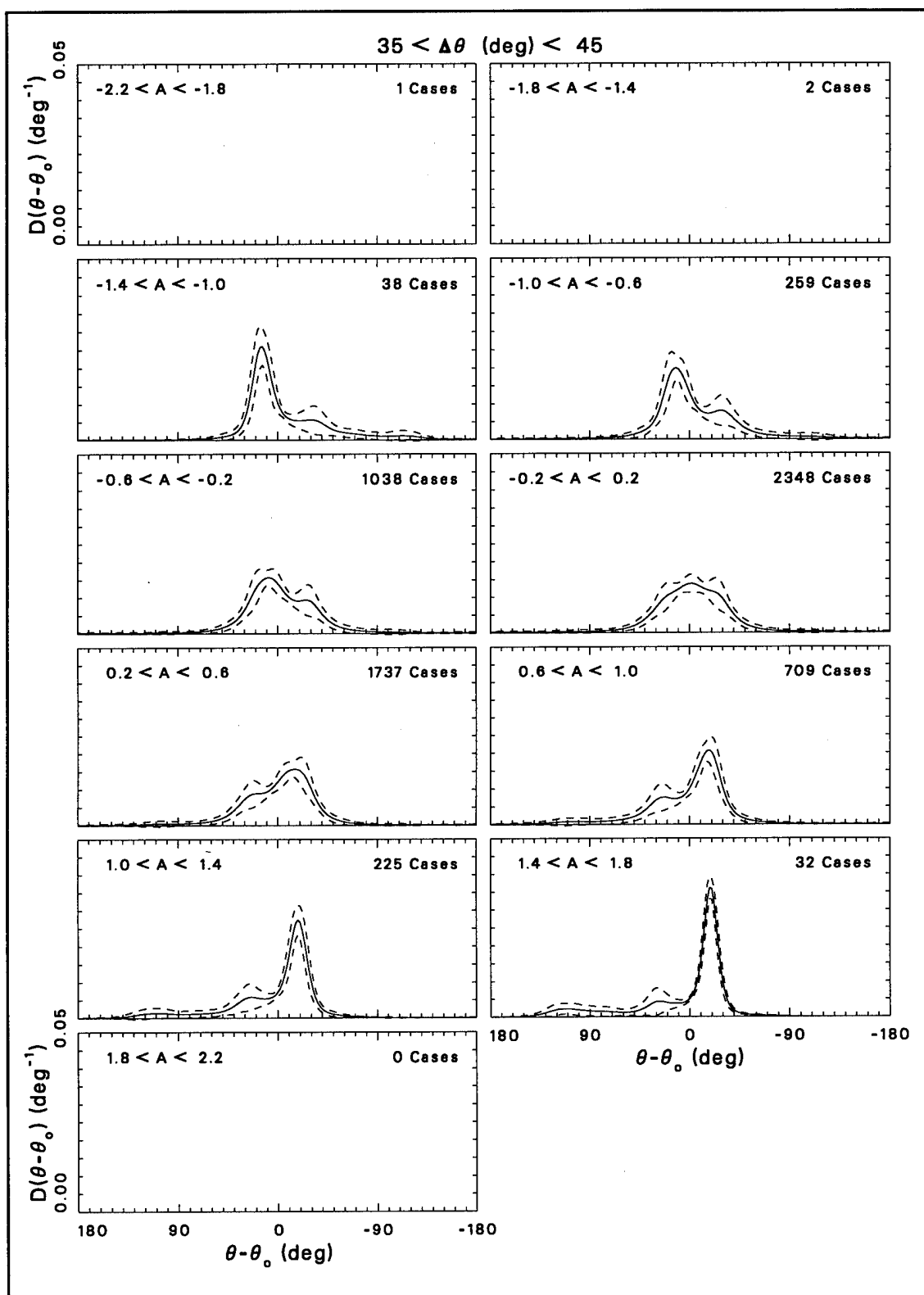


Figure C4. Distribution functions with  $\Delta\theta$  in the range 35 to 45 deg

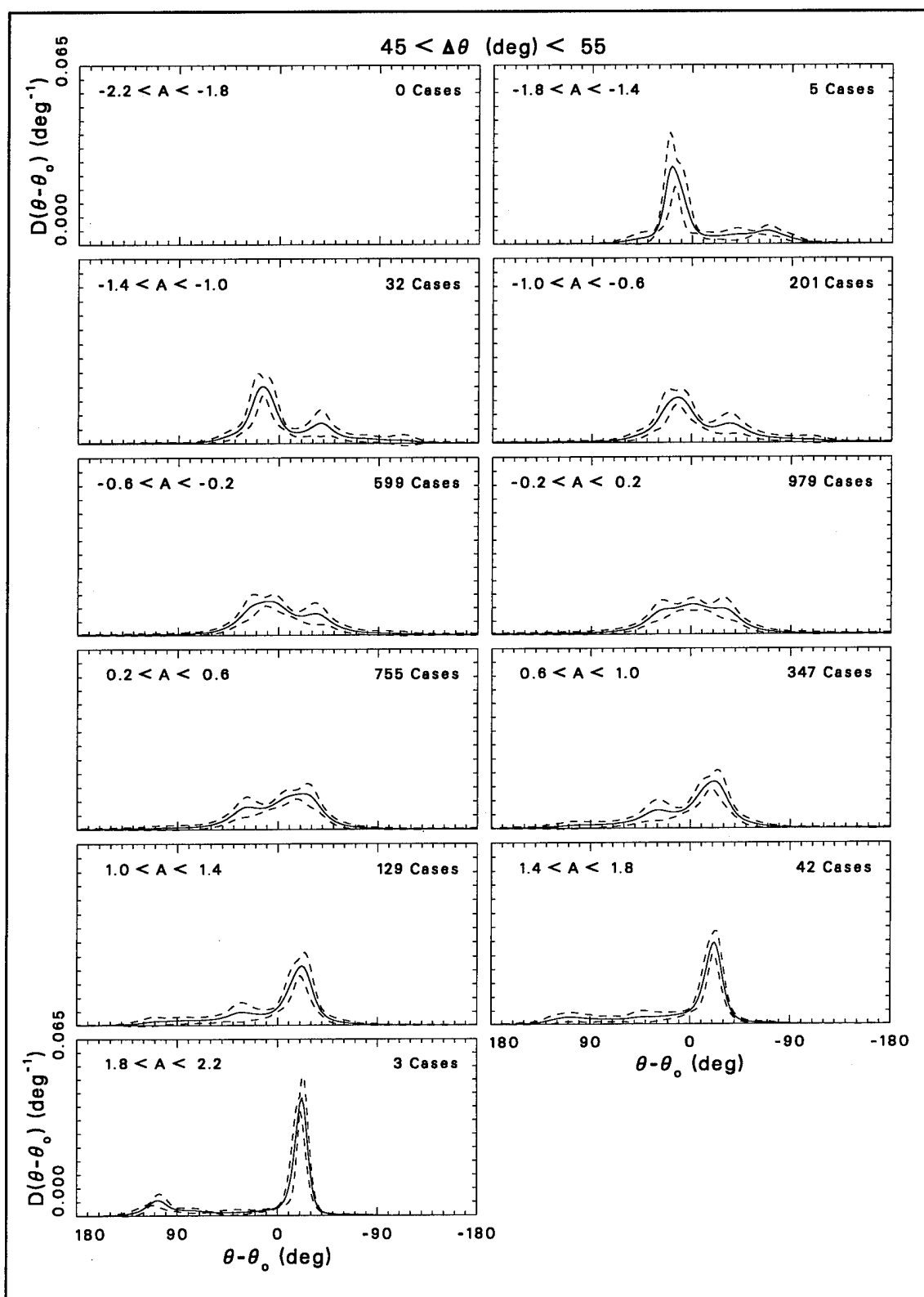


Figure C5. Distribution functions with  $\Delta\theta$  in the range 45 to 55 deg

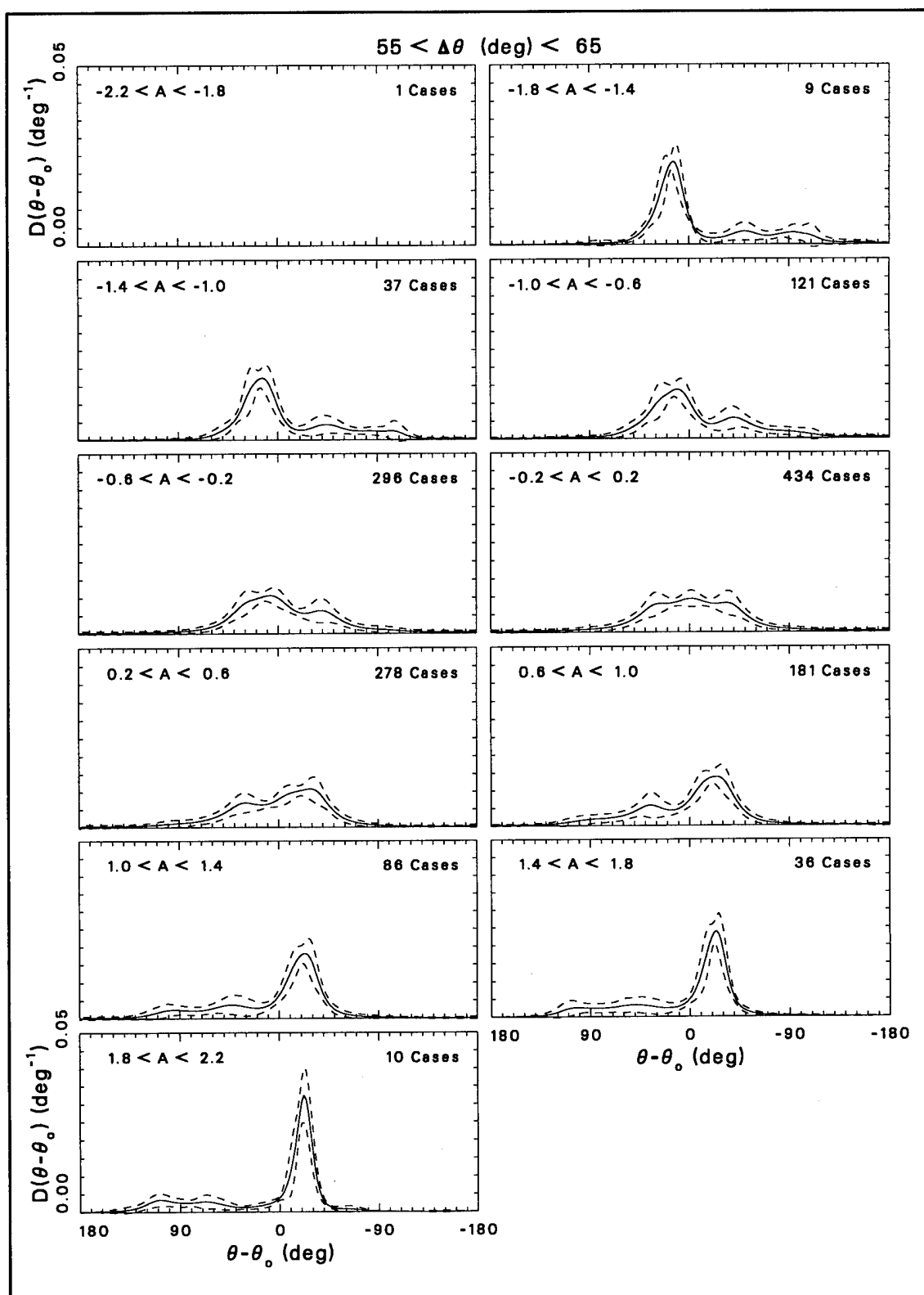


Figure C6. Distribution functions with  $\Delta\theta$  in the range 55 to 65 deg

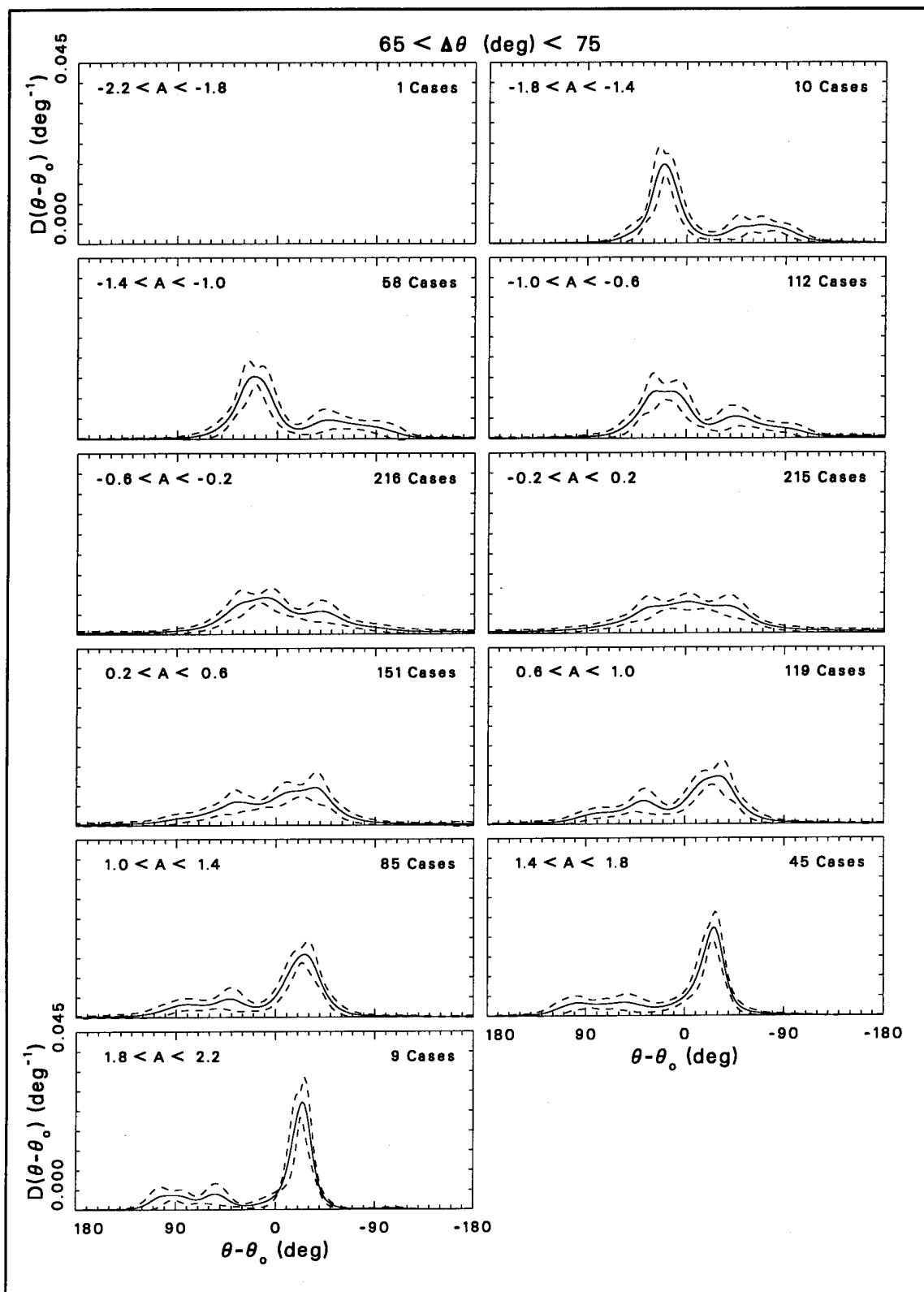


Figure C7. Distribution functions with  $\Delta\theta$  in the range 65 to 75 deg

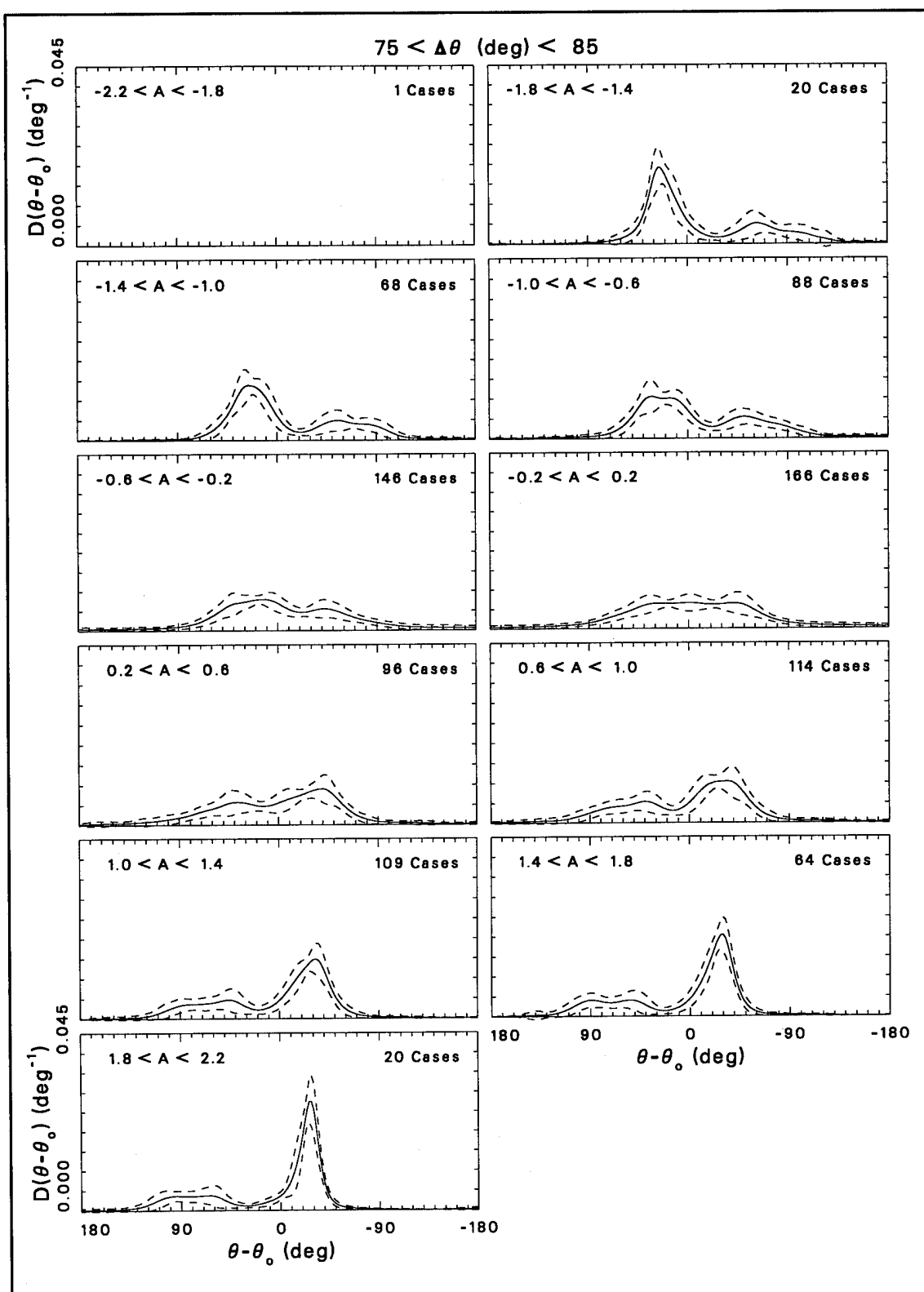


Figure C8. Distribution functions with  $\Delta\theta$  in the range 75 to 85 deg



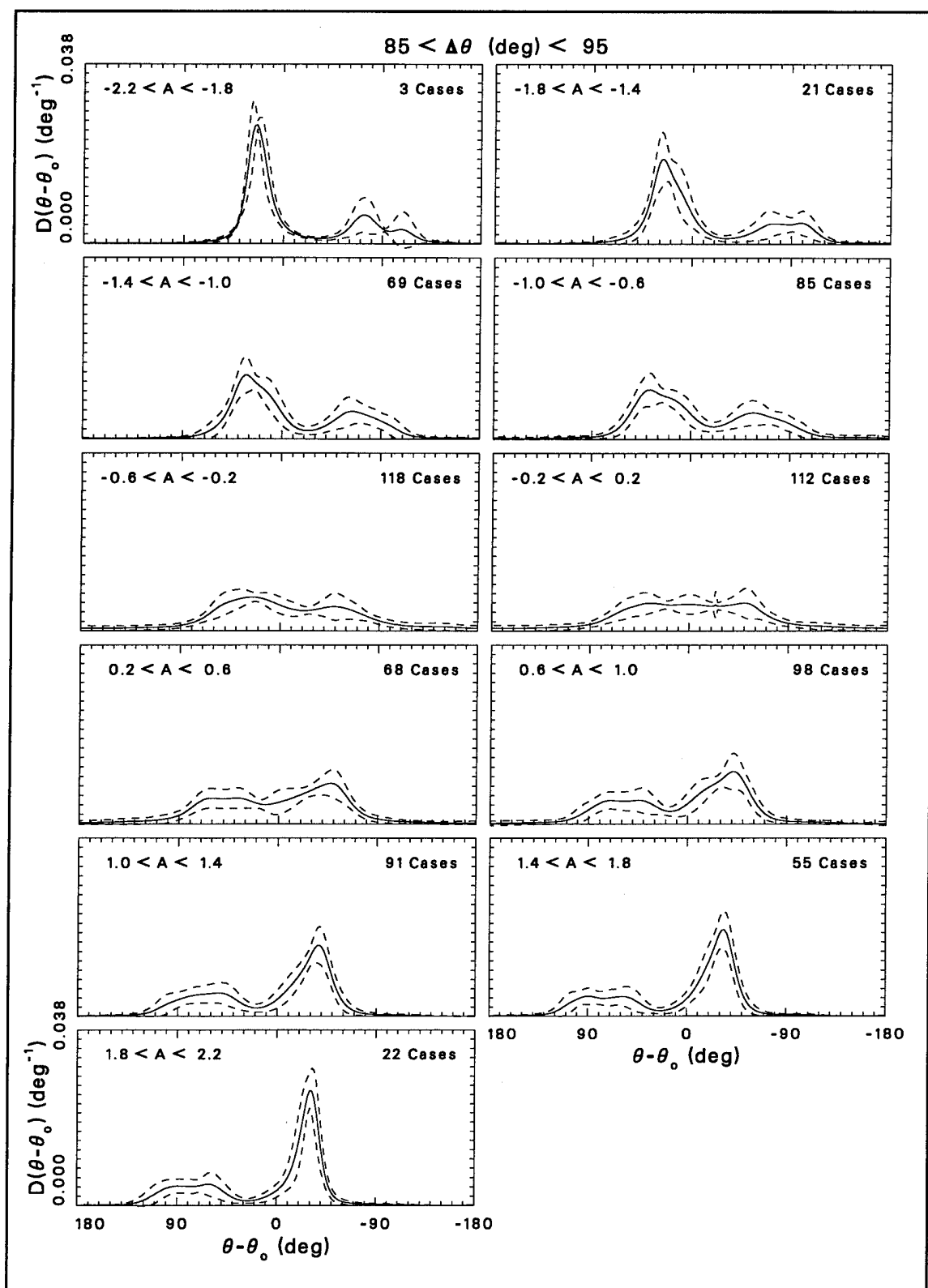


Figure C9. Distribution functions with  $\Delta\theta$  in the range 85 to 95 deg

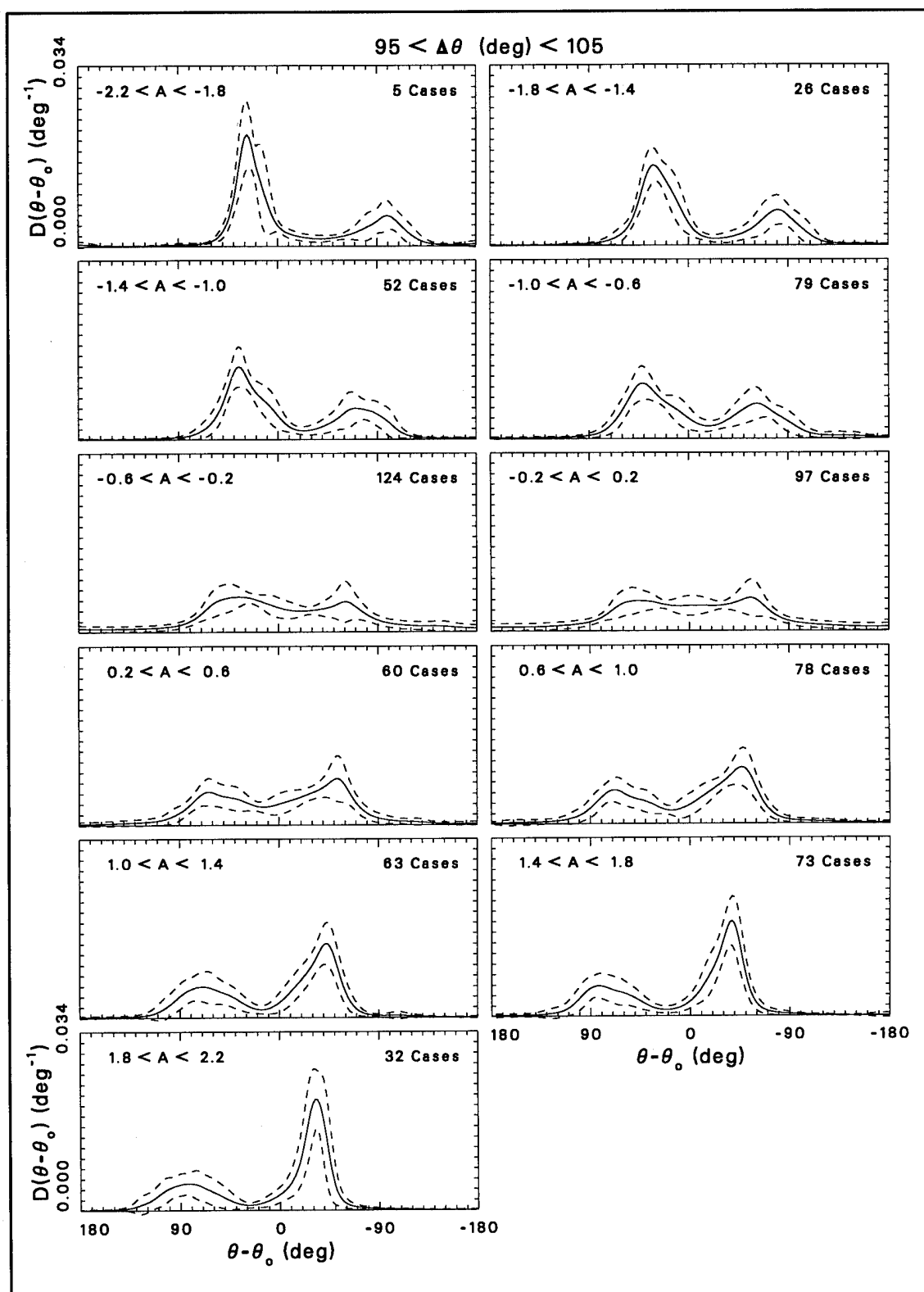


Figure C10. Distribution functions with  $\Delta\theta$  in the range 95 to 105 deg

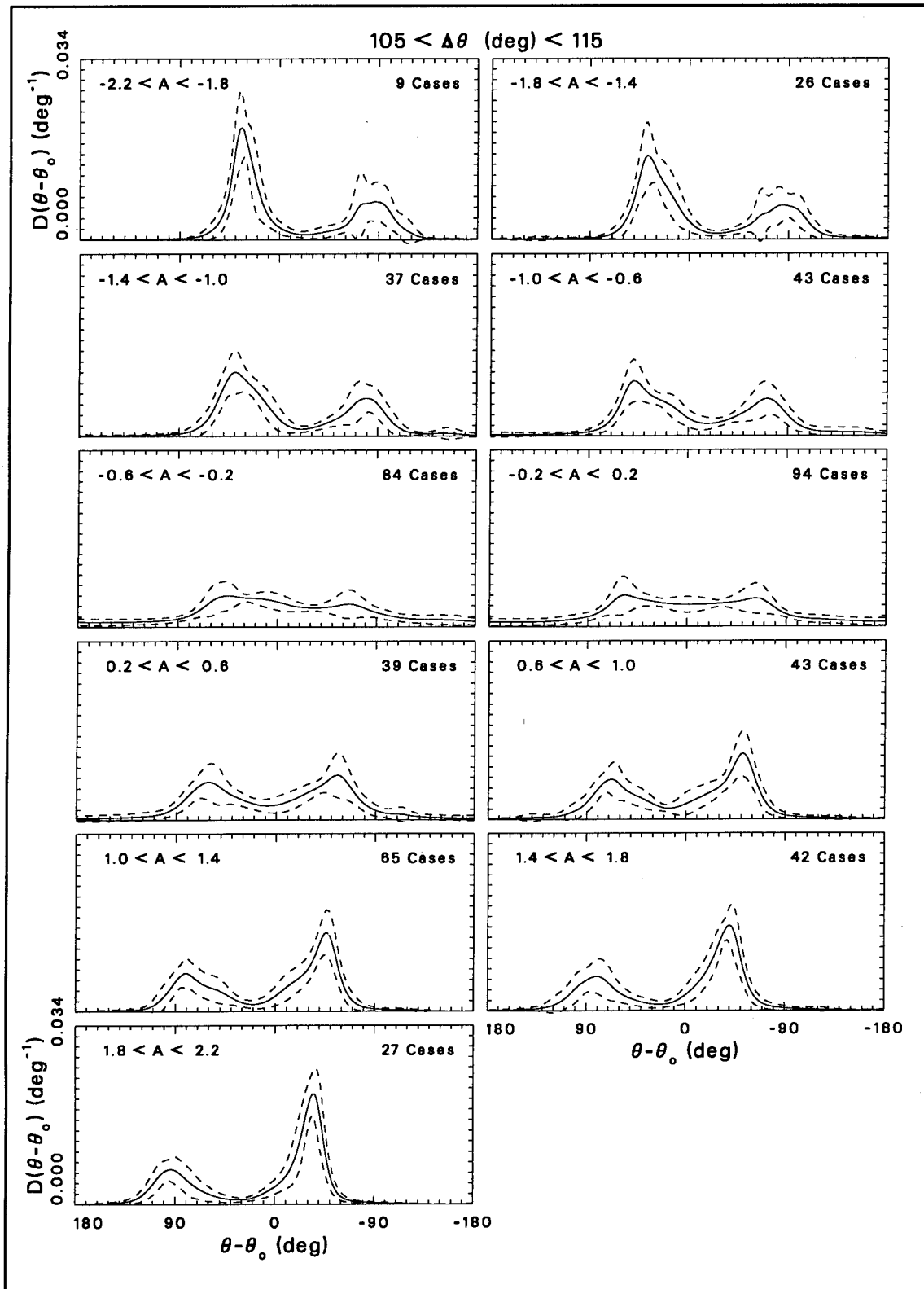


Figure C11. Distribution functions with  $\Delta\theta$  in the range 105 to 115 deg

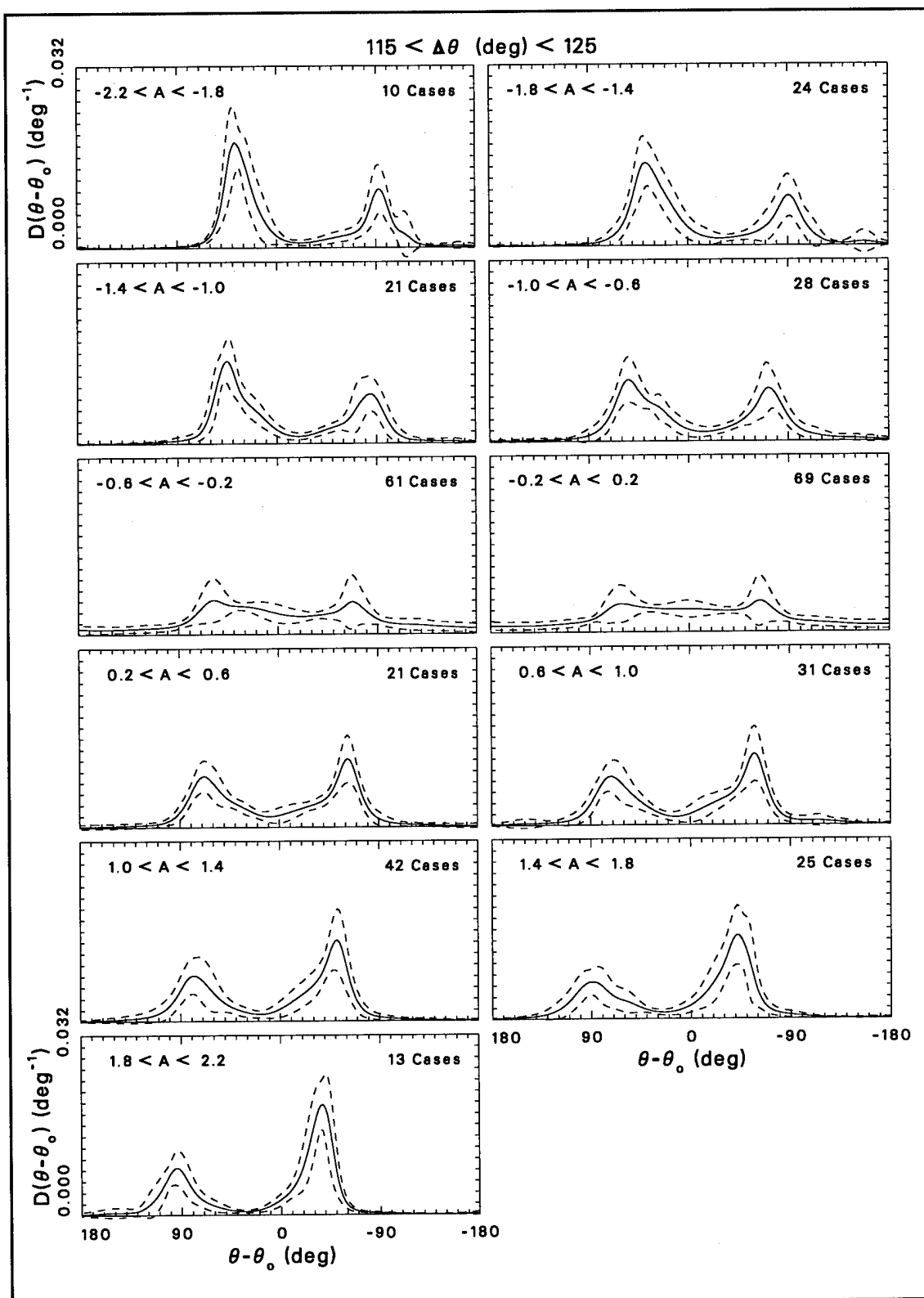


Figure C12. Distribution functions with  $\Delta\theta$  in the range 115 to 125 deg

# **Appendix D**

## **Graphs of Test Results**

---

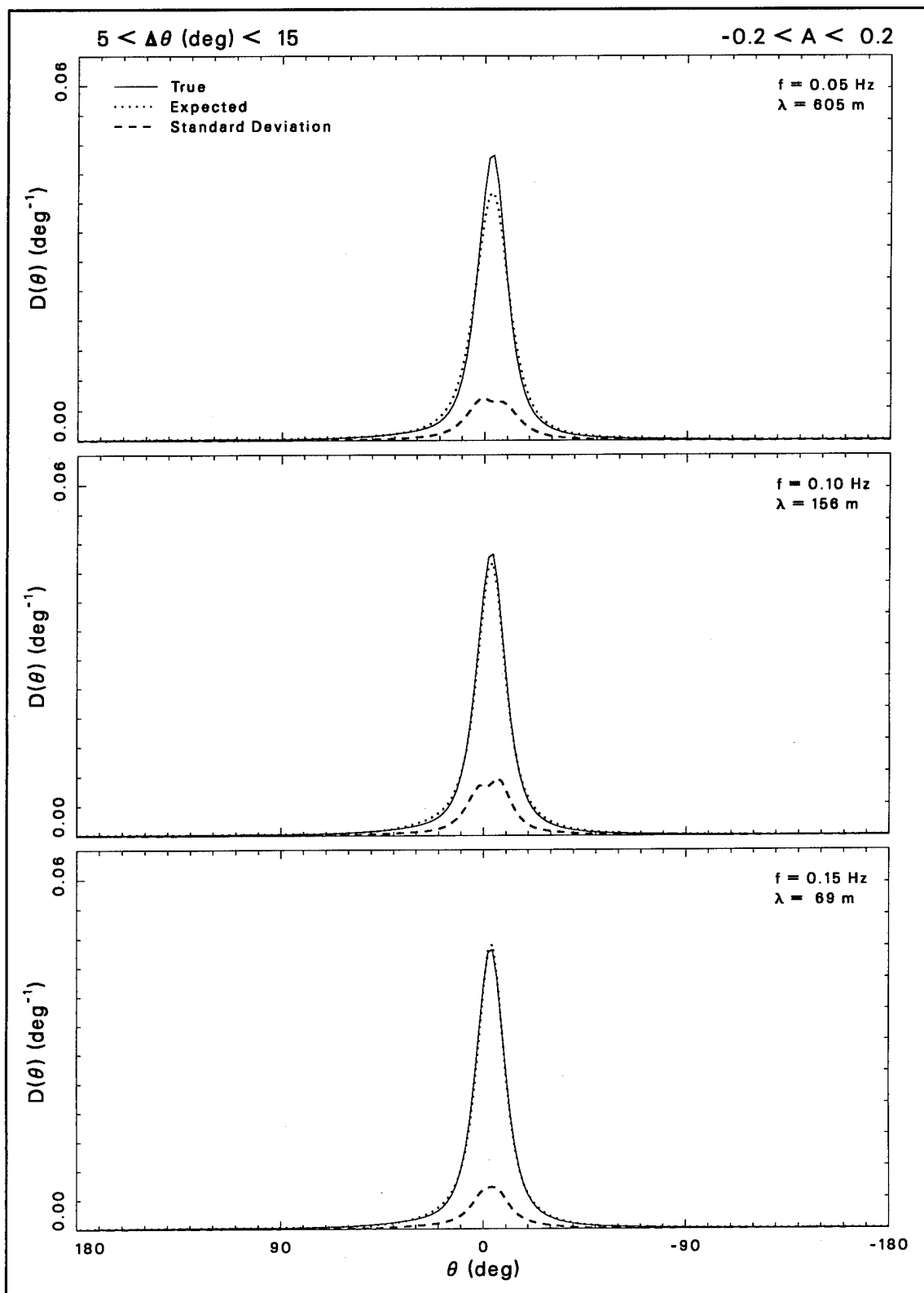


Figure D1. Test results for  $5 < \Delta\theta \text{ (deg)} < 15$ , and  $-0.2 < A < 0.2$

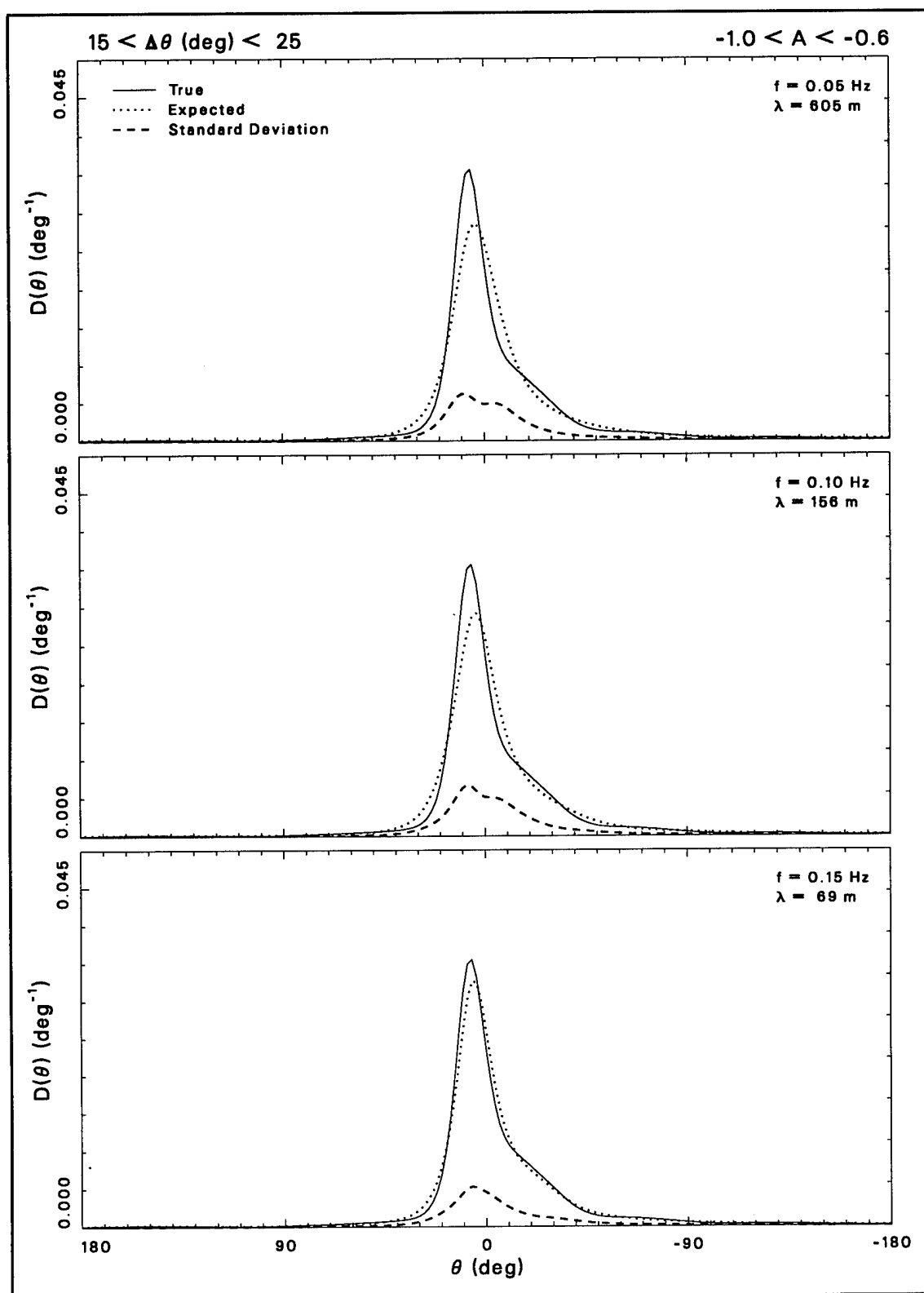


Figure D2. Test results for  $15 < \Delta\theta$  (deg) < 25, and  $-1.0 < A < -0.6$

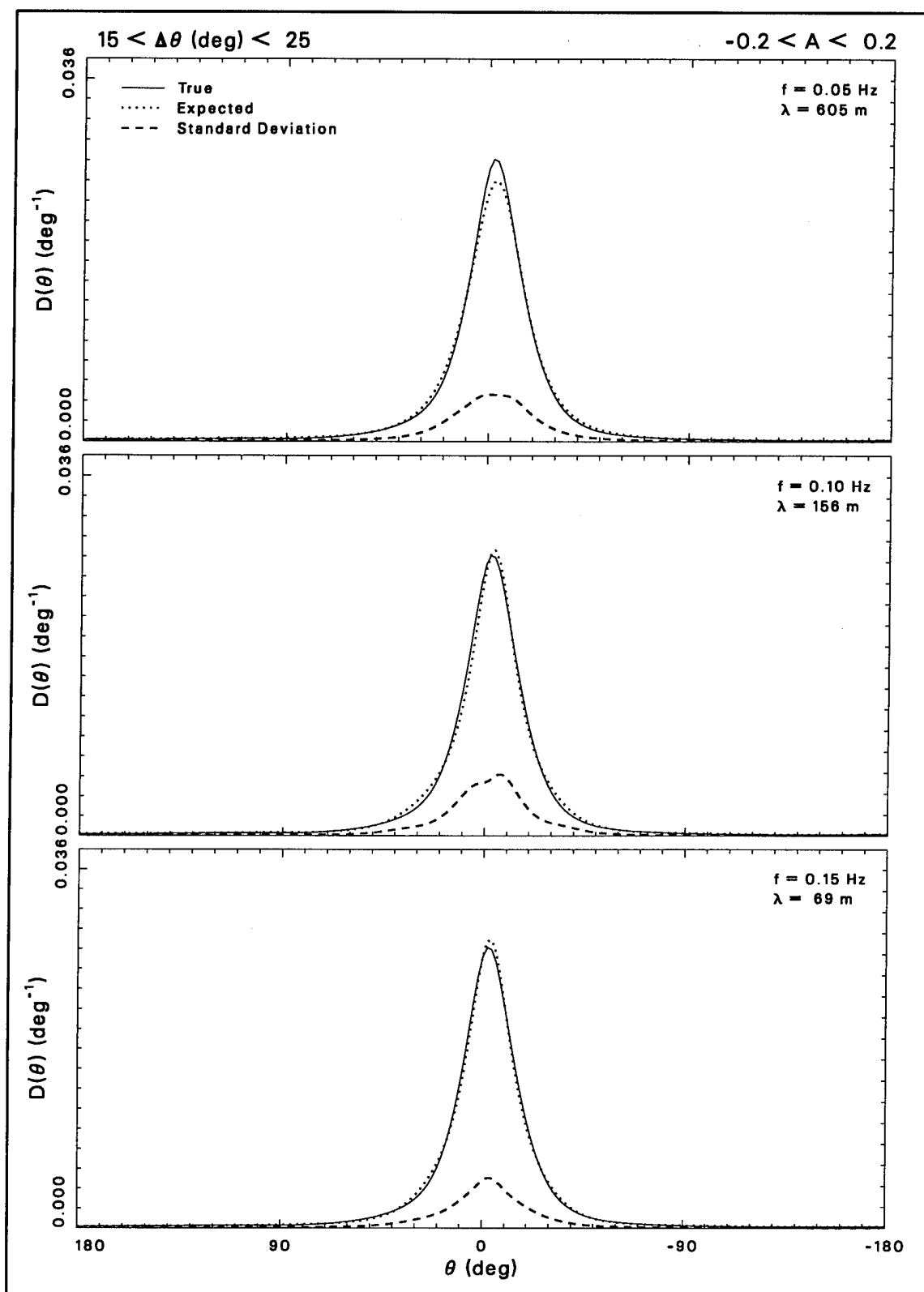


Figure D3. Test results for  $15 < \Delta\theta$  (deg)  $< 25$ , and  $-0.2 < A < 0.2$



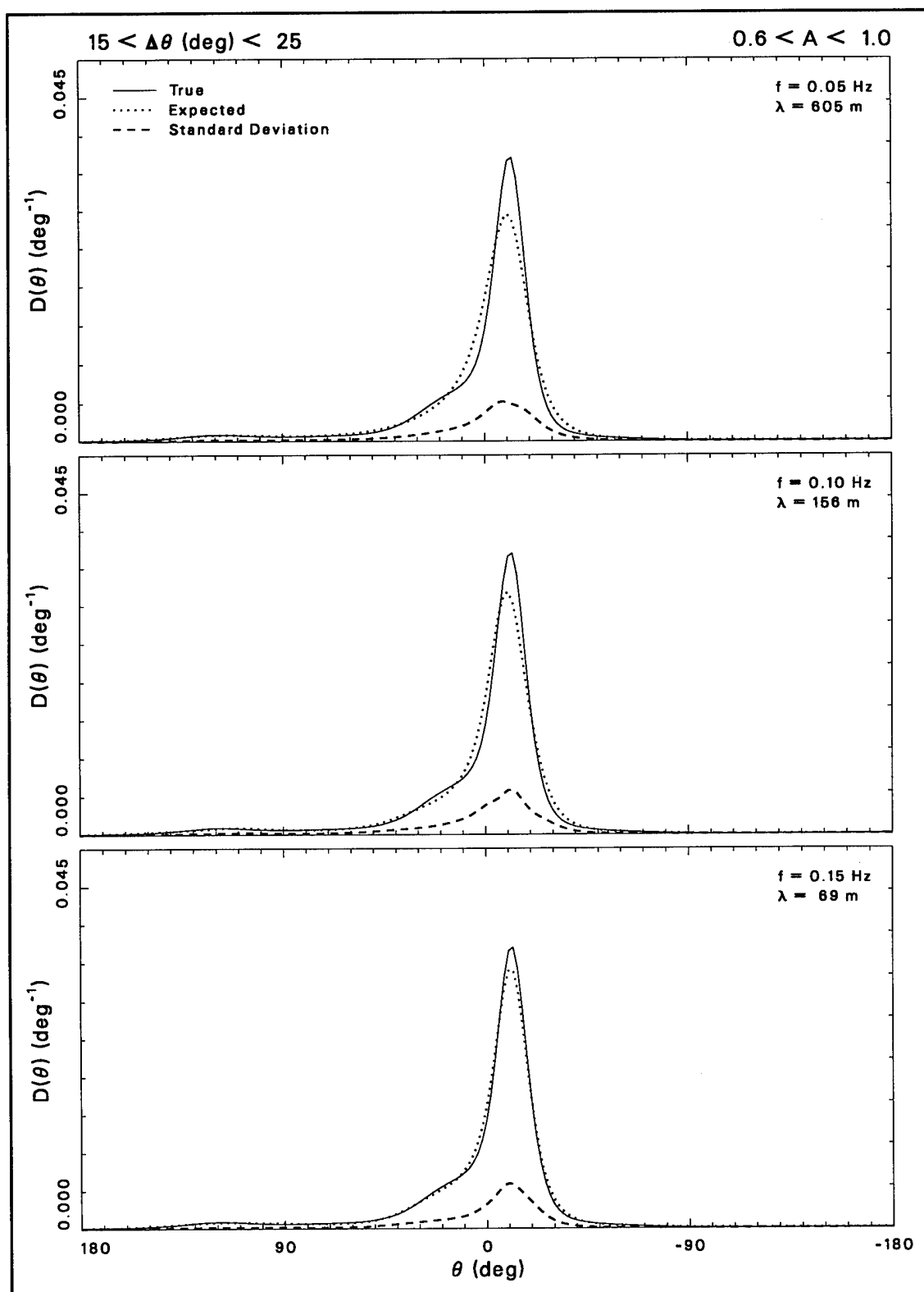


Figure D4. Test results for  $15 < \Delta\theta$  (deg) < 25, and  $0.6 < A < 1.0$

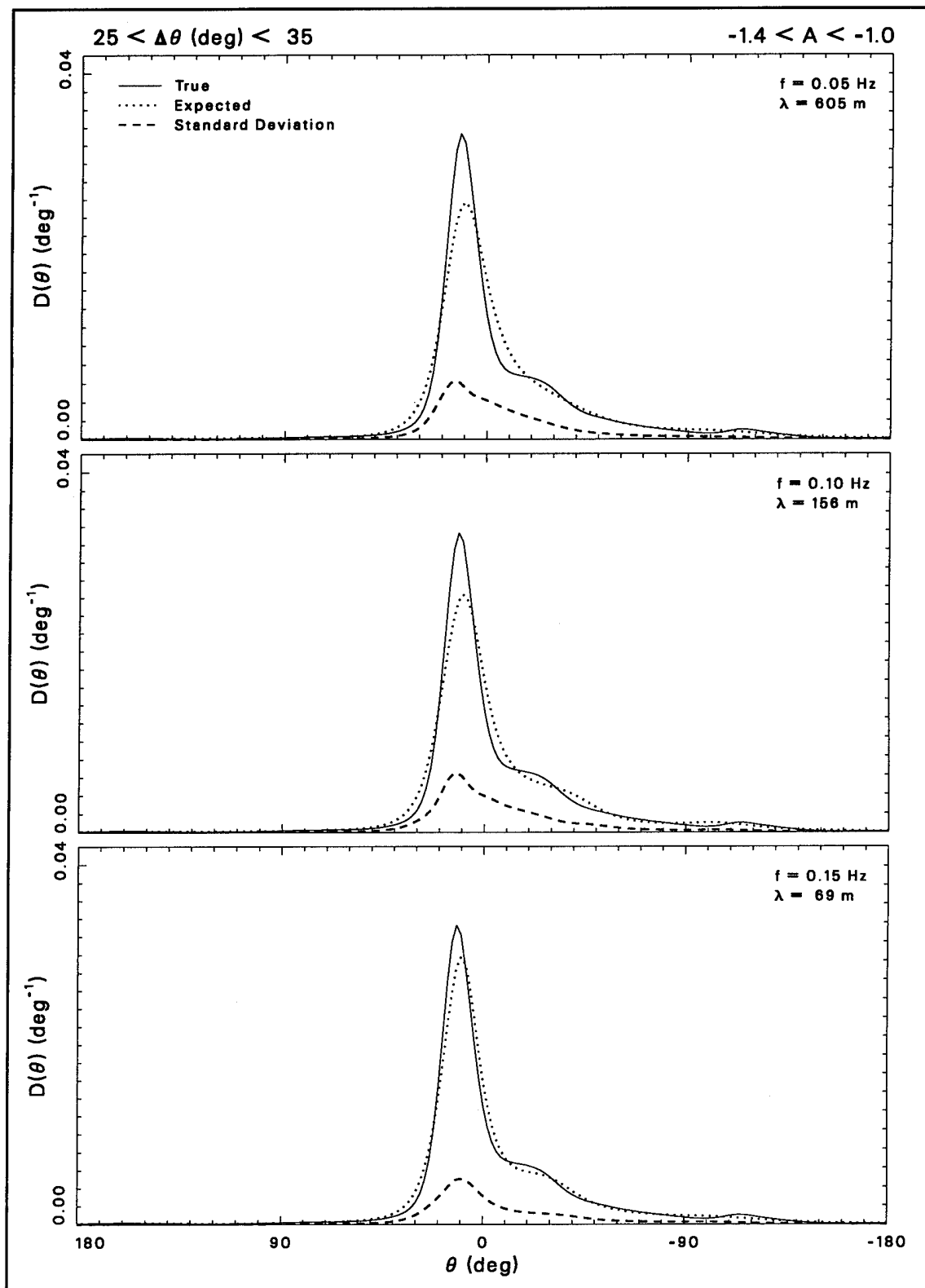


Figure D5. Test results for  $25 < \Delta\theta$  (deg)  $< 35$ , and  $-1.4 < A < -1.0$

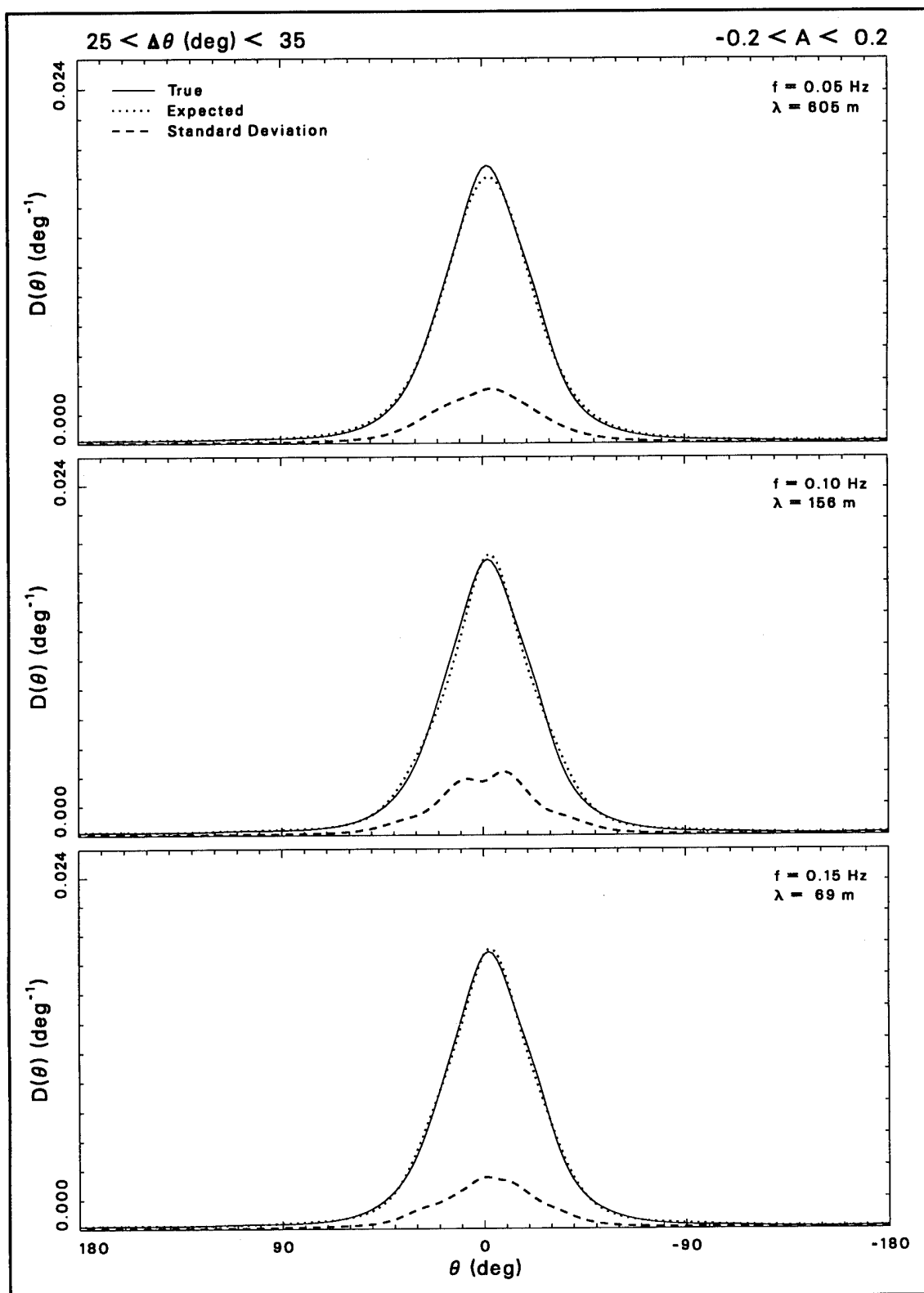


Figure D6. Test results for 25 <  $\Delta\theta$  (deg) < 35, and -0.2 < A < 0.2

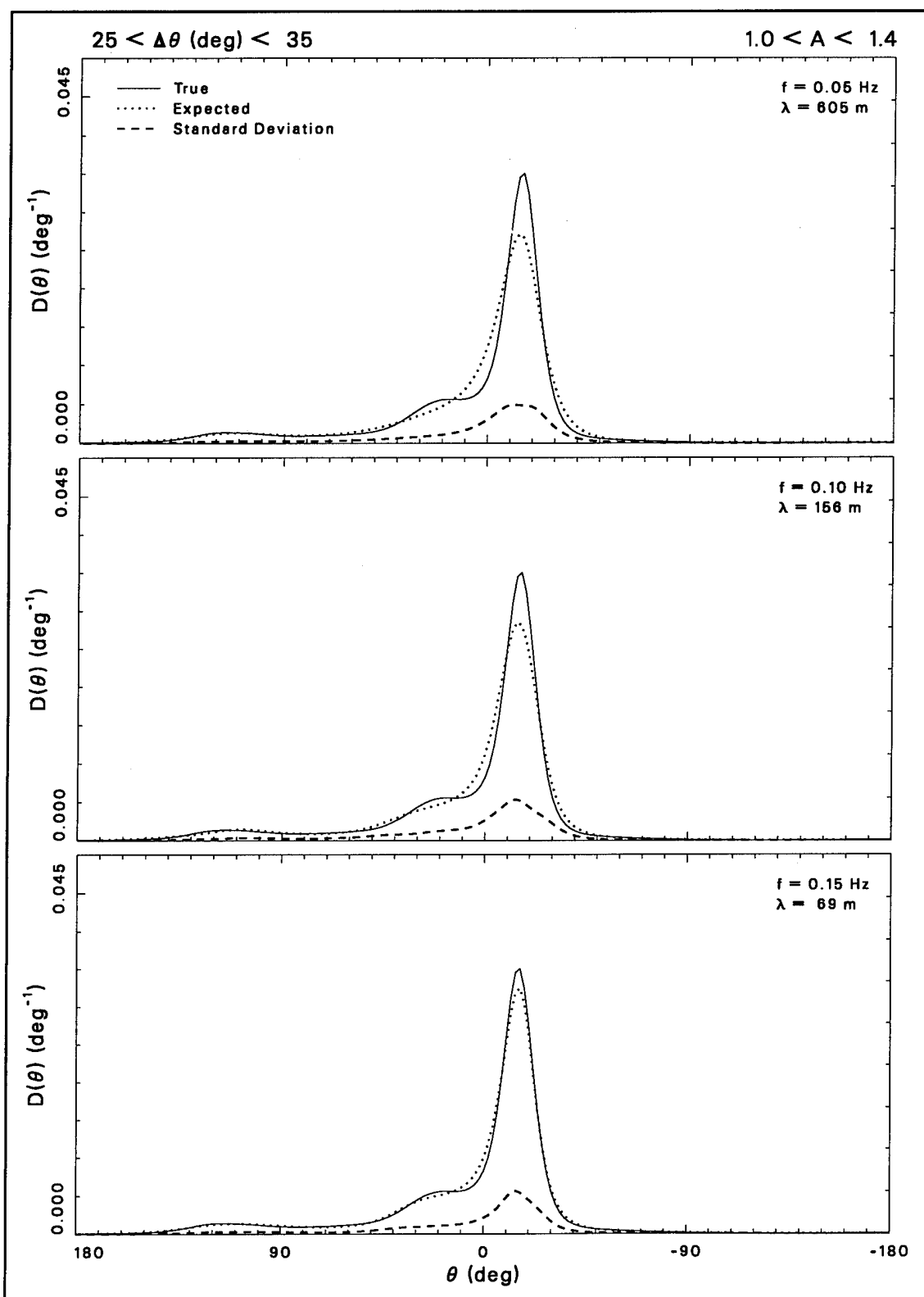


Figure D7. Test results for  $25 < \Delta\theta$  (deg) < 35, and  $1.0 < A < 1.4$

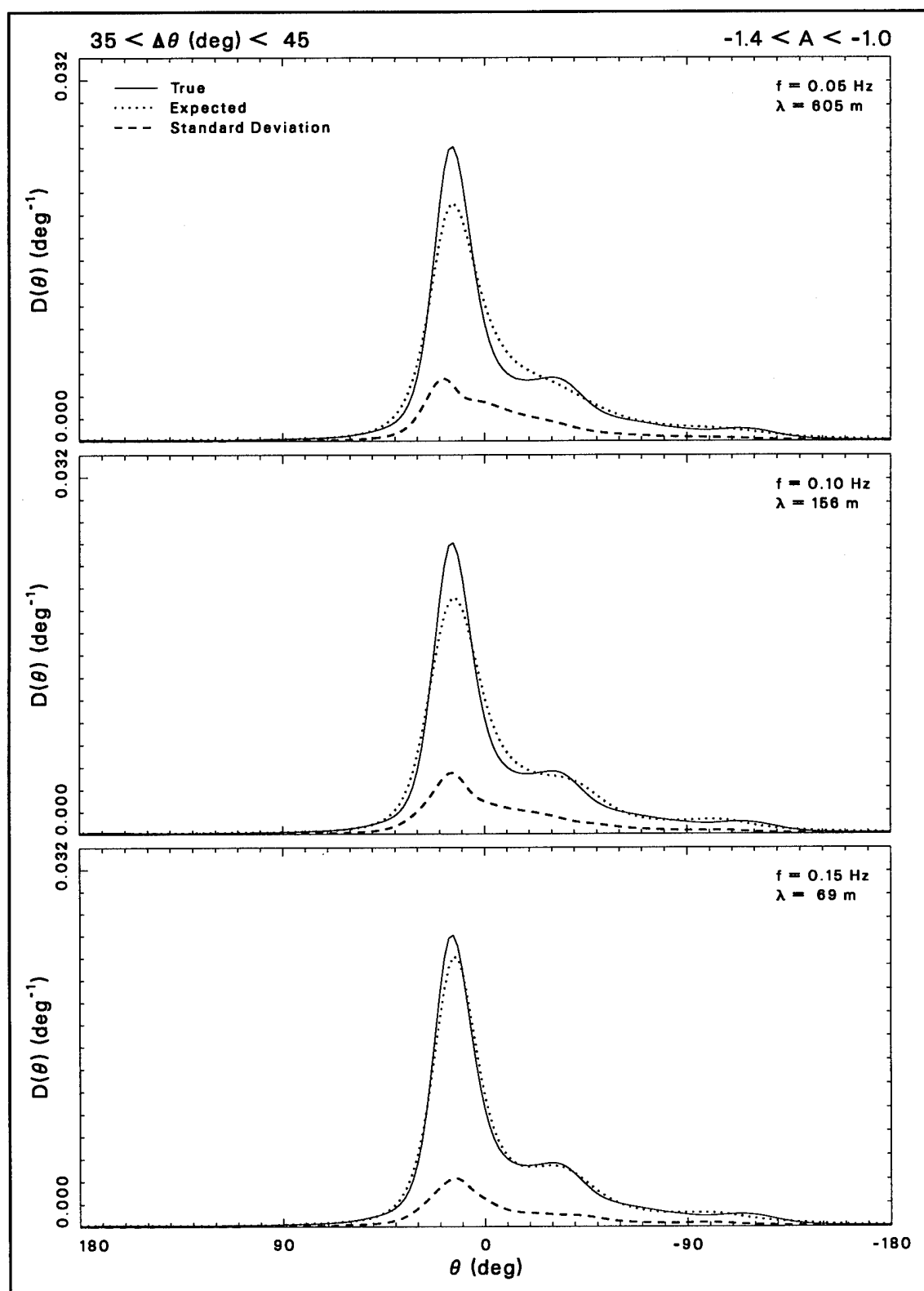


Figure D8. Test results for 35 <  $\Delta\theta$  (deg) < 45, and -1.4 < A < -1.0

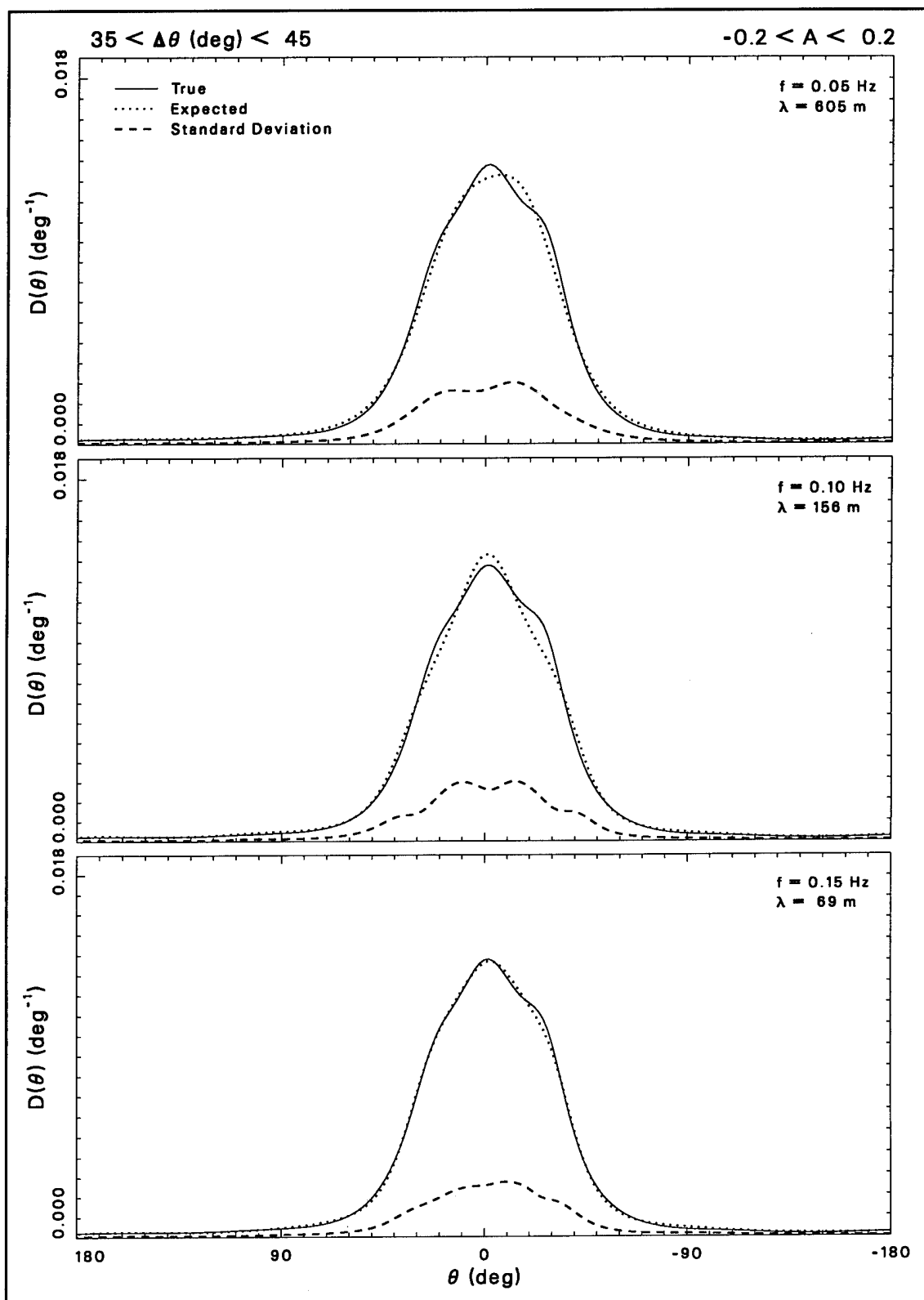


Figure D9. Test results for 35 <  $\Delta\theta$  (deg) < 45, and -0.2 < A < 0.2

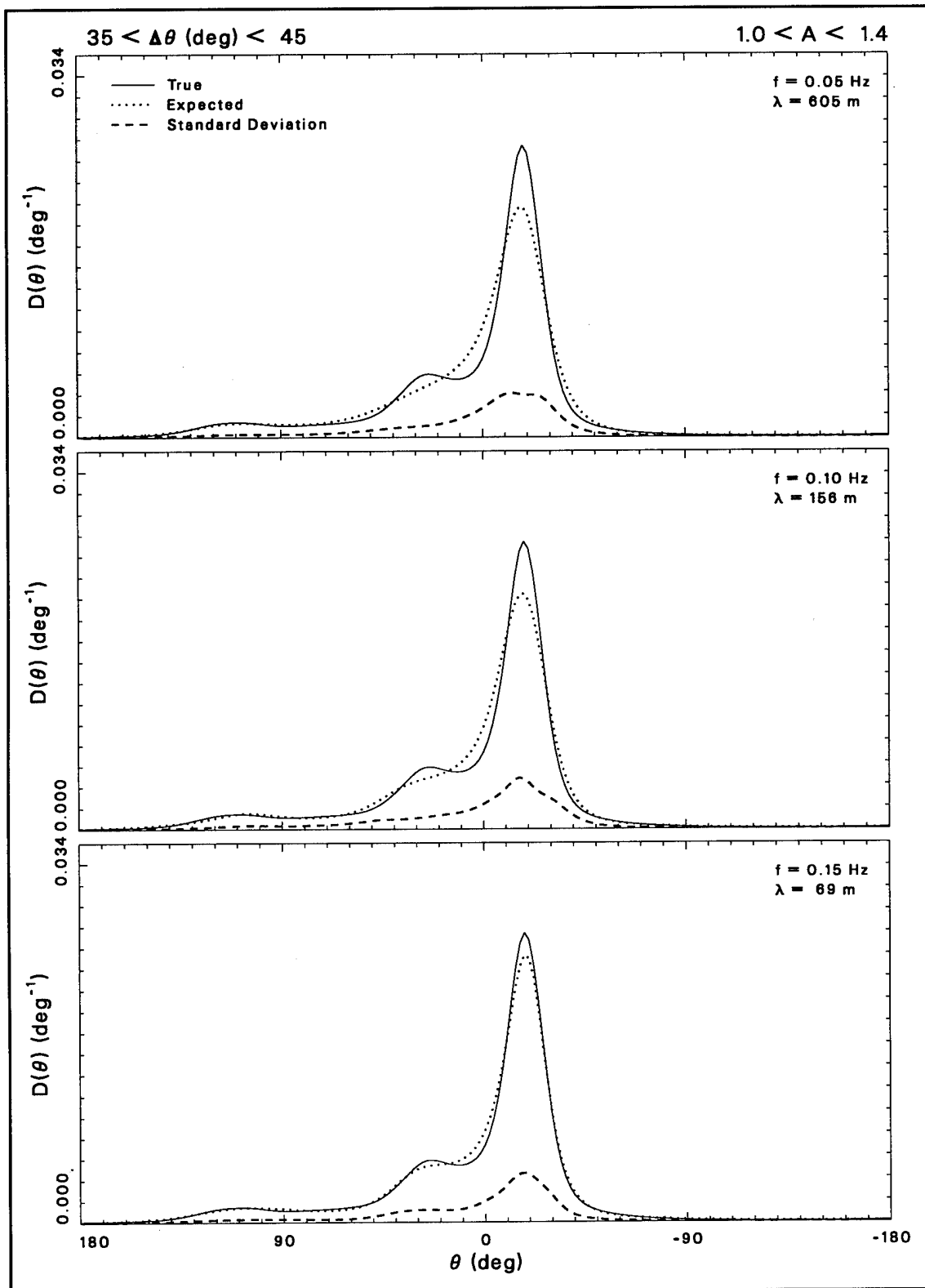


Figure D10. Test results for  $35 < \Delta\theta$  (deg) < 45, and  $1.0 < A < 1.4$

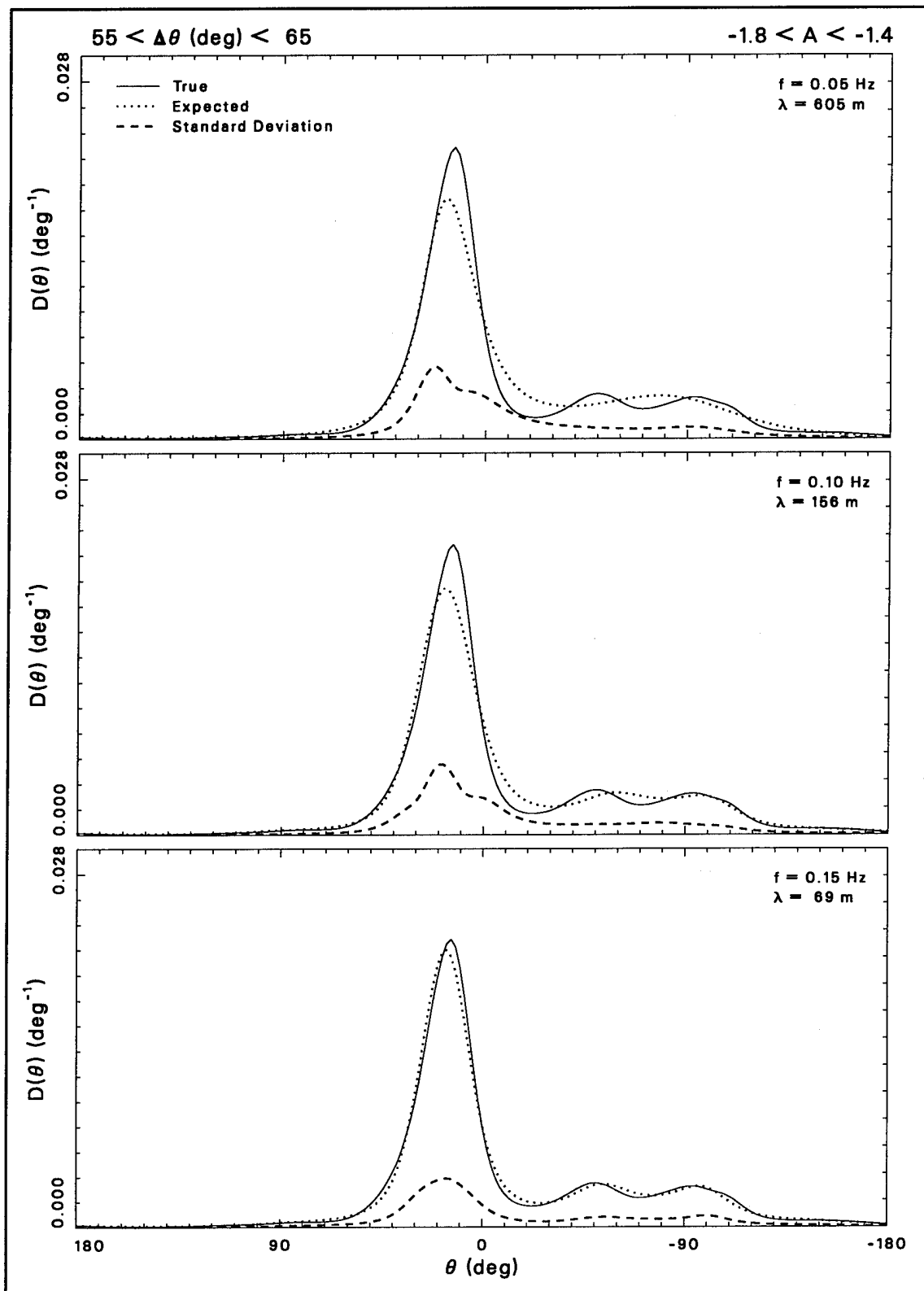


Figure D11. Test results for  $55 < \Delta\theta$  (deg)  $< 65$ , and  $-1.8 < A < -1.4$



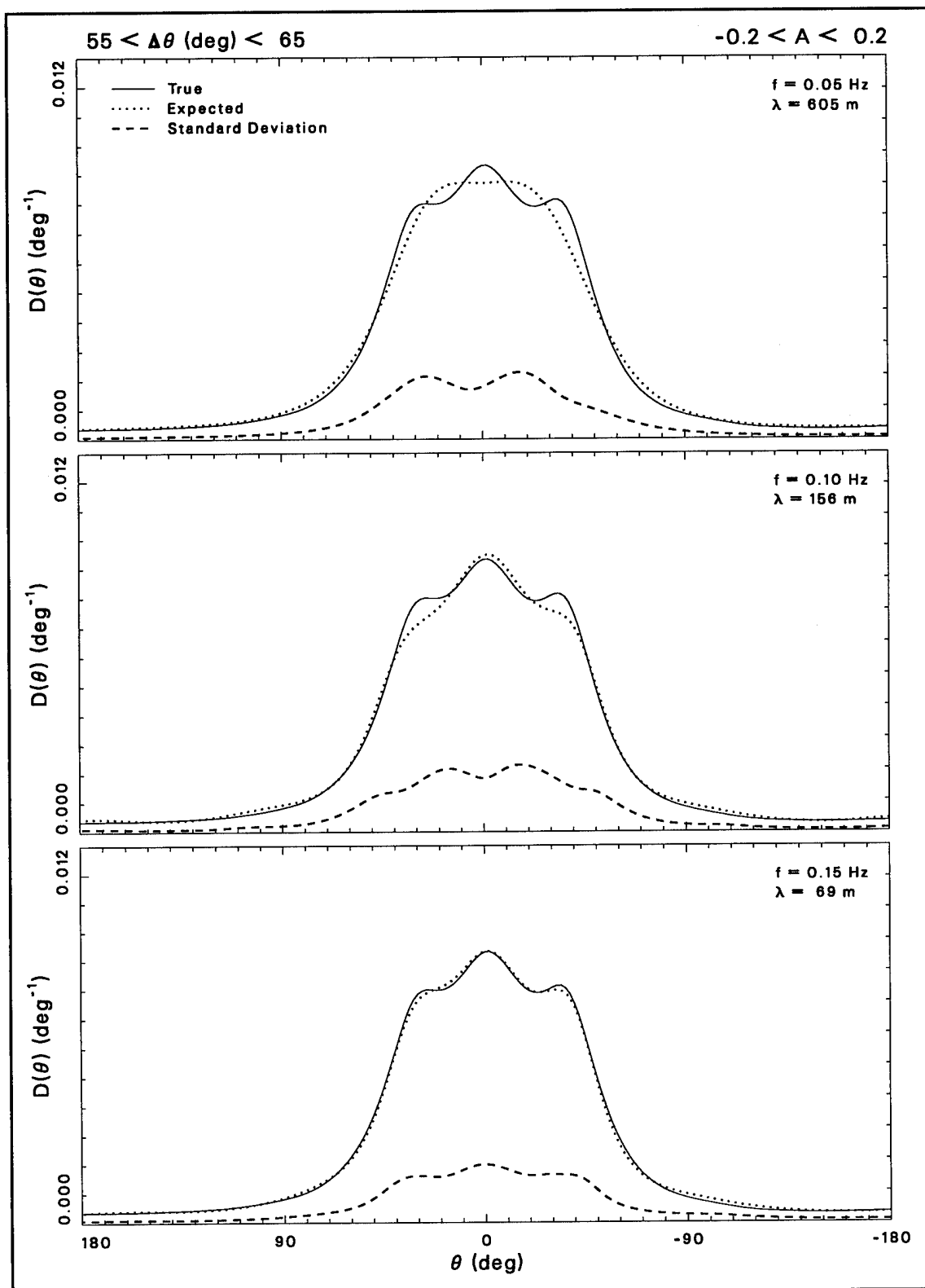


Figure D12. Test results for  $55 < \Delta\theta$  (deg)  $< 65$ , and  $-0.2 < A < 0.2$

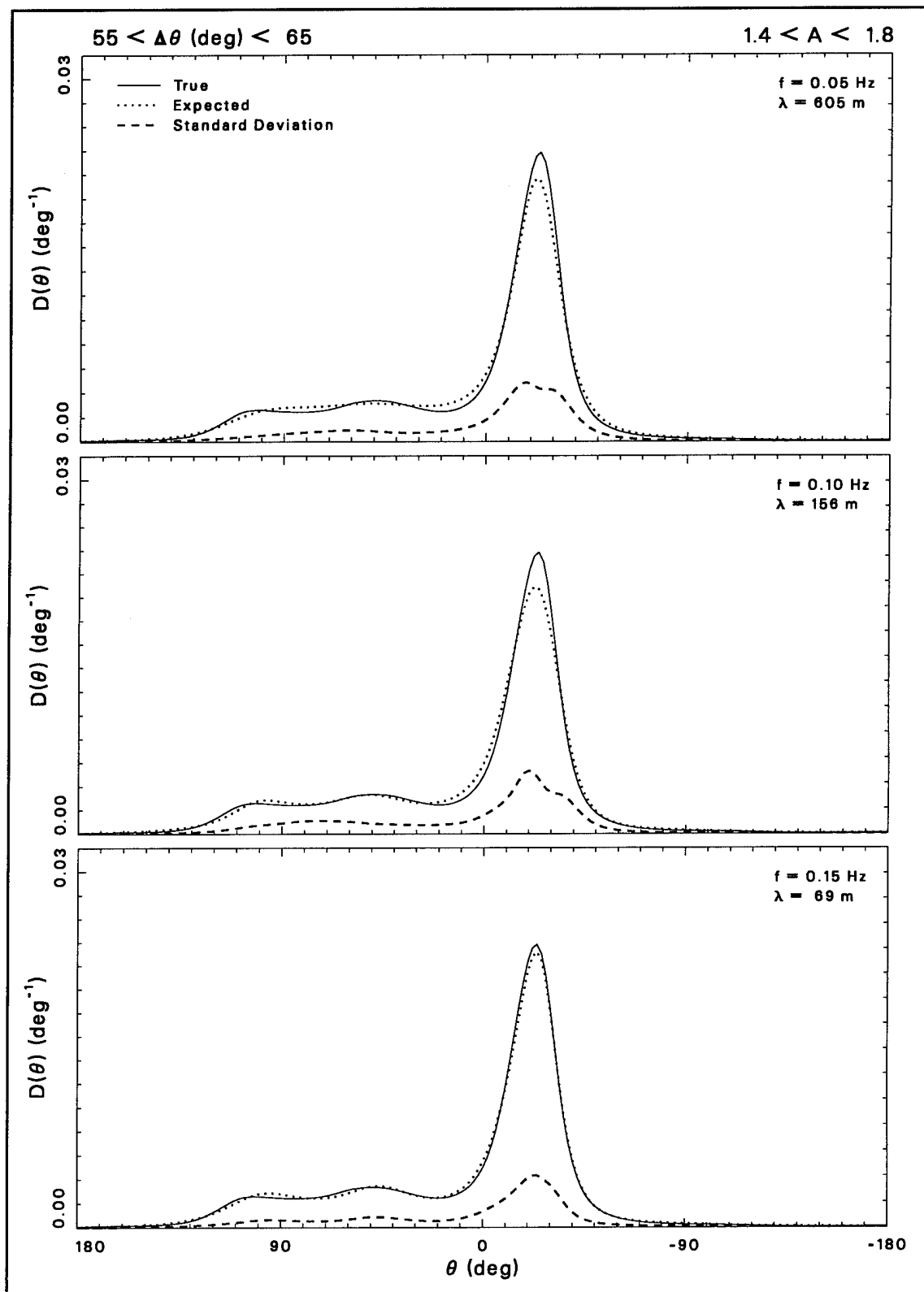


Figure D13. Test results for 55 <  $\Delta\theta$  (deg) < 65, and 1.4 < A < 1.8

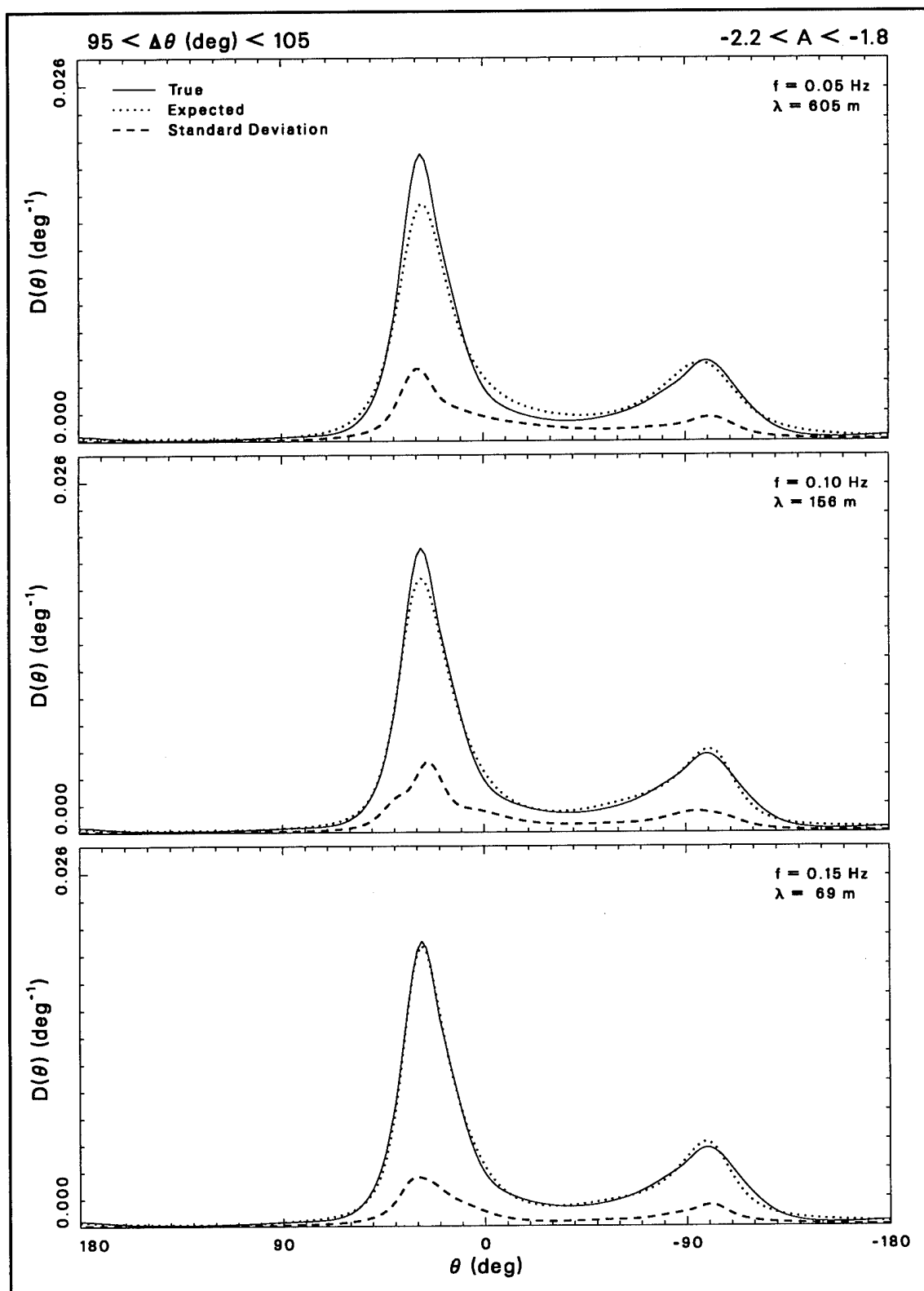


Figure D14. Test results for  $95 < \Delta\theta$  (deg) < 105, and  $-2.2 < A < -1.8$

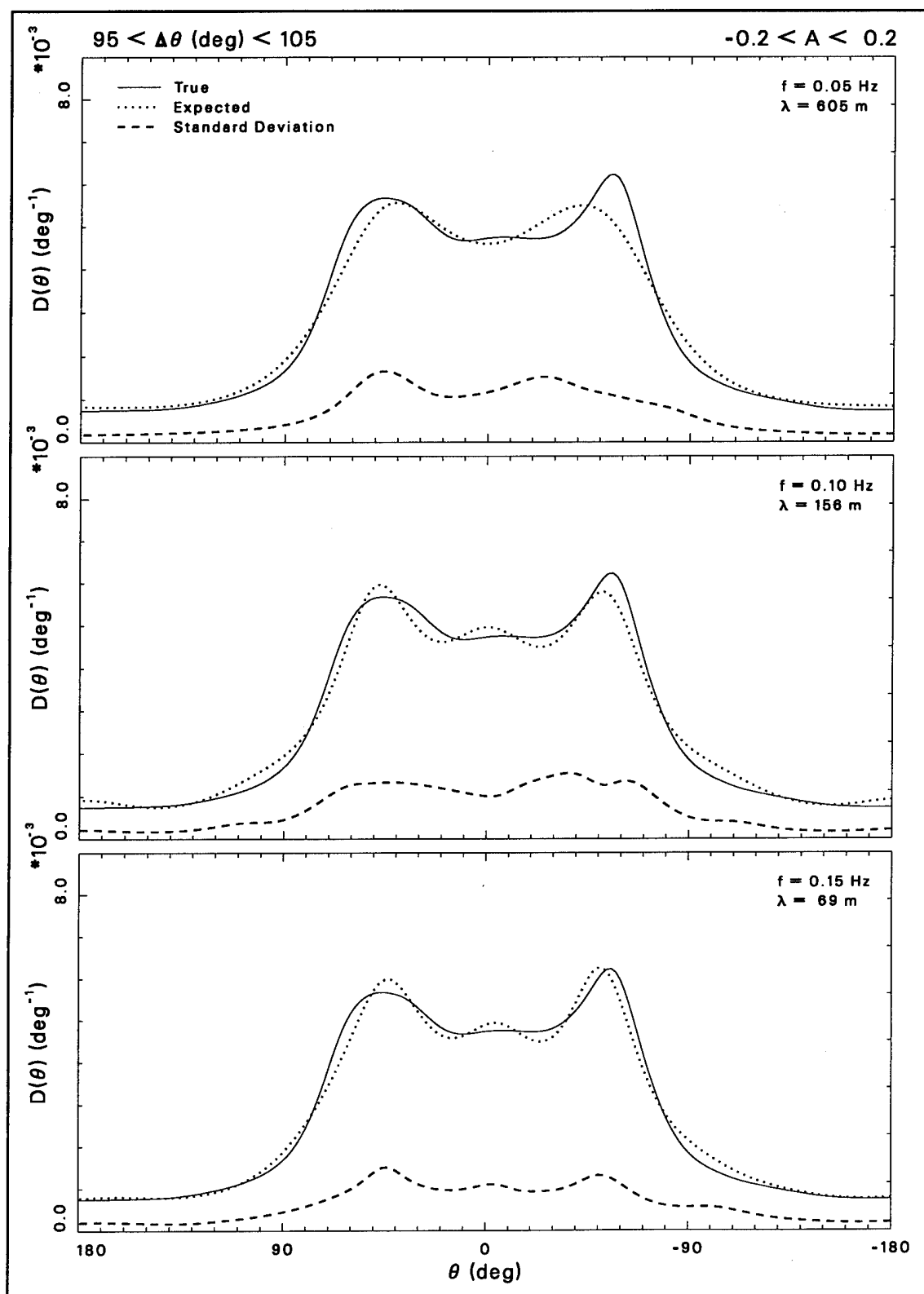


Figure D15. Test results for  $95 < \Delta\theta$  (deg) < 105, and  $-0.2 < A < 0.2$

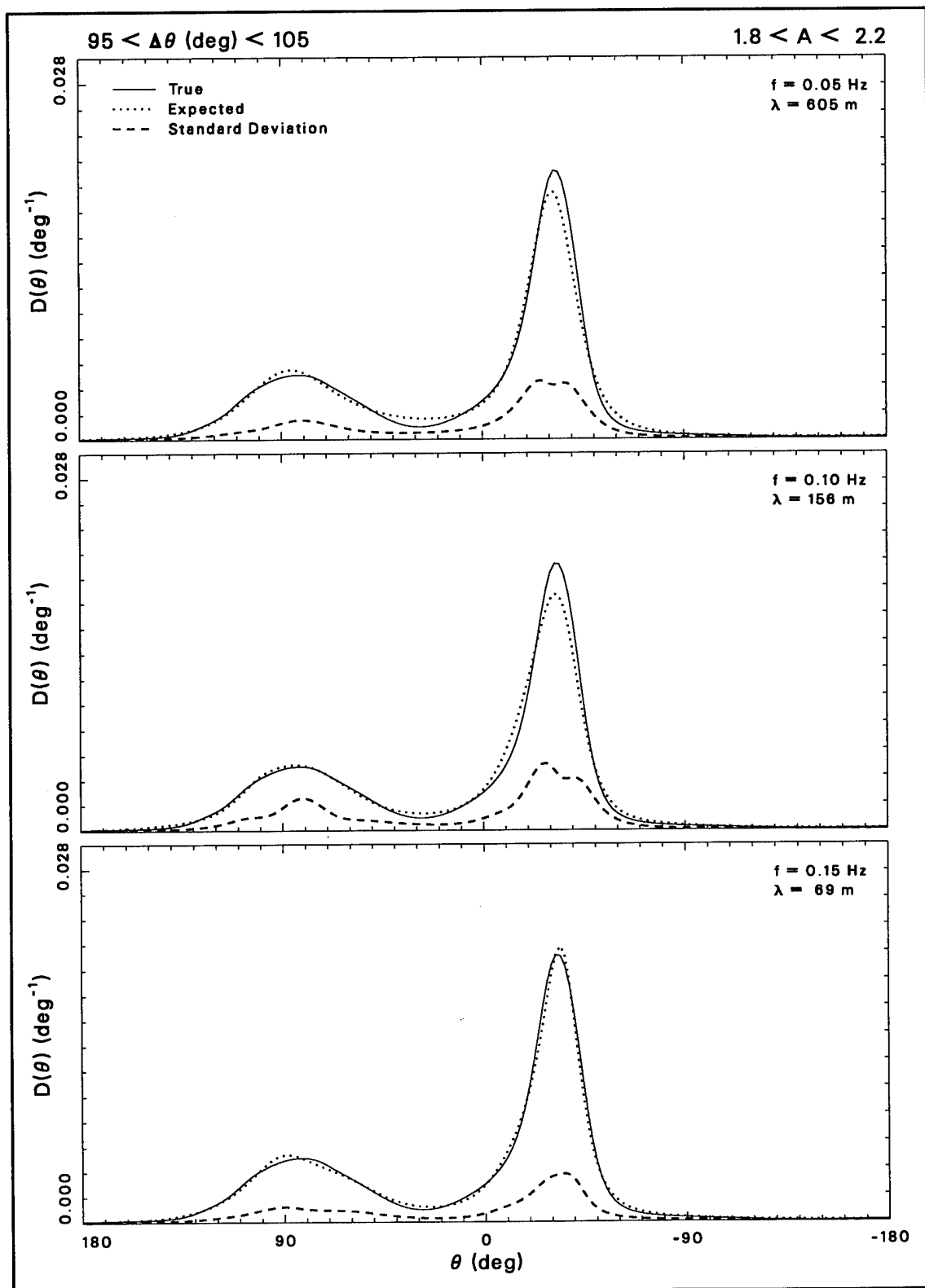


Figure D16. Test results for  $95 < \Delta\theta$  (deg) < 105, and  $1.8 < A < 2.2$

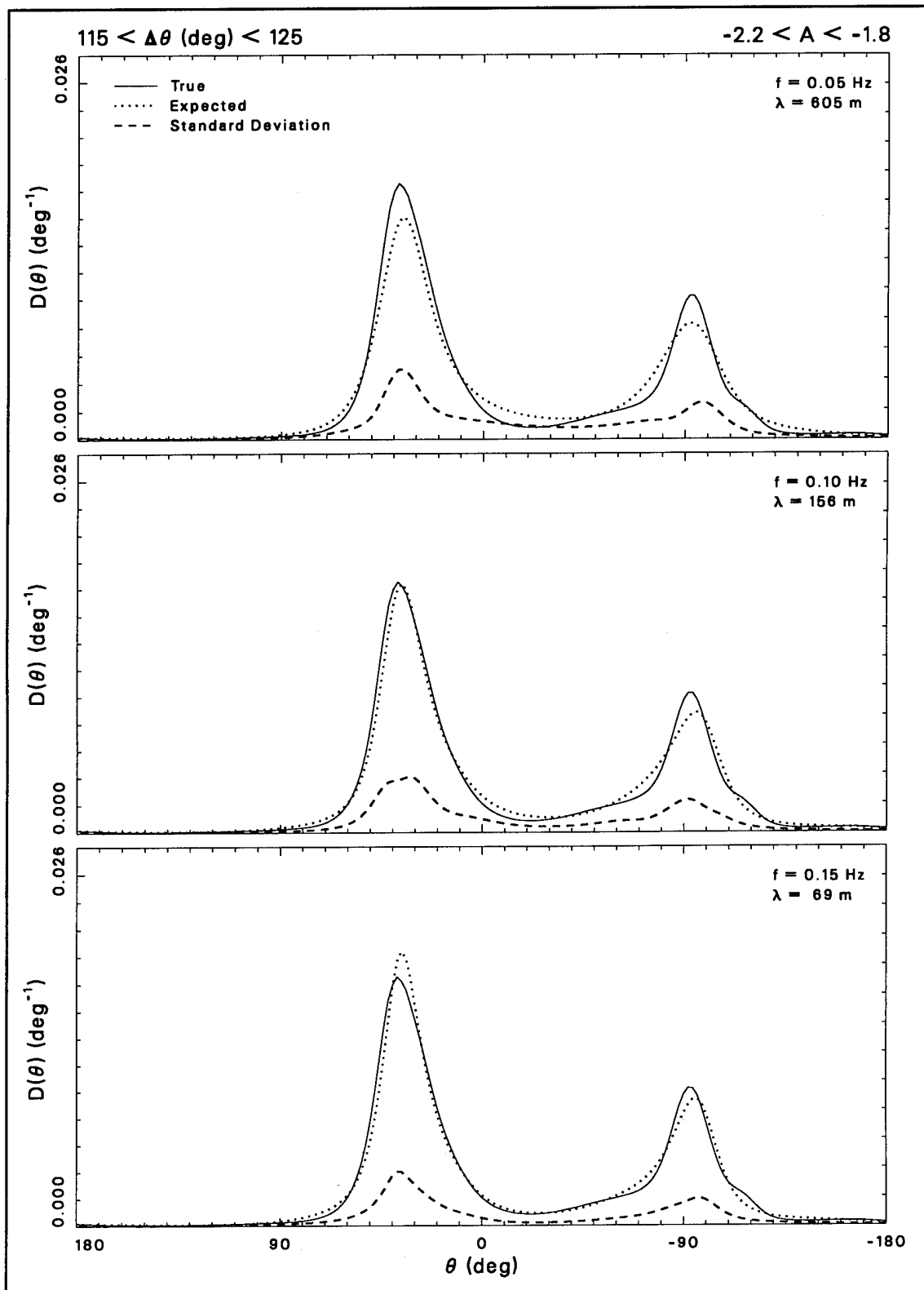


Figure D17. Test results for  $115 < \Delta\theta$  (deg)  $< 125$ , and  $-2.2 < A < -1.8$

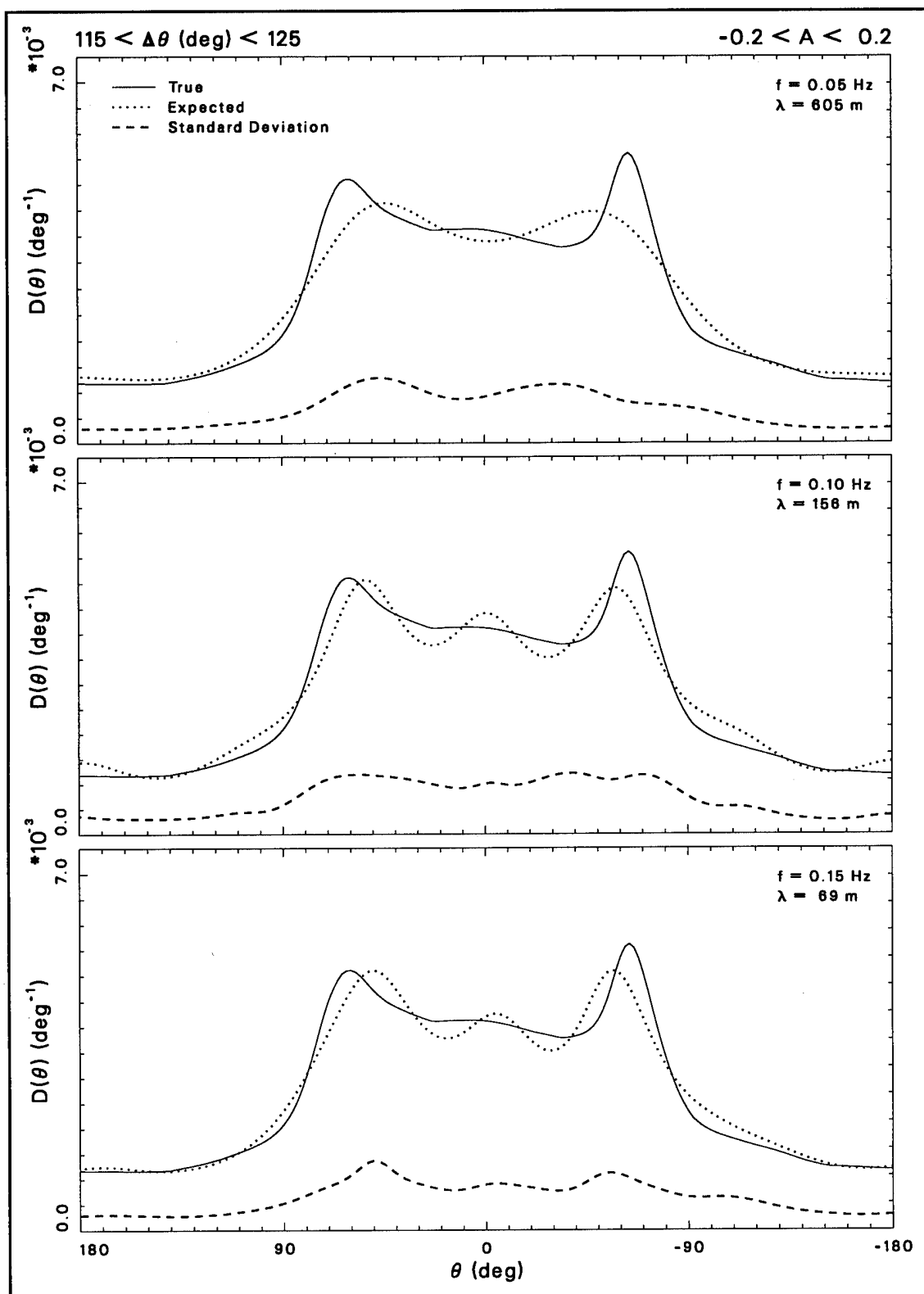


Figure D18. Test results for  $115 < \Delta\theta \text{ (deg)} < 125$ , and  $-0.2 < A < 0.2$

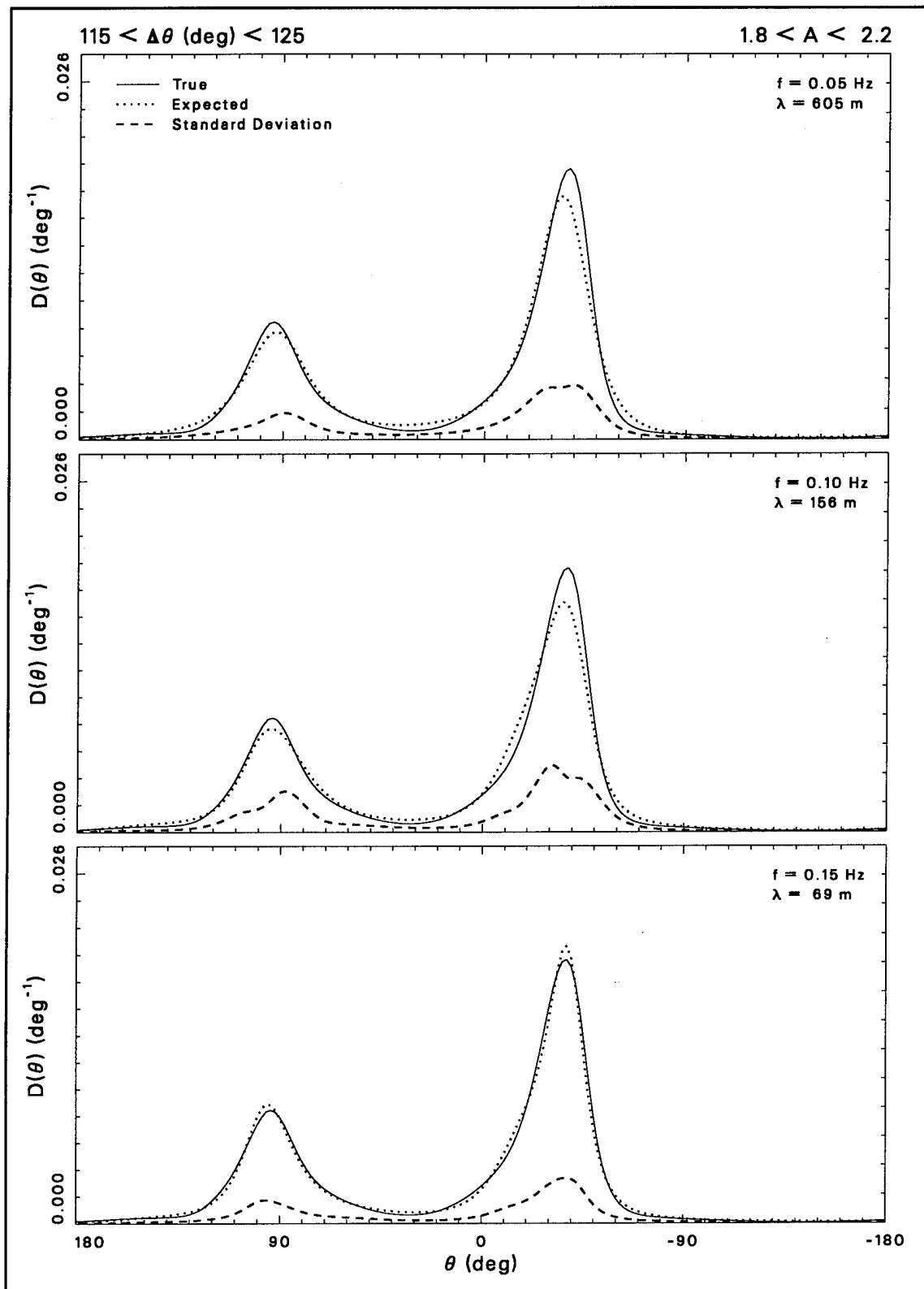


Figure D19. Test results for  $115 < \Delta\theta$  (deg) < 125, and  $1.8 < A < 2.2$



# Appendix E

## Notation

---

$*$	Complex conjugation operator
$a_0$	Normalizing coefficient in MLE to ensure unit area in a directional distribution estimate
$a_r$	Normalizing coefficient for $r^{th}$ iteration of IMLE to ensure unit area in a directional distribution estimate
$A$	Bulk quartile asymmetry parameter
$A_n$	Frequency-dependent quartile asymmetry parameter at $n^{th}$ discrete frequency
$C_{ij}(f_n)$	Coincident spectral density between gauges $i$ and $j$ at frequency $f_n$
$d$	Water depth
$df$	Discrete frequency increment
$d\theta$	Discrete direction increment
$D(\theta_m)$	Bulk directional distribution function formed by integrating frequency-direction spectrum with respect to frequency, and normalizing by total variance
$D(f_n, \theta_m)$	Directional distribution function at frequency $f_n$
$\bar{D}(f_n, \theta_m)$	Mean directional distribution function at test frequency $f_n$ , derived as the average at each $\theta_m$ of a number of synthetic estimates

$D_0(f_n, \theta_m)$	MLE estimate of directional distribution function at frequency $f_n$
$\bar{D}_{ij}(\theta_m - \theta_0)$	Mean directional distribution function displaced by its mean direction $\theta_0$ for the $i^{th}$ asymmetry class, and the $j^{th}$ directional spread class
$D_{ijk}(\theta_m - \theta_0)$	$k^{th}$ directional distribution function displaced by its mean direction in the $i^{th}$ asymmetry class and $j^{th}$ directional spread class
$\tilde{D}_k(f_n, \theta_m)$	$k^{th}$ directional distribution function at test frequency $f_n$ of a set of estimates subject to synthetic noise
$D_r(f_n, \theta_m)$	IMLE estimate of directional distribution function at frequency $f_n$ after $r^{th}$ iteration
$D'_r(f_n, \theta_m)$	Intermediate, uncorrected IMLE estimate of directional distribution function at frequency $f_n$ during $r^{th}$ iteration
$D_\sigma(f_n, \theta_m)$	Standard deviation directional distribution function at test frequency $f_n$ , derived as the square root of the variance at each $\theta_m$ of a number of synthetic estimates
$D_{\sigma ij}(\theta_m - \theta_0)$	Standard deviation directional distribution function displaced by its mean direction $\theta_0$ for the $i^{th}$ asymmetry class, and the $j^{th}$ directional spread class
$\hat{e}_x$	Unit vector in the $x$ -direction
$\hat{e}_y$	Unit vector in the $y$ -direction
$E[ \ ]$	Expectation operator
$f$	Frequency
$f_n$	$n^{th}$ discrete wave frequency
$f_p$	Spectral peak frequency
$g$	Gravitational acceleration
$H_{mo}$	Characteristic wave height

$i$	Complex notation $\sqrt{-1}$ [in exponent or on main equation line]
	Gauge index [as subscript in all chapters except Chapter 8]
	Asymmetry class index [as subscript Chapter 8]
$I$	Number of gauges in an array
$I(\theta_m - \theta_{m_{\min}})$	Integral of $D(\theta_m)$ beginning at direction $\theta_{m_{\min}}$
$I_n(\theta_m - \theta_{m_{\min}})$	Integral at the $n^{\text{th}}$ discrete frequency of $D(f_n, \theta_m)$ beginning at direction $\theta_{m_{\min}}$
$I$	Identity matrix
$j$	Gauge index [as subscript in all chapters except Chapter 8]
	Directional spread class index [as subscript in Chapter 8]
$k$	Index of contributing distribution function [as subscript in Chapter 8]
	Directional distribution estimate counter [as subscript in Chapter 9]
$k_n$	Magnitude of wave number vector associated with $n^{\text{th}}$ discrete frequency
$\overline{k}_n(\theta_m)$	Wave number vector for wave direction $\theta_m$ associated with $n^{\text{th}}$ discrete frequency
$l$	Summation index
$m$	Discrete direction index [as subscript]
$m_1$	First cosine moment of $D(\theta_m)$
$m_2$	Second cosine moment of $D(\theta_m)$
$m_{1n}$	First cosine moment of $D(f_n, \theta_m)$
$m_{2n}$	Second cosine moment of $D(f_n, \theta_m)$

$m_{\min}$	Discrete index of direction of minimum $D(f_n, \theta_m)$
$M$	Upper limit of direction index $m$
$M_{ij}(f_n)$	Element of cross-spectral matrix between gauges $i$ and $j$ at frequency $f_n$
$\tilde{M}_{ij}(f_n)$	Element of cross-spectral matrix with added synthetic noise between gauges $i$ and $j$ at test frequency $f_n$
${}^rM_{ij}(f_n)$	Estimate of element of cross-spectral matrix between gauges $i$ and $j$ at frequency $f_n$ during $r^{\text{th}}$ iteration of IMLE
$M$	Cross-spectral matrix
$\tilde{M}$	Cross-spectral matrix with added synthetic, Gaussian noise
$n$	Discrete frequency index [as subscript]
$n_1$	First sine moment of $D(\theta_m)$
$n_2$	Second sine moment of $D(\theta_m)$
$n_{1n}$	First sine moment of $D(f_n, \theta_m)$
$n_{2n}$	Second sine moment of $D(f_n, \theta_m)$
$N$	Upper limit of discrete frequency index
$Q_{ij}(f_n)$	Quadrature spectral density between gauges $i$ and $j$
$r$	Iteration count for IMLE
$R$	Upper limit for IMLE iterations
$\tilde{s}_1(f_n, \theta_m)$	Sum of synthetic directional distribution functions at each $\theta_m$ for test frequency $f_n$
$\tilde{s}_2(f_n, \theta_m)$	Sum of squares of synthetic directional distribution functions at each $\theta_m$ for test frequency $f_n$

$s_{1ij}(\theta_m - \theta_0)$	Sum of contributing directional distribution functions shifted by their mean directions in quartile asymmetry class $i$ and directional spread class $j$
$s_{2ij}(\theta_m - \theta_0)$	Sum of squares of contributing directional distribution functions shifted by their mean directions in quartile asymmetry class $i$ and directional spread class $j$
$S(f_n)$	Frequency spectrum
$S(\theta_m)$	Direction spectrum
$S(f_n, \theta_m)$	Frequency-direction spectrum
$S(f_p, \theta_m)$	Directional spectrum at spectral peak frequency $f_p$
$T$	Matrix transpose operator [as subscript in Chapter 9]
$U$	Eigenvector matrix of $M$
$V$	Matrix product of conjugate of eigenvector matrix and square root of eigenvalue matrix
$\tilde{V}$	Matrix product of $V$ and column vector $Z$ of random Gaussian deviates
$\bar{x}_i$	Position vector of $i^{\text{th}}$ gauge
$\bar{x}_j$	Position vector of $j^{\text{th}}$ gauge
$x$	Horizontal coordinate increasing northward
$y$	Horizontal coordinate increasing westward
$Z$	Column vector of random Gaussian deviates
$\beta$	Exponential convergence rate parameter in IMLE
$\gamma$	Convergence coefficient in IMLE
	Circular skewness
$\gamma_n$	Frequency-dependent circular skewness at frequency $f_n$
$\Gamma_{ij}(f_n)$	Coherence of signals from gauges $i$ and $j$ at frequency $f_n$

$\delta$	Circular kurtosis
$\delta_n$	Frequency-dependent circular kurtosis at frequency $f_n$
$\Delta\theta$	Quartile directional spread
$\Delta\theta_n$	Frequency-dependent quartile directional spread at frequency $f_n$
$\epsilon_r$	Convergence check parameter at $r^{th}$ IMLE iteration
$\theta_0$	Mean direction
$\theta_{0n}$	Frequency-dependent mean direction at frequency $f_n$
$\theta_{25\%}$	First quartile direction of $D(\theta_m)$
$\theta_{50\%}$	Second quartile direction of $D(\theta_m)$
$\theta_{75\%}$	Third quartile direction of $D(\theta_m)$
$\theta_{25\%,n}$	First frequency-dependent quartile direction of $D(f_n, \theta_m)$ at frequency $f_n$
$\theta_{50\%,n}$	Second frequency-dependent quartile direction of $D(f_n, \theta_m)$ at frequency $f_n$
$\theta_{75\%,n}$	Third frequency-dependent quartile direction of $D(f_n, \theta_m)$ at frequency $f_n$
$\theta_l$	$l^{th}$ discrete direction
$\theta_m$	$m^{th}$ discrete direction
$\theta_{m_{min}}$	Direction of minimum energy
$\theta_p$	Peak direction of $D(\theta_m)$
$\theta_{pn}$	Peak direction of $D(f_n, \theta_m)$ at frequency $f_n$
$\lambda$	Wavelength
$\lambda_r(f_n, \theta_m)$	IMLE correction function at the $r^{th}$ iteration
$\Lambda$	Diagonal matrix containing eigenvalues of $M$

$\sigma$	Circular width
$\sigma_n$	Frequency-dependent circular width at frequency $f_n$
$\phi_{ij}(f_n)$	Cross-spectral phase function of signals between gauges $i$ and $j$ at frequency $f_n$

**REPORT DOCUMENTATION PAGE**Form Approved  
OMB No. 0704-0188

Public reporting burden for this collection of information is estimated to average 1 hour per response, including the time for reviewing instructions, searching existing data sources, gathering and maintaining the data needed, and completing and reviewing the collection of information. Send comments regarding this burden estimate or any other aspect of this collection of information, including suggestions for reducing this burden, to Washington Headquarters Services, Directorate for Information Operations and Reports, 1215 Jefferson Davis Highway, Suite 1204, Arlington, VA 22202-4302, and to the Office of Management and Budget, Paperwork Reduction Project (0704-0188), Washington, DC 20503.

<b>1. AGENCY USE ONLY (Leave blank)</b>		<b>2. REPORT DATE</b> May 1995	<b>3. REPORT TYPE AND DATES COVERED</b> Final report	
<b>4. TITLE AND SUBTITLE</b> Directional Wind Wave Characteristics at Harvest Platform			<b>5. FUNDING NUMBERS</b>	
<b>6. AUTHOR(S)</b> Charles E. Long				
<b>7. PERFORMING ORGANIZATION NAME(S) AND ADDRESS(ES)</b> U.S. Army Engineer Waterways Experiment Station 3909 Halls Ferry Road, Vicksburg, MS 39180-6199			<b>8. PERFORMING ORGANIZATION REPORT NUMBER</b> Technical Report CERC-95-4	
<b>9. SPONSORING/MONITORING AGENCY NAME(S) AND ADDRESS(ES)</b> U.S. Army Corps of Engineers Washington, DC 20314-1000			<b>10. SPONSORING/MONITORING AGENCY REPORT NUMBER</b>	
<b>11. SUPPLEMENTARY NOTES</b> Available from National Technical Information Service, 5285 Port Royal Road, Springfield, VA 22161.				
<b>12a. DISTRIBUTION/AVAILABILITY STATEMENT</b> Approved for public release; distribution is unlimited.			<b>12b. DISTRIBUTION CODE</b>	
<b>13. ABSTRACT (Maximum 200 words)</b> <p>A high-resolution directional wave gauge has been installed on the Texaco Oil Company Harvest Platform, located at about the 200-m depth contour approximately 20 km west of Point Conception, California. This report describes the physical attributes of the gauge, data error checking and analysis algorithms, typical results, and tests that quantify wave direction resolving ability. Included are climatological and statistical analyses of 2,339 directional-spectral observations made during calendar year 1993.</p>				
<b>14. SUBJECT TERMS</b> Deep water Frequency-direction spectra Wave climate Wind Waves			<b>15. NUMBER OF PAGES</b> 182	
			<b>16. PRICE CODE</b>	
<b>17. SECURITY CLASSIFICATION OF REPORT</b> UNCLASSIFIED	<b>18. SECURITY CLASSIFICATION OF THIS PAGE</b> UNCLASSIFIED	<b>19. SECURITY CLASSIFICATION OF ABSTRACT</b>	<b>20. LIMITATION OF ABSTRACT</b>	



Destroy this report when no longer needed. Do not return it to the originator.